Measurement of the muon neutrino charged current pion production cross-section on water using the T2K near detector

Linda Cremonesi

School of Physics and Astronomy

Queen Mary University of London

Submitted in partial fulfillment of the requirements of the

Degree of Doctor of Philosophy,

April 2015

Declaration

I, Linda Cremonesi, confirm that the research included within this thesis is my own work or that where it has been carried out in collaboration with, or supported by others, that this is duly acknowledged below and my contribution indicated. Previously published material is also acknowledged below.

I attest that I have exercised reasonable care to ensure that the work is original, and does not to the best of my knowledge break any UK law, infringe any third partys copyright or other Intellectual Property Right, or contain any confidential material.

I accept that the College has the right to use plagiarism detection software to check the electronic version of the thesis.

I confirm that this thesis has not been previously submitted for the award of a degree by this or any other university.

Signature:

Date:

Abstract

T2K is a long baseline neutrino experiment which uses a beam of muon neutrinos, produced at J-PARC and detected at Super-Kamiokande, to study the neutrino oscillation parameters. The measurement of cross-sections in the T2K energies can constrain the uncertainties on the model predictions and help the oscillation analyses reach the necessary sensitivity to measure CP violation in the lepton sector.

This thesis describes the measurement of the ν_μ CC1π^+ cross-section in water using Run II-IV T2K data. The T2K near detector, ND280, is used to select a sample of ν_μ CC1π^+ events having vertices in the water layers of the downstream fine-grained detector (FGD). The Time Projection Chambers (TPC) are used for the particle identification and to measure their momenta. The Electromagnetic Calorimeters (ECals) are used to reject events that produce electromagnetic showers coming from neutral pions. A Bayesian unfolding method with background subtraction and two control samples is used to extract the cross-section. The control samples constrain the background coming from interactions on carbon and deep inelastic scattering. The single differential cross-section is presented as a function of the muon kinematics, the pion kinematics, the angle between the muon and the pion, and the reconstructed neutrino energy.

A future long baseline experiment between J-PARC and Hyper-Kamiokande is presented as a natural continuation to the T2K experiment. Hyper-Kamiokande will be a next generation water Cherenkov detector with a total (fiducial) mass of 0.99 (0.56) million metric tons. A total exposure of $7.5\,\mathrm{MW} \times 10^7\,\mathrm{sec}$ integrated beam power will lead to the measurement of δ_{CP} to better than 19 degrees for all possible values of δ_{CP}. CP violation in the lepton sector could be established at better than $3\,\sigma$ ($5\,\sigma$) for 76% (58%) of the δ_{CP} parameter space.

Acknowledgements

I am deeply grateful to Prof Francesca Di Lodovico for her constant support, supervision and mentoring throughout these almost 4 years at Queen Mary. I would like to acknowledge the enormous help I received from Dr Ryan Terri and Dr Samantha Short including daily conversations about the different analyses I worked on and their development.

I would also like to thank my examiners, Prof David Waters and Dr Steven Boyd, for the extremely interesting discussion and comments received during the viva.

Special thanks go to Dr Martin Hierholzer who designed and helped us develop the `xsTool`. I am deeply grateful to Raquel Castillo and Enrico Scantamburlo with whom I shared the challenge of the single pion selection and water analysis, respectively. This analysis would have not been possible without the contribution of the ND280 NuMu and NuE analysis groups which developed most of the detector systematic uncertainties.

I would also like to thank Dr Megan Friend and Dr Motoyasu Ikeda for the great help I received while adapting the `Simple Fitter` analysis to the Hyper-Kamiokande long baseline experiment.

I am extremely grateful to all of my colleagues at Queen Mary who were there for the moments of success and desperation, and who heard me cheering and complaining for each and every step of the analysis. Sophie, Ela, Paul, Pierre, Marc, Cristiano, Ruth and Terry; thank you.

During my PhD I had the great opportunity to spend 10 months in Tokai-mura and then travel there several times following my return to the UK. Japan turned out to be an amazing experience thanks to the friendship of Sarah, Megan, Jevon, Ben, Matt, Andy and Aya.

I am incredibly thankful for the constant support provided by my parents, my brother and my sister throughout my academic and personal life. Finally, none of this would have been possible without Jenni's unique way of supporting, challenging and encouraging me in my professional life. Thank you.

Contents

List of Figures

List of Tables

Glossary

PØD π^0 detector

CC Charged Current

CCCOH Charged Current COHerent

CCDIS Charged Current Deep Inelastic Scattering

CCQE Charged Current Quasi-Elastic

CCRES Charged Current RESonant

CP Charge Parity

CT Current Trasformers

DAQ Data AQuisition

Ds-ECal Downstream ECal module

ECals Electromagnetic Calorimeters

FGDs Fine Grained Detectors

FSI Final State Interactions

Highland High level analysis at the near detector

ID Inner Detector

INGRID Interactive Neutrino GRID

J-PARC Japan Proton Accelerator Research Complex

LINAC LINear ACcelerator

MC Monte Carlo

MCM Master Clock Module

MEC Meson Exchange Currents

MIP Minimum Ionising Particle

MPPC Multi-Pixel Photon Counter

MR Main Ring

NC Neutral Current

NCQE Neutral Current Quasi-Elastic

ND280 Near Detector at 280 m

OD Outer Detector

PID Particle IDentification

PMT PhotoMultiplier Tube

POT Protons On Target

RCS Rapid Cycling synchrotron

RFG Relativistic Fermi Gas

RMM Readout Merger Module

SCM Slave Clock Module

SK Super-Kamiokande

SMRDs Side Muon Range Detectors

T2K Tokai to Kamioka

TFB Trip-t Front end Board

TPCs Time Projection Chambers

WLS fibre WaveLength Shifting fibre

1

Introduction

This thesis presents a measurement of the ν_μ charged current single positive pion production cross-section on water using the T2K near detector, ND280.

Chapter 2 briefly introduces the neutrino properties, the most recent results from currently running experiments, and open questions for future experiments to answer. Neutrino oscillation experiments rely on the detection of charged particles to infer neutrino interactions. Therefore, the neutrino interaction models need to be extremely well understood to infer the neutrino properties correctly. Section 2.5 highlights the dominant interactions at the T2K energy scales, the theoretical models considered, and the latest experimental results. Discrepancies between data and corresponding models are especially seen in the CC1π^+ channel (Subsection 2.5.3), which is the main interest of this thesis.

The T2K experiment layout is presented in Chapter 3. First the beamline and far detector are described, then the near detector, ND280, used for the selection of the analysis described in this thesis, is delineated in detail. Chapter 4 summarises the ND280 software, from the neutrino simulation, to the reconstruction and analysis of the events.

As part of the service task undertaken during my PhD, I monitored the data quality of the Electromagnetic Calorimeters (ECals) inside the ND280 detector. Chapter 5 summarises the weekly checks performed and the global data quality flag used in the analysis.

The selection of the ν_μ CC1π^+ sample in the water layers of the fine-grained detectors (FGDs) of ND280 is explained in Chapter 6. A summary of the detector and theory systematic uncertainties associated with the event selection is given in Chapter 7.

Chapter 8 introduces the Bayesian unfolding method as the chosen technique to extract the cross-section. Several tests with different fake data-sets are performed to check the robustness of the unfolding algorithm. Several variables are used for the flux integrated single differential cross-section:

- the pion kinematics variables: $\frac{d\sigma}{dp_{\pi^+}}$, $\frac{d\sigma}{d\cos\theta_{\pi^+}}$ (p_{π^+} and θ_{π^+} are the charged pion momentum and angle with the beam direction) ;
- the muon kinematics variables: $\frac{d\sigma}{dp_{\mu}}$, $\frac{d\sigma}{d\cos\theta_{\mu}}$ (p_{μ^-} and $\cos\theta_{\mu^-}$ are the muon momentum and angle with the beam direction);
- the muon-pion angle: $\frac{d\sigma}{d\cos\theta_{\mu^-,\pi^+}}$;
- the reconstructed neutrino energy: $\sigma(E)$ (the flux averaged cross-section is presented).

These single differential measurements, together with the total flux averaged cross-sections, and a comparison with the simulation are presented in Section 8.4.

Chapter 9 provides a look to a future experiment. The sensitivity for a long baseline neutrino oscillation experiment between J-PARC and the new generation water Cherenkov detector, Hyper-Kamiokande, is presented.

Chapter 10 provides a brief summary of the contents of this thesis.

2

Neutrinos

2.1 Introduction

Neutrinos are fundamental particles of the Standard Model of Particle Physics. They are chargeless and colourless, hence only interact through gravity and the weak nuclear force.

Their existence was first postulated by Wolfgang Pauli in 1930 [1] to explain the continuous spectrum of β decay. Later, in 1953, Reines and Cowan observed $\overline{\nu}_{\mathrm{e}} + \mathrm{p} \rightarrow \mathrm{e}^{+} + \mathrm{n}$ at the Savannah River reactor [2], providing the first experimental observation of neutrinos.

According to the Standard Model, neutrinos come in three flavours: ν_{e}, ν_{μ} and ν_{τ}, and they are paired with their corresponding charged lepton: the electron (e), the muon (μ) and the tau (τ). The number of light neutrinos (i.e. below the Z mass) weakly interacting was confirmed to be $N_{\nu} = 2.984 \pm 0.008$ by the LEP experiment [3], by looking at Z production in $\mathrm{e}^{-}\mathrm{e}^{+}$ collisions.

In the Standard Model all neutrinos are considered to be massless; this implies that all neutrinos have left-handed chirality and all antineutrinos have right-handed chirality.

2.2 Neutrino Oscillations

2.2.1 Historical notes

Neutrinos are constantly produced (mainly from the p − p chain and the CNO cycle) in the Sun with a net reaction of:

$$4\mathrm{p} \rightarrow^{4} \mathrm{He} + 2\mathrm{e}^{+} + 2\nu_{\mathrm{e}} + 26.731\,\mathrm{MeV}\ .$$

From the late 1960s several experiments (Homestake [4], SAGE [5] and GALLEX [6]) tried to measure the solar electron neutrino flux and found that the number of neutrinos detected was between one third and one half of what the Standard Solar Model predicts.

In 1957, Bruno Pontecorvo proposed the idea of neutrino oscillations between neutrinos and antineutrinos [7] to explain the missing neutrinos. In 1962 Z. Maki, M. Nakagawa and S. Sakata formulated the theory for neutrino flavour oscillation [8], which combined with the theory of matter effects on neutrinos proposed by Mikheyev, Smirnov and Wolfenstein (the so-called MSW effect) could account for the observed discrepancies in the solar neutrino flux.

In 1998 the Super-Kamiokande (SK) [9] experiment provided evidence for neutrino oscillations, when it detected a deficit of ν_{μ} produced by cosmic rays interacting with the atmosphere. Looking at the zenith angle it was possible to reconstruct the path distance travelled by the neutrinos from the production in the upper atmosphere to the detection point. The deficit showed a dependence in this distance that could be explained by the theory of neutrino oscillations.

In 2001 the SNO experiment measured the flux of all the 3 flavours of neutrinos and found consistent results with the prediction of the Standard Solar Model [10].

Both these measurements firmly established the existence of neutrino oscillations and started the contemporary neutrino oscillation experiments era.

2.2.2 Neutrino oscillation framework

The fundamental principle of neutrino oscillations is that the neutrino flavour eigenstates are not identical to the neutrino mass eigenstates; this implies that neutrinos

are not massless and that they can change their flavour during propagation (hence the name "neutrino oscillations").

The neutrino flavour eigenstate $|\nu_\alpha\rangle$ can be expressed as a superposition of the mass eigenstates $|\nu_i\rangle$ using the unitary matrix U, known as the Pontecorvo-Maki-Nakagawa-Sakata (PMNS) [11] neutrino mixing matrix:

$$|\nu_\alpha\rangle = \sum_{i=1}^{3} U^*_{\alpha i}|\nu_i\rangle \ , \tag{2.1}$$

where $\alpha \in \{\mathrm{e}, \mu, \tau\}$.

The PMNS matrix is a 3×3 complex unitary matrix that can be parametrised as:

$$U = \begin{pmatrix} 1 & 0 & 0 \\ 0 & c_{23} & s_{23} \\ 0 & -s_{23} & c_{23} \end{pmatrix} \begin{pmatrix} c_{13} & 0 & s_{13}e^{-i\delta} \\ 0 & 1 & 0 \\ -s_{13}e^{+i\delta} & 0 & c_{13} \end{pmatrix} \begin{pmatrix} c_{12} & s_{12} & 0 \\ -s_{12} & c_{12} & 0 \\ 0 & 0 & 1 \end{pmatrix} \begin{pmatrix} 1 & 0 & 0 \\ 0 & e^{i\alpha} & 0 \\ 0 & 0 & e^{i\beta} \end{pmatrix} , \tag{2.2}$$

where $s_{ij} = \sin\theta_{ij}$, $c_{ij} = \cos\theta_{ij}$ and θ_{ij} is the mixing angle; δ is a CP-violating phase, and α and β are Majorana phases that have no effect on neutrino oscillations.

If a neutrino is produced at a time $t = 0$ in the state ν_α, the time evolution of neutrino flavour states is given by:

$$|\nu_\alpha(t)\rangle = \sum_{i=1}^{3} U^*_{\alpha i} e^{-iE_i t}|\nu_i\rangle \ . \tag{2.3}$$

Similarly, a mass eigenstate can be expressed as a superposition of the flavour eigenstates:

$$|\nu_i\rangle = \sum_{\beta} U_{\beta i}|\nu_\beta\rangle, \qquad \beta = \mathrm{e}, \mu, \tau \ . \tag{2.4}$$

Then, the state $|\nu_\alpha(t)\rangle$ can be expressed in the basis of the weak flavour $|\nu_\beta\rangle$:

$$|\nu_\alpha(t)\rangle = \sum_{\beta}\sum_{i=1}^{3} U_{\beta i} e^{-iE_i t} U^*_{\alpha i}|\nu_\beta\rangle \ . \tag{2.5}$$

Then, the probability of $\nu_\alpha \to \nu_\beta$ transitions is given by:

$$P(\nu_\alpha \to \nu_\beta) = |A_{\nu_\alpha \to \nu_\beta}(t)|^2 = |\sum_{i=1}^{3} U_{\beta i} e^{-iE_i t} U^*_{\alpha i}|^2 \ . \tag{2.6}$$

As neutrinos are highly relativistic ($E \approx |p|$), this approximation can be made:

$$E_i = \sqrt{p^2 + m_i^2} \approx E + \frac{m_i^2}{2E} \,, \tag{2.7}$$

and the oscillation probability can be re-written as:

$$P(\nu_\alpha \to \nu_\beta) = \sum_{i,j=1}^{3} U^*_{\alpha i} U_{\beta i} U_{\alpha k} U^*_{\beta j} e^{-i\frac{\Delta m^2_{i,j}}{2E}t} \,. \tag{2.8}$$

where $\Delta m^2_{ij} = m^2_j - m^2_i$ is the mass squared difference of neutrino mass eigenstates in eV^2.

The T2K neutrino oscillation experiment probes oscillations coming from a muon neutrino beam. The oscillation and survival probabilities are:

$$P(\nu_\mu \to \nu_\mathrm{e}) \simeq \sin^2 2\theta_{13} \sin^2 \theta_{23} \sin^2 \left(1.27 \frac{\Delta m^2_{32}}{(\mathrm{eV}^2)} \frac{L}{(\mathrm{km})} \frac{(\mathrm{GeV})}{E_\nu} \right) \,, \tag{2.9}$$

$$P(\nu_\mu \to \nu_\mu) \simeq 1 - \cos^4 \theta_{13} \sin^2 2\theta_{23} \sin^2 \left(1.27 \frac{\Delta m^2_{32}}{(\mathrm{eV}^2)} \frac{L}{(\mathrm{km})} \frac{(\mathrm{GeV})}{E_\nu} \right) \,, \tag{2.10}$$

where L is the distance travelled by neutrinos in km, E_ν is neutrino energy in GeV, and the factor 1.27 comes from $1/\hbar c$ in the conversion of units to km and GeV. These equations show that the magnitude of the $\nu_\mu \to \nu_\mathrm{e}$ oscillations is governed by the mixing angles θ_{13} and θ_{23}, whereas the frequency of oscillations depends on Δm^2_{32}.

When we measure θ_{23} with the survival probability $P(\nu_\mu \to \nu_\mu)$ which is proportional to $\sin^2 2\theta_{23}$ to first order, there is an octant ambiguity: either $\theta_{23} \leq 45°$ (in the first octant) or $\theta_{23} > 45°$ (in the second octant). By combining the measurements of $P(\nu_\mu \to \nu_\mu)$ and $P(\nu_\mu \to \nu_\mathrm{e})$, future long baseline experiments, like Hyper-Kamiokande [12] and DUNE [13], can reach the necessary sensitivity to determine the θ_{23} octant.

The formal 3-flavour probability for neutrino oscillations in vacuum can be written as:

$$P(\nu_\alpha \to \nu_\beta) = \delta_{\alpha\beta}$$

$$-4\sum_{i>j}\Re(U^*_{\alpha i}U_{\beta i}U^*_{\alpha j}U^*_{\beta j})\sin^2[1.27\Delta m^2_{ij}(L/E)]$$

$$+2\sum_{i>j}\Im(U^*_{\alpha i}U_{\beta i}U^*_{\alpha j}U^*_{\beta j})\sin[2.54\Delta m^2_{ij}(L/E)] \tag{2.11}$$

where the symbols are those previously defined, and U it the PMNS matrix.

2.2.3 Neutrino oscillations in matter

When neutrinos travel through matter, their propagation is modified by the coherent forward scattering from particles they encounter, consequently changing their oscillation probability.

Mikhaev, Smirnov and Wolfenstein (MSW) were the first to study neutrino oscillations in matter [14]. The MSW effect relies on the fact that electron (anti)neutrinos have different interactions with matter compared to muon and tau (anti)neutrinos. This is because matter is made up of electrons (but not of muons or taus), hence ν_{e} can have both charged current and neutral current elastic scattering with electrons, whereas ν_μ and ν_τ can only interact with matter via neutral current channels. An effective potential term is added to the Hamiltonian to take into account of the MSW effect: this term is proportional to the neutrino energy and the density of electrons in the material it traverse, and it has opposite sign for ν_{e} and $\overline{\nu}_{\mathrm{e}}$.

By considering this extra-potential, we obtain an oscillation probability that is dependent on the mass hierarchy. The oscillation probability from ν_μ to ν_{e} in accelerator experiments is expressed, to first order in the matter effect, as the sum of five terms [15]:

$$P(\nu_\mu \to \nu_{\mathrm{e}}) = T_{\mathrm{leading}} + T_{\mathrm{CPC}} + T_{\mathrm{CPV}} + T_{\mathrm{solar}} + T_{\mathrm{matter}}\ , \tag{2.12}$$

where T_{leading} is the leading term, T_{CPC} is the CP conserved term, T_{CPC} is the CP violating term, T_{solar} is the CP solar term, and T_{matter} is the matter term. These terms

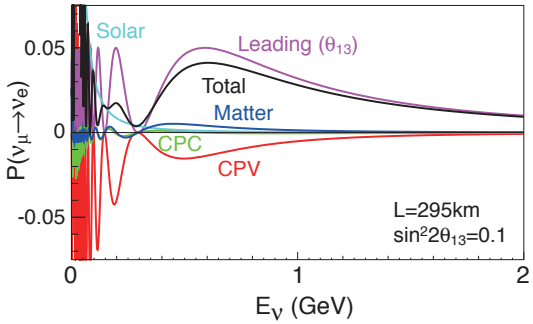

Figure 2.1: Different contributions of the oscillation probability formula for $\nu_\mu \to \nu_e$ transitions as a function of the neutrino energy, as detailed in Equations 2.12 and 2.13. A baseline of 295 km, $\sin^2 2\theta_{13} = 0.1$, $\delta_{CP} = \frac{1}{2}\pi$ and normal mass ordering are assumed.

are defined as:

$$
\begin{aligned}
T_{\text{leading}} &= +\,4c_{13}^2 s_{13}^2 s_{23}^2 \cdot \sin^2 \Delta_{31} \\
T_{\text{CPC}} &= +\,8c_{13}^2 s_{12} s_{13} s_{23} (c_{12} c_{23} \cos\delta_{CP} - s_{12} s_{13} s_{23}) \cdot \cos\Delta_{32} \cdot \sin\Delta_{31} \cdot \sin\Delta_{21} \\
T_{\text{CPV}} &= -\,8c_{13}^2 c_{12} c_{23} s_{12} s_{13} s_{23} \sin\delta_{CP} \cdot \sin\Delta_{32} \cdot \sin\Delta_{31} \cdot \sin\Delta_{21} \\
T_{\text{solar}} &= +\,4s_{12}^2 c_{13}^2 (c_{12}^2 c_{23}^2 + s_{12}^2 s_{23}^2 s_{13}^2 - 2c_{12} c_{23} s_{12} s_{23} s_{13} \cos\delta_{CP}) \cdot \sin^2 \Delta_{21} \\
T_{\text{matter}} &= -\,8c_{13}^2 s_{13}^2 s_{23}^2 \cdot \frac{aL}{4E_\nu} (1 - 2s_{13}^2) \cdot \cos\Delta_{32} \cdot \sin\Delta_{31} \\
&\quad +\,8c_{13}^2 s_{13}^2 s_{23}^2 \frac{a}{\Delta m_{31}^2} (1 - 2s_{13}^2) \cdot \sin^2 \Delta_{31} \,,
\end{aligned}
\tag{2.13}
$$

where Δ_{ij} is $\Delta m_{ij}^2 L/4E_\nu$, and $a[\text{eV}^2] = 7.56 \times 10^{-5} \times \rho[\text{g/cm}^3] \times E_\nu[\text{GeV}]$. T_{CPV} containing $\sin\delta_{CP}$, is the CP violating term which flips sign between ν and $\overline{\nu}$ and introduces CP asymmetry if $\sin\delta_{CP}$ is non-zero. Figure 2.1 shows the different contributions of each term in the oscillation probability formula. Assuming $\sin^2 2\theta_{13} = 0.1$, $\sin^2 2\theta_{23} = 1.0$, and $\delta_{CP} = \pi/2$ with normal mass ordering, the effect of the CP violating term can be as large as 27% of the leading term, making long baseline experiments one of the most promising ways of discovering CP violation in the lepton sector.

2.3 Current status of neutrino oscillation physics

Current neutrino oscillation experiments can use sources of neutrinos that are natural (solar and atmospheric experiments) or artificial (reactor and accelerator experiments).

Table 2.1: Experimentally determined values of neutrino oscillation parameters, as reported by Particle Data Group in 2014 [22].

Parameter	Current Value
$\sin^2(2\theta_{12})$	0.846 ± 0.021
$\sin^2(2\theta_{23})$	$0.999^{+0.001}_{-0.018}$
$\sin^2(2\theta_{13})$	0.093 ± 0.008
Δm^2_{21}	$(7.53 \pm 0.18) \times 10^{-5}\,\mathrm{eV}^2$
$\lvert\Delta m^2_{32}\rvert$	$(2.52 \pm 0.07) \times 10^{-3}\,\mathrm{eV}^2$ [assuming IH]
	$(2.44 \pm 0.06) \times 10^{-3}\,\mathrm{eV}^2$ [assuming NH]
δ_{CP}	$(-\pi, \pi)$ unknown

Solar experiments detect low energy (in the MeV scale) ν_e produced in nuclear reactions in the core of the sun. These experiments were the first to prove the existence of solar neutrinos (Homestake [4], SAGE [5] and GALLEX [6], Super-Kamiokande [9], SNO [10]), and they are most sensitive to θ_{12} and Δm^2_{21}.

Atmospheric experiments detect the neutrinos produced by the interactions of cosmic rays with nuclei in the upper atmosphere. Cascades of pions, kaons, muons and electrons produce in turn ν_μ, $\overline{\nu}_\mu$, ν_e and $\overline{\nu}_\mathrm{e}$ at energies from MeV to TeV. Super-Kamiokande and MINOS [16] are examples of atmospheric neutrino experiments that are mainly sensitive to θ_{23} and Δm^2_{32}.

Reactor experiments measure the disappearance spectrum of $\overline{\nu}_\mathrm{e}$ at MeV energies produced by nuclear reactors. KamLAND [17] using the old Kamiokande tank is sensitive to θ_{12}, whereas Daya Bay [18], RENO [19] and Double CHOOZ [20] precisely measure θ_{13}.

Long baseline accelerator experiments, like MINOS, T2K and NOνA [21] use GeV muon neutrinos produced by pion decay in an accelerator complex. These experiments are mostly sensitive to θ_{13}, θ_{23} and Δm^2_{32}. Future experiments, like Hyper-Kamiokande [12] and DUNE [13], could also lead to the measurement of δ_{CP}.

Table 2.1 shows the neutrino oscillation measured parameters, evaluated from a global analysis performed by the Particle Data Group.

2.4 Open questions in neutrino physics

In this Section we will explore the major open questions in neutrino physics.

2.4.1 Normal or inverted ordering?

Although Δm^2_{21} has been measured with better than 3% uncertainty (see Table 2.1), the sign of Δm^2_{32} is still unknown. Two mass orderings are then possible: *the normal ordering* (NO) where $m_1 < m_2 < m_3$ or *the inverted ordering* (IO) where $m_3 < m_1 < m_2$. By considering matter effects in long baseline experiments, neutrino-less double β decay, and other experimental techniques, we will be able to determine the correct ordering.

2.4.2 Hierarchical or degenerate?

Depending on the value of the lightest neutrino mass, the mass spectrum can be: *hierarchical* with $m_1 \ll m_2 < m_3$ for NO (NH) and $m_3 \ll m_1 < m_2$ for IO (IH), or *quasi-degenerate* (QD) where $m_1 \cong m_2 \cong m_3$. As seen in Equation 2.11, the neutrino oscillation probability depends only on the mass squared difference, but not on the absolute mass of neutrinos. Oscillation experiments cannot measure the absolute mass of neutrinos.

Cosmological and astrophysical data can put upper bounds on the sum of the masses of the three neutrino flavours at 0.3 eV [23].

Direct neutrino mass measurements are possible by measuring the spectrum of electrons at the end point of Tritium decay $^3\mathrm{H} \rightarrow ^3\mathrm{He} + \mathrm{e}^- + \overline{\nu}_\mathrm{e}$. The KATRIN [24] experiment will reach the sensitivity of $m(\overline{\nu}_\mathrm{e}) \approx 0.2\,\mathrm{eV}$.

2.4.3 Dirac or Majorana?

Neutrinos are massless in the Standard Model, and since neutrino oscillations have been confirmed by many experiments, a formalism to account for neutrino masses is needed. If neutrinos are Dirac particles, their mass could be generated using the standard Higgs mechanism and by requiring the addition of right-handed components of the neutrino field (i.e. sterile neutrinos). If neutrinos are Majorana particles, then they can be described by a real wave-function and hence be their own anti-particle.

Experiments looking for neutrino-less double beta decay, such as SuperNEMO [25] and SNO+ [26], will determine whether neutrinos are Majorana or Dirac particles.

2.4.4 CP violation in the lepton sector?

CP violation has been observed in the quark sector, but it is not sufficient to explain the matter/anti-matter asymmetry in the present universe. Measuring a δ_{CP} phase different than 0 or π would produce CP violation in the leptonic sector and hence complete the picture of the PMNS matrix (although lepton and baryion CP violations by themselves will not be sufficient to describe the mater/anti-matter asymmetry in the present universe). Current long baseline neutrino experiments, such as T2K or NOνA, could give some hints on the preferred values of δ_{CP}. Future experiments, like Hyper-K or DUNE, will measure δ_{CP} more precisely.

2.4.5 Do sterile neutrinos exist?

Short baseline neutrino experiments found large mass splittings that are inconsistent with the three-flavour neutrino oscillation framework. These anomalies can be explained by the addition of a fourth neutrino generation that must not interact through the weak force (hence the name *sterile* neutrinos).

The LSND experiment [27] was the first to observe these anomalies when it found $\overline{\nu}_{\mathrm{e}}$ appearance in a $\overline{\nu}_{\mu}$ beam, consistent with $\Delta m^2 \approx 0.2 - 10\,\mathrm{MeV}$. The MiniBooNE experiment looking at the ν_{e} appearance in a ν_{μ} beam found an excess at low energy which is not compatible with the LSND measurement. Looking at $\overline{\nu}_{\mathrm{e}}$ in a $\overline{\nu}_{\mu}$ beam, they found an excess consistent with $0.01 < \Delta m^2 < 1.0\,\mathrm{MeV}$ [28].

Nonetheless, these anomalies have not been observed by long-baseline muon neutrino disappearance analyses (e.g. in Super-Kamiokande [29] and MINOS [29]) and tensions with cosmological data [30] make the existence of sterile neutrinos still uncertain.

2.5 Neutrino interactions

As previously stated, neutrinos are chargeless, colour-less, and can only interact through the weak nuclear force and gravity (which is extremely weak since the mass of neutrinos

has an upper limit of 0.3 eV). Neutrino oscillation experiments detect the products of the neutrino interactions, and therefore it is fundamental to understand neutrino interactions to infer any neutrino property.

Weak nuclear interactions are mediated by the W boson (Charge Current interactions, CC) or by the Z boson (Neutral Current interactions, NC).

CC interactions produce a charged lepton associated with the flavour of the interacting neutrino; detecting this lepton makes it possible to understand the flavour of the neutrino. NC interactions do not involve any charge exchange, hence the outgoing product is still a neutrino, which, being electrically neutral, cannot be directly detected. When an NC interaction occurs, it is impossible to determine the flavour of the incoming neutrino.

The dominant interaction modes for GeV-scale neutrinos are: charge current quasi-elastic (CCQE), neutral current quasi-elastic (NCQE), charge current resonant pion production (CCRES), neutral current resonant pion production (NCRES), and charge current deep inelastic scattering (CCDIS).

CCQE (Figure 2.2a) and NCQE interactions are the dominant processes for neutrino energies below 1 GeV (above threshold). In CCQE interactions the neutrino converts a d quark to a u quark with the exchange of a W boson. In NCQE interactions the nucleon is left unchanged: in both cases the neutrino interacts with the nucleon as a whole.

At neutrino energies above 1 GeV, the target nucleon can be excited into a baryonic resonance that soon decays into a nucleon and a pion. These are CCRES (Figure 2.2b) interactions. Even in this case, the neutrino interacts with the nucleon as a whole.

Neutrinos can also interact with the entire target nucleus coherently and still produce one single pion in the final state. These coherent processes can occur in both neutral current interactions, and charged current interactions, (Figure 2.2c). In either case, the target nucleus remains in the same state it was in before the interaction.

Above 5 GeV the dominant reaction mechanism is Deep Inelastic Scattering (DIS); in this case the neutrino interacts with an individual quark in the target nucleon and produces a hadronic shower, X (Figure 2.2d).

In between these extremes there is a transition region where neither CCRES not CCDIS dominate. This region is currently poorly modelled and additional contributions

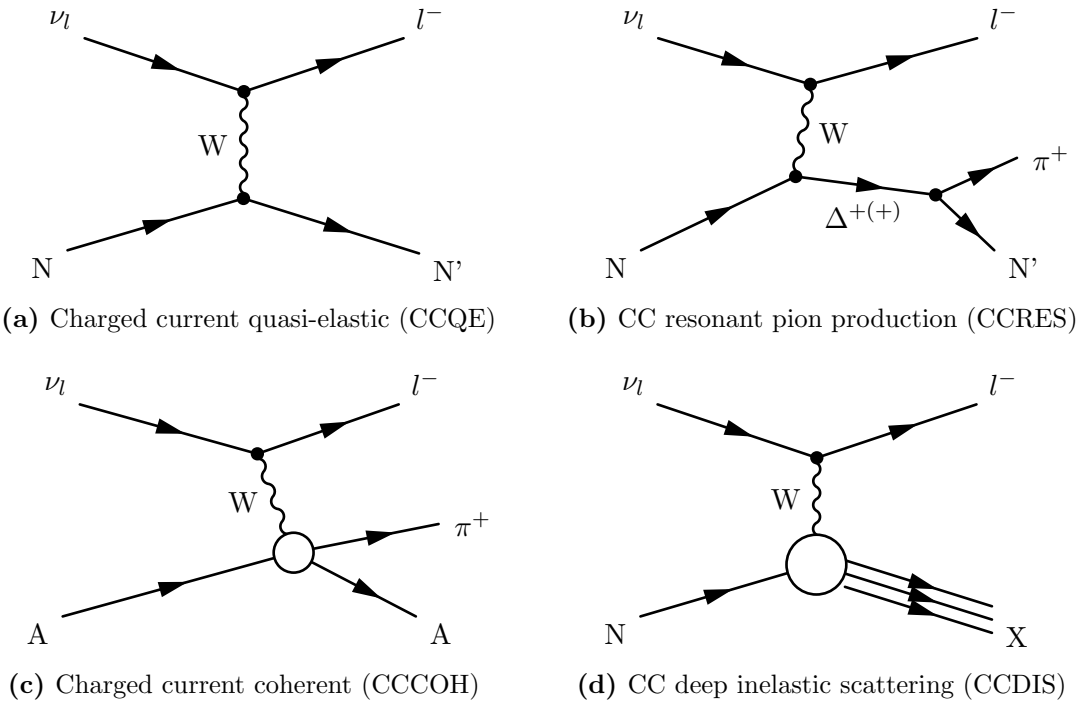

(a) Charged current quasi-elastic (CCQE)

(b) CC resonant pion production (CCRES)

(c) Charged current coherent (CCCOH)

(d) CC deep inelastic scattering (CCDIS)

Figure 2.2: Diagrams of the main neutrino-nucleon interactions relevant to the analysis presented in this thesis. N and N' indicate nucleons, A indicates that the reaction happened with the whole nucleus.

are believed to come from interactions where the hadronic system is neither completely fragmented nor forms a recognisable resonance.

Figure 2.3 shows some of the most recent ν_μ cross-section measurements for neutrino energies between 0.1 GeV and 400 GeV. The plot shows the measured cross-section per nucleon divided by the neutrino energy, which simplifies the comparison between experiments using different targets.

The T2K neutrino beam peaks at an energy of around 0.7 GeV, where the main interaction cross-section transitions from CCQE to CCRES. In this region the CCCOH processes should turn on, making it necessary to understand these interactions in details. The tail of the T2K neutrino energy extends to approximately 30 GeV, covering also the transition between CCRES and CCDIS.

High energy cross-section measurements have relatively small errors compared to measurements in the 0.1-1 GeV region. More interaction cross-section measurements

are necessary to ensure oscillation experiments reach higher sensitivities.

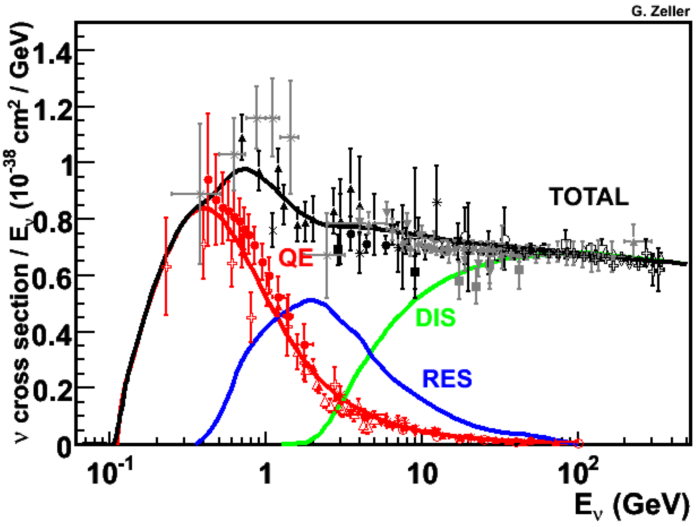

Figure 2.3: Total muon neutrino CC cross sections per nucleon divided by the neutrino energy and plotted as a function of the energy. The CC coherent contribution is not shown as it is negligible compared to the other channels. See Reference [31] for details of the experimental results shown.

2.5.1 Nuclear effects

Nucleons used in neutrino experiments are very often bound in nuclei, since a solid neutrino target is more common than liquid hydrogen or deuterium targets. Plastic scintillators are mainly composed of carbon, sampling calorimeters mainly contain iron, and Cherenkov detectors mainly use water as a target.

The Relativistic Fermi Gas (RFG) model is currently used in many simulations to model the nucleons inside the nucleus. The nucleons are treated with a uniform momentum spectrum below the cut-off Fermi momentum, p_F. Only interactions in which the outgoing nucleon has a momentum higher than p_F are allowed, all other interactions are Pauli blocked. Also, since the target nucleons are in a bound state, some energy is consumed in liberating the outgoing nucleon. Both Pauli blocking and nuclear binding reduce the number of interactions possible at low $Q^2 = -q^2$ (i.e. the four momentum transferred from the leptonic system to the hadronic system).

Nuclear effects complicate the neutrino-nucleon cross-section predictions such that multi-nucleon effects of internal nucleons by particles on the surface of the nucleus must be taken into account. These effects include nuclear binding, particle motion, and interactions between correlated pairs of nucleons (meson exchange currents, MEC [32, 33], see Figure 2.4).

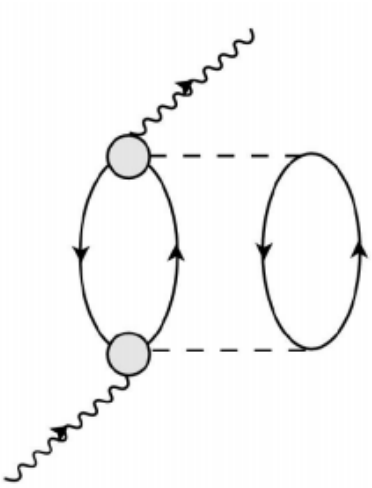

Figure 2.4: MEC interactions are also known as $2p2h$ (two particle two hole), because the calculation of cross sections for these interactions involve the excitation of a pair of particles and holes, which are connected by a meson propagator. Solid lines represent particles or holes, dashed lines represent mesons, wavy lines represent the incoming or outgoing W. Grey circles represent any possible vertex with the corresponding initial/final particles [34].

In addition, the products of the interactions must traverse the nuclear medium before they can be detected. The interactions that the product particles undergo between production and exit from the nucleus are called Final State Interactions (FSI). These effects can alter the observed number of hadrons and their kinematics.

Pions are particularly sensitive to the FSI effects, therefore the nuclear medium can influence the production of pions or their fate. Once produced, charged pions can either be absorbed, or converted into neutral pions via $n + \pi^+ \rightarrow p + \pi^0$, scatter or also knock out nucleons.

2.5.2 Charged current quasi-elastic interactions

CCQE interactions ($\nu_\mu + n \rightarrow \mu^- + p$) are of particular utility to study, because the parent neutrino energy can be reconstructed from the lepton kinematics. Additionally, these are the main interactions in many oscillation experiments' energy region.

A priori unknown form factors are used to parametrise CCQE interaction models. The leading terms are the vector form factor $F_V^1(Q^2)$ (which is measured from electron scattering data) and the axial-vector form factor $F_A(Q^2)$. $F_A(Q^2)$ is parametrised as a function of Q^2 and is defined as:

$$F_A(Q^2) = \frac{F_A(0)}{\left(1 + Q^2 / \left(M_A^{QE}\right)^2\right)^2} , \tag{2.14}$$

where $F_A(0)$ is the form factor at $Q^2 = 0$, that is constrained from nuclear beta decay measurements, and M_A^{QE} is the "axial mass" (which is expected to be 1). It should be noted that the dipole form is just an assumption, and to date neutrino experiments do not have the precision to test whether it is a good assumption or not.

The NOMAD experiment in 2009 [35] and the MiniBooNE experiment in 2010 [36] both measured the *effective* axial mass, due to the nuclear environment where interactions take place.

The NOMAD experiment used neutrinos between 3 and 10 GeV; their target was mostly carbon and they could reconstruct both the muon and the recoiling proton. The NOMAD experiment reported $M_A^{QE} = 1.05 \pm 0.02(\text{stat}) \pm 0.06(\text{syst})\,\text{GeV}$.

The MiniBooNE experiment used neutrinos with mean energy around 0.8 GeV and by using oil Cherenkov technology (CH_2), it could only view muons. Just like for the NOMAD experiment, they used a carbon target. The MiniBooNE experiment measured $M_A^{QE} = 1.35 \pm 0.17\,\text{GeV}$.

Figure 2.5 shows the clear tensions between the model predictions with the M_A^{QE} values that best fit the NOMAD and the MiniBooNE data-sets.

More recently, the MINERνA experiment analysed interactions on scintillator target [37] and found disagreements between the CCQE differential cross-section and the RFG model. In addition, the MINERνA experiment also measured the energy deposited by the nucleons around the interaction vertex (i.e. vertex activity), and found this in agreement with the RFG model when accounting for correlations between the

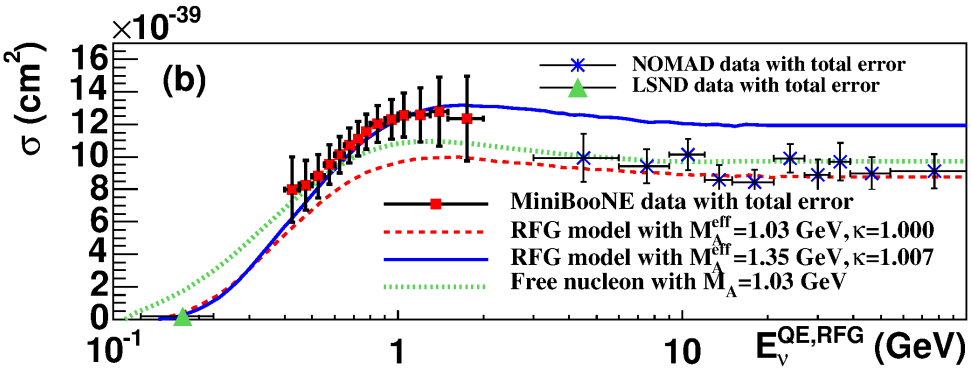

Figure 2.5: Comparison of MiniBooNE and NOMAD ν_μ CCQE cross-section measurements, and model predictions with M_A^{QE} values that best describe each data-set [36].

nucleons within the nucleus. Their results suggest that a model for the nucleus is necessary in addition to a model of the nucleon.

Recent work by the Neutrino Interaction Working Group (NIWG) inside the T2K collaboration [34] suggests that adding two nuclear effects in the RFG model would lead to good agreement between the MiniBooNE and MINERνA data. The two effects are: the Random Phase Approximation (RPA) which is a nuclear screening effect due to long range nucleon-nucleon correlations, and the Nieves model of MEC which accounts for interactions between correlated pairs of nucleons inside the nucleus [32] (see Figure 2.4).

Different experiments measuring the same quantity seem to be in disagreement. Nonetheless, the measurement of the axial mass is of extreme importance because of the impact on the model predictions of the interaction rates. More data in this region is necessary to understand the nuclear effects, and disentangle the effect of correlations between nucleon pairs from FSI effects.

2.5.3 Charged current resonant interactions

Whilst it is essential to understand CCQE interactions, because they are used in oscillation experiments to reconstruct the incoming neutrino energy, it is also important to successfully select CCRES interactions as they are the second largest cross-section in energies around 1 GeV (see Figure 2.3).

Most simulations use the Rein-Sehgal model for resonant interactions [38]. These are described in terms of helicity amplitudes and the cross section contains interference

terms as well as non-resonant background. The vector and axial-vector form factors have a similar form to the ones in case of quasi-elastic scattering, but there is an additional factor related to the resonance excitation. In this case, M_{RES}^{A} is the "axial mass" for resonant interactions. Each of the form factors has one free parameter.

In resonant interactions the target nucleon is excited into a resonant state (usually $\Delta(1232)$) and then decays to a muon, a pion and a nucleon, as in:

$$\nu_\mu + \mathrm{n} \rightarrow \mu^- + \mathrm{n} + \pi^+ \ ,$$

$$\nu_\mu + \mathrm{p} \rightarrow \mu^- + \mathrm{p} + \pi^+ \ ,$$

$$\nu_\mu + \mathrm{n} \rightarrow \mu^- + \mathrm{p} + \pi^0 \ .$$

The ANL [39] and BNL [40] bubble chamber experiments both made measurements of charged current resonant pion production on deuterium for muon neutrinos of energy about 1 GeV, but their measurements had a long discussed disagreement. Recent re-analyses of these data [41, 42] produced cross-section ratios for various interaction channels and found good agreement between the experiments. By multiplying the cross-section ratios by the CCQE cross-section on free nucleons, they extracted the single pion production cross-section (not dependent on flux) and found good agreement between the ANL and BNL data-sets.

More recently, experiments started to measure the CC1π cross-section which is described by the particles leaving the nucleus, i.e. one muon, one pion and any number of nucleons. This means that CC1π^+ measurements contain resonant interactions, coherent interactions, DIS interactions where additional pions are absorbed before leaving the nucleus, and CCQE interactions where the proton interacts with the nuclear medium and produces a positive pion.

In 2011 the MiniBooNE Collaboration provided a high statistics sample of CC1π measurements [43] in mineral oil. The measured differential cross-section is on average 23% higher than the prediction from the simulation. Figure 2.6a shows the $\sigma(E_\nu)$ measurement and Figure 2.6b shows the $\partial\sigma/\partial(KE_\pi)$ measurement. Comparing these results to the bubble chamber data is not simple, since the discrepancies seen could emerge from nuclear effects as well as from the cross-section itself.

In 2014 the MINERνA Collaboration [44] released results on the charged current pion production cross-section from a CH target. Both the $d\sigma/d\theta_\pi$ (where θ_π is the

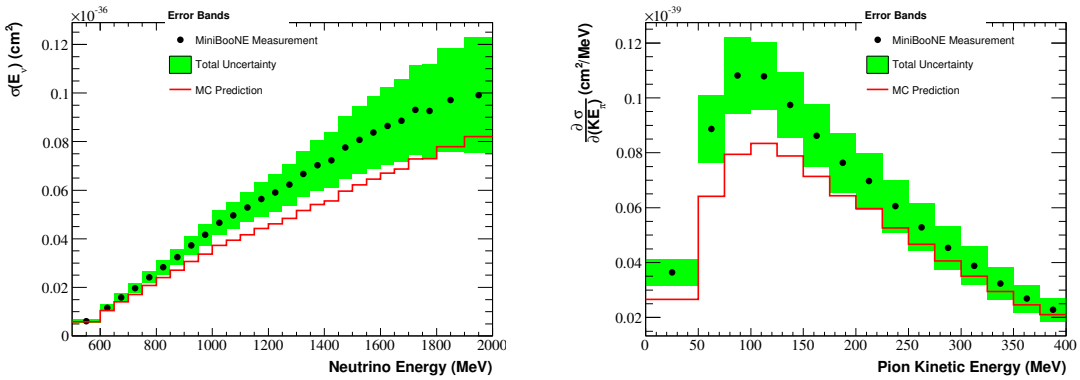

(a) The MiniBooNE $\sigma(E_\nu)$ data.

(b) The MiniBooNE $\partial\sigma/\partial(KE_\pi)$ data.

Figure 2.6: Charged current single pion production cross-section measurements released by the MiniBooNE Collaboration [43].

angle between the beam and pion directions) and $d\sigma/dT_\pi$ (where T_π is the pion kinetic energy) shapes strongly favour models with FSI. Figure 2.7 shows that the MINERνA and the MiniBooNE $d\sigma/dT_\pi$ data have a similar shape above $T_\pi = 100\,\text{MeV}$, which is where the pion FSI effects are expected to be the largest. There are nonetheless significant normalisation and shape discrepancies between the two measurements.

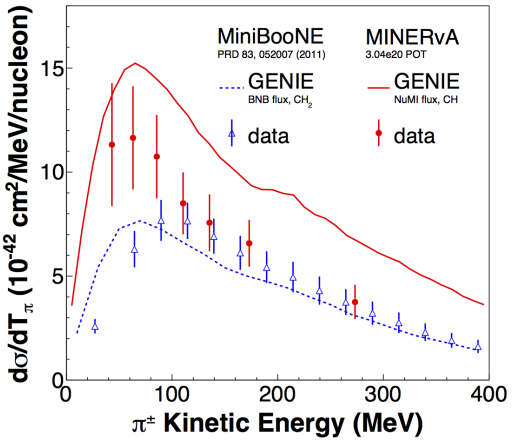

Figure 2.7: Comparison between the MINERνA and MiniBooNE $d\sigma/dT_\pi$ data with the GENIE generator model including FSI treatment [44].

Reference [45] reports a summary of different models and compares them to the

MiniBooNE data. Figure 2.8 shows a comparison of the MiniBooNE data to different theoretical models and to some of the most common generator predictions.

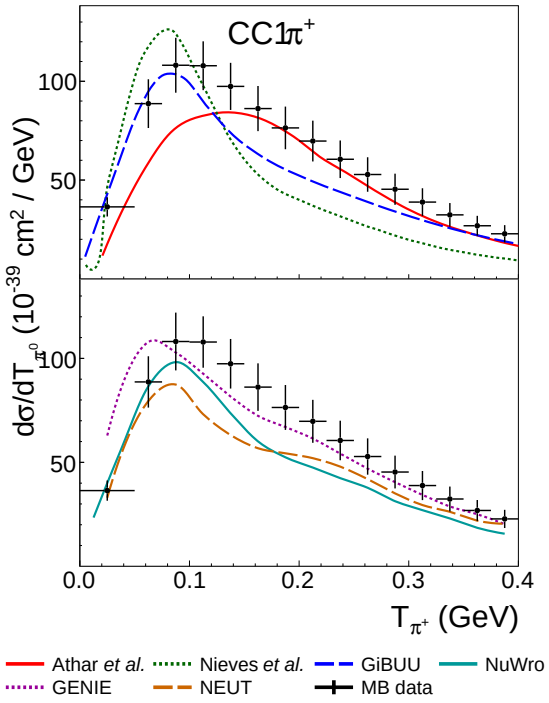

Figure 2.8: Predictions and MiniBooNE data for the differential cross sections in pion kinetic energy for CC1π^+ processes. The top plot shows the theoretical model predictions, while the bottom plot shows the generator predictions [45]. It should be noted that the Athar model does not include FSI effects.

Currently no theoretical model can explain all the pion production data available. Developing and understanding single pion production at energy below 2 GeV is of fundamental importance for the interaction cross-section community, as well as for all the oscillation experiments, since a reduction on the uncertainty related to pion production would result in a higher sensitivity.

2.5.4 Charged current coherent interactions

In addition to resonance pion production, coherent interactions can also produce single pion final states. Neutrinos coherently scatter from the entire nucleus (Figure 2.2c),

producing no nuclear recoil and a more forward-scattered pion compared to resonance interactions. Coherent pion production is possible in both NC and CC interactions.

At neutrino energies above 2 GeV coherent interactions have been measured precisely and agree quite well with the model predictions [46]. At lower neutrino energies, both the K2K and SciBooNE experiments measured no CC coherent pion production data than expected by the model [47, 48], whereas the SciBooNE experiment measured a NC coherent pion production cross-section consistent with the model prediction [49].

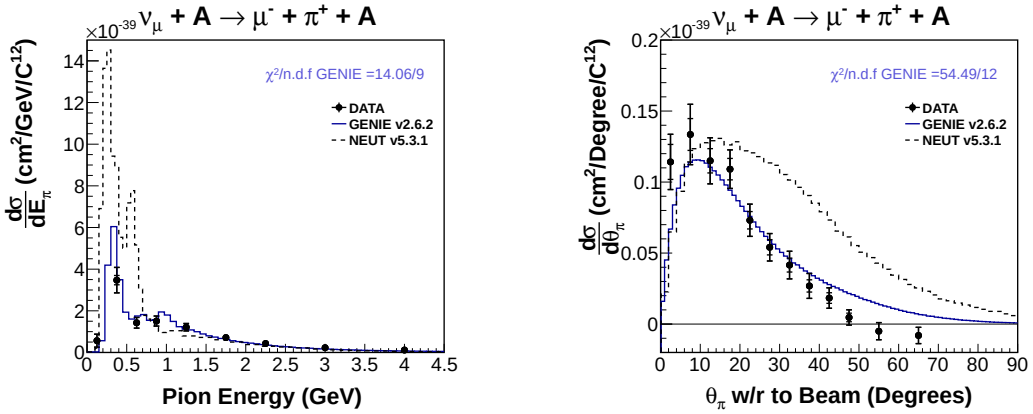

(a) The MINERνA $d\sigma/dE_\pi$ measurement.

(b) The MINERνA $d\sigma/d\theta_\pi$ measurement.

Figure 2.9: Charged current muon neutrino coherent pion production cross-section measurements released by the MINERνA Collaboration [50].

More recently, the MINERνA Collaboration released the measurement of charged-current coherent pion production on carbon in both neutrinos and antineutrinos. Figure 2.9 shows the measurement in neutrino running compared to the model predictions. A large deficit compared to the NEUT prediction (see Subsection 4.1.1) is especially seen at low pion energies and high pion angle.

3

T2K and the ND280 near detector

The T2K (Tokai To Kamioka) experiment is a long baseline neutrino experiment which uses a beam of muon neutrinos to study the appearance of electron neutrinos and the disappearance of muon neutrinos, and consequently measure the oscillation parameters as described in Chapter 2.

A high purity ν_μ beam is produced at J-PARC (Japan Proton Accelerator Research Complex) in Tokai-mura (Ibaraki). The energy spectrum and beam profile are measured at the near detector complex at 280 m from production. The Super-Kamiokande (SK) detector in Kamioka (Gifu), at 295 km from production, detects the oscillated neutrinos. Comparing the near and far detector measurements, the T2K experiment can put stringent constraints on the oscillation parameters.

The main goals of the T2K experiment were highlighted in the original proposal (see Reference [51]) as the discovery of $\nu_\mu \to \nu_\mathrm{e}$ oscillations, the precise measurement of ν_μ disappearance oscillation parameters and the search for sterile neutrino components in the ν_μ disappearance spectrum.

The T2K experiment was the first to indicate direct evidence of $\nu_\mu \to \nu_\mathrm{e}$ appearance [52] in 2011. In 2012 the value of θ_{13} was then constrained by $\overline{\nu}_\mathrm{e}$ disappearance in reactor experiments [18, 19]. In 2013 the T2K experiment excluded $\theta_{13} = 0$ at $7.3\,\sigma$ significance [53].

The T2K experiment also provided independent measurements of θ_{23} and Δm^2_{32} [54]. Combining the T2K results with precise measurements of θ_{13} obtained by reactor experiments allows regions of the δ_{CP} space to be excluded at 90% confidence level: $\delta_{CP} = [0.15, 0.83]\pi$ for normal hierarchy and $\delta_{CP} = [-0.08, 1.09]\pi$ for inverted hierarchy [55].

The near detectors (INGRID and ND280) produced a series of cross-section measurements [56, 57, 58, 59], and more are being worked on, which are important to reduce the systematic uncertainties in the oscillation analysis, and can help constrain the neutrino interaction model in different channels.

This chapter presents an overview of the components of the T2K experiment. The accelerator and neutrino beamline are described in Section 3.1. The on-axis near detector (INGRID), off-axis detector (ND280) and far detector (Super-Kamiokande) are described in Section 3.2, 3.3 and 3.4, respectively. Section 3.5 explains the relevance of the analysis presented in this Thesis to the T2K experiment.

3.1 Accelerator and neutrino beam

At J-PARC a proton synchrotron produces a proton beam fast-extracted in a single turn and fired against a graphite target to produce pions and kaons. Electromagnetic horns focus these hadrons to the decay pipe to produce muons that then decay to muon neutrinos.

3.1.1 Proton accelerators

Figure 3.1 shows a schematic view of the J-PARC accelerator complex. There are three main accelerator phases: the linear accelerator (LINAC), the rapid-cycling synchrotron (RCS), and the main ring synchrotron (MR).

A H^- beam is accelerated by the 300 m LINAC to 181 MeV, and converted to a H^+ beam by charge-stripping foils at the RCS injection.

The beam is accelerated up to 3 GeV by the RCS, and then extracted to be injected into the MR. The proton beam is then accelerated to 30 GeV by the MR. Eight bunches (six bunches before June 2010) are fast-extracted in a single turn by a set of five kicker magnets, and are directed down the neutrino beamline (NU) to the target.

Each spill lasts less than 5 μs and consists of 8 bunches, each containing approximately 3×10^{14} protons and lasting 58 ns. The short duration of the spill is critical to rejecting background events, including cosmic rays, at the near and far detectors.

The J-PARC MR has achieved a world record for beam intensity, when in the fast extraction mode operation it reached a beam power of 240 kW, corresponding to 1.24×10^{14} protons per pulse beam intensity.

Figure 3.1: Schematic view of the J-PARC accelerator complex. The three accelerator phases are highlighted (LINAC, RCS and MR), as well as the beamline (NU) and the location of the near detector complex (ND280).

3.1.2 Neutrino beamline

The neutrino beamline is divided into two sequential steps: the primary beamline which transports the protons from the MR to the target and the secondary beamline which handles the secondary pions that are focused by magnetic horns and then decay into neutrinos.

Figure 3.2a shows the primary beamline which consists of a preparation section, an arc section and a final focusing section. The preparation section aligns the beam for entry to the arc section. In the arc section superconducting magnets direct the protons at 2.5^{o} away from Super-Kamiokande. The final focusing section then aligns the beam for entry to the secondary beamline.

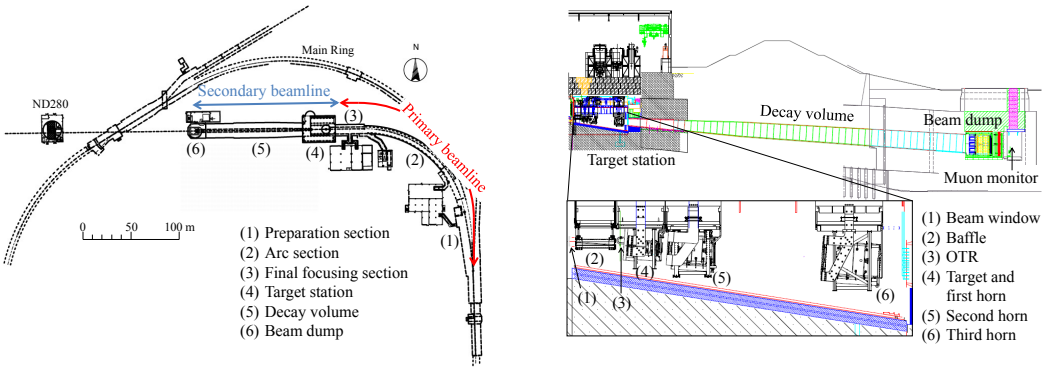

(a) View of the primary and secondary beamline from above.

(b) View of the secondary beamline from the side and looking south.

Figure 3.2: Schematic view of neutrino beamline at J-PARC.

The primary beamline is equipped with 96 separate instruments for measuring the position, intensity, profile and loss of the beam. In particular, the current transformers (CT) are 50-turn toroids around the beam pipe that are used to measure the intensity of the beam. The induced current in the CT is measured when each bunch passes through the coil and is converted into the number of protons in the spill. The final CT, CT5, is located just before the protons reach the target, and it is used to determine the number of protons on target (POT) delivered. Figure 3.3 shows the total POT delivered by the neutrino beamline since the start of the experiment. From March 2010 to January 2015, 8.7×10^{20} good POT has been delivered to the T2K target, of which 6.9×10^{20} good POT in neutrino running and 1.8×10^{20} good POT in antineutrino running. The analysis described in this Thesis only uses T2K Run I-IV which corresponds to 6.53×10^{20} good POT in neutrino running mode.

The secondary beamline consists of the graphite target, three magnetic horns to focus the secondary pions, a decay volume for the hadrons to decay into neutrinos and other particles, and a beam dump to absorb the non-neutrino products. Figure 3.2b shows a schematic view of the secondary beamline.

The target is composed of a graphite rod (2.6 cm in diameter and 91.4 cm long), surrounded by a graphite tube 2 mm thick and a 0.3 mm titanium case. Protons interacting with the graphite produce charged pions and kaons, which are focused by three magnetic horns. The charged particles are either focused or deflected depending on

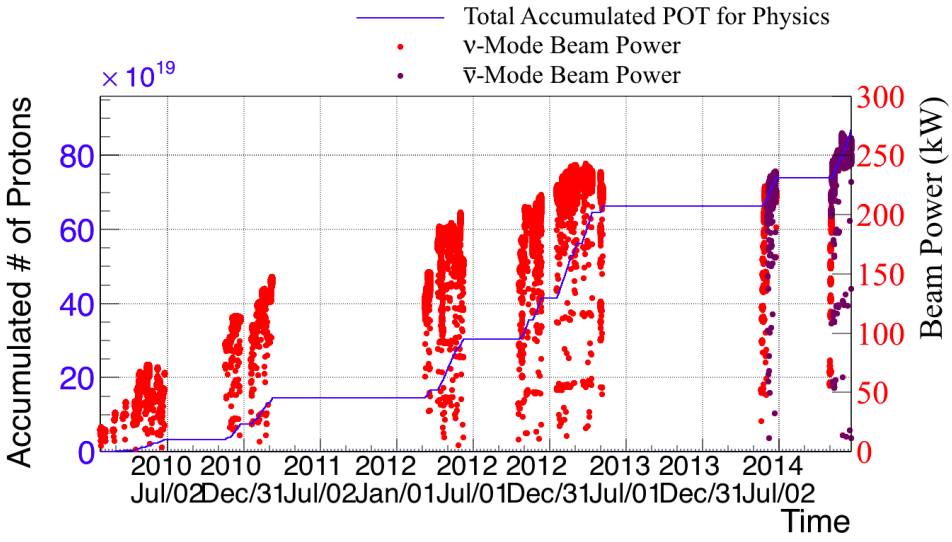

Figure 3.3: Number of protons on target delivered by the neutrino beamline from Run I to Run VI. The red dots the beam power during neutrino running and the blue dots show the beam power during antineutrino running. The first long break is related to the damages from the 2011 Great Tohoku earthquake, the second long break was due to budget cuts after the radiation accident in the J-PARC hadron hall.

the charge of the particle and the direction of the current. For Run I-IV T2K chose to focus positive hadrons and defocus negative hadrons (which lead to the production of mainly μ^+ and ν_μ), for T2K Run V-VI negative hadrons are focused and positive hadrons defocussed (which lead to the production of mainly μ^- and $\overline{\nu}_\mu$).

Hadrons travel through a 96 m long decay volume which is filled with helium to reduce pion absorption and prevent the production of tritium and other unwanted materials. The hadrons decay to produce neutrinos (or antineutrinos). Figure 3.4 (left) shows the predicted neutrino flux for different angles from the beam axis. Due to the kinematics of pion decay, an off-axis beam has a much narrower energy spectrum [60]. This translates into a reduction of the high-energy unoscillated ν_μ background at the far detector which in turn improves the sensitivity to both ν_μ disappearance and ν_e appearance. Furthermore the peak neutrino energy is lower and even the intrinsic ν_e background is lower. The beam is directed 2.5° off-axis from ND280 and Super-Kamiokande.

When T2K runs in neutrino mode, the majority of pions decay through $\pi^+ \rightarrow$

$\mu^+ + \nu_\mu$ producing a 93.3% pure ν_μ beam. The main backgrounds are the $\overline{\nu}_\mu$ (5.6%) that are produced by forward going π^- that are not focuses ($\pi^- \rightarrow \mu^- + \overline{\nu}_\mu$) and ν_e (1.1%) which are mainly produced by muon decay $\mu^+ \rightarrow e^+ + \overline{\nu}_\mu + \nu_e$. Figure 3.4 (right) also shows the predicted flux at ND280 broken down by neutrino type.

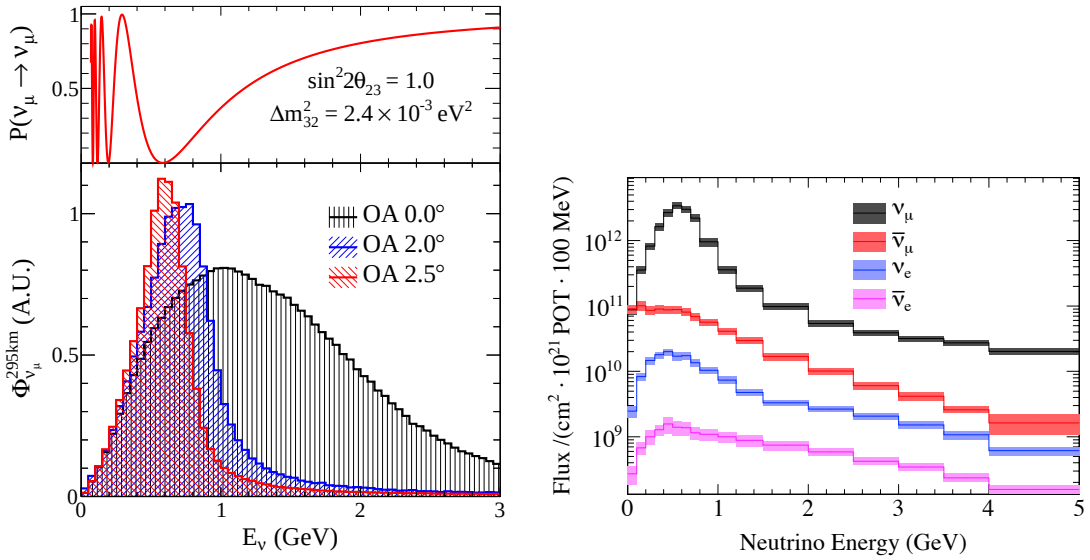

Figure 3.4: Expected T2K flux, showing the off-axis configuration has a much narrower energy spectrum [61] (left) and the neutrino type composition (right).

After the neutrinos have been produced, a 75 ton graphite dump at the end of the decay volume absorbs all the the hadrons, charged leptons (apart from muons with energy higher than 5 GeV) and other by-products. Behind the beam dump, there is a muon monitor (MUMON) that monitors the direction of the beam by detecting the muons that were not absorbed [62].

3.2 INGRID on-axis near detector

Interactive Neutrino GRID (INGRID) is the on-axis near detector, located at 280 m from the target. The main purpose of INGRID is to monitor the neutrino beam rate, profile, and centre, by detecting neutrino interactions. INGRID is composed of 14 identical modules arranged in two identical groups along the horizontal and vertical axes, with 2 extra off-diagonal modules, as shown in Figure 3.5.

Table 3.1: Specifications of the T2K MPPCs [63].

Number of pixels	667
Active area	$1.3 \times 1.3\,\mathrm{mm}^2$
Pixel size	$50 \times 50\,\mu\mathrm{m}^2$
Operational voltage	68 - 71 V
Gain	$\approx 10^6$
Photon detection efficiency at 525 nm	26-30%
Dark rate above 0.5 PEU, at 25°C	≤ 1.35 MHz

Each module consists of eleven tracking scintillator planes interleaved with nine iron target plates. Scintillation light produced by muons from ν_μ CC interactions is collected from each bar and transported to a photo-detector with a wavelength shifting fibre (WLS fibre). The light is read out by a Multi-Pixel Photon Counter (MPPC) attached to an end of the WLS fibre. See Table 3.1 for specifications of the T2K MPPCs. Tracking scintillator layers in alternating orientations enable 3D reconstruction of the muon paths.

An additional proton module with 34 tracking scintillator planes (without iron) is installed in front of the central INGRID module. The scintillator planes allow 3D tracking of low energy particles which INGRID is unable to detect. Detecting low energy particles allows a better understanding of the neutrino interactions in INGRID, and consequently of the neutrino beam properties.

3.3 ND280 off-axis near detector

ND280 is the off-axis near detector, located at 280 m from the target and 2.5° off-axis. Figure 3.6 shows an exploded view of ND280, where the coordinate convention is also indicated. The y axis is vertical and, the x and z axes are in the horizontal plane. The origin is at the centre of the magnet and the 0.2 T magnetic field is along the $+x$ direction. The z axis is the direction to SK projected onto the horizontal plane. The

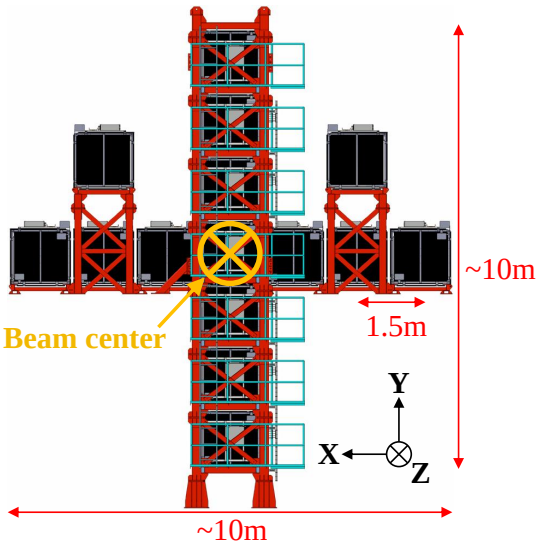

Figure 3.5: Schematic view of the INGRID on-axis detector: the centre module of the vertical row and of the horizontal row corresponds to the neutrino beam centre.

UA1/NOMAD magnet was refurbished and its inner volume is used for the tracking sub-detectors.

The ND280 Tracker region contains two fine-grained detectors (FGDs [63]) which are used as the neutrino interaction target, sandwiched between three gaseous time projection chambers (TPCs [64]) which are used to track charged particles. Upstream of the Tracker there is a π^0 detector (PØD [65]), consisting of scintillator, water and brass layers. The electromagnetic calorimeters (ECals [66]), made of layers of lead and scintillator bars, surround the Tracker and PØD regions. A magnet return yoke surrounds the entire detector to make the magnetic field uniform and contain it inside the detector. Plastic scintillators in the yoke form the side muon range detectors (SMRDs [67]). The analyses presented in this Thesis use neutrino interactions within the ND280 Tracker, so the PØD and SMRD will not be described in detail.

3.3.1 Fine-grained detectors

The most upstream FGD (FGD1) primarily consists of polystyrene scintillator bars with layers oriented alternately in the x and y directions allowing 3D tracking of charged particles. Most of the interactions in FGD1 are on carbon nuclei. The downstream FGD (FGD2) has a similar structure but the polystyrene bars are interleaved with water

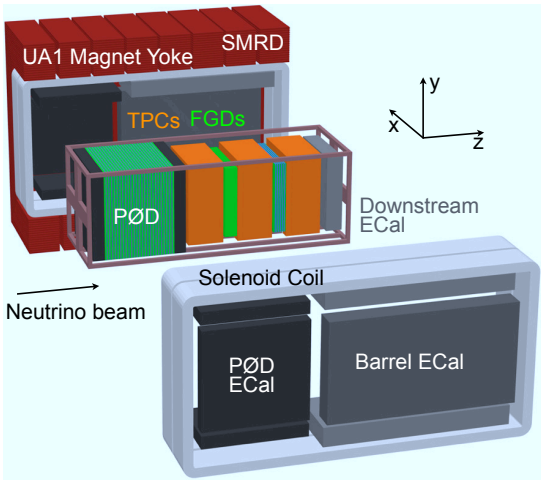

Figure 3.6: Exploded view of the ND280 off-axis near detector, where the coordinate convention is also given.

layers to allow the measurement of neutrino interactions on water. As the far detector is a water Cherenkov detector, the cross-sections on water are extremely important to be understood. The analysis of this Thesis uses FGD2 as the active interaction target, hence in a signal event the neutrino interacts with an atom in the water layer, and the charged lepton coming from a CC interaction is tracked in the scintillator layers.

Each scintillator bar has dimension 9.61 mm×9.61 mm×1864.3 mm, hence most of the penetrating particles produced in neutrino interactions (especially muons) pass through to the TPCs. Short-ranged particles such as recoil protons can be reconstructed in the FGDs, although the analysis of this Thesis does not use these tracks.

FGD1 is composed of 15 xy modules, providing a target mass of 1.1 ton. FGD2 is made of 7 xy modules, interleaved by 6 water layers.

Just like for the INGRID detector, each scintillator bar has a hole in the middle for the WLS fibre to run through. The emission spectrum of the plastic scintillator is centred at 420 nm, the WLS fibre has an absorption spectrum centred at 430 nm, and the WLS fibre emission spectrum is centred at 476 nm. The small overlap between the emission and absorption spectra creates a small self-absorption as the light travels along the fibre. One end of the fibre is attached to an MPPC (see Figure 3.7a), and the other end is coated with aluminium to form a mirror.

An MPPC consists of 667 individual pixels covering an area of $1.3 \times 1.3\,\mathrm{mm}^2$. Each

pixel in its detection surface is treated as a binary (i.e. hit or not-hit) element that is insensitive to the incident amplitude in that particular pixel. When a photon from the fibre strikes a pixel, an avalanche is created and the signal is counted. The MPPC signal is a linear sum of the number of fired pixels. Individual pixels can generate a signal when there is no incident photon, this is called "dark noise", and it is ignored when trying to reconstruct particle tracks. An example signal demonstrating the single photon resolution of a standard MPPC is shown in Figure 3.7b.

See Reference [63] for more information on the FGDs.

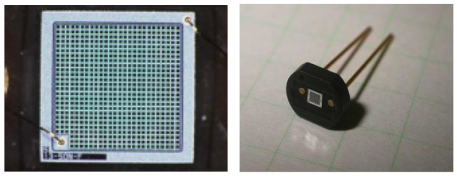

(a) Photographs of a 1.3×1.3 mm^2 MPPC and the packaging in which it is mounted.

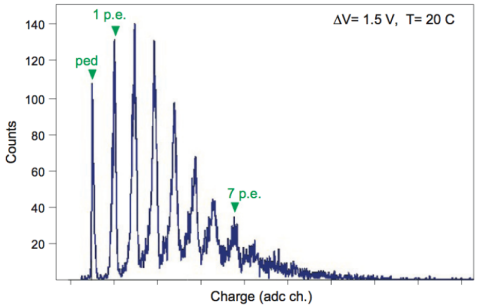

(b) Example of charge amplitude spectrum measured with an LED source.

Figure 3.7: MPPC photographs and performance.

3.3.2 Time projection chambers

Each of the three ND280 TPCs consists of an inner box that holds an argon-based drift gas, contained within an outer box that holds CO_2 as an insulating gas. An electric field, parallel to the 0.2 T magnetic field, is applied through the gas from a central cathode to anodes at each side of the TPC. When a charged particle travels through the TPC, it ionises the gas and the ionisation electrons drift to the anodes. Each side of the TPC is instrumented with 12 MicroMEGAS detectors that amplify the signal before being recorded. Each MicroMEGAS module is divided into 1728 pads arranged in 48 rows and 36 columns. Each pad is 7.0 mm×9.8 mm. All the pads are aligned to be in the same yz plane, and the x co-ordinate is determined by the relative time different between hits. Figure 3.8 shows a simplified diagram of the TPC features.

The TPCs provide excellent tracking, since it can provide 3D hit position, whereas the FGD can only provide alternating xz and yz information. The spatial resolution of the TPCs depends on the drift distance and it is always lower or $\approx 1\,\text{mm}$. The curvature due to the magnetic field provides measurements of the particle momentum and charges. The relative momentum resolution of the TPCs is 0.1 $p_T/(GeV/c)$. Particle identification is also possible by looking at the ionisation measurements. The resolution of the deposited energy for minimum ionizing particles 7.8±0.2% and it allows muons to be distinguished from electrons in the TPCs.

See Reference [64] for more information on the TPCs.

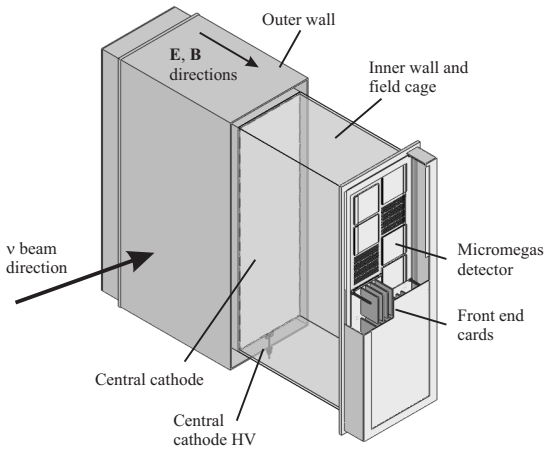

Figure 3.8: Simplified diagram of the TPC features. The cathode is in the middle of each TPC and ionisation electrons drift to the anodes on the side.

3.3.3 Electromagnetic calorimeters

The ECals use the same scintillator technology as the FGDs, but their granularity is coarser. Each bar is $1\,\text{cm}\times 4\,\text{cm}$, and the scintillator layers are interleaved with 1.75 mm thick lead. The lead layers are used to contain electromagnetic showers and to increase the probability for a photon to shower. The ECals can provide complementary information to the rest of the Tracker and provide additional particle identification information in regions of phase space where the TPC cannot distinguish between particles.

There are 13 separate ECal modules, as shown in Figure 3.6: six Barrel-ECal modules surround the Tracker region, one downstream module (Ds-ECal) covers the down-

stream exit of the Tracker volume, and six PØD-ECal modules surround the PØD detector. The 6 Barrel-ECal modules consist of 32 layers each for a total thickness of 9.7 radiation lengths ($9.7\,X_0$). The bars running on the z direction are read out by two MPPCs at the end of the fibre, the bars perpendicular to them are much shorter, hence are read out by one MPPC and have the over end coated with aluminium to form a mirror. The Ds-ECal consists of 34 layers for a total thickness of $10.6\,X_0$, and each bar is read out by two MPPCs.

A drawing of a completed module is shown in Fig. 3.9.

The ECal energy resolution is 10% for particles with momentum higher than 1 GeV, 10-15% for particles with momentum 0.5-1 GeV, and 15-20% for particles with momentum lower than 0.5 GeV. See Reference [66] for more information on the ECals.

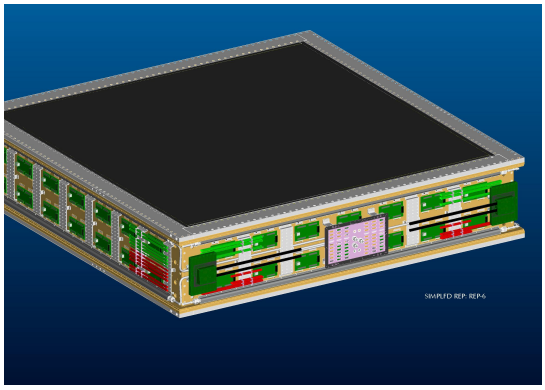

Figure 3.9: External view of one ECal module.

3.4 Super-Kamiokande far detector

Super-Kamiokande (SK) is a 50 kiloton water Cherenkov detector, located underground in the Mozumi zinc mine (Gifu prefecture). The detector has an average of 1000 m (2700 m water equivalent) of rock overburden to reduce the rate of cosmic rays by about five orders of magnitude compared to that on the surface of the Earth.

Figure 3.10 shows a diagram of the SK detector. SK is divided in regions. The inner detector (ID) has a diameter of 33.8 m and height of 36.2 m and it is completely covered by 11,146 50cm-photomultiplier tubes (PMTs). The photocatode covers 40 % of the ID surface. A set of horizontal and vertical Helmholtz coils reduce the Earth

magnetic field to below 50 mG, such that the PMTs are not affected by it. The outer detector (OD) is covered by 1,885 outward facing 20cm-PMTs, that serve as an active veto counter against incoming particles, as well as a passive shield for neutrons and γ rays from the surrounding rocks.

Water Cherenkov detectors use Cherenkov light [68] to detect the charged particles produced by CC interactions. When a charged particle travels faster than the speed of light in a medium, it polarises the molecules of the medium, which then turn back rapidly to their ground state, emitting prompt radiation (i.e. Cherenkov radiation). The emitted light forms a coherent wave front at an angle of $\cos\theta = 1/(n\beta)$, where n is the refractive index of the material, $\beta = v/c$, and v is the speed of the particle in the medium. For relativistic particles in water, the opening angle is 42°.

As the charged particles travel through the medium, they lose energy and stop emitting Cherenkov radiation and a ring of light is detected by the SK walls. Electrons tend to create an electromagnetic shower producing multiple Cherenkov rings in slightly different directions, while muons generate a single ring with well defined shape. A particle identification (PID) likelihood can be used to distinguish electrons and muons looking at the charge left in the hit PMTs, timing and patterns.

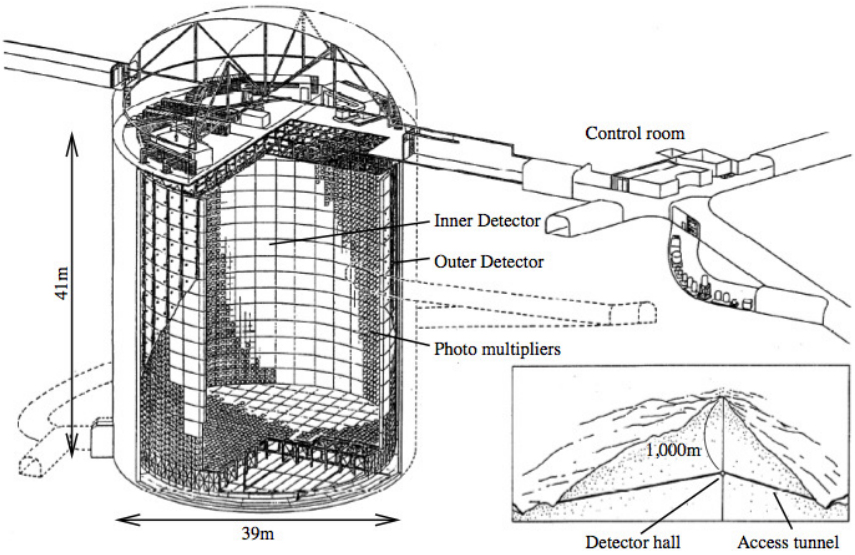

Figure 3.10: Diagram of Super-Kamiokande detector.

3.5 Importance of measuring cross-sections for T2K

The neutrino event rate observed at SK depends on the oscillation probability, neutrino flux, neutrino interaction cross-section, and the detection efficiency. The model of the neutrino flux, cross-section and detection efficiency needs to be understood with sufficient precision to reach high sensitivity in the oscillation measurements. Our model of neutrino cross-section must include the dependence on the neutrino energy, the kinematics of the outgoing lepton, and the kinematics of final state hadrons.

Three ν_μ CC samples from the ND280 detector are currently used in a fit to the models for the beam flux, the neutrino interactions and the ND280 detector (as explained in Section 7.2). The three samples from the ND280 detector are selected by looking at the particles leaving the nucleus:

- The *CC0π* sample that requires 1 muon, no pions and any number of nucleons in the final state. This sample is enhanced in the CCQE interactions.
- The *CC1π*$^+$ sample that requires 1 muon, 1 positive pion and any number of nucleons in the final state. This sample is enhanced in the CCRES interactions.
- The *CCOther* sample that requires 1 muon, at least one negative/neutral pion or more than one positive pion, and any number of nucleons in the final state. This sample is enhanced in the CCDIS interactions.

These three samples are selected in **FGD1**, hence an uncertainty needs to be taken into account for the difference in the neutrino target between FGD1 (i.e. carbon) and SK (i.e. water). Figure 3.11 shows the error reduction on the uncertainties for the SK ν_μ flux and the cross-section parameters constrained by the fit to the near detector data.

A future improvement of this fit will include samples from the **FGD2** detector, providing a direct constraint to the interactions in water. This Thesis describes the first T2K single differential cross-section for CC1π^+ events on water.

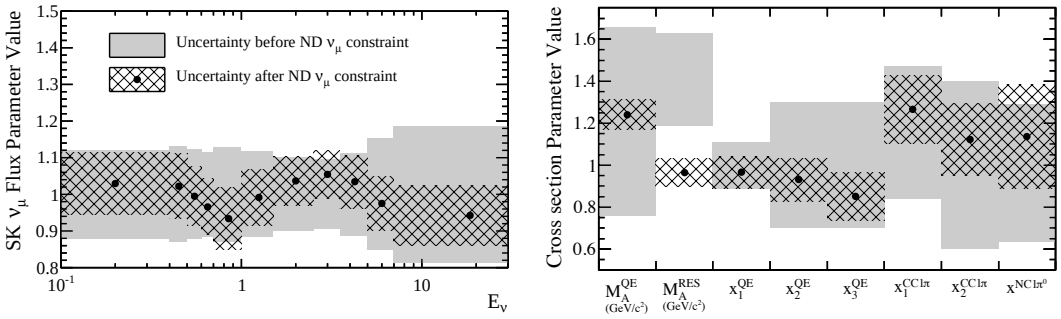

Figure 3.11: Prior and fitted values and uncertainties for the SK ν_μ flux normalisation parameters (left) and cross section parameters (right) constrained by the near detector analysis for the oscillation analyses [55]. The flux parameters are given as a function of the reconstructed neutrino energy, the cross-section parameters are the axial mass for CCQE and CCRES interactions (M_A^{QE} and M_A^{RES}) and energy dependent normalisation parameters for CCQE (3 energy bins), CC1π (2 energy bins) and NC1π^0 (1 energy bin) interactions. See Section 7.2 for more information on the flux and cross-section models.

4

The ND280 simulation

The analyses performed using the near detector depend on the ND280 software, which includes different tools for data collection, simulation and analysis. The ND280 software is based on ROOT [69] and Geant4 [70] classes. The aim of the ND280 software is to create a Monte Carlo (MC) data-set as representative as possible of the real data.

The ND280 MC simulation is split in three steps:

1. MC event simulation;
2. detector calibration;
3. event reconstruction.

After the last step, the truth and reconstructed information are summarised into a format ready for analysis.

4.1 MC event simulation

An initial prediction of the neutrino beam flux is obtained by using FLUKA2008 [71] to simulate the 30 GeV protons in the primary beamline and on the target, and Geant3 to propagate the by-products in the decay volume. The initial prediction is tuned using both external data (NA61/SHINE is a dedicated hadron interaction experiment at CERN [72]) and beamline measurements. The differences between the measured and simulated beam profile in each T2K run are used to re-weight the flux.

4.1.1 The NEUT simulation

The NEUT [73] event generator is used to simulate neutrino interactions on all the elements of ND280, up to and including the magnet yoke. In reality, interactions can also happen in the concrete wall of the pit or the sand surrounding it. Hence a separate "sand" MC sample is produced to estimate the contribution of these events in the analyses.

Events are simulated from a few MeV to hundreds of TeV, following the input given by the beam group to better model the energy, position, direction and flavour of the produced neutrinos. Considering the geometry of ND280, NEUT can track the neutrino and also the interaction probability on all the materials that it crosses. A pseudo-random number generator determines whether an interaction happens or not.

Simulations of neutrino interactions usually follow a chosen nuclear model (to describe the movement of the nucleons in the nucleus), integrate it with the selected neutrino interaction with the target nucleon, and then propagate the products of the interaction in the nuclear medium until they exit the nucleus.

NEUT needs to follow specific models to simulate each of these steps.

For CCQE and NCQE interactions, NEUT uses the Llewellyn Smith model [74] integrated with the relativistic Fermi gas (RFG) model by Smith and Moniz to describe the nucleons within the nucleus [75]. The outgoing nucleon is also required to have larger momentum than the Fermi surface momentum (Pauli blocking), which is 217 MeV/c for carbon and 225 MeV/c oxygen.

As explained in Subsection 2.5.3, NEUT uses the Rein-Sehgal model for resonant interactions [38], considering 18 resonances with masses below $2\,\mathrm{GeV/c^2}$ and their interference terms. In addition 20% of the Δ resonances undergo pion-less Δ decay, in which the Δ is absorbed by the nuclear medium without emitting any pions: $\Delta + N \rightarrow N' + N''$.

Coherent pion production is simulated for both NC and CC interactions using the Rein-Sehgal model [76], including the PCAC (Partially Conserved Axial vector Current) lepton mass correction for CC interactions [77].

DIS processes are simulated using GRV98 parton distribution functions [78] and corrections following the Bodek and Yang model [79] to improve the agreement with experiments in the low-Q^2 region. To avoid double counting with the single pion resonant production, only multiple pion production processes are considered for $W < 2\,\mathrm{GeV/c^2}$

(where W is the hadronic invariant mass). PYTHIA/JETSET [80] is used for hadronisation at energies above 2 GeV, and an internal NEUT method is used at lower energies.

After the simulation of the initial neutrino-nucleon interaction, final state interactions are simulated with the *cascade model*. Each particle is propagated inside the nucleus with steps determined by the mean free path. The mean free path depends on the position inside the nucleus and the momentum of the particle. At each step the probability of interaction (such as charge exchange, absorption or scattering) is calculated. If an interaction occurs, the resulting particles are used for stepping through the rest of the nucleus. This process continues until all particles are either absorbed in the nucleus or escape it. Data from several pion scattering experiments are used to tune this model.

4.1.2 The GENIE simulation

While NEUT is the "official" generator, GENIE [81] is an alternative neutrino event generator. Since GENIE provides a general framework valid over a large range of experiments, targets and neutrino energies, it is often used as a baseline to compare results from experiments with different neutrino flux or targets.

GENIE uses essentially the same models as NEUT for the neutrino interactions simulation, but they differ in the implementation and value of some of the parameters.

GENIE uses an extension of the RFG formulated by Bodek and Ritchie [82] which considers a longer energy tail compared to NEUT. The value of the axial masses for QE and RES interactions are also different: M_A^{QE} is 1.21 GeV/c^2 in NEUT and 0.99 GeV/c^2 in GENIE, and M_A^{RES} is 1.21 GeV/c^2 in NEUT and 1.12 GeV/c^2 in GENIE.

The resonant pion production interactions are still modelled using the Rein-Sehgal model, but 16 resonances are used and no interference terms are considered.

The version of the Bodek-Yang correction used to model DIS interaction is slightly different than the one used in NEUT [83]. GENIE also uses the AGKY [84] (Andreopoulos-Gallagher-Keyahias-Yang) model for hadronisation below 2 GeV, and PYTHIA above this threshold.

Finally, the intranuclear transport model in GENIE has large differences with the model considered in NEUT. Rather than calculating a cascade of hadronic interactions, which could be computationally expensive, the total cross-section for each possible

nuclear process involving pions and nucleons is computed as a function of the energy up to 1.2 GeV. This simplified model shows good agreement with the full cascade model implementation, and it has been tuned to similar data-sets to the ones used in NEUT.

Even if the models used are the same, the implementation and parametrisation of the models is slightly different in NEUT and GENIE, and the predicted cross-sections can differ.

4.1.3 Detector simulation and electronics response

NEUT/GENIE only simulate individual neutrino interactions, so the ND280 detector simulation groups them in spills, and then simulates the passage through the detector by using Geant4 [70].

The last step of this first stage is the simulation of the response of the electronics. In the scintillator sub-detectors (FGDs, ECals, PØD), the simulation describes the light emitted in response to the energy deposition, the transportation of the light through the bar to the optical fibres, and the response of the MPPCs. For the TPCs, the simulation describes the electron drifts, the MicroMEGAS response and the electronics chain afterwards.

The simulation of the passage through the detector and electronics response produces an output which is in the same format as the real data.

4.2 Detector calibration

The calibration of ND280 events is done using calibration constants that are valid for specific periods of data.

For the scintillator-based detectors, "pedestal" triggers and "cosmic" triggers are used to calibrate the light yield and time of hits. Pedestal triggers measure the dark noise of the MPPCs; whereas cosmic triggers can be used to calibrate the response of different bars to minimally ionising particles (MIPs). Timing calibration accounts for both bar-to-bar variations and delays introduced by readout electronics. Since there is no precise inter-detector time calibration, delays up to 10 ns are observed between TPCs and ECals.

For the TPCs, a dedicated laser system is used to calibrate the energy deposited in the gas by charged particles, the drift velocity and the gain of the electric field.

4.3 Event reconstruction

The event reconstruction happens in two phases: local reconstruction by each sub-detector and then global reconstruction.

Each sub-detector gathers hits, coming from MPPCs or MicroMEGAS pads, together to form tracks or showers (local reconstruction). The global reconstruction then combines tracks/showers from all sub-detectors to form a complete picture of the event.

Even though an attempt to evaluate a global particle identification (PID) is made, it is more powerful to use PID information from each sub-detector separately (e.g. this analysis uses the TPC PID and ECal PID). The momentum of each global track is reconstructed according to different particle hypotheses (electron, muon, proton), and generally assuming a forward going particle (unless the track goes through both FGDs and the FGD2 segment is before the FGD1 one).

At the end of the reconstruction step, the truth and the reconstructed information are summarised into a format ready for analysis.

4.3.1 Highland

`Highland` (`high` level `a`nalysis at the `n`ear `d`etector) is a set of global tools developed for all analyses at ND280.

Before the selection is applied, a series of corrections are applied to the MC/data events:

1. It was discovered after the data production that a faulty FGD front-end board (FEB 4-2) created problems in 3 periods of Run I data taking. As a result these periods are ignored.

2. During the Great Tohoku earthquake in March 2011, two of the electronics boards in the right-side Barrel ECal were damaged. One of these boards (TFB 25) handles data from bars near FGD2 that only have an MPPC at one end, thus these bars are now dead. These missing bars affect the reconstruction, PID and energy estimation of any particles entering that region, but the simulation does not currently reproduce these dead channels. Rather than applying a large systematic uncertainty to account for this, the right-side Barrel ECal are entirely ignored for Runs III and IV.

3. Measurements from CT5 are normally used for the POT accounting. The beam group reported that this measurement cannot be trusted for a short period during Run IV for which the measurements from CT4 are used instead.

4. Corrections to the TPC dE/dx measurement for data and MC, as well as to the expected dE/dx, as detailed in Reference [85].

5. Pile up corrections to take into account possible sand muon events happening at the same time as the beam events, as explained in Subsection 7.1.5.3.

The selection and systematic uncertainties for the analysis of this thesis are described in Chapter 6 and 7.

5

Data Quality for the Electromagnetic calorimeters

The Data Quality group of the T2K experiment assesses the quality of the data coming from both beam and cosmics triggers and collected by the near detector complex. Every week of data taking each sub-detector performs different tests, from checking the hardware status of the detector to performing checks that involve reconstructed variables and to assessing the quality of the data to use in all the analyses involving the near detectors. To summarise all the checks, a flag is uploaded to the offline database for each sub-detector, with the flag being 0 indicating good data quality, -1 indicating that data is not being written, and any other positive value indicating the bad status of the sub-detector. The global ND280 data quality flag combines the flags for all sub-detectors and is good only when all sub-detectors have a good data quality flag. Analyses using the ND280 Tracker require all the sub-detectors (excluding the PØD) to have a good data quality flag. PØD analyses usually only require good data taking in the PØD.

Section 5.1 explains the structure of the data acquisition system (DAQ) and the triggering of the ND280 detector. Section 5.2 presents the checks performed every week to asses the quality of the data taken by the ECal. Section 5.3 summarises the status of the quality of data for the whole of ND280 during Run I-IV.

5.1 The ND280 Data acquisition system

As explained in Section 3.3, every scintillator bar in the ND280 detector is read out by one or two MPPCs. Up to 64 MPPCs are connected to one Trip-t Front end Board (TFB). Readout Merger Modules (RMMs) process the bidirectional data (control and readout) from up to 48 TFBs, and provide the communication interface with the ND280 DAQ.

Accelerator timing signals are given to the Master Clock Module (MCM), which issues triggers across the whole detector to the Slave Clock Modules (SCMs), one for each sub-detector, and to the RMMs. The SCM allows the sub-detectors to configure its electronics independently and, when necessary, to run separated from the rest of the ND280 (i.e. "local DAQ") for calibration and debugging.

There are three main triggers considered by the ND280 DAQ. The beam trigger is issued when an accelerator timing signal is sent to the MCM. The FGD cosmic trigger is issued when there is no beam trigger, but coincident hits are seen in both FGDs. The TripT cosmic trigger is issued when there is no beam trigger, but coincident hits are seen on opposite sides of the detector (top and bottom SMRDs, left and right SMRDs, PØD-ECal and Ds-ECal). In the last two cases these events are usually cosmic ray muons, which are useful for calibration or for the evaluation of systematic uncertainties.

A schematic view of the ND280 triggering system is given in Figure 5.1 For more information on the ND280 DAQ see Reference [86].

5.2 ECal data quality assessment

For the ECal data quality assessment several checks are performed every week, and the ECal rate is monitored quarterly. The weekly checks include the monitoring of temperature, voltage and current sensors located on the ECal TFBs and on the flow-meters of the cooling system, as well as raw data analysis.

The summary of the quality of the data is given by a 12 bit flag where 0 means good data quality, -1 means that data is not written and any positive number indicates a problem with one or more RMMs. The encoding of the status of the ECal modules in the data quality flag is given in Table 5.1. When more than one RMM is showing problems, the encoding of the "bad" RMMs is linearly summed. For example a flag of

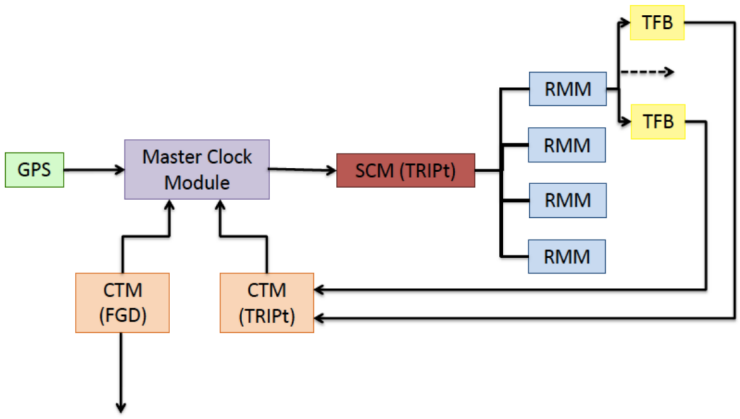

Figure 5.1: Schematic view of the ND280 triggering system, where the arrows flows of trigger signals, GPS indicates the inputs from the beam trigger, CTMs are the Cosmic Trigger Modules, SCM the Slave Clock Module, RMMs the Readout Merger Modules and TFB the Trip-T Front end Boards.

136 (i.e. $2^3 + 2^7$) indicates a problem with RMM 3 and RMM 7, and a flag of 4095 (i.e. $2^0 + 2^1 + 2^2 + 2^3 + 2^4 + 2^5 + 2^6 + 2^7 + ^8 + 2^9 + 2^{10} + 2^{11}$) indicates a problem with the whole ECal.

Only the main raw data analysis checks are presented here, i.e. the beam timing and the gain/pedestal monitoring. The other checks include the monitoring of timing offsets between RMMs, and the production of hit maps using cosmic triggers.

5.2.1 Beam Timing

Track reconstruction in ND280 involves multiple sub-detectors and time correlation between signals is necessary to determine track direction and to veto background signals. On beam triggers, the hit time relative to the beam trigger time is monitored. By taking into account all the offsets introduced by the readout electronics, the bunch structure within the TFB readout cycles can be predicted.

Figure 5.2 shows the timing distribution for RMM 0 during Run IV. Each point is the mean time of received bunches and the dashed blue regions correspond to the 100 ns reset windows between 480 ns readout cycles.

Short RMM offsets are common and need to be flagged as bad for the specific RMM where they occurred.

Table 5.1: Encoding of the status of the ECal modules in the data quality flag.

bit number	decimal	binary value	ECal module
1	1	2^0	RMM 0 - Ds-ECal
2	2	2^1	RMM 1 - Ds-ECal
3	4	2^2	RMM 2 - PØD-ECal South
4	8	2^3	RMM 3 - Barrel-ECal Top South
5	16	2^4	RMM 4 - Barrel-ECal Bottom South
6	32	2^5	RMM 5 - Barrel-ECal Side South
7	64	2^6	RMM 6 - Barrel-ECal Side South
8	128	2^7	RMM 7 - PØD-ECal North
9	256	2^8	RMM 8 - Barrel-ECal Side North
10	512	2^9	RMM 9 - Barrel-ECal Side North
11	1024	2^{10}	RMM 10 - Barrel-ECal Bottom North
12	2048	2^{11}	RMM 11 - Barrel-ECal Top North

High-voltage problems can create noise as the one seen in Figure 5.2 around March 2013. This does not affect the quality of the data taking, although it needs to be monitored regularly.

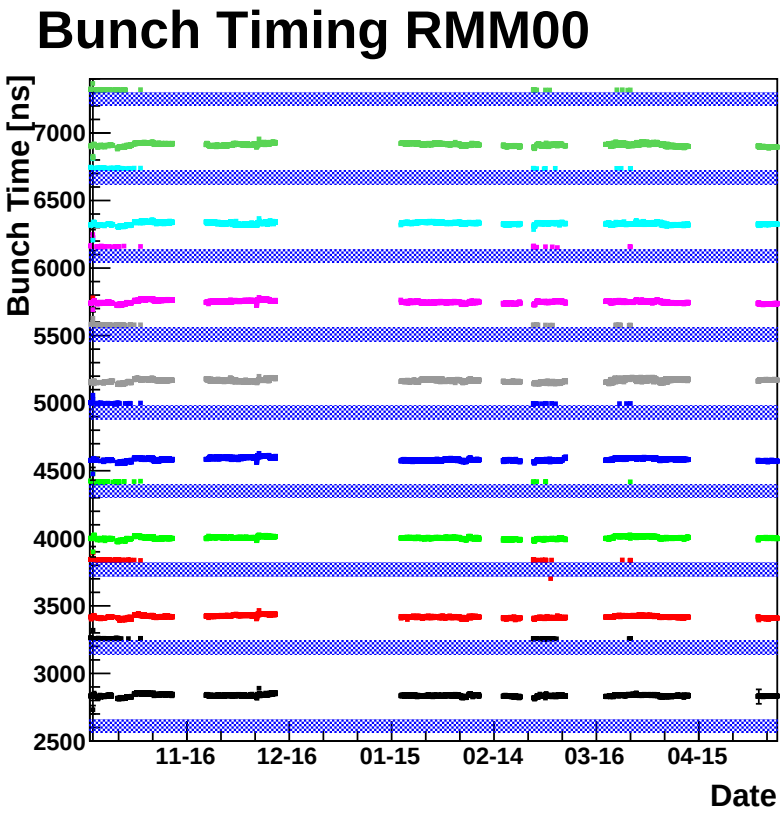

Figure 5.2: Hit time relative to beam trigger time for ECal hits in RMM 0 during Run IV. The dashed blue regions correspond to the 100 ns reset windows between 480 ns readout cycles.

5.2.2 Electronics pedestals and MPPC gains

Electronics pedestals and MPPC gains are monitored over time as large variations could affect the efficiency and resolution of the detector. Small variations are usually due to temperature excursions (the day/night effects are clearly visible in the plots), whereas large variations could indicate issues in the voltage supply.

The gain and pedestal for a channel is calculated from a histogram of ADC counts

when showing only thermal noise (i.e. no input signal). This spectrum shows a large peak (i.e. "pedestal", corresponding to no pixels having fired) and a series of uniformly spaced peaks with decreasing amplitudes, corresponding to the number of pixels fired. The pedestal is given by the fitted position of the pedestal peak, and the gain from the spacing between the first and second peaks (corresponding to 1 and 2 pixel fired). The gain and pedestals are evaluated with a granularity of 3 hours.

The T2K readout system must be able to resolve time signals of a few photo-electrons as well as receive the full range of MPPC signal sizes of the ND280 detector. If the input signal is read by a single channel, the noise and threshold voltage dispersions would affect the resolution of a few photo-electrons. Hence, the input signals coming from each MPPC are divided in low and high gain channels, and the pedestal peaks are evaluated for them separately.

Figure 5.3 shows the gain variation of RMM 1 during Run IV, and Figure 5.4 shows the pedestal variation for RMM 2 during Run IV for low and high gain channels. Red lines correspond to 0.5 ADC counts and show good operation.

High gain channels amplify the noise much more than low gain channels, and that is why the pedestals for low gain channels are cleaner than those for high gain channels. Small fluctuations can happen during the calibration period before the start of beam data taking, especially during the settings of high voltage trims. These variations can be calibrated out and do not affect the good quality of data taking.

The large spikes seen in April 2013 are due to RMM 2 and RMM 7 addresses being swapped after the substitution of one front end processing node. This problem was fixed as soon as it was found and this period (3 days only) was flagged as bad. The bad flag only limited the cosmic data taking since there was no beam during this time.

The gain variations are also used to monitor the number of dead/non-instrumented channels, i.e. when the fitting algorithm cannot find any peak. At the end of Run IV, 53 channels were reported to be dead. Since the Great Tohoku earthquake TFB 13 and TFB 25 of RMM 9 are completely silent (64+64 channels), bringing the total number of dead channels to 181, which is a very small fraction of the total 22336 channels in the ECals.

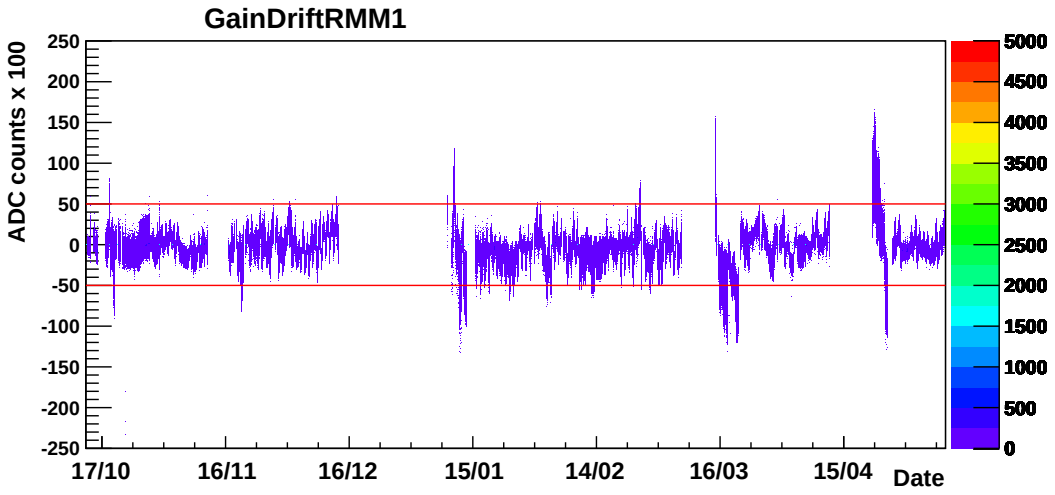

Figure 5.3: Gain variation in RMM 1 as a function of time during Run IV.

5.2.3 ECal cluster rate

The ECal cluster rate is monitored quarterly to check the neutrino event rate in the ECal. Hits are selected in beam spills, calibrated and clustered using the two 2D views of the ECal scintillators. The resulting rate is shown in bins of 24 hours in Figures 5.5 and 5.6.

The main ring (MR) runs 44 and 45 ECal cluster rate was measured to be:

$$4.2787 \pm 0.0155 \text{ Clusters}/10^{14} \text{ POT}\,.$$

The MR runs 46, 47 and 48 ECal cluster rate was measured to be:

$$4.2666 \pm 0.0121 \text{ Clusters}/10^{14} \text{ POT}\,.$$

Problems with the temporary calibration used in this study created a small increase in the event rate for main ring run 48; this increase is not seen when re-analysing the same events after the full calibration is applied.

5.3 ND280 data quality during Run I-IV

The flags for all the sub-detectors are combined to calculate the global ND280 data quality flag, which is 0 only if the flag of each sub-detector is 0. For the Run I-IV period

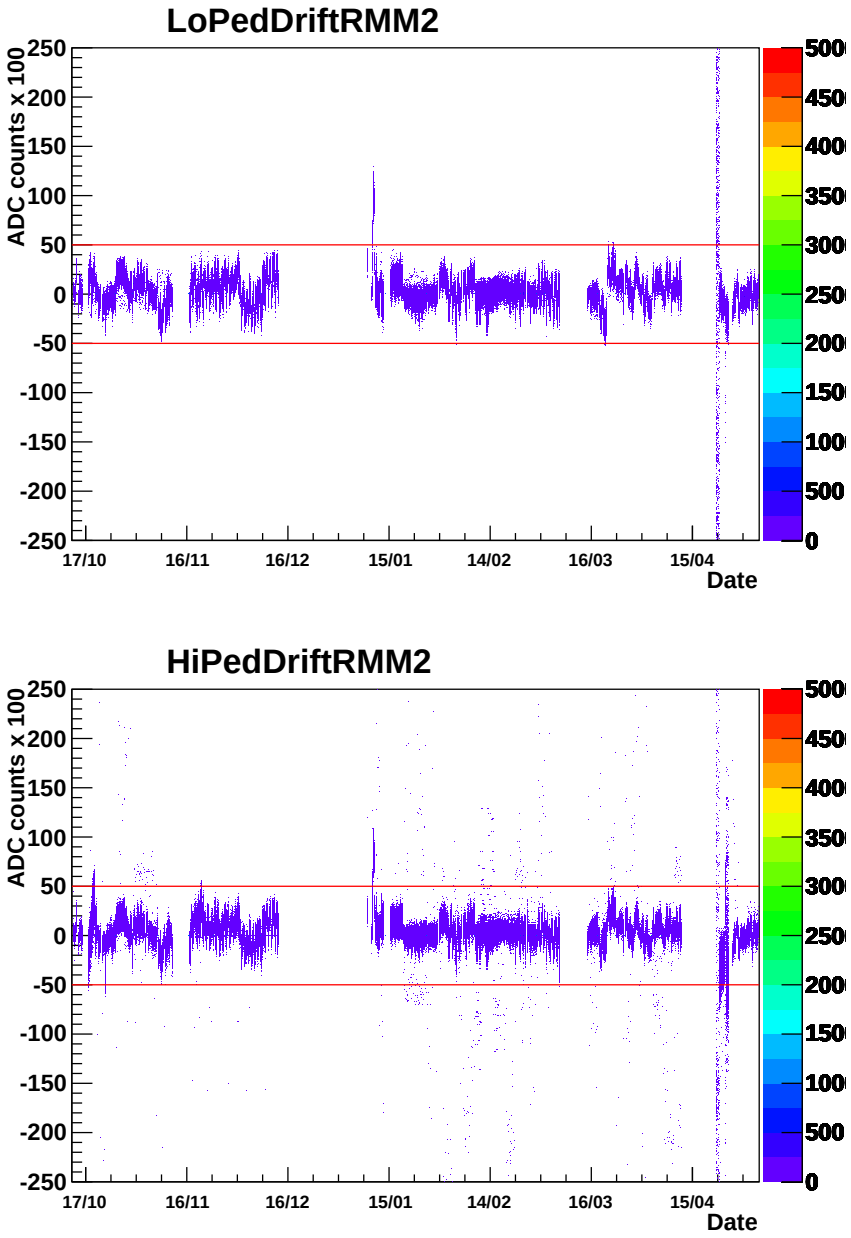

Figure 5.4: Pedestal variation for low gain (top) and high gain (bottom) channels as a function of time for RMM 2 during Run IV.

ND280 had a 98.45% spill efficiency, where the spill efficiency indicates the time when the ND280 DAQ was on and ready to record data. The combination of the ND280 spill

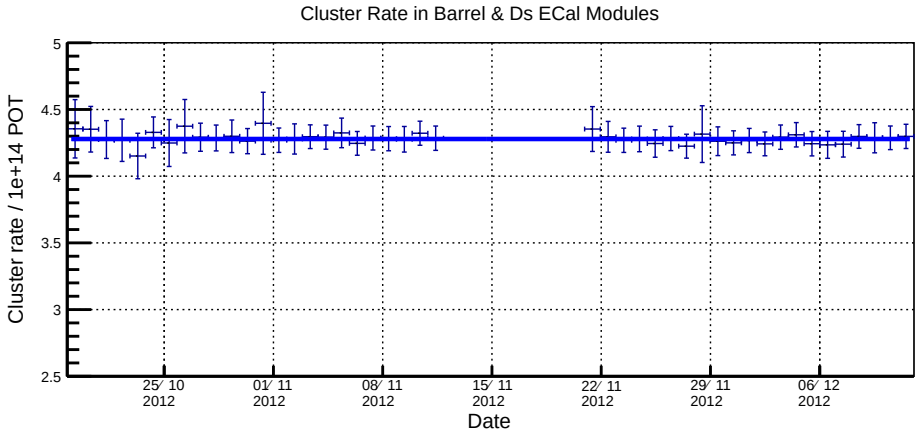

Figure 5.5: ECal cluster rate during MR run 44 and 45.

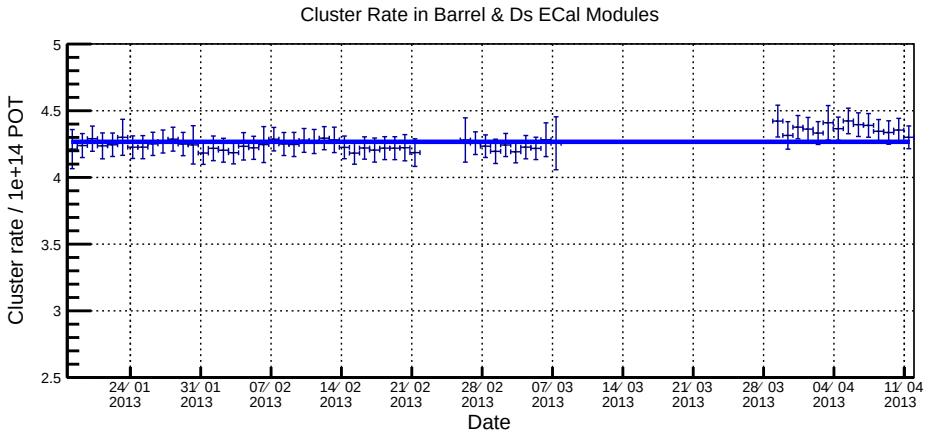

Figure 5.6: ECal cluster rate during MR run 46, 47 and 48.

efficiency and good data quality flag for all the sub-detectors lead to 91.53% efficiency with respect to the POT delivered for Run I-IV. The major events that caused bad data quality flags are a faulty FGD front end bar that created problems during Run I and two faulty TPC front end bars that caused half of Run II (water) to be flagged as bad.

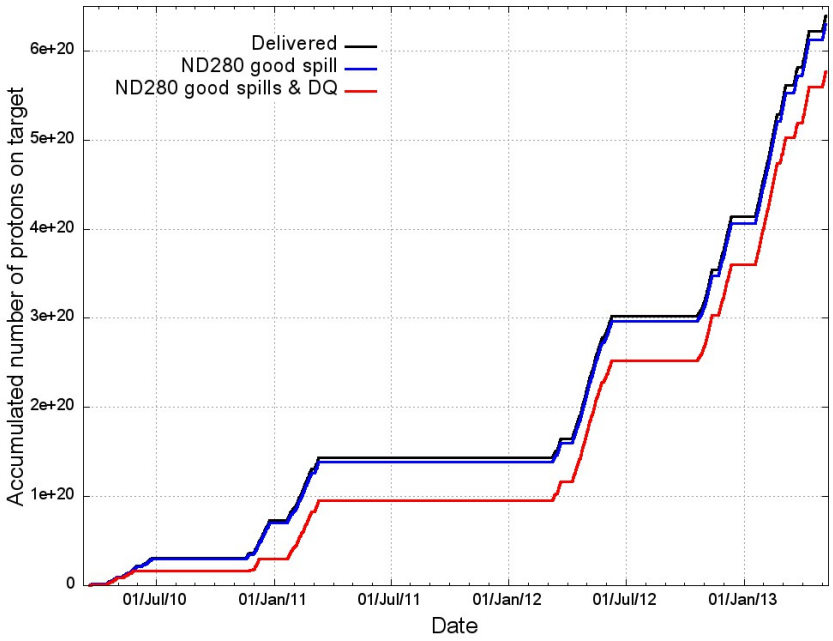

Figure 5.7: Accumulated number of protons on target during Run I-IV with good ND280 spill efficiency and good data quality flag.

6

Selection for the ν_μ CC1π^+ analysis

The aim of the analysis described in this thesis is the measurement of the ν_μ CC1π^+ cross-section on water. Section 6.1 details the selection of a ν_μ CC1π^+ water-enhanced sample using the T2K near detector, ND280. The sample is selected by looking at the particles exiting FGD2 after final state interactions (i.e. requiring 1 μ^- + 1 π^+, any number of nucleons and no additional pions). There are two significant backgrounds in this analysis: one comes from interactions on carbon, and one from DIS interactions. Two separate samples are used to constrain these backgrounds and their selection is described in Section 6.2.

6.1 ν_μ CC1π^+ selection in FGD2

The selection used in this analysis is very similar to the ν_μ CC multiple pions selection described in Reference [55, 85, 87], except for being performed in the FGD2.

6.1.1 Sample

The data-set includes the Run II-IV ND280 events that pass the standard beam quality and ND280 data quality checks (as explained in Chapter 5). The Run I data-set is not used because the Barrel-ECal modules were not installed, and this analysis uses the

ECal to perform the selection. As a result of different beam and detector conditions, the Monte Carlo is separated into different samples and weighted to the equivalent POT of each run, as shown in Table 6.1. The main configuration differences between each run are:

- The PØD contains water bags that were filled with air or water depending on the run period.
- The beam power was increased over time, and three separate beam powers were considered in the simulation.
- In Run IIIa, the magnetic horns that focus the beam were switched off, hence the data from this period is not used.
- In Run IIIb, the magnetic horns were operating at a current of 205 kA, rather than the nominal 250 kA.

Overall, the MC statistics is more than 10 times larger than the data statistics. The NEUT version `5.1.4.2_nd280` was used to generate the MC sample, and the beam flux was tuned based on measurements made by the Beam Group, as explained in Subsection 4.1. NEUT versions below `5.4` contain a bug resulting in NEUT incorrectly simulating coherent interactions on hydrogen; these interactions are manually removed from the MC sample.

For studies of particles originating outside of the ND280 detector, separate samples are produced using a description of the concrete that forms the near detector cavern and the surrounding sand. The sum of the events coming from the interactions with the sand and with the detector are what is really observed. The contribution of sand muons to this analysis is actually negligible, and it will be ignored (see Subsection 7.1.5.2).

6.1.2 Signal definition

The signal definition for this analysis is ν_μ CC1π^+ after final state interactions; this translates into a topology definition of one muon, one positive pion, any number of nucleons, and no additional pions exiting the nucleus after final state interactions.

The true CC1π^+ topology includes not only resonant and coherent interactions, but also some CCQE interactions producing a pion after FSI and CCDIS interactions after

Table 6.1: Definition of T2K runs and the amount of data and MC POT used in this analysis. The last two columns show whether they had water or air in the PØD and the beam power used in the MC files.

T2K run	Data POT	MC POT	PØD water status	MC beam power
Run II Water	4.286×10^{19}	0.6×10^{21}	water	120 kW
Run II Air	3.552×10^{19}	0.6×10^{21}	air	120 kW
Run III b	2.146×10^{19}	0.3×10^{21}	air	178 kW
Run III c	1.348×10^{20}	1.5×10^{21}	air	178 kW
Run IV Water	1.585×10^{20}	1.8×10^{21}	water	178 kW
Run IV Air	1.625×10^{20}	1.614×10^{21}	air	178 kW
Total	5.556×10^{20}	6.314×10^{21}		

additional pions are absorbed during FSI. The resonant interactions in the CC1π^+ true topology sample are 73.2%, the coherent interactions are 14.1%, the CCQE interactions are 2.6%, and the DIS interactions are 10.0%, according to the NEUT event generator.

Throughtout this Chapter we will refer to true final state topologies as predicted by NEUT. The true final state topology is defined by looking at the number of pions exiting the nucleus after final state interactions; the "non ν_μ CC" category denotes ν_e CC, $\bar{\nu}$ CC and NC interactions; the "out of FV" category denotes all the interactions happening outside the FGD2 FV.

6.1.3 ν_μ CC-inclusive in FGD2

Before starting the selections, tracks are grouped together in bunches according to their times. This effectively treats neutrino interactions in two different bunches within the same beam spill as two different events, effectively eliminating accidental pile-up of events.

The ν_μ CC-inclusive selection criteria are as follows:

1. *Data quality flag.* The full spill must have a good global ND280 data quality flag.
2. *Total multiplicity requirement.* Events without any TPC tracks are discarded.

3. *Muon candidate identification.* Among all tracks that originate in the FGD2 and enters the TPCs, the highest momentum negatively-charged one is identified as the μ^- candidate. The negatively charged track is identified using its curvature in the magnetic field, and must start inside the FGD2 fiducial volume (FV). The FGD2 FV begins 58 mm inward from the edges of the FGD2 in x and y and 7.5 mm inward from the upstream FGD2 edge in z (i.e. the first upstream x layer is outside the FV). A schematic view of the FGD1 and FGD2 FVs is shown in Figure 6.1. The negative track must have more than 18 vertical clusters in the TPC ("TPC track quality" requirement) to reject short tracks for which the reconstruction is less reliable.

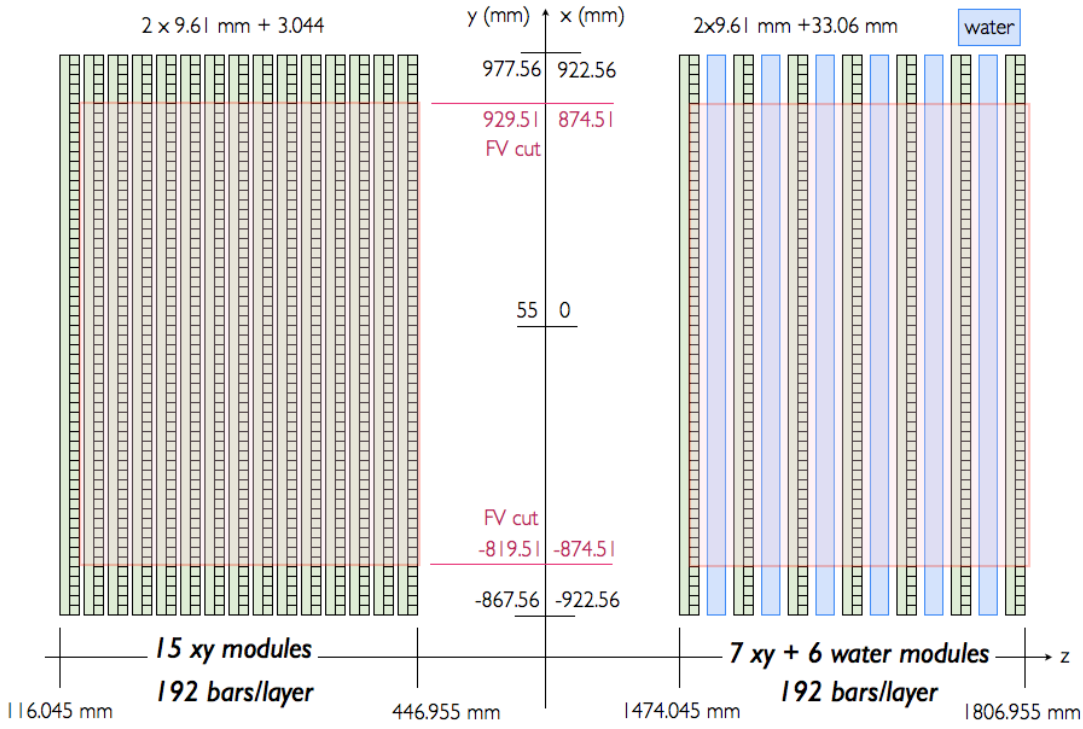

Figure 6.1: Schematic view of the FGD1 and FGD2 detectors, and their FV delimited by the red lines. The coordinate system is also indicated: the y coordinate is displaced 55 mm upwards relative to the centre of the ND280 coordinate system, which is centred in the magnet.

4. *External veto requirement.* The goal of this requirement is to remove mis-recon-

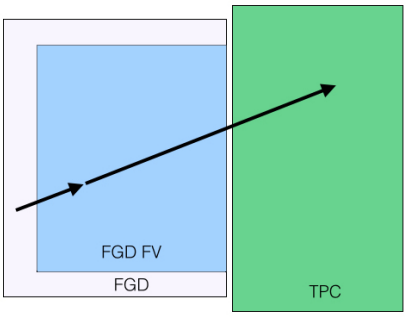

Figure 6.2: Schematic example of a broken track. The long track is reconstructed as two different tracks, one FGD-only track starting outside of the FGD FV, and one FGD-TPC track.

structed events that originate outside the FGD2 FV. By looping over all the TPC tracks, the highest momentum secondary[1] track (no requirement on the TPC track quality criteria) is found. If this track has its start position more than 150 mm upstream than the muon candidate, the event is rejected.

5. *Broken track veto.* External background coming from the last two layers of the FGD2 is rejected by vetoing events with the muon candidate starting in the last two layers of the FGD2 and one FGD-only track starting/finishing out of the FGD2 FV. The FGD-only tracks are defined as tracks with segments in the FGD and no segments in any TPC. A schematic example of a broken track is shown in Figure 6.2.

6. *Muon PID cut.* The muon TPC PID criteria is applied to the muon candidate using the dE/dx distribution as explained in Reference [88].

   The TPC PID uses functions that give the expected value of the deposited energy in the track for different particle hypotheses. A discrimination function for muon, pion and proton hypothesis is evaluated from the estimated momentum of the muon candidate. To reject electrons (first requirement) and pions/protons (second requirement), two cuts are applied:

$$L_{MIP} = \frac{L_\mu + L_\pi}{1 - L_p} > 0.8 \qquad \text{if } p < 500 \text{ MeV/c}\,, \tag{6.1}$$

[1] "secondary" here refers to a track that is not the muon candidate

$$L_\mu > 0.05\,. \tag{6.2}$$

Figure 6.3 shows the distributions of L_{MIP} and L_μ after the broken cut veto is applied. The red lines show the cut value decided to enhance the muon candidate purity.

The likelihood L_{particle} is defined as:

$$L_i = \frac{e^{-\text{Pull}_i^2}}{\Sigma_l e^{-\text{Pull}_l^2}}\,, \tag{6.3}$$

where the pulls are defined as:

$$\text{Pull}_i = \frac{(dE/dx_{\text{measured}} - dE/dx_{\text{expected},i})}{\sigma_{(dE/dx_{\text{measured}} - dE/dx_{\text{expected},i})}}\,. \tag{6.4}$$

The dE/dx is estimated as a truncated mean of the energy released in the TPC as described in Reference [89]. The value $dE/dx_{\text{expected},i}$ is the value of the truncated mean for the particle hypothesis 'i' ($i = \mu^-, \pi^{+/-}, p$).

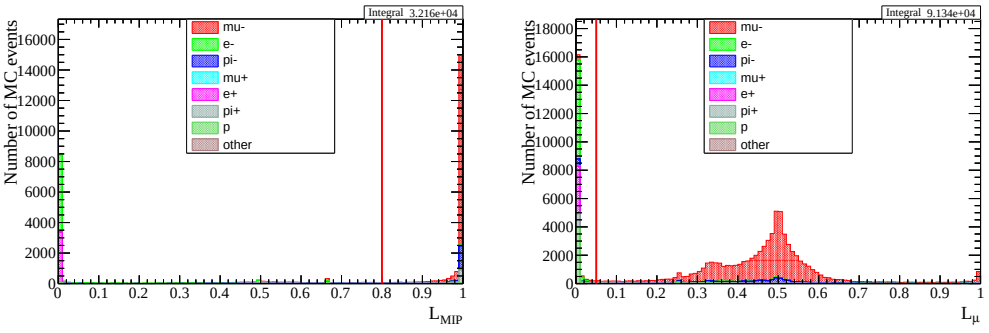

Figure 6.3: Distributions of the L_{MIP} (after the $p < 500\,\text{MeV/c}$ cut is applied) and L_μ. The red lines show the cut value decided to improve the muon candidate purity of the sample.

Events passing these requirements correspond to ν_μ CC-inclusive events in FGD2.

The CC-inclusive sample is then divided in 3 sub-samples, based on the number of reconstructed pions: the CC0π-like, CC1π^+-like and the CC Other-like samples.

6.1.4 One positive pion requirement

The CC1π^+-like sample is selected by requiring one secondary track in the same bunch as the muon candidate, starting in the FGD2 FV, satisfying the TPC track quality requirement and identified as a positive pion with the TPC PID. If any additional pion or electron/positron is found, the event is rejected.

The PID assignment is based on the "most probable particle" method. First negative and positive particles in the TPC are separated: negative particles are tested against the probability of being a negative pion or an electron; positive particles are tested against the hypothesis of a positive pion, a positron or a proton.

The pull and likelihood for each particle hypothesis are computed as described in Equations 6.3 and 6.4. To check which type is the most probable particle type, the ratio of the probability for a given particle type over the sum over all the probabilities is computed:

$$P_i = \frac{L_i}{\Sigma_l L_l}\,, \tag{6.5}$$

where i is the particle checked, l is either a positive pion, positron or proton in the positive case, and is a negative pion or electron in the negative case. Particles are tagged with the type that has the highest probability.

6.1.5 ECal π^0 veto

In addition to the previous requirements, π^0 objects are rejected by looking at showers in the ECal modules.

An event is rejected (and moved to the CC Other-like sample) if these requirements are met:

- There are isolated objects in the ECal (i.e. no segments in any other sub-detector) in the same time bunch as the muon candidate.
- The most energetic object has electromagnetic energy larger than 0, and the likelihood to distinguish MIPs and showers is compatible with an electromagnetic shower.
- The object has hits in the 5 innermost layers of the ECal.

- The distance between the muon candidate and the isolated ECal object must be larger than 70 cm; this is to prevent tagging the muon candidate that might have reached the ECal and is mis-identified as a π^0.

- The distance between all TPC positive tracks and the isolated ECal object must be larger than 70 cm (in case the positive pion reaches the ECal and is mis-identified as a π^0).

If all these requirements are met, the event is moved to the CC Other-like sample.

The lifetime of a neutral pion is extremely short ($\approx 10^{-16}$ s) hence the decay into γ rays happens extremely quickly; this veto manages to reject CC events producing π^0 by tagging the e^+/e^- showers.

The objects tagged by the ECal π^0 veto come mainly from a CCXπ^0 interaction (i.e. a CC interaction producing any number of π^0 in the final state) (51.3%). The rest are true CC Other (17.4%), non ν_μ CC (9.4%) and out of FV (4.6%) interactions. Some of these objects come also from true CC1π^+ (15.6%), but this loss in efficiency (from 28.2% to 26.6% following the definition that will be shown in Section 6.1.7, Equation 6.6) is compensated by a CC1π^+ purity increase from 43.6% to 49.1%, whilst the CC Other background is reduced from 41% to 35%.

Two of the electronics boards in the right-side Barrel ECal were damaged during the 2011 earthquake, hence the simulation ignores the right-side Barrel ECal entirely for Run III and Run IV. When all the ECals are operational (Run II Air) the ECal π^0 is more effective, vetoing 40% of the CCXπ^0 interactions in the sample. After the right-side Barrel ECal were damaged (Run IIIc Air), the ECal π^0 is less effective, vetoing 32.8% of the CCXπ^0 interactions in the sample.

6.1.6 Selecting interactions in water

The FGD2 consists of polystyrene scintillator bars alternately oriented in the x and y directions and interleaved with water layers. The polystyrene scintillator bars allow 3D tracking of the charged particles. The water layers serve as target for measurements of neutrino interactions in water.

The z position of an interaction can only be reconstructed in the x layers or in the y layers (as shown in Figure 6.4). When an interaction happens in the water modules,

the first hits are seen in the scintillator layer downstream of the water module, i.e. in the x layer (Figure 6.5).

To select a water-enhanced sample, the muon candidate is required to have the start position in the x layers of FGD2. This effectively generates a consistent intrinsic background of interactions on scintillator (i.e. in the x layer), as seen in Figure 6.4 and 6.5.

A future improvement of this analysis will use the *Global vertexing algorithm* to determine the vertex position more accurately. Looking at the geometry of the muon and pion tracks it would be possible to reconstruct the vertex in the water modules. Evaluating the systematic uncertainties related to the *Global vertexing algorithm* would require running the ND280 reconstruction multiple times and this kind of study is not feasible at the moment.

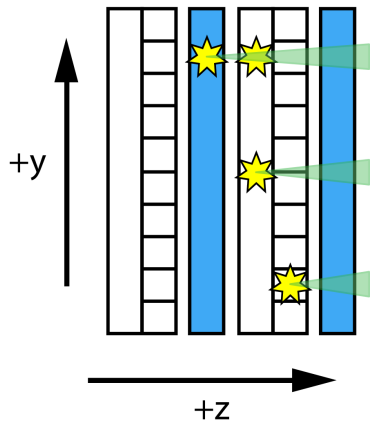

Figure 6.4: Diagram showing the structure of layers in the FGD2 (x layer, y layer, water module, etc) and an interaction in the water layers (with first hits registered in the x layer), an interaction in the x layer and an interaction in the y layer.

6.1.7 Efficiency and Purity

Table 6.2 shows the efficiency of true CC1π^+ interactions (on any target) and true CC1π^+ interactions in the water layers for the ν_μ CC-inclusive, CC1π^+-like and CC1π^+-like water-enhanced samples. The efficiency is defined as the ratio between the true CC1π^+ interactions in the selected sample and the number of true CC1π^+ interactions

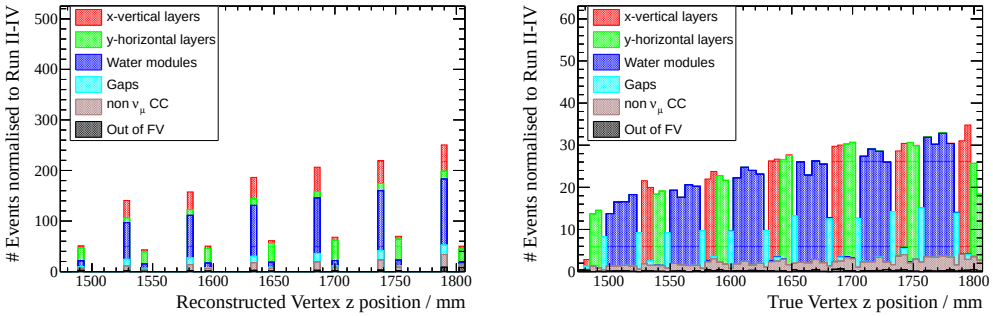

Figure 6.5: Comparison of reconstructed (left) and true (right) z position of ν_μ CC-inclusive sample in FGD2. Colour legend shows where the true interaction happened.

Table 6.2: True CC1π^+ and true CC1π^+ in water layers efficiency for the ν_μ CC-inclusive, CC1π^+-like and CC1π^+-like water-enhanced samples.

	ν_μ CC-inclusive	CC1π^+-like	CC1π^+-like water-enhanced
$\epsilon_{CC1\pi^+}$	0.495	0.138	0.105
$\epsilon_{CC1\pi^+ \text{ on water}}$	0.510	0.140	0.131

in the FV of the FGD2:

$$\epsilon_{CC1\pi^+} = \frac{N^{\text{selected, true } CC1\pi^+}}{N^{\text{true } CC1\pi^+}} . \tag{6.6}$$

Similarly the definition for the efficiency of true CC1π^+ interactions in water is defined as:

$$\epsilon_{CC1\pi^+ \text{ on water}} = \frac{N^{\text{selected, true } CC1\pi^+ \text{ in water}}}{N^{\text{true } CC1\pi^+ \text{ in water}}} . \tag{6.7}$$

The final true CC1π^+ efficiency for this selection anywhere in FGD2 is 13.8% and the efficiency with respect to true CC1π^+ interactions in the water modules is 13.1%.

Tables 6.3 and 6.4 show the true final state topology and reaction composition of the ν_μ CC-inclusive, CC1π^+-like and CC1π^+-like water-enhanced samples. The final CC1π^+ purity is 50.6%.

The CC Other true topology is the main background (35.2%): sometimes additional pions are not detected due to secondary interactions (e.g. pion absorption or charge exchange) or reconstruction difficulties. Non ν_μ CC interactions also constitute an

Table 6.3: True final state topology composition of the ν_μ CC-inclusive, CC1π^+-like and CC1π^+-like water-enhanced samples.

True final state topology	ν_μ CC-inclusive	CC1π^+-like	CC1π^+-like water-enhanced
CC-0π	51.6%	3.8%	3.9%
CC1π^+	14.4%	49.4%	50.6%
CC Other	24.8%	35.5%	35.2%
non ν_μ CC	4.2%	8.9%	8.6%
out of FV	5.0%	2.4%	1.7%
Total number of MC events	275744	22552	16784

important background (8.6%): these are mainly NC and $\bar{\nu}$ interactions where a negative pion is identified as the muon candidate.

The "out of FV" interactions are less in the CC1π^+ water-enhanced sample than in the whole CC1π^+ sample, because of the FV definition. In the complementary analysis performed in FGD1, the first xy module is removed from the FV (see Figure 6.1). In the FGD2 analysis, only the first x layer is removed from the FV, as removing the whole xy module would make it impossible to use the first water module. For this reason the first and the last layers of the FGD2 FV (i.e. the ones containing more "out of FV" background) are both y layers (see Figure 6.5, left) and only contribute to the CC1π^+ scintillator sample, which therefore contains more "out of FV" background than the water-enhanced sample.

Table 6.5 shows the percentage of interactions in each layer of FGD2 and Table 6.6 shows the percentage of interactions on the different target materials. The final water purity is 52.7% and the oxygen purity is 45.3%. The difference between the water and oxygen purity comes from the fact that the water modules are rectangular vessels made of polycarbonate and containing the water (see Reference [63]): interactions in these modules can happen on oxygen, but also on carbon and other target materials. Moreover, the water sample contains interactions that were reconstructed in both the water and x layers. The irreducible background of interactions in scintillator (22.3%) can be constrained with a control sample as explained in Section 6.2. Migrations

Table 6.4: True reaction composition of the ν_μ CC-inclusive, CC1π^+-like and CC1π^+-like water-enhanced samples.

True reaction	ν_μ CC-inclusive	CC1π^+-like	CC1π^+-like water-enhanced
CCQE	44.6%	2.4%	2.4%
RES	22.9%	37.6%	38.6%
DIS	21.2%	38.5%	38.1%
COH	2.1%	10.2%	10.5%
NC	3.1%	5.8%	5.6%
anti-ν_μ	0.6%	2.5%	2.4%
ν_e	0.4%	0.5%	0.5%
out of FV	5.0%	2.4%	1.7%

between the x and y layers also contribute to this background and they are studied in Subsection 7.1.3.

Table 6.7 shows the percentage of true CC1π^+ and CC non-1π^+ in different modules of the FGD2.

6.1.8 Variables used in the cross-section measurement

The aim of this analysis is to present the single differential ν_μ CC1π^+ cross-section in water as a function of the muon and pion kinematic variables, the angle between the muon and pion, and the reconstructed neutrino energy. In this Subsection, the distributions of the variables used in the cross-section measurement are presented.

Table 6.8 details the binning considered for the different kinematic variables. Since the purity of the signal is fairly low, the binning has to be coarse enough to have at least 100 data events from Run II-IV in each bin. Appendix A contains correlation and resolution of all the variables used to evaluate the cross-section.

For the reconstructed neutrino energy two formulae are considered:

Table 6.5: Percentage of interactions in different modules of the FGD2 for the ν_μ CC-inclusive, CC1π^+-like and CC1π^+-like water-enhanced samples.

FGD2 module type	ν_μ CC-inclusive	CC1π^+-like	CC1π^+-like water-enhanced
x layer	18.6%	18.9%	22.3%
y layer	19.9%	19.4%	6.8%
water	45.4%	43.5%	52.7%
gaps	7.0%	6.9%	7.9%
non $\nu\mu$ CC	4.2%	8.8%	8.6%
out of FV	5.0%	2.4%	1.7%

Table 6.6: Percentage of interactions on different targets for the ν_μ CC-inclusive, CC1π^+-like and CC1π^+-like water-enhanced samples.

Target	ν_μ CC-inclusive	CC1π^+-like	CC1π^+-like water-enhanced
Carbon	48.2%	46.4%	39.4%
Oxygen	43.3%	38.5%	45.3%
Hydrogen	4.1%	12.6%	13.4%
Aluminium	1.3%	0.8%	0.6%
Iron	0.6%	0.1%	0.1%
Lead	1.1%	0.5%	0.3%
Other	1.4%	1.1%	0.9%

Table 6.7: Percentage of true CC1π^+ and CC non-1π^+ in different modules of the FGD2 for the ν_μ CC-inclusive, CC1π^+-like and CC1π^+-like water-enhanced samples.

	ν_μ CC-inclusive	CC1π^+-like	CC1π^+-like water-enhanced
CC1π^+ water	7.2%	24.5%	30.9%
CC1π^+ XY	6.1%	20.9%	15.2%
CC1π^+ other	1.1%	4.0%	4.6%
CC non-1π^+ water	38.2%	19.0%	21.8%
CC non-1π^+ XY	32.4%	17.4%	13.9%
CC non-1π^+ other	5.9%	3.0%	3.4%
non ν_μ CC	4.2%	8.8%	8.6%
Out of FV	5.0%	2.4%	1.7%

Table 6.8: Binning of the kinematic variables used in the cross-section measurement, where the momentum and energy variables are given in GeV.

Variable	Bins
p_{π^+}	[0, 0.3, 0.35, 0.4, 0.5, 0.6, 0.7, 0.85, 1.1, 1.4, 1.85, 30]
$\cos\theta_{\pi^+}$	[-1, 0.57, 0.68, 0.75, 0.79, 0.83, 0.86, 0.89, 0.91, 0.93, 0.95, 0.97, 0.98, 0.99, 1]
p_{μ^-}	[0, 0.3, 0.4, 0.5, 0.6, 0.75, 0.95, 1.15, 1.4, 1.75, 2.1, 2.5, 3.05, 3.7, 4.9, 30]
$\cos\theta_{\mu^-}$	[-1, 0.62, 0.72, 0.78, 0.83, 0.87, 0.90, 0.93, 0.95, 0.96, 0.98, 0.99, 1]
E_ν	[0, 0.8, 1, 1.2, 1.5, 1.8, 2.1, 2.55, 3, 3.6, 4.35, 5.4, 30]
$\cos\theta_{\mu^-,\pi^+}$	[-1, 0.15, 0.25, 0.4, 0.5, 0.6, 0.7, 0.8, 0.9, 1]

- CCQE formula with a Δ resonance:

$$E_\nu = \frac{m_\Delta^2 - m_p^2 + 2m_p E_\mu - m_\mu^2}{2(m_p - E_\mu + P_\mu \cos\theta_\mu)} \tag{6.8}$$

  where $m_\Delta = 1232\,\text{MeV}$, $m_p = 938.27\,\text{MeV}$ and $m_\mu = 105.66\,\text{MeV}$ are the masses of the Δ particle, proton and muon, respectively; E_μ is the energy of the muon,

P_μ is the momentum of the muon, and $\cos\theta_\mu$ is the angle between the muon and the neutrino beam direction projected to the xy plane of the ND280 detector coordinates.

- Improved CC1π^+ formula (presented by the MiniBooNE collaboration in Reference [43]) assuming the target nucleus is at rest and the remaining final state particle is a nucleon:

$$E_{\nu,MB} = \frac{m_\mu^2 + m_\pi^2 - 2m_N(E_\mu + E_\pi) + 2E_\mu E_\pi - 2p_\mu p_\pi \cos\theta_{\mu,\pi}}{2(E_\mu + E_\pi - p_\mu \cos\theta_{\nu,\mu} - p_\pi \cos\theta_{\nu,\pi} - m_N)} \tag{6.9}$$

where $m_\mu = 105.66\,\text{MeV}$, $m_\pi = 139.57\,\text{MeV}$ and $m_N = 939.57$ are the masses of the muon, pion and nucleon respectively; E_μ and E_π are the energies of the muon and pion; p_μ and p_π are the momenta of the muon and pion; $\cos\theta_{\mu,\pi}$ is the angle between the muon and pion directions; and $\cos\theta_{\nu,\pi}$ is the angle between the pion and neutrino beam directions projected to the xy plane of the ND280 detector coordinates.

Figure 6.6 shows the pion and muon kinematic variables distributions for the CC1π^+ water-enhanced sample. Figure 6.7 shows the $\cos\theta_{\mu^-,\pi^+}$, and reconstructed neutrino energy distributions for the selected sample.

All the variables used in the cross-section measurement show good correlation between the reconstructed and the true variables, and the resolution is fairly small compared to the chosen bin width (see Appendix A).

6.1.9 Phase space reduction

Figures 6.8 and 6.9 show the efficiency and purity of true CC1π^+ interactions on water in the selected sample.

The efficiency at low p_{π^+}, because the only pions reconstructed are those that make it to the TPC. Low energy pions tend to stop in the FGD. Future analyses will use information from Michel electrons or FGD-only tracks to select pions in this part of the phase-space.

To avoid being model dependent when unfolding this low efficiency regions, a phase-space reduction is applied in the momentum variables, such that only events with $p_\mu > 200\,\text{MeV}$ and $p_\pi > 200\,\text{MeV}$ are considered.

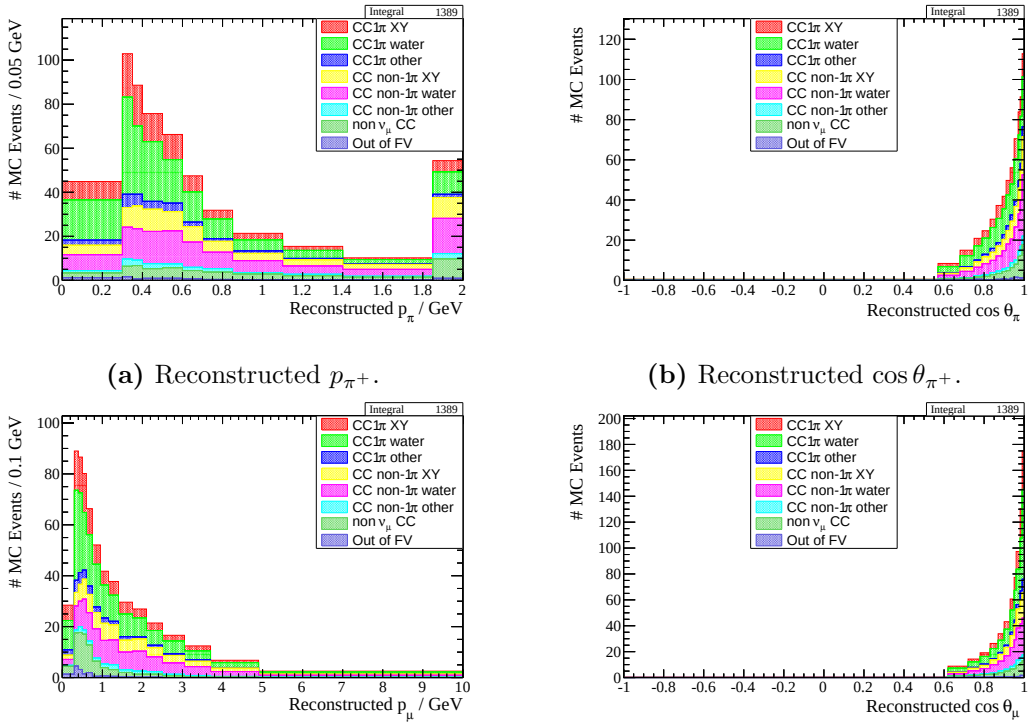

(a) Reconstructed p_{π^+}.

(b) Reconstructed $\cos\theta_{\pi^+}$.

(c) Reconstructed p_{μ^-}.

(d) Reconstructed $\cos\theta_{\mu^-}$.

Figure 6.6: Reconstructed pion and muon kinematic variables for the CC1π^+ water-enhanced sample.

For $\cos\theta_{\pi^+}$ and $\cos\theta_{\mu^-}$, the efficiency is very low at high backward angle, due to limitations in the reconstruction. For this reason a cut in the phase-space should be applied considering only events with $\cos\theta_\pi > 0.3$ and $\cos\theta_\mu > 0.3$. The phase-space requirement is applied in the reconstructed and true variables, and in all the cross-sections.

The efficiency of the CC1π^+ water-enhanced sample goes from 13.3% in the full phase-space to 30.7% in the reduced phase-space.

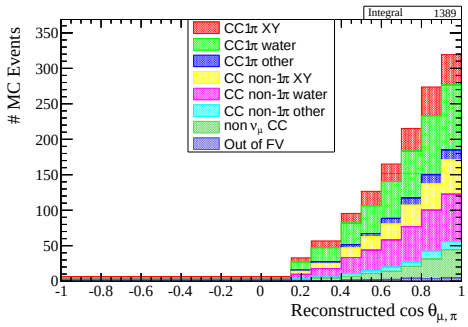

(a) Reconstructed $\cos\theta_{\mu^-,\pi^+}$.

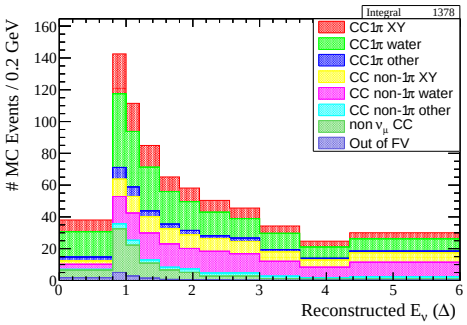

(b) $E_{\nu,\Delta}$ (Δ resonance formula).

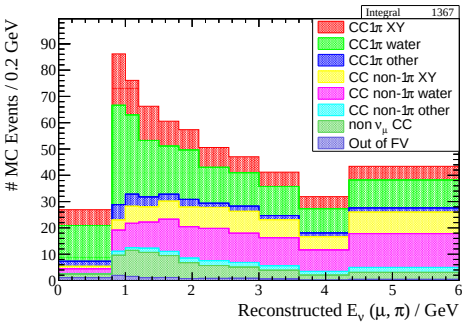

(c) $E_{\nu,MB}$ (MiniBooNE formula).

Figure 6.7: Reconstructed $\mu^- - \pi^+$ angle and neutrino energy for the CC1π^+ water-enhanced sample.

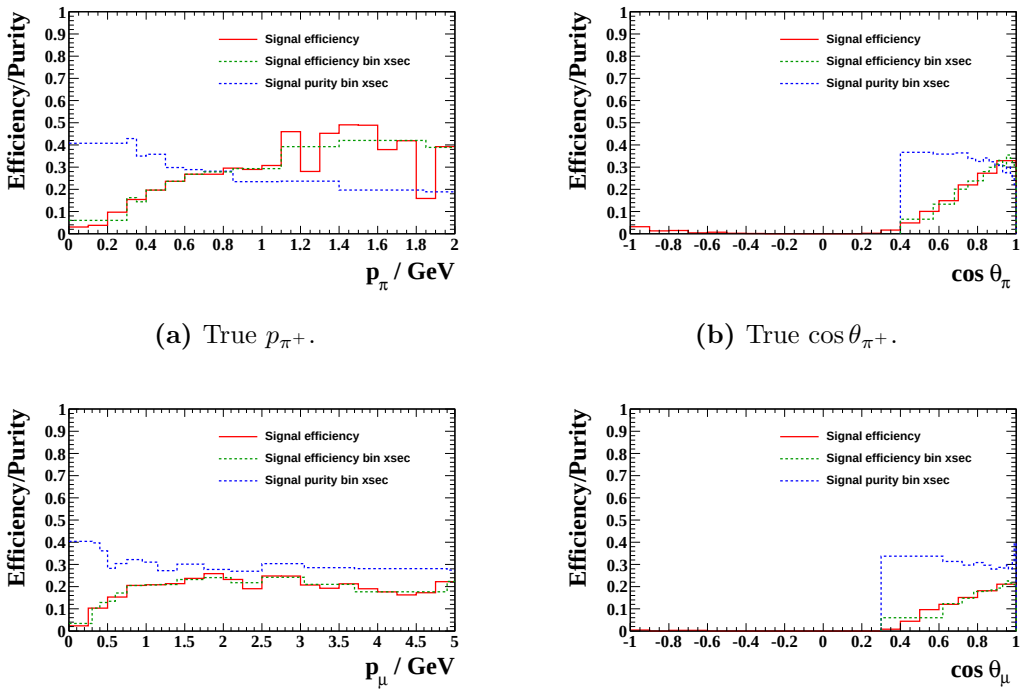

(a) True p_{π^+}.

(b) True $\cos\theta_{\pi^+}$.

(c) True p_{μ^-}.

(d) True $\cos\theta_{\mu^-}$.

Figure 6.8: Efficiency of true CC1π^+ interactions on water. The solid red line indicates the signal efficiency in fine binning used to look at the phase-space, the green dashed line indicates the signal efficiency in the binning used for the cross-section, and the blue dashed line indicated the signal purity in the binning used for the cross-section.

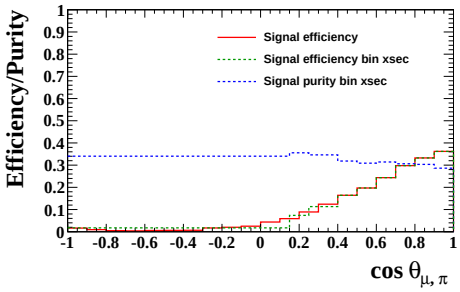

(a) True $\cos\theta_{\mu^-,\pi^+}$.

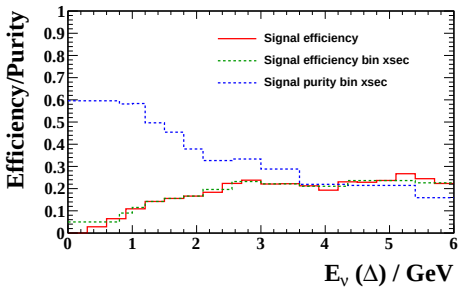

(b) $E_{\nu,\Delta}$ (Δ resonance formula).

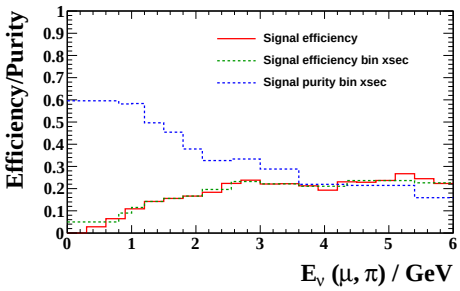

(c) $E_{\nu,MB}$ (MiniBooNE formula).

Figure 6.9: Efficiency of true CC1π^+ interactions on water. The solid red line indicates the signal efficiency in fine binning used to look at the phase-space, the green dashed line indicates the signal efficiency in the binning used for the cross-section, and the blue dashed line indicated the signal purity in the binning used for the cross-section.

6.2 Selection of control samples

The background in the selected CC1π^+ water-enhanced sample can be constrained with two selected control samples.

As seen in Table 6.7, the main sources of background are:

CC1π^+ interactions in scintillator: intrinsic background that comes from the way the water-enhanced sample is selected. It corresponds to the interactions with true vertex in the x layer (61.9%), in the gaps between layers (23.8%) and in the y layer (14.3%).

CC non-1-π^+ interactions in water/scintillator: background coming from deep inelastic scattering (82.3 %), resonant interactions (13.1%) and CCQE interactions (4.6%). Difficulties in the reconstruction (one or more pions are not reconstructed, or the proton from a CCQE interaction is mis–identified as a π^+) or pion secondary interactions cause this kind of background.

Non ν_μ-CC interactions: NC (63.7%), $\overline{\nu}_\mu$ (30.3%) and ν_e (5.7%) interactions, where a π^- is mis–identified as the μ^- candidate in 92.5% of events (in the other cases it is a kaon, a proton or a μ^+).

Out of FGD2 FV: interactions happening outside the FV of the FGD2.

These backgrounds can be constrained with the selection of two control samples: a CC1π^+ carbon control sample (Subsection 6.2.1) and a CC Other water control sample (Subsection 6.2.2).

6.2.1 CC1π^+ carbon control sample

The background coming from CC1π^+ interactions in scintillator can be constrained with a sample of selected CC1π^+-like events in the y layers of the FGD2; this sample has the exact same selection as the one described in Section 6.1, only the last cut requires the vertex to be reconstructed in the y layers instead of the x layer. The final sample is then enhanced in the CC1π^+ interactions on carbon. Table 6.9 details the purity of this sample (Sideband 1) and the background it describes (Background 1).

This sample has a 6.1% signal contamination in it, which as underlined by studies showed in Subsection 8.2.4, does not add any appreciable bias to the analysis.

It has been proposed to substitute Sideband 1 with the complementary signal sample in FGD1, which does not contain any interactions in water and would provide larger statistics. This analysis does not include any sample from FGD1, because using the FGD1 sample would not improve the CC1π^+ purity of the control sample, as the CC-Other contamination would still be around 40% and would not result in a significant improvement for the analysis. Furthermore, including a sample from FGD1 would require the evaluation of the correlations between detector systematic uncertainties associated with FGD1 and FGD2, something which has not yet been studied in T2K.

6.2.2 CC Other water control sample

Since it is quite difficult to find a selected sample to control the non ν_μ-CC and the out of FV interactions, they are added to the CC non $1\pi^+$ background to form the combined **non CC1π^+ background**, (Background 2) which can be constrained with a sample of selected CC Other-like water-enhanced events with maximum 4 tracks in the FGD2 (Sideband 2).

The selection of this sample is the same as the ν_μ CC-inclusive in FGD2, with the following additional criteria:

- There is at least one π^+ and one other pion, with a maximum of 4 pions in total.
- The vertex is reconstructed in an x layer of the FGD2.

The choice to require at least one π^+ and to put a limit on the maximum number of tracks is dictated by the necessity to better describe the CC Other events entering in the CC1π^+-like sample.

Table 6.9 shows the purity of the true final state topology combined with the true interaction position inside the FGD2. Background 1/2 refer to the background in the selected signal sample, whereas Sideband 1/2 refer to the control regions selected to describe background 1/2. Sideband 1 is less pure in CC1π^+ interactions than the background 1, but it is the only available sample that can describe interactions on carbon. Sideband 2 has a very similar composition to Background 2 (which is the main background) and we expect it to describe quite well the background coming from non-CC1π interactions.

Table 6.9: Percentage of true CC1π^+ and CC non-1π^+ in different modules of the FGD2. Background 1: CC1π^+ interactions in the scintillator within the selected signal sample; Background 2: non CC1π^+ interactions within the selected signal sample; Sideband 1: selected CC1π^+ like events in the y layers of the FGD2; Sideband 2: selected CC Other-like water-enhanced events with maximum 4 tracks in the FGD2.

	Background 1	Sideband 1	Background 2	Sideband 2
CC1π^+ water	0%	6.1%	0%	5.9%
CC1π^+ XY	76.5%	37.5%	0%	2.9%
CC1π^+ other	23.5%	2.0%	0%	0.8%
CC non-1π^+ water	0%	10.9%	28.4%	26.7%
CC non-1π^+ XY	0%	27.7%	44.1%	44.5%
CC non-1π^+ other	0%	2.0%	6.7%	6.4%
non ν_μ CC	0%	9.5%	17.3%	7.7%
Out of FV	0%	4.4%	3.5%	5.3%
Number of MC events	3455	6089	8760	46631

6.2.3 Background and control region comparison

Although the method implemented in the cross-section calculation to constrain the background with a control region is quite simple (it relies only on the total number of events in the background and control regions), it is important to check that the control regions and the backgrounds describe similar regions of the phase-space.

Figure 6.10 shows the p_{π^+} distributions of the Backgrounds 1 and 2, and Sidebands 1 and 2. Appendix A presents the same distributions for all the variables used in the cross-section measurement. In all cases, the control regions have a similar shape to the background that they describe.

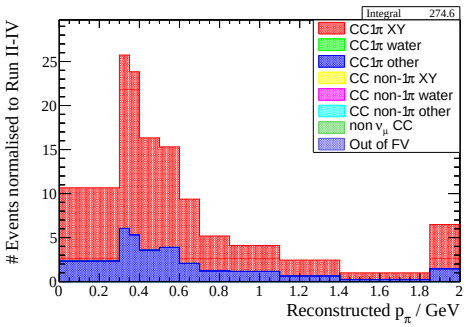

(a) CC1π^+ background in CC1π^+ water-enhanced sample.

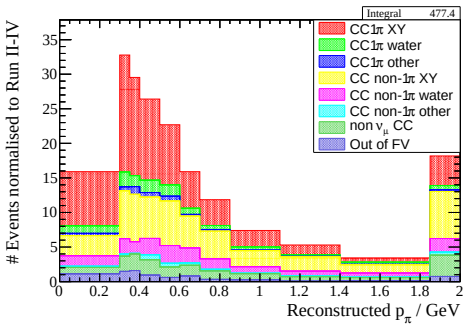

(b) CC1π^+ scintillator sample.

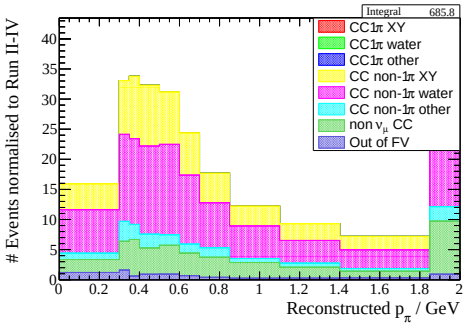

(c) Non-CC1π^+ background in CC1π^+ water-enhanced sample.

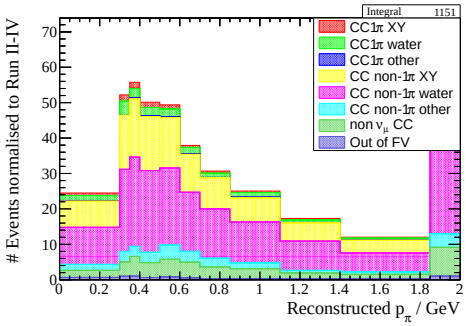

(d) CC Other (max 4 tracks) water-enhanced sample.

Figure 6.10: p_{π^+} distributions: background and control sample distributions.

7

Systematic uncertainties for the ν_μ CC1π^+ analysis

This Chapter highlights the systematic uncertainties considered in this analysis; the propagation of the uncertainties to the cross-section measurement is described in Chapter 8.

The near detector systematic uncertainties are described in Section 7.1; most of these uncertainties have been evaluated by the NuMu, NuE and PiZero ND280 working groups [85]. Emphasis is given to the FGD layer migrations because they are studied for the first time in this thesis. The flux and theory cross-section uncertainties are highlighted in Section 7.2.

7.1 Detector systematic uncertainties

The ND280 detector consists of many sub-detectors, hence there are a large number of sources of systematic uncertainties. For some sources of uncertainties, the MC sample does not match the data, and in these cases a correction is applied, in addition to computing the systematic uncertainty. In the other cases, only the systematic uncertainty is computed.

The systematic uncertainties mainly fall into two categories: weighting or migration systematics. Weighting systematics do not alter the observables of an event, but only re-weight the event to increase or reduce its contribution to the selection (either

with an efficiency or a normalisation parameter). Migration systematics can alter the observables of an event, and hence can cause a migration between momentum bins, or selections.

Table 7.1 details the list of the detector systematic uncertainties considered in this analysis, how the uncertainty is propagated in the analysis and whether a correction is applied or not. The next sections will explain the systematic uncertainties related to the TPC (Subsection 7.1.1), FGD (Subsection 7.1.2), ECals (Subsection 7.1.4), migrations between FGD layers (Subsection 7.1.3), and external contributions (Subsection 7.1.5). Particular emphasis will be given to the studies of the migration between FGD layers, as this is a new ND280 systematic uncertainty.

For reference, the largest sources of detector systematic uncertainty in this analysis are the pion secondary interactions and the TPC PID.

7.1.1 TPC systematic uncertainties

The TPC systematic uncertainties have been studied in depth by the NuMu ND280 working group, and are described in detail in Reference [85]. These systematic uncertainties are studied with a control sample of particles that cross all three TPCs, unless otherwise stated.

Magnetic field distortions were measured with a Hall probe before the detectors were installed, and the reconstruction accounts for these measured deviations from the ideal field. The systematic uncertainty is evaluated by looking at the difference in reconstructed momentum for each track turning on/off the magnetic field corrections.

TPC charge confusion is calculated by comparing the charge assignment in each TPC; this uncertainty is found to be less than 1% for momenta less than 5 GeV. In the very low momentum bins (i.e. $p < 0.3\,\text{GeV}$), the uncertainty can get up to a few %, because low momentum particles are less likely to cross the three TPCs, and mis-matching of tracks belonging to different particles is more likely to happen.

TPC momentum resolution is studied by evaluating the effect on the reconstructed momentum when the information from one of the TPCs is removed. The inverse

Table 7.1: List of detector systematic uncertainties considered in this analysis and their treatment.

Systematic error source	Treatment	Correction
B Field distortion	Observable variation	No
TPC charge confusion	Efficiency	Yes
TPC momentum resolution	Observable variation	Yes
TPC momentum scale	Observable variation	No
TPC cluster efficiency	Efficiency	Yes
TPC track efficiency	Efficiency	Yes
TPC PID	Observable variation	Yes
Track übermerging	Efficiency	Yes
FGD mass	Normalisation	No
TPC-FGD matching efficiency	Efficiency	Yes
Pion secondary interactions	Efficiency	Yes
Forward migrations	Efficiency	No
Backward migrations	Efficiency	No
ECal reconstruction	Efficiency	Yes
ECal PID	Efficiency	Yes
Out of FV	Efficiency	No
Pile-up	Normalisation	Yes

momentum resolution is found to be better in MC than in data, and a correction as a function of the transverse momentum is applied to the MC to account for this.

TPC momentum scale varies as a function of the overall magnetic field strength. Uncertainties in the magnetic field strength lead to an uncertainty on the momentum scale of 0.6%, which is confirmed using a sample of cosmic muons passing through both FGDs.

TPC cluster efficiency describes the efficiency of reconstructing a cluster where one is expected and it is found to be $99.5 \pm 0.01\%$.

TPC track efficiency is found to be ($99.8^{+0.2}_{-0.4}\%$) for data and simulation (for tracks with 16 clusters or more) for all angles, momenta and track lengths and shows no dependence on the number of clusters. The inefficiency due to the overlap from a second nearly collinear track is found to be negligible for both data and simulation.

TPC PID is evaluated by comparing the energy deposit of data and MC in high-purity control samples of electrons, muons and protons. The muon control sample has the highest statistics and is composed of through-going sand muons; the electron control sample is based on a γ conversion sample studied by the NuE group; and the proton control sample is found by selecting positive tracks with $0.3 < p < 1.1\,\text{GeV}$.

Track übermerging is the uncertainty related to a small "bug" in the TPC reconstruction. Two tracks with exactly the same z position are incorrectly merged. This "bug" only affects the MC sample, because of the small MicroMEGAS misalignment in the real detector. The effect of this uncertainty is below 0.0001% for all tracks and it will not be shown in the rest of the Thesis.

7.1.2 FGD systematic uncertainties

Some of the FGD systematic uncertainties were evaluated by the NuMu group for the FGD1 analyses (see Reference [85]), and in some cases can be used for the FGD2

analyses. Subsection 7.1.3 details the studies on the vertex migration between different layers of the FGD2.

TPC-FGD matching efficiency is evaluated with a sample of through-going muons that pass through TPC2 and TPC3, where the assumption that the presence of a single track in TPC2 and TPC3 means that the track passed through FGD2. If the event contains a FGD2-TPC3 segment, then it is considered a good match. The efficiency is found to be $99.979 \pm 0.004\%$ in data and $99.980 \pm 0.004\%$ in MC for tracks with momentum greater than 200 MeV, and $99.35 \pm 0.13\%$ in data and $99.71 \pm 0.06\%$ in MC for tracks with momentum lower than 200 MeV.

Pion secondary interactions refer to any interactions that pions can undergo once they have left the nucleus. Although these interactions are modelled in Geant4, the predictions are significantly different from external data measurements. The most significant interactions considered in this study are *absorption* (the pion is completely absorbed by the nucleus), *charge exchange* (the pion interacts with the nucleus and creates a π^0), *quasi-elastic scattering* (the pion scatters off the nucleus without producing any additional pions). Absorption and charge exchange lead to mis-categorising a CC1π^+ interaction as a CC0π interaction, or a CC Other interaction (producing one positive pion and another pion) as a CC1π^+ interaction. Quasi-elastic scattering can cause a change in the momentum or direction of the track. The systematic uncertainty is propagated by looking at all the pions in the FGD2 associated to each event. Each pion trajectory is broken down into steps, and a correction (to bring data and MC in agreement) and a weight (to consider the uncertainty on the data measurements) are applied. See Reference [90] for more information on the uncertainties related to pion secondary interactions.

FGD mass uncertainty: is evaluated by looking at the error on the density of the scintillator and water modules. The FGD2 is composed of 7 *xy* modules interleaved by 6 water modules. For the scintillator module, the uncertainty has been evaluated for FGD1, and is 0.67 %. The densities of the water modules have been evaluated with a 0.46% uncertainty (dominated by the uncertainty on the masses of the pastic and glue). There is also a 0.26% difference between the measured densities and those in the simulation. A total uncertainty of 0.55% (which comes

by combining the two uncertainties in quadrature) is reccommended for the FGD2 water module mass. The FGD2 mass uncertainties for the scintillator and water modules are implemented and propagated separately.

7.1.3 FGD layer migration uncertainties

The analysis described in this Thesis relies on the ability to divide the interactions in the water layers from the interactions in scintillator. Hence, the migrations between the water and the scintillator samples must be studied thoroughly.

There are two kinds of migrations:

- *forward migrations* happen when missing hits move the vertex to the downstream layer, see Figure 7.1.
- *backward migrations* happen when a low energy nucleon travelling backward moves the vertex to the upstream layer, see Figure 7.2.

Table 7.2 and Table 7.3 show the percentage of events reconstructed in the right layer or migrated to the upstream or downstream layer using the NEUT and the GENIE [81] neutrino MC events, respectively. Looking at two different generators can hint on whether these migrations come from the interaction models considered or from reconstruction effects.

Both tables suggest that the forward migrations are mainly a reconstruction effect (i.e. the percentages do not change with number of reconstructed tracks) coming from a hit inefficiency. Water to scintillator forward migrations (i.e. missed hits in x layers) are less likely to happen than scintillator to scintillator forward migration. This happens because in the first case even if the interaction happened at the edge of the water layer, the track would need to traverse all the x layer before reaching the y layer. In the second case the interaction could have happened at the edge of the scintillator layer.

As suggested by both tables, backward migrations *depend* on the number of reconstructed tracks, being higher for interactions producing multiple pions. Backward migrations due to interactions on carbon have similar percentages to backward migrations due to interactions on oxygen (difference of $< 0.3\%$ in NEUT and $< 0.4\%$ in GENIE, with the percentages in GENIE being slightly smaller).

Table 7.2: Percentage of events reconstructed in the right layer or migrated to the upstream or downstream layer. The results are obtained using Run II-IV MC produced with the NEUT generator. The statistical error is of the order of 0.1%.

NEUT

	CC-inclusive	CC0π-like	CC1π^+-like	CC Other-like
Matched scintillator to scintillator	31.2%	31.1%	33.3%	30.4%
Matched water to x layer	39.8%	41.0%	40.7%	35.8%
Gap	12.5%	12.1%	10.3%	14.4%
Forward scintillator to scintillator	3.7%	3.7%	4.1%	3.5%
Backward scintillator to scintillator	5.4%	5.0%	5.0%	6.7%
Forward water to scintillator	2.1%	2.1%	1.8%	2.4%
Backward water to scintillator	5.4%	5.0%	4.8%	6.8%

Table 7.3: Percentage of events reconstructed in the right layer or migrated to the upstream or downstream layer. The results are obtained using Run II-IV MC produced with the GENIE generator. The statistical error is of the order of 0.1%.

GENIE

	CC-inclusive	CC0π-like	CC1π^+-like	CC Other-like
Matched scintillator to scintillator	32.1%	32.4%	34.7%	30.4%
Matched water to x layer	42.4%	42.7%	43.6%	41.0%
Gap	12.8%	12.9%	9.9%	13.9%
Forward scintillator to scintillator	4.0%	3.9%	4.0%	4.1%
Backward scintillator to scintillator	3.3%	3.0%	3.0%	4.3%
Forward water to scintillator	1.8%	1.8%	1.6%	1.9%
Backward water to scintillator	3.5%	3.4%	3.3%	4.4%

The smearing matrix, as introduced in Section 8.1, accounts for these migrations as modelled by our MC simulation. A series of studies are performed to understand the size of the systematic uncertainty related to these effects.

7.1.3.1 Forward migrations

The *forward migration* happens when the first hits in a track are missed due to a reconstruction inefficiency and the event is put in the wrong sample. Figure 7.1 shows a schematic view of the FGD2 modules, the true tracks (red) and the reconstructed tracks (blue). Missing some hits at the beginning of the track can cause a migration from the scintillator to the water sample (left) or a migration from the water to the scintillator sample (right).

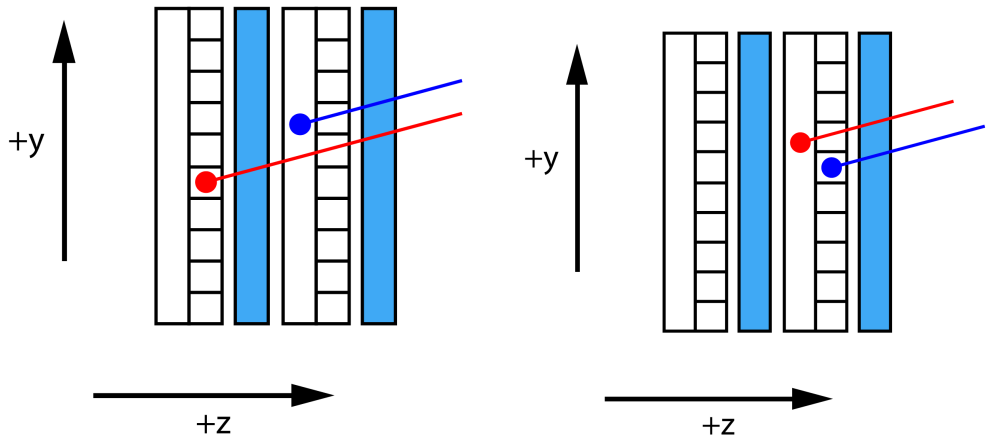

Figure 7.1: Structure of the FGD2 modules with true tracks (red) and reconstructed tracks (blue). (left) Missing hits in the y layer cause the migration from the scintillator to the water sample. (right) Missing hits in the x layer cause the migration from the water to the scintillator sample.

A sample of through going muons is used to evaluate this effect. The procedure is to mask some of the FGD layers, and then rerun the reconstruction to verify that the vertex is reconstructed in the first non-masked layer.

The efficiency found might depend on the depth in the FGD or if the last masked layer was x or y layer. The reconstruction has been re-run 4 times, following the configurations defined in Table 7.4.

Table 7.4: For the FGD forward migration efficiency evaluation the ND280 reconstruction was re-run in these 4 configurations. Layers are numbered 0-29 for FGD1 and 30-43 for FGD2, even numbers for x layers, odd numbers for y layers.

mask	masked layers in FGD1	masked layers in FGD2	last masked layer
1/3 FGD up to y	0-9	30-33	y
1/3 FGD up to x	0-10	30-34	x
2/3 FGD up to y	0-19	30-39	y
2/3 FGD up to x	0-20	30-38	x

The efficiency is evaluated as:

$$\text{efficiency} = \frac{\text{tracks starting in the first NON-masked layer}}{\text{through going tracks in the original analysis files}} \,. \tag{7.1}$$

Events are selected from the control sample files such that there is only 1 track that satisfies these conditions:

- it has a TPC segment (TPC2 for FGD1 selection, TPC3 for FGD2 selection);
- it has a FGD segment (FGD1 or FGD2 respectively);
- this FGD segment starts in a layer that is masked in the tweaked file;
- and it stops at the end of the FGD.

The number of events meeting the above criteria gives the denominator for the efficiency.

In the masked file, those events are selected and if the upstream position of the FGD segment starts exactly on the first **non-masked** layer, then the event is counted in the *numerator* of the efficiency.

Table 7.5 shows the efficiency found in data and simulation for the 4 configurations. The efficiency in data is always slightly lower than the efficiency in the MC, but the values are always compatible. The highest MC efficiency and the lowest data efficiency are used for the propagation of the uncertainty inside the analysis.

Table 7.5: Efficiency of finding tracks after the masking was performed. Numbers provided by Enrico Scantamburlo.

mask	FGD1 MC	FGD1 data	FGD2 MC	FGD2 data
1/3 FGD up to Y	0.960 ± 0.006	0.941 ± 0.008	0.960 ± 0.006	0.948 ± 0.007
1/3 FGD up to X	0.949 ± 0.007	0.930 ± 0.008	0.949 ± 0.006	0.933 ± 0.008
2/3 FGD up to Y	0.966 ± 0.005	0.948 ± 0.007	0.962 ± 0.005	0.944 ± 0.007
2/3 FGD up to X	0.960 ± 0.006	0.945 ± 0.007	0.962 ± 0.005	0.947 ± 0.007

7.1.3.2 Backward migrations

A backward migration happens when a low energy nucleon/particle produced in the interaction travels backward for a short distance and is fitted together with the muon candidate. This effect moves the reconstructed vertex in the layer upstream of the true vertex, as shown in Figure 7.2.

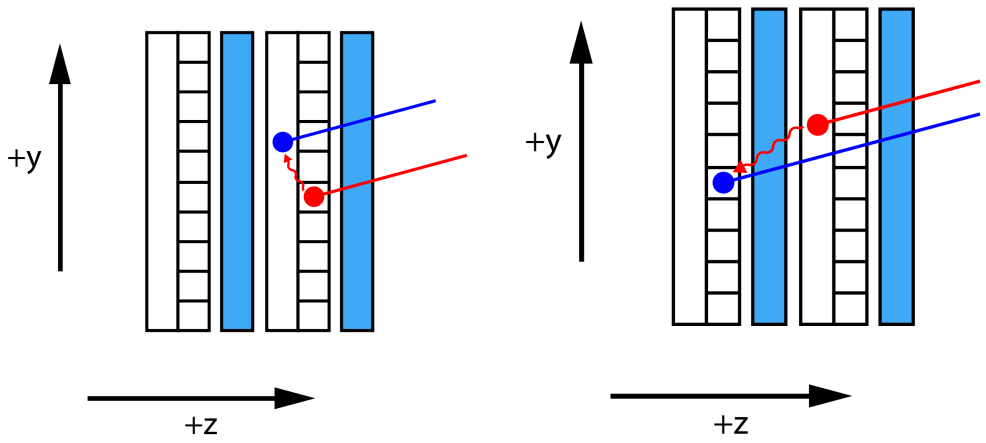

Figure 7.2: Structure of the FGD2 modules with true tracks (red) and reconstructed tracks (blue). (left) Backward going nucleon in the y layer cause the migration from the scintillator to the water sample. (right) Backward going nucleon in the x layer cause the migration from the water to the scintillator sample.

This Subsection first highlights some theory studies to try to understand the origin of these backward migrations, and then shows a data driven measurement that provides

a systematic uncertainty to assign to this effect.

Theory studies on backward migrations

Backward migrations could be generated by backward going nucleons that can be caused by FSI effects or by the Fermi momentum[1].

To study backward going protons, we generated 1 million ν_μ events on water using the beam flux at ND280 for Run IV and GENIE. The sample can then be studied using true information on the outgoing hadrons and leptons to select a true CC-inclusive, true CC0π, true CC1π^+ and true CC Other samples.

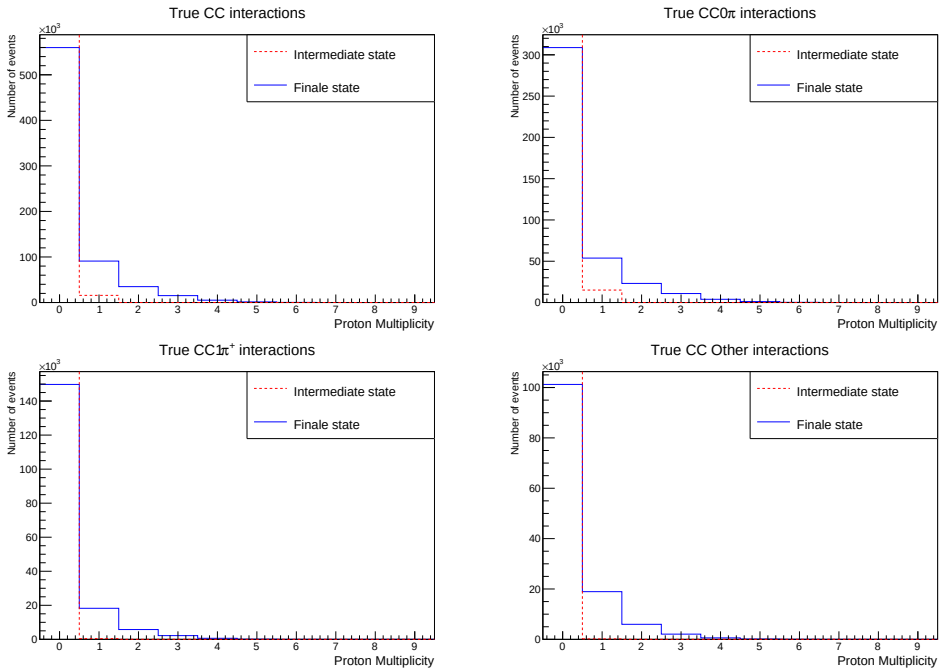

Figure 7.3: Distributions of number of backward going protons before and after FSI, divided into the true CC-inclusive (top left), true CC0π (top right), true CC1π^+ (bottom left) and true CC Other samples (bottom right).

Figure 7.3 shows the number of backward going protons in the intermediate state

[1]Meson Exchange Currents (MEC) could also cause background going protons, but since this analysis was performed using NEUT 5.1.4.2 which does not include MEC, this contribution could not be studied.

(i.e. before FSI) and in the final state (i.e. after FSI) for the different selected samples considered. The ratio of the number of events with at least one backward going proton in the intermediate state to the number of events with at least one backward going proton in the final state is 0.11 for the true CC-inclusive sample, 0.17 for the true CC0π sample, 0.02 for the true CC1π^+ sample and 0.007 for the true CC Other sample. The FSI effects produce most of the backward going protons after final state interactions. These numbers also confirm the dependency on the number of pions produced in the interactions, as FSI effects after true CC Other interactions produce much more backward going protons than FSI effects after true CC0π interactions.

To check the effect of the Fermi momentum on the backward migrated events, a study using the NEUT MC (Run IV air only) was performed. The intermediate proton momentum direction and magnitude could affect these backward migrations.

Table 7.6: Variations in percentage of backward migrated events when the intermediate proton is backward (second column) or forward directed (third column).

			Intermediate proton	
			Backward	Forward
		nominal	$p_p^i(z) < 0$	$p_p^i(z) > 0$
General	Matched scintillator to scintillator	32.0 %	34.3 %	31.9 %
	Matched water to x layer	40.6 %	44.5 %	40.5 %
	Gap	11.4 %	8.5 %	11.5 %
Backward/ Forward study	Forward scintillator to scintillator	3.6 %	3.2 %	3.6 %
	Backward scintillator to scintillator	5.2 %	4.1 %	5.2 %
	Forward water to scintillator	2.2 %	2.0 %	2.2 %
	Backward water to scintillator	5.1 %	3.4 %	5.2 %
	Events	55562	1404	54158

Table 7.6 shows the percentage of the backward migrated events in the ν_μ CC-inclusive sample when the intermediate proton is backward (second column) or forward going (third column). The percentage of backward going events is slightly lower

when the intermediate proton is already moving backward than when the intermediate proton is moving forward. This is probably linked to the momentum magnitude of the intermediate proton momentum; intermediate backward going protons have lower momentum magnitude that forward going protons.

Table 7.7: Variations in percentage of backward migrated events as a function of the intermediate proton momentum. Bins are 300 MeV wide and the last bin includes all events with intermediate proton momentum above 0.9 GeV.

	p_p^i (GeV)	0-0.3	0.3-0.6	0.6-0.9	>0.9
General	Matched scintillator to scintillator	36.7 %	34.0 %	30.6 %	28.4 %
	Matched water to X layer	46.4 %	44.1 %	39.1 %	34.7 %
	Gap	8.3 %	9.6 %	11.9 %	14.7 %
Backward/ Forward study	Forward scintillator to scintillator	3.4 %	3.4 %	4.0 %	3.8 %
	Backward scintillator to scintillator	2.1 %	4.0 %	5.7 %	7.4 %
	Forward water to scintillator	1.6 %	1.5 %	2.8 %	2.9 %
	Backward water to scintillator	1.5 %	3.5 %	5.9 %	8.2 %
	Events	5399	22493	15898	15375

Another study links the backward migrations to the magnitude of the momentum of the intermediate proton. The intermediate proton momentum distribution is divided in 4 bins of 300 MeV (with all events with intermediate proton momentum above 0.9 GeV in the last bin). The variations in the number of backward migrated events are shown in Table 7.7. The percentage of backward migrations (and also that of the forward migrations) is higher when the intermediate proton momentum is higher.

Even though several attempts have been made to understand the backward migrated events, it was not possible to point at the origin of these migrations.

Measuring backward migrations in data

When a backward migration happens, the first hits in the FGD might be slightly offset with respect to the fitted track, hence the distance between the fitted track and the

hit position can be used to try to isolate these migrations. The distance between the position of the first hit and the fitted track is defined as:

$$\Delta d_1 = d_1 - f_d(z_1)\,, \tag{7.2}$$

where d_1 is the x or y position of the first hit (depending if it is on the xz or yz layers), and $f_d(z_1)$ is the x or y position of the fitted track at the same z position of the first hit.

Figure 7.4 shows the distributions of the distance between the the first hit position and the fitted track for the FGD2 CC0π, CC1π^+ and CC Other samples: the left plots show the distribution for the events that do not undergo the backward migration and the right plots show the same distribution for the backward migrated events. All distributions are normalised to an area of 1, to better compare their shapes.

Other similar variables were checked and they all show a very similar behaviour:

- the sum of the distances between the first 2 hits and the fitted track:

$$\Delta d_{1,2} = (d_1 - f_d(z_1)) + (d_2 - f_d(z_2))\,, \tag{7.3}$$

  where if d is in the x coordinate for the first hit, it is in the y coordinate for the second hit, and viceversa;

- the Δ^2 between the first hit position and the fitted track:

$$\Delta^2 d_1 = d_1^2 - f_d(z_1)^2\,, \tag{7.4}$$

- the sum of the Δ^2 between the first 2 hits position and the fitted track:

$$\Delta^2 d_{1,2} = (d_1^2 - f_d(z_1)^2) + (d_2^2 - f_d(z_2)^2)\,. \tag{7.5}$$

The backward migrations in the CC0π sample should be caused by backward going protons, those in the CC1π^+ sample would have also a contribution by backward going positive pions, and those in the CC Other sample should have a larger contribution by backward going pions. Figures 7.4a-7.4c show the distribution of d_1 for the CC0π, CC1π^+ and CC Other samples in FGD2.

The charge left on the first and second hits can give additional information about these migrations. As a low energy particle should generate the migration, it is expected

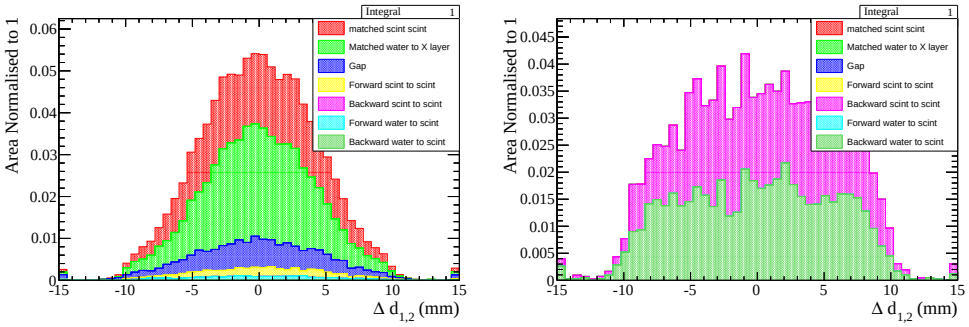

(a) FGD2 CC0π enhanced sample

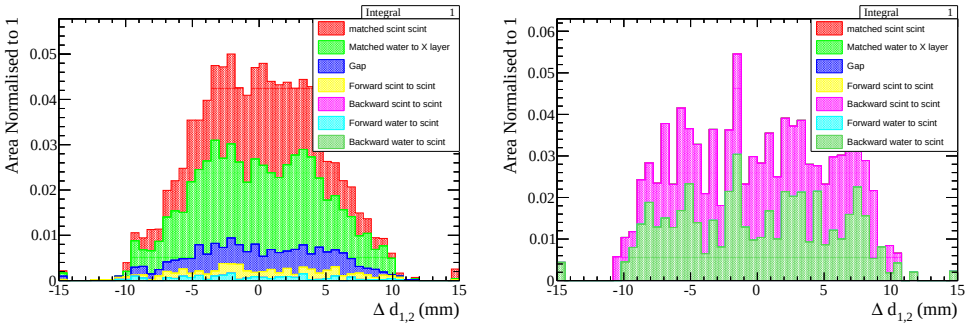

(b) FGD2 CC1π^+ enhanced sample

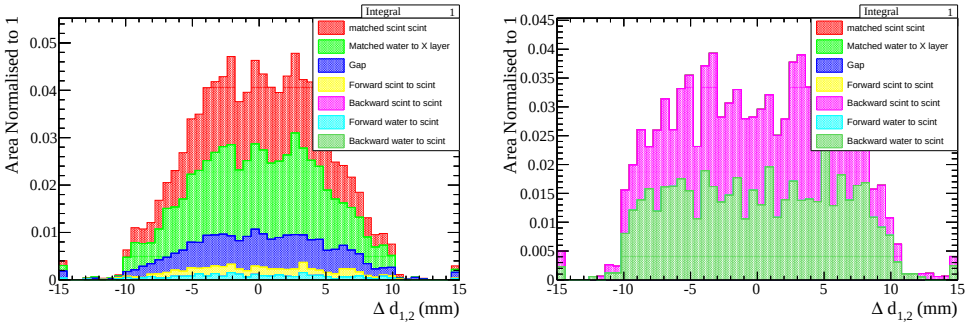

(c) FGD2 CC Other enhanced sample

Figure 7.4: Distance between the first hit position and the fitted track: for (left) non backward migrated events and (right) backward migrated events.

that in these cases the second hit (possibly the "real" vertex hit) should have contributions of various tracks and vertex activity, whereas the first hit (the "fake" vertex hit) should only have a contribution from a low energy backward going particle. Hence, the ratio between the charge left on the first and second hits should be smaller for events

that undergo backward migrations. Figure 7.5 shows the distributions of the ratio of the charges on the first and second hits for the CC0π^+, CC1π^+ and CC Other samples.

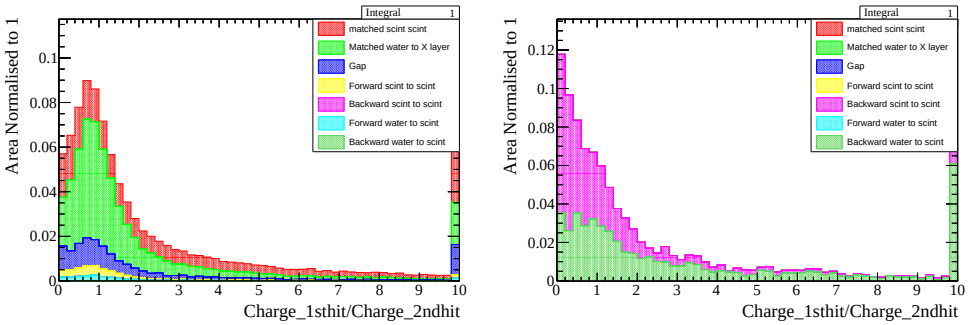

(a) FGD2 CC0π enhanced sample

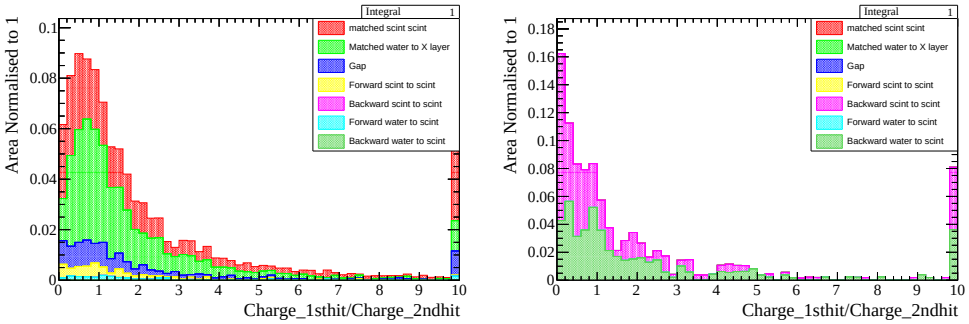

(b) FGD2 CC1π^+ enhanced sample

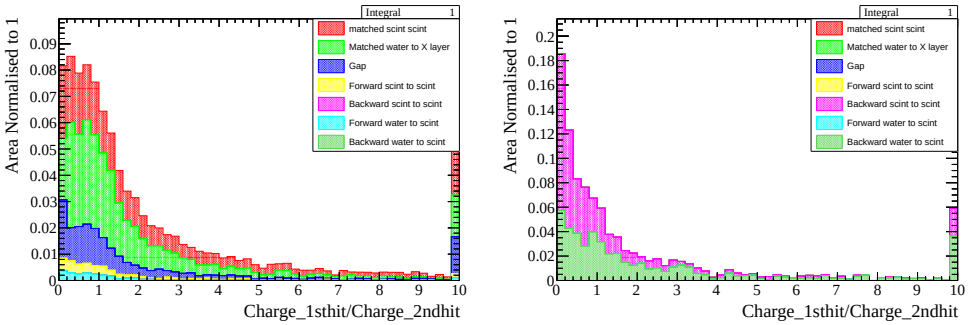

(c) FGD2 CC Other enhanced sample

Figure 7.5: Ratio of the charge on the first hit over the charge on the second hit for the (left) non backward migrated events and the (right) backward migrated events.

A simple 2-component fit to the shapes of these distribution enables the extraction of the fraction of backward migrated events and their error. The fit is performed using

a χ^2 minimisation and by looking at the shape of the distributions of the non migrated events and migrated events. The data distrubution is normalised to 1 and it is fitted using this function (also normalised to 1):

$$f_{MC}(X)^{\text{non migrated}} + \beta \times f_{MC}(X)^{\text{migrated}} \,, \tag{7.6}$$

where X is a vector denoting the two variables used in the fit, $f_{MC}(X)^{\text{non migrated}}$ is the shape of the non migrated events, $f_{MC}(X)^{\text{migrated}}$ is the shape of the migrated events, and β is the only free parameter in the fit that will give the fraction of migrated events. The fit is performed on the CC0π and CC Other samples separately and the largest error is used for the propagation of the systematic uncertainty.

Before performing the fit to data, a self-consistency check is performed to check that by using the nominal NEUT distributions as fake data-sets, the fraction of backward migrated events expected by NEUT is retrieved. For the CC0π sample the NEUT prediction is 10.0% and the result found is (10.3 $\pm$ 0.5)%; for the CC Other sample the NEUT prediction is 13.5% and the result found is (15.2 $\pm$ 1.5)%. The self-consistency checks were performed also considering fits between the ratio of charges and the other variables presented above ($\Delta d_{1,2}$, $\Delta^2 d_1$, $\Delta^2 d_{1,2}$): in all cases the results are compatible with the NEUT prediction.

The results of the fit to data are shown in Table 7.8 for the CC0π sample and Table 7.9 for the CC Other sample. When fitting the CC0π sample, the relative uncertainties are around 20%, when fitting the CC Other sample, they are around 30%. The largest uncertainty (i.e. 30%) is used to propagate this systematic uncertainty into the analysis.

As an example, Figures 7.6 and 7.7 show the fit to data for the CC0π and CC Other samples, respectively. The top plots show the 2D planes where the differences between the non migrated events (left) and the migrated events (right) are clear. The bottom plots show the fitted function projected on the ratio of charges axis (left) and on the Δd_1 axis (right).

Table 7.8: Backward migration fraction extracted from 4 different 2D fits to data using the CC0π sample. The NEUT prediction is 10.0%.

CC0π

2D fit	Result	Relative uncertainty	χ^2/NDF
Ratio of charges vs Δd_1	9.8 ± 1.7%	17.6%	482/256 = 1.9
Ratio of charges vs $\Delta d_{1,2}$	11.8 ± 2.3%	19.3%	533/373 = 1.4
Ratio of charges vs $\Delta^2 d_1$	10.6 ± 2.2%	20.9%	561/389 = 1.4
Ratio of charges vs $\Delta^2 d_{1,2}$	10.7 ± 2.2%	20.8%	548/389 = 1.4

Table 7.9: Backward migration fraction extracted from 4 different 2D fits to data using the CC Other sample. The NEUT prediction is 13.5%.

CC Other

2D fit	Result	Relative uncertainty	χ^2/NDF
Ratio of charges vs Δd_1	9.9 ± 3.0%	30.0%	370/221 = 1.7
Ratio of charges vs $\Delta d_{1,2}$	11.8 ± 3.2%	27.2%	392/333 = 1.2
Ratio of charges vs $\Delta^2 d_1$	12.6 ± 3.3%	26.3%	518/350 = 1.5
Ratio of charges vs $\Delta^2 d_{1,2}$	12.5 ± 3.3%	26.3%	507/350 = 1.5

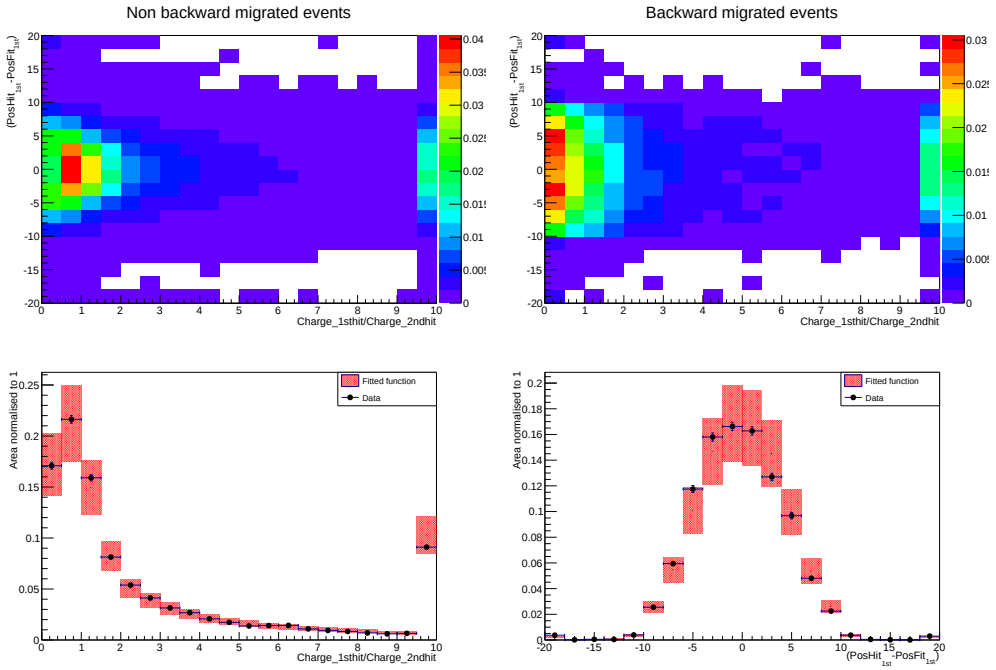

Figure 7.6: Fit to CC0π sample in Data Run II-IV. Top plots show the 2D planes for the non migrated events (left) and migrated events (right). Bottom plots show the fitted function projected on the ratio of charges axis (left) and on the Δd_1 axis (right).

7.1.4 ECal systematic uncertainties

7.1.4.1 ECal reconstruction

The reconstruction efficiency for ECal objects is evaluated for both FGD1 and FGD2. The control sample is found by selecting good TPC tracks originating in the FV of FGD1/FGD2, which are not the highest momentum negative track (this requirement is to remove muons and create a control sample complementary to the selection of the cross-section analyses in FGD1 and FGD2) and have a reconstructed ECal object less than 70 cm away from the end of the TPC track. The latter requirement is to ensure that there is a signal in the ECal. Since the control sample includes both isolated and non-isolated ECal objects, the efficiency of reconstructing an isolated ECal object is evaluated in the FGD1/FGD2 cross-section analyses, and combined with the efficiency found in the control samples.

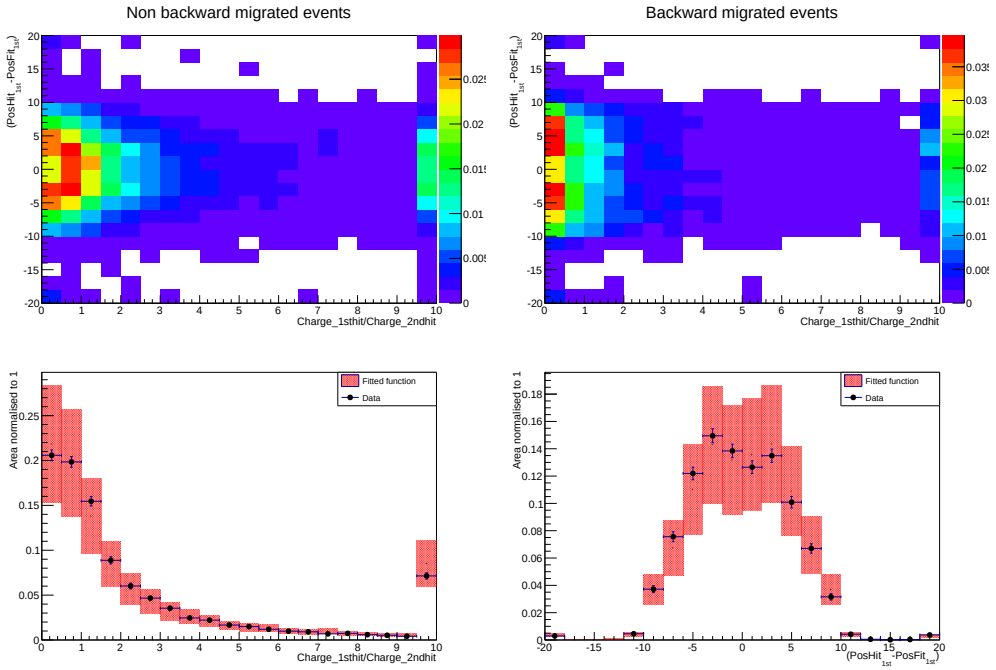

Figure 7.7: Fit to CC Other sample in Data Run II-IV. Top plots show the 2D planes for the non migrated events (left) and migrated events (right). Bottom plots show the fitted function projected on the ratio of charges axis (left) and on the Δd_1 axis (right).

The systematic uncertainty is then applied as an efficiency correction:

$$\epsilon = \frac{\epsilon_{\text{data,CS}}}{\epsilon_{\text{MC,CS}}} \epsilon_{\text{MC,analysis}} \tag{7.7}$$

$\epsilon_{\text{data,CS}}$ is the data efficiency in the control sample, $\epsilon_{\text{MC,CS}}$ is the simulation efficiency in the control sample, and $\epsilon_{\text{MC,analysis}}$ is the simulation efficiency in the ν_μ CC-inclusive sample in FGD2.

Table 7.10 shows the ECal reconstruction efficiency in the FGD2 CC-inclusive sample and in the control sample. The Ds-ECal efficiency is much lower in the FGD2 CC-inclusive sample than in the control sample, and this difference is taken care of with the efficiency correction formula (Equation 7.7).

7.1.4.2 ECal PID

The ECal PID systematic uncertainty is evaluated using high-purity control samples of electrons and muons. The PID likelihood ($R_{MIP/EM}$) distributions are compared

Table 7.10: ECal reconstruction efficiency in the FGD2 CC-inclusive sample and in the control sample.

	$\epsilon_{\text{MC,analysis}}$	$\epsilon_{\text{MC,CS}}$	$\epsilon_{\text{data,CS}}$
Barrel-ECal	0.352	0.303	0.315
Ds-ECal	0.163	0.826	0.839

between data and simulation. The efficiency of cutting at $R_{MIP/EM} > 0$ (i.e. shower-like) in data and MC is evaluated, and the systematic uncertainty is found by summing in quadrature the data-MC differences with the statistical uncertainty.

This systematic uncertainty has been evaluated by the NuE group, and more details on the control samples and efficiency evaluation are found in Reference [57].

7.1.5 External systematic uncertainties

External systematic uncertainties include the uncertainties coming from interactions outside the FV, and interactions not modelled with the standard ND280 simulation. Interactions outside the ND280 detector (i.e. sand muons) are studied with a separate MC sample and can either be mis-identified as a ν_μ CC1π^+ event (this is actually negligible) or can trigger the veto cut in the analysis because of pile-up.

7.1.5.1 Out of FV (OOFV)

The out-of-fiducial volume (OOFV) systematic uncertainty is calculated by studying different categories of events that contribute to this background. These categories are:

- Interactions out of FV but inside the FGD scintillator;
- Interactions in the upstream tracker dead material;
- Interactions in the downstream tracker dead material;
- Neutral particles from outside the tracker;
- Backward-going tracks;

- High-angle tracks;
- Double skipped layers[1];
- Last module failure[2];
- Hard elastic scatters.

Each of these categories is assigned a rate uncertainty, that is 0 for particles originating inside the Tracker and 20%[3] for particles originating outside the Tracker (see Reference [91]), and a reconstruction-related uncertainty. The reconstruction-related uncertainty is below 40% for almost all categories. For the high-angle tracks category a reconstruction uncertainty of 150%[4] is considered because the matching sometimes fails to include some hits that are outside the FGD FV.

7.1.5.2 Sand muons

The particles produced by neutrinos interacting in the pit walls and the surrounding sand and entering the ND280 region are described by a separate MC simulation. The sand muon MC sample corresponds to 2.6×10^{20} POT (which is 44% of the POT taken for Run I-IV). Table 7.11 shows the number of sand muon events in the CC-inclusive sample and in the 3 selected samples considered in this analysis. Since the contamination of sand muons in the analysis is negligible, this sample is not used and the systematic uncertainty is not propagated.

[1] When matching FGD hits to TPC tracks, the matching routine will skip over a single missed layer, but if two layers in a row lack FGD hits the matching routine gives up and the track is broken, and will appear to start inside the FGD FV, even if there are further upstream hits that show it should have been a throughgoing track.

[2] A time off-set in the TPC drift velocity can affect the x coordinate reconstruction: the TPC-FGD matching software will match hits up to the last module of the FGD and then stop, so that it would appear that the track originated in the last module.

[3] It was decided to assign a rate uncertainty of 20% to particles originating outside the Tracker after studies on the GENIE-NEUT and data-MC differences for ν_μ CC events in the SMRD pointed at normalisation differences that are at most $\approx 20\%$.

[4] This uncertainty has been evaluated with a sample of high angle cosmics and by looking at the number of failure in the reconstructed FGD-TPC tracks ending in the FGD FV, i.e. failure to recognise this event and through-going. The data-MC differences in this sample are as high as 150% which has been chosen as the reconstruction uncertainty for this category.

Table 7.11: Number of sand muon events passing the CC-inclusive selection in the FGD2 and entering the 3 selected samples considered in this analysis.

	Number of MC events scaled to data	Contamination to the selected data samples
CC-inclusive	66	0.28 %
CC1π^+ water-enhanced	0	0 %
CC1π^+ scintillator	0	0 %
CC Other max 4 tracks water-enhanced	5	0.12 %

7.1.5.3 Pile up

When a beam event happens at the same time as a sand muon event, the event is rejected by the TPC2 veto. Since the beam spill and the sand muon samples are simulated separately, a correction is applied to the simulated events to take into account possible event pile up between a beam spill event and a sand muon event.

The correction is evaluated for each run, as the pile-up depends on the beam intensity, and it is defined as:

$$C_{\text{pile-up}} = \frac{N_{\text{TPC}} \cdot I_d}{POT_{\text{sand}} \cdot N_b} \,, \tag{7.8}$$

where N_{TPC} is the number of TPC2 events in the sand muon MC that trigger the veto cut, $I_d = POT_{\text{beam}}/nSpills$ is the beam intensity, POT_{sand} is the POT in the sand muon MC, and N_b is the number of bunches per spill (6 for Run I, and 8 otherwise).

The uncertainty on this systematic uncertainty is computed by comparing N in data and simulation, where the MC is weighted to the beam intensity, and the sum of the beam and sand MC is used for the comparison. The difference between data and MC is taken as the systematic uncertainty. If the data-MC difference is less than $0.1 \cdot C_{\text{pile-up}}$, then the uncertainty considered is just $0.1 \cdot C_{\text{pile-up}}$, since there is a 10% normalisation uncertainty on the sand muon MC.

Table 7.12 shows the pile up correction and uncertainty used for each run.

Table 7.12: Pile-up correction and uncertainty for each data set. The first 3 columns show the percentage of TPC tracks per bunch in Data, MC and Sand muon simulation. The last 2 columns give the pile-up correction and systematic uncertainty related to it.

	TPC2/bunch (%)				
Sample	Data	MC	Sand	C_{pileup}	σ_{pileup}
Run I	1.75	0.49	0.43	0.0043	0.0083
Run II (water)	1.62	0.82	0.70	0.0070	0.00098
Run II (air)	1.90	0.94	0.84	0.0084	0.0012
Run III b	1.80	0.92	0.82	0.0082	0.00083
Run III c	2.09	1.02	0.91	0.0091	0.0016
Run IV (water)	2.32	1.16	0.99	0.0099	0.0017
Run IV (air)	2.65	1.31	1.16	0.0116	0.0018

7.2 Flux and cross-section systematic uncertainties

As seen in Section 3.5, the T2K oscillation analyses use the output of the fit to the near detector samples to tweak the nominal NEUT distributions. The Beam And ND280 Flux task Force (BANFF) fit uses external data and ND280 data to fit parameters describing the flux and cross-section models. These parameters are:

- ND280 flux (11 ν_μ energy bins, 5 $\overline{\nu}_\mu$ bins, 7 ν_e bins, and 2 $\overline{\nu}_\mathrm{e}$ bins);
- Super-Kamiokande flux (not relevant for this analysis);
- final state interactions (6 parameters);
- CCQE cross-section (4 parameters);
- pion production cross-section (8 parameters);
- nuclear model (3 parameters).

Constraints from the MiniBooNE experiment are used to modify three of the pion production cross-section parameters to form the BANFF pre-fit prediction. A fit to

the ND280 ν_μ samples in FGD1 is used to constrain all the parameters and form the BANFF post-fit prediction [55].

The BANFF group provides the parameters and covariance matrix for the pre-fit and post-fit predictions. All the signal and background events that enter the selection, and all the signal events that are missed in this analysis, are re-weighted according to the BANFF **pre-fit** covariance matrix and used to evaluate the flux and cross-section uncertainties.

7.2.1 Beam flux systematic uncertainties

The neutrino flux prediction is affected by uncertainties on different parts of the simulation. The hadron production uncertainties are constrained with external data from a dedicated experiment at CERN (NA61/SHINE) [72]. Uncertainties related to the proton beam, including the beam profile and alignment, are constrained by T2K data for each run. The uncertainties on the alignment of the target and magnetic horns are studied by rotating the target and shifting the horns in the simulation. Similarly, the uncertainties on the horn current and magnetic field are varied in the MC.

A covariance matrix in bins of neutrino energy, flavour and detector (ND280 or SK) is evaluated for each source of uncertainty; and then all covariance matrices are summed to get the total covariance matrix.

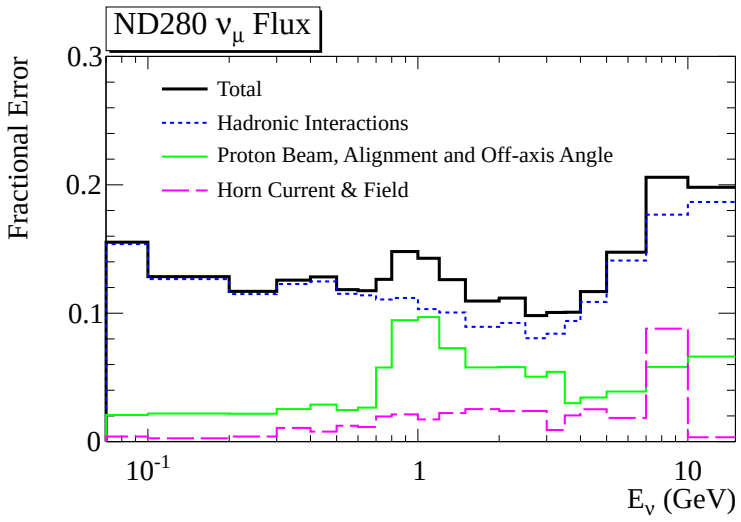

Figure 7.8: Fractional flux uncertainty on the ND280 ν_μ flux prediction [61].

Figure 7.8 shows the ND280 ν_μ flux uncertainty as a function of the neutrino energy. The hadron production uncertainties are dominant especially at low neutrino energy. For future analyses this uncertainty will be significantly reduced by using higher-statistics NA61 samples using a T2K replica target.

7.2.2 Cross-section parametrisation systematic uncertainties

Uncertainties related to the cross-section model can be split into four categories: final state interactions, CCQE model, pion production model and nuclear model. A summary of all these uncertainties can be found in Table 7.13 and a detailed description of them in Reference [55].

7.2.2.1 Final state interactions uncertainties

The final state interactions parameters describe the uncertainties on the pion final state after the neutrino interaction but before they leave the nucleus. Six FSI parameters are considered in the model: inelastic scattering at low and high energy (F^{Inel}_{low} and F^{Inel}_{high}), pion production (F^{Prod}), pion absorption (F^{Abs}), and charge exchange at low and high energy (F^{CX}_{low} and F^{CX}_{high}). The uncertainties on these parameters are obtained by fit to the MiniBooNE data, as described in Reference [55]. Table 7.13 summarises the central value and uncertainty for each parameter.

7.2.2.2 CCQE model uncertainties

As explained in Section 2.5.2, the MiniBooNE experiment measured a value of M^{QE}_A much larger than the model prediction. As a consequence, the uncertainty assigned to this parameter is large enough to cover both the NEUT nominal value and the NEUT best fit to MiniBooNE data.

The discrepancy between MiniBooNE and NOMAD could also be explained by an incorrect model of the flux for one of the experiment [55]. Hence three CCQE normalisation parameters, x^{CCQE}, are introduced to cover different energy regions. For energies below 1.5 GeV, the MiniBooNE uncertainty of 11% is assigned to the x^{CCQE} parameter. For the other two energy regions, a 30% uncertainty is considered, to cover the difference between MiniBooNE and NOMAD.

Table 7.13: Nominal values and uncertainties on the FSI and cross-section model parameters.

Parameter	Nominal Value	Uncertainty	Category
F_{low}^{Inel}	0	0.41	FSI
F_{high}^{Inel}	0	0.34	FSI
F^{Prod}	0	0.57	FSI
F^{Abs}	0	0.28	FSI
F_{low}^{CX}	0	0.50	FSI
F_{high}^{CX}	0	0.41	FSI
M_A^{CCQE} (GeV/c^2)	1.21	0.45	CCQE
x^{CCQE} ($E_\nu < 1.5$ GeV)	1	0.11	CCQE
x^{CCQE} ($1.5 < E_\nu < 3.5$ GeV)	1	0.30	CCQE
x^{CCQE} ($E_\nu > 3.5$ GeV)	1	0.30	CCQE
M_A^{RES} (GeV/c^2)	1.41	0.11	Pion production
$x^{\mathrm{CC\ other}}$ (GeV)	0	0.40	Pion production
$x^{\pi-\mathrm{less}}$	0.2	0.2	Pion production
$x^{\mathrm{CC1}\pi}$ ($E_\nu < 2.5$ GeV)	1.15	0.43	Pion production
$x^{\mathrm{CC1}\pi}$ ($E_\nu > 2.5$ GeV)	1	0.40	Pion production
$x^{\mathrm{CC\ coh}}$	1	1	Pion production
$x^{\mathrm{NC\ other}}$	1	0.3	Pion production
$x^{\mathrm{NC1}\pi^0}$	0.96	0.43	Pion production
x^{SF}	0	1	Nuclear
E_B (MeV)	25	9	Nuclear
p_F (MeV/c)	217	30	Nuclear

7.2.2.3 Pion production uncertainties

The pion production uncertainties are evaluated using a joint fit to MiniBooNE CC1π^+ [43] CC1π^0 [92], and NC1π^0 [93] data. The following three parameters are used in the fit:

- M_A^{RES}, the axial mass in the pion production model,
- CC1π normalisation ($x^{\mathrm{CC1}\pi}$) for $E_\nu < 2.5\,\mathrm{GeV}$, and
- NC1π^0 normalisation ($x^{\mathrm{NC1}\pi^0}$).

The best fit values of these parameters are shown in Table 7.13.

An uncertainty of 100% is assigned to the fraction of Δ that de-excites without emitting any pion ($x^{\pi-\mathrm{less}}$).

Since both the K2K [47] and the SciBooNE [48] experiment did not see any CC coherent pion production, an uncertainty of 100% is also assigned to the CC coherent pion production parameter ($x^{\mathrm{CC\ coh}}$).

For DIS interactions, an energy dependent uncertainty, $x^{\mathrm{CC\ other}}$, is used to apply a weight $w = 1 + x^{\mathrm{CC\ other}}/E_\nu(\mathrm{GeV})$. This parameter is allowed to vary from 0 with an uncertainty of 0.4 [55].

An uncertainty of 30% is assigned to the NC pion production parameter ($x^{\mathrm{NC\ other}}$).

7.2.2.4 Nuclear model uncertainties

As explained in Section 2.5.1, the Relativistic Fermi Gas model is used in the NEUT simulation to describe the movement of the nucleons in the nucleus. The cut-off Fermi momentum, p_F, and binding energy, E_B, are determined from electron scattering data, and their given uncertainties are 30 MeV/c and 9 MeV, respectively.

An alternative to the RFG model is the "Spectral Function" (SF) model [94]. A parameter x^{SF} is used to interpolate linearly between the lepton kinematics with the RFG ($x^{SF} = 0$) and spectral function ($x^{SF} = 1$) models. The discrepancy between the two models is assigned as an uncertainty. Due to the interaction models implemented in NEUT, this uncertainty only affects CCQE interactions.

8

ν_μ CC1π^+ cross-section measurement in water

This Chapter describes the measurement of the ν_μ charged current positive pion production cross-section on water using the ND280 detector. Section 8.1 explains the cross-section definition and describes the Bayesian unfolding method: this is the technique used for the cross-section extraction in the analysis. Section 8.2 shows a series of fake data-sets used to check that the unfolding procedure is working properly, and Section 8.3 presents the results of the cross-section analysis when using the GENIE MC as a fake data-set. Finally, Section 8.4 highlights the results of the extracted charged current single positive pion production cross-section in water using the T2K Run II-IV data. The strategy of the analysis includes different cross-section measurements:

- total flux averaged cross-section;
- single differential cross-section in the pion kinematics variables: $\frac{d\sigma}{dp_\pi}$, $\frac{d\sigma}{dcos\theta_\pi}$;
- single differential cross-section in the muon kinematics variables: $\frac{d\sigma}{dp_\mu}$, $\frac{d\sigma}{dcos\theta_\mu}$;
- single differential cross-section in the muon-pion angle: $\frac{d\sigma}{dcos\theta_{\mu,\pi}}$;
- total flux averaged cross-section using the reconstructed neutrino energy unfolded to the true NEUT prediction: $\sigma(E)$.

8.1 Cross-section calculation

8.1.1 Cross-section definition

In the analysis presented in this Thesis, the differential cross-section is computed as a function of different variables, that are referred to as X for the purpose of this Section.

The total number of true interactions in the bin t_k of variable X is given by:

$$N_{t_k} = T \cdot \Phi \int_{X_{t_k}} \left\langle \frac{\partial \sigma}{\partial X} \right\rangle_{\Phi} dX = T \cdot \Phi \int_{X_{t_k}} \frac{\partial \langle \sigma \rangle_{\Phi}}{\partial X} dX \ , \tag{8.1}$$

where T is the number of target nucleons, Φ is the total integrated flux, and $\langle ... \rangle_{\Phi}$ indicates a quantity averaged over the flux. The second step of Equation 8.1 comes from the fact that flux-averaging is independent of the derivatives.

By defining ΔX_{t_k} as the width of the bin t_k, Equation 8.1 can be rearraged to find the *flux averaged differential cross-section* per nucleon in bin t_k:

$$\left\langle \frac{\partial \langle \sigma \rangle_{\Phi}}{\partial X} \right\rangle_{t_k} = \frac{N_{t_k}}{T \cdot \Phi \cdot \Delta X_{t_k}} \, . \tag{8.2}$$

By integrating over all X, the total flux averaged cross-section per nucleon is found to be:

$$\langle \sigma \rangle_{\Phi} = \frac{N_{\text{total}}}{T \cdot \Phi} \ , \tag{8.3}$$

where N_{total} is the sum of N_{t_k} in all bins t_k.

N_{t_k} is calculated using the Bayesian unfolding method (see Subsection 8.1.3) and includes the subtraction of background constrained using the two control samples presented in Section 6.2.

8.1.2 Predicted ν_μ CC1π^+ cross-section

To measure the cross-section as defined by Equations 8.2 and 8.3, it is necessary to know the number of target nucleons, T, and the total integrated flux, Φ.

Separate flux histograms are provided for each T2K run by the beam group. The histograms are weighted by the good POT for each run and then integrated to give the total flux histogram as shown in Figure 8.1.

The number of target nucleons is computed considering all the materials present in the water modules of the FGD2 FV. Table 8.1 shows a summary of the average module composition based on the water modules used in the FGD2.

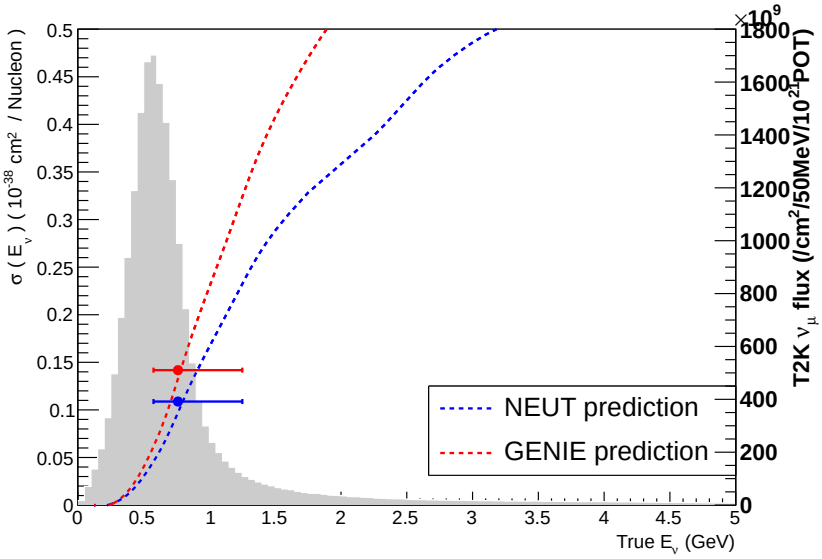

Figure 8.1: ν_μ CC1π^+ cross-section predictions from NEUT and GENIE in the FGD2 water modules for the **full phase-space**. The gray histogram shows the T2K ν_μ flux, and the two curves are the cross-sections as a function of the neutrino energy. The points are flux averaged cross-sections.

Table 8.1: Elemental composition of the FGD2 water modules in mg/cm^2 of each element.

	Water Module
C	421.07 ± 3.19
O	2066.17 ± 2.04
H	293.17 ± 0.41
Mg	7 ± 0.41
Si	11 ± 0.41
Total	2798.67 ± 5.37

The total number of target nucleons is found to be:

$$T = N_A \cdot V_{FV} \cdot \rho = 3.09 \cdot 10^{29} \ ,$$

where $N_A = 6.022 \cdot 10^{23} mol^{-1}$ is the Avogadro number, V_{FV} is the volume of the

modules considered inside the FV, $\rho = \rho_{area}/\Delta z$ is the total density of the water modules of the FGD2 in units of g/cm^3 (ρ_{area} is the total areal density of each module as seen in Table 8.1 and $\Delta z = 2.79$ cm is the width of the FGD2 water modules).

Table 8.2 shows the abundance of the different nuclei in the FGD2 water modules. The water in the FGD2 is contained in vessels made of polycarbonate and polypropylene, hence the target material is only $\approx$ 84% water, and it contains some carbon, silicium and magnesium.

Table 8.2: Abundance of the different isotope of the different nuclei. The fraction of each atoms inside the scintillator is obtained from Table 8.1.

Atoms	A	Natural abundance	Fraction in a water module
C	12	98.90%	15.05%
C	13	1.10%	
O	16	99.76%	73.83%
O	17	0.04%	
O	18	0.20%	
H	1	99.99%	10.48%
H	2	0.01%	
Si	28	92.22%	0.39%
Si	29	4.68%	
Si	30	3.10%	
Mg	24	79.00%	0.25%
Mg	25	10.00%	
Mg	26	11.00%	

Figure 8.1 also shows the predicted ν_μ CC1π^+ cross-section in the FGD2 water modules as a function of the neutrino energy for the NEUT (blue) and GENIE (red) simulations. Both the NEUT and the GENIE simulations base their pion production prediction on the Rein Seghal model, but the parametrisation chosen is different for each simulation, making the GENIE predicted cross-section higher than the NEUT predicted

cross-section over all the energy range considered. The flux averaged cross-section predictions are shown at the mean neutrino energy. The horizontal bars represent 68% of the flux at each side of the mean energy. These values are $\sigma_{NEUT} = 0.1088 \times 10^{-38}$ cm^2/nucleon for NEUT, and $\sigma_{GENIE} = 0.1418 \times 10^{-38}$ cm^2/nucleon for GENIE.

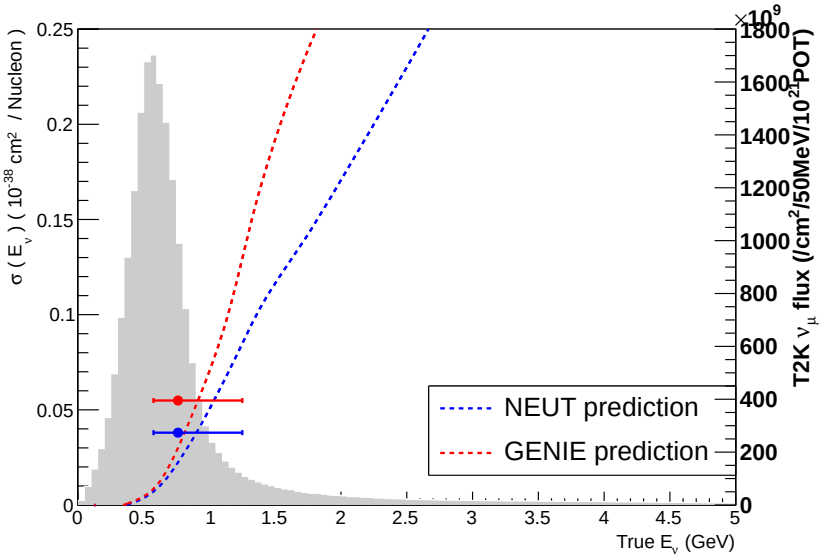

Figure 8.2: ν_μ CC1π^+ cross-section predictions from NEUT and GENIE in the FGD2 water modules for the **reduced phase-space**. The gray histogram shows the T2K ν_μ flux, and the two curves are the cross-sections as a function of the neutrino energy. The points are flux averaged cross-sections.

The analysis described in this Thesis uses a reduced phase-space ($p_\mu > 200\,\text{MeV}$, $p_\pi > 200\,\text{MeV}$, $\cos\theta_{\mu^-} > 0.3$ and $\cos\theta_{\pi^+} > 0.3$), Figure 8.2 accordingly shows the ν_μ CC1π^+ cross-section prediction in the reduced phase-space. In this case, the value of the flux averaged cross-section is $\sigma_{NEUT} = 3.80 \times 10^{-40}$ cm^2/nucleon for NEUT, and $\sigma_{GENIE} = 5.49 \times 10^{-40}$ cm^2/nucleon for GENIE.

8.1.3 The Bayesian unfolding method

The Bayesian unfolding technique was used for the ν_μ CC-inclusive cross-section measurement [56] and the ν_e CC-inclusive cross-section measurement [57]. This technique is based on unfolding from a reconstructed data-set to the true distribution, with the

unfolding accounting for detector inefficiencies and mis-reconstruction [95].

From the MC simulation, the *initial estimator* of the number of signal events in each true bin is calculated as:

$$N_{t_k} = \sum_{j=1}^{n_r} S_{r_j t_k} + M_{t_k} \ , \tag{8.4}$$

where $S_{r_j t_k}$ is the number of true simulated signal events in true bin t_k that are reconstructed in the reconstructed bin r_j (*signal matrix*), and M_{t_k} is the *missed vector*, i.e. the number of true simulated signal events in true bin t_k that are not selected.

The *smearing matrix* which accounts for migrations between bins and selection efficiencies, is then defined as:

$$P(r_j|t_k) = \frac{S_{r_j t_k}}{N_{t_k}} \ . \tag{8.5}$$

The efficiency for a true bin t_k is found by summing up the smearing matrix over all the reconstructed bins r_j:

$$\epsilon_{t_k} = \sum_{j=1}^{n_r} P(r_j|t_k) = \sum_{j=1}^{n_r} \frac{S_{r_j t_k}}{N_{t_k}} \ . \tag{8.6}$$

A prior estimate of the probability of finding a true signal event in a given true bin t_k can be found as:

$$P_0(t_k) = \frac{N_{t_k}}{\sum_{\beta=1}^{n_t} N_{t_\beta}} \ . \tag{8.7}$$

Using the *Bayes' theorem*, the *unsmearing matrix* $P_m(t_k|r_j)$ is found as:

$$P_m(t_k|r_j) = \frac{P(r_j|t_k) P_m(t_k)}{\sum_{\beta=1}^{n_t} P(r_j|t_\beta) P_m(t_\beta)} \ . \tag{8.8}$$

where m refers to the iteration index, which is initially set to 0. The unsmearing matrix describes the probability that an event observed in the true bin t_k was reconstructed in bin r_j.

The first estimate of the true distribution is found by applying the smearing matrix to the data distribution:

$$N_{t_k}^{m+1} = \frac{1}{\epsilon_{t_k}} \sum_{j=1}^{n_r} P_m(t_k|r_j)(N_{r_j}^{meas} - \sum_{\beta}^{\text{all backgrounds}} \alpha_\beta B_{r_j,\beta}) \ , \tag{8.9}$$

where $N_{r_j}^{meas}$ is the number of reconstructed events in bin r_j, $B_{r_j,\beta}$ is the number of predicted events in bin r_j of background type β, α_β is a normalisation constant derived

from the control region β, and ϵ_{t_k} is the efficiency in bin t_k. $N_{t_k}^{m+1}$ is often referred to as the *unfolded* number of events.

Equation 8.9 uses a background subtraction where the coefficient α_β are equal to 1 if that part of the background is not constrained by any control sample, or otherwise calculated as:

$$\alpha_\beta = \frac{C_{\text{data},\beta}}{C_{\text{MC},\beta}} \,, \tag{8.10}$$

where $C_{\text{data},\beta}$ is the total number of events in the control sample β in data and $C_{\text{MC},\beta}$ is the total number of events in the control sample β in MC. This effectively scales the background up/down according to a data measurement, but without adding any shape information.

For this analysis the background is divided in two groups (as explained in Section 6.2):

1. **the CC1π^+ interactions in scintillator**, that is constrained with a sample of *selected CC1π^+-like events in the y layers of the FGD2*;
2. **the non CC1π^+ background**, that is constrained with a sample of *selected CC Other-like water-enhanced events with maximum 4 tracks in the FGD2.*

A future improvement of this analysis would be to unfold the CC1π^+ water-enhanced and scintillator samples at the same time.

Equation 8.9 gives the the first estimate of the number of unfolded events that can be inserted into Equation 8.7 to initiate an iterative method that will evaluate a new unsmearing matrix and again another estimate for $\hat{N_{t_k}}$. It is then possible to keep iterating to allow the data to train the unfolding.

Nonetheless, too many iterations would amplify the statistical uncertainties and lead to large fluctuations. The statistical uncertainties gets amplified because each iteration takes information from data distributions. The large fluctuations arise when the algorithm starts to train on statistical fluctuations in data. For this reason a small number of iterations is preferred. This analysis uses 1 iteration and Subsection 8.2.2 describes the studies done to identify the best number of iterations.

In the purpose of this analysis, the unfolded distribution after all iterations is referred to as $\hat{N_{t_k}}$, hence the differential cross-section is calculated as:

$$\left\langle \frac{\partial\langle\sigma\rangle_\phi}{\partial X} \right\rangle_{t_k} = \frac{\hat{N}_{t_k}}{T \times \Phi \times \Delta X_{t_k}} \,. \tag{8.11}$$

The total flux averaged cross-section is evaluating by summing the differential cross-sections in each bin:

$$\sigma_{total} = \sum_{i=1}^{N_{bins}} \sigma_i \ , \tag{8.12}$$

where σ_i is the differential cross-section in each bin. This analysis uses the (`xsTool`), a tool developed by the T2K collaboration to evaluate cross-sections at the near detector. The tool is based on the `RooUnfold` package [96].

8.1.4 Uncertainties

The propagation of uncertainties is done using pseudo-experiments to build a covariance matrix. For each source of uncertainty, s, 2000 pseudo-experiments are performed. Each pseudo-experiment gives a new differential cross-section, σ^{s_n}, which is compared to the nominal differential cross-section, σ^{nom}, to calculate the covariance matrix:

$$V_{ij}^{s} = \frac{1}{N} \sum_{s_n=1}^{N} (\sigma_i^{s_n} - \sigma^{nom})(\sigma_j^{s_n} - \sigma^{nom}) \ , \tag{8.13}$$

where $\sigma_i^{s_n}$ is the differential cross-section in bin i evaluated with throw n of the systematic uncertainty s, and σ_i^{nom} is the nominal differential cross-section in bin i.

The error on the total cross-section is then given by:

$$\sigma_\sigma = \sqrt{\sum_{i=1}^{N_{bins}} \sum_{j=1}^{N_{bins}} (V_{ij} \Delta X_i)} \ , \tag{8.14}$$

where ΔX_i is the width of bin i.

Statistical uncertainties are evaluated using 2000 pseudo-experiments for both data and MC. The contents of each histogram that is an input to the unfolding are varied according to a continuous Poisson distribution.

Correlated Gaussian throws are used for the systematic uncertainties. Throws with negative values are set at 0, rather than re-throw. Chapter 7 explains all the systematic error sources.

8.2 Fake data-sets studies

8.2.1 Fake data-sets used

The data-sets used to test the unfolding are the following:

- The nominal NEUT MC: this is the distribution of events that enter the selection of the signal and control region samples after the detector systematic uncertainties are applied. This sample is used to "train the unfolding" (i.e. to evaluate the signal matrix, background vector etc) hence, by using it as a fake data-set, it is possible to test for pathological problems in the unfolding.

- The GENIE MC: this sample is used as a fake data-set to check if, by training using a model (i.e. NEUT), the unfolding can recover a different model (GENIE).

- The nominal NEUT MC with CC Other background increased by 50%. The CC Other background is increased by 50%, while the signal and all the other background types are kept the same. By using this sample it is possible to check the effectiveness of the control region that constrains the CC Other background.

- The nominal NEUT MC with scintillator background increased by 50%. The scintillator background (both in the x and in the y layer) is increased by 50%, while the interactions in water and in the gaps are kept the same. By using this sample it is possible to check the effectiveness of the control region that constrains the interactions in the scintillator.

- The nominal NEUT MC with a "crazy" signal implementation. In this sample true signal events are re-weighted as a function of their reaction ($w_{CCQE} = 1.2$, $w_{RES} = 0.9$, $w_{COH} = 0.9$, $w_{DIS} = 1.2$) and of their true neutrino energy:

  - a linear weight from 1 to 0.5 is assigned to events with true neutrino energy between 0 and 0.5 GeV;
  - a linear weight from 0.5 to 1.5 is assigned to events with true neutrino energy between 0.5 and 1.5 GeV;
  - a linear weight from 1.5 to 1 is assigned to events with true neutrino energy between 1.5 and 2 GeV;
  - all events with true energy above 2 GeV are assigned a weight of 1.

  Hence, the "crazy" signal implementation assigns a smaller weight (0.5) when the true neutrino energy is around the T2K energy peak region (0.5 GeV). The idea for this "crazy" signal implementation is based on the "crazy" signal defined in the CC0π analysis in Reference [97].

- The nominal NEUT MC with M_A^{RES} re-weighted at $+5\ \sigma$ from the nominal value (where 1 σ corresponds to 1.41±0.11).

The fake data-sets are scaled to 5.556 x 10^{20} POT (equivalent to the T2K data Run II-IV statistics).

All the fake data-set studies use the reduced phase-space defined by $\cos\theta_\mu > 0.3$ and $\cos\theta_\pi > 0.4$. The reduced phase-space was updated after the data were unblinded to the region defined by $p_\mu > 200\,\text{MeV}$, $p_\pi > 200\,\text{MeV}$, $\cos\theta_\mu > 0.3$ and $\cos\theta_\pi > 0.3$, as cuts on the momentum variables were also necessary. These fake data-set studies were not repeated after the modification of the phase-space as they already showed the robustness of the unfolding algorithm.

8.2.2 Bias and number of iterations

In case of infinite statistics it is suggested that the Bayesian unfolding method is applied using approximately 3 iterations. Reference [56] describes the T2K ν_μ CC-inclusive measurement in FGD1 and found 1 iteration to be optimal due to the low statistics. The CC1π^+ analysis in the water modules of FGD2 has about 10% of the statistics of the ν_μ CC-inclusive sample in FGD1, hence 1 iteration is expected to be optimal.

The choice of how many iterations to perform is based on three parameters:

- the quadratic sum of the data and MC statistical errors in every bin;
- the relative bias in every bin, defined as:

$$\text{Bias}^i = \frac{x^i_{UNFOLD} - x^i_{TRUTH}}{x^i_{TRUTH}}\ , \tag{8.15}$$

  where x^i represents the differential cross-section in bin i; and the mean relative bias, defined as:

$$\langle\text{Bias}\rangle = \sum_i \text{Bias}^i / N_{\text{bins}} \tag{8.16}$$

- the χ^2 of the change between iterations:

$$\chi^2 = \sum_i^{\text{all bins}} \frac{(x^i_N - x^i_{N-1})^2}{(\sigma^i_N)^2}\ , \tag{8.17}$$

where x_N^i represents the differential cross-section in bin i evaluated with N iterations and σ_N^i is the statistical error related to it. The χ^2 of change gives an estimate on how much the distributions change between iterations.

For N = 0 (i.e. no iterations), an efficiency correction is applied to each bin, assuming that there is no migration between bins. The χ^2 of change at N=0 is calculated as a difference between the N=0 iteration and the true distributions.

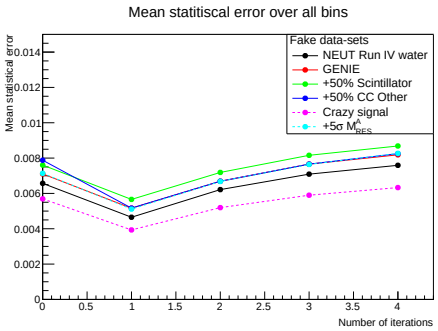

(a) Mean statistical uncertainty as a function of the number of iterations.

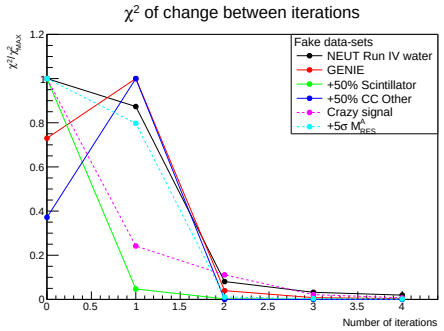

(b) χ^2 of change between iterations divided by the maximum χ^2 over all iterations as a function of the number of iterations performed.

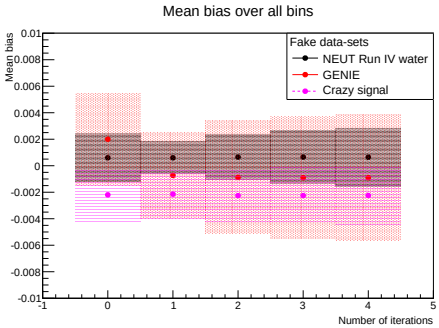

(c) Mean and RMS of the bias over all bins as function of the number of iterations.

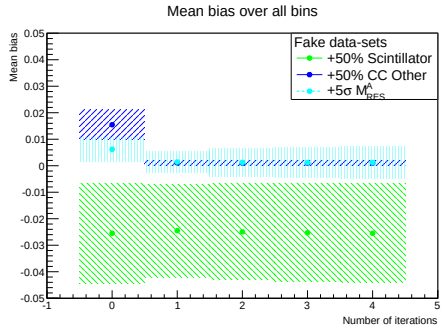

(d) Mean and RMS of the bias over all bins as function of the number of iterations.

Figure 8.3: Studies on the number of iterations to use in the Bayesian unfolding method. Legend shows the different fake data-sets considered.

Figure 8.3 highlights the results of these three tests for the different fake data-sets considered. Figure 8.3a shows the mean statistical uncertainty over all bins as a

function of the number of iterations. In all cases this is minimised when 1 iteration is performed.

Figure 8.3b presents the χ^2 of change between the iterations as a function of the number of iterations. To better compare the different fake data-sets sample, the χ^2 has been divided by the maximum χ^2 over all the iterations. A small χ^2 of change between one iteration and the previous one means that unfolded spectrum did not change very much from the previous iteration. A large χ^2 of change indicates large difference with the unfolded spectrum in the previous iteration. In all cases the best number of iterations is 1.

Figures 8.3c and 8.3d show the mean and RMS bias over all bins, as a function of the number of iterations. The mean and RMS of the bias are both minimised at 1 iterations for all cases.

Table 8.3: Total flux averaged cross-section evaluated with 1 iteration of the Bayesian unfolding method starting from the nominal NEUT MC. Different fake data-sets are used. Total cross-sections are expressed in 10^{-40}cm^2/Nucleon units.

Fake data-set	σ_{TRUTH}	$\sigma_{UNFOLDED}$
Nominal NEUT	4.706	$4.706 \pm 0.493(\text{stat}) \pm 2.074(\text{syst})$
GENIE	6.471	$6.497 \pm 0.522(\text{stat}) \pm 2.150(\text{syst})$
+50% CC Other	4.706	$5.201 \pm 0.532(\text{stat}) \pm 1.621(\text{syst})$
+50% Scintillator	4.706	$5.370 \pm 0.517(\text{stat}) \pm 1.717(\text{syst})$
Crazy signal	3.787	$3.285 \pm 0.390(\text{stat}) \pm 1.844(\text{syst})$
$+5\,\sigma$ M_A^{RES}	5.354	$6.322 \pm 0.519(\text{stat}) \pm 2.038(\text{syst})$

Tables 8.3 highlights the total cross-section found using 1 iteration, and compares it with the prediction from truth information. In all cases the truth prediction is within the statistical and systematic uncertainties of the unfolded results (starting from the NEUT MC).

Figures 8.4-8.7 presents the single differential unfolded cross-section in p_{μ^-} using 1 iteration of the Bayesian unfolding method when using different fake data-sets. The relative bias per bin is also shown. In almost all cases the unfolded cross-section result

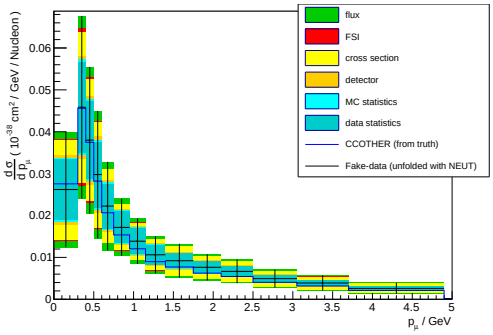

(a) Single differential cross-section in p_μ.

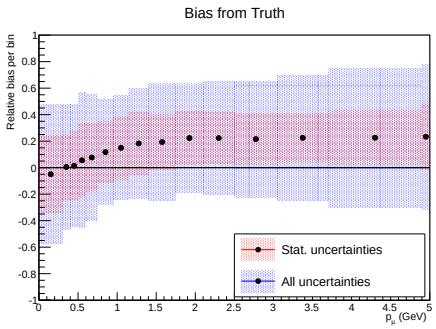

(b) Relative bias per bin.

Figure 8.4: Differential cross-section results using the NEUT MC for training and the NEUT MC with increased CC Other background as a fake data-set.

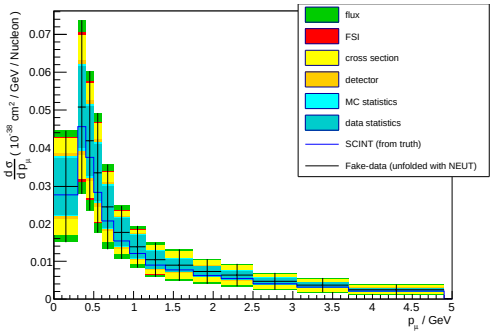

(a) Single differential cross-section in p_μ.

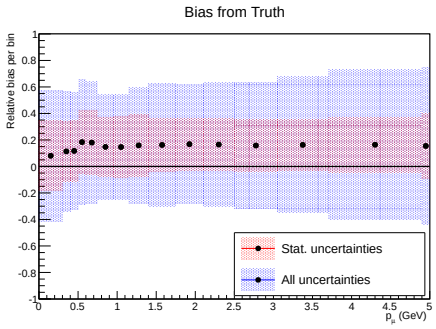

(b) Relative bias per bin.

Figure 8.5: Differential cross-section results using the NEUT MC for training and the NEUT MC with increased scintillator background as a fake data-set.

in each bin is compatible with the prediction from truth. The only exception is the $+5\,\sigma$ M_A^{RES} fake data-set in which the bias from truth is outside the statistical and systematic uncertainty at high p_μ. This is not surprising since the theory cross-section systematic used in this analysis assume $1\,\sigma$ deviation from the nominal value.

Section 8.3 shows all the single differential cross-section results using the GENIE MC as fake data-set.

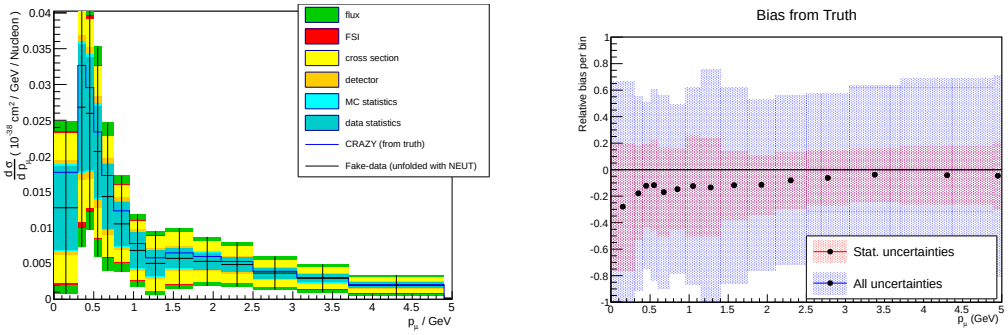

(a) Single differential cross-section in p_μ. **(b)** Relative bias per bin.

Figure 8.6: Differential cross-section results using the NEUT MC for training and the NEUT MC with "crazy" signal implementation as a fake data-set.

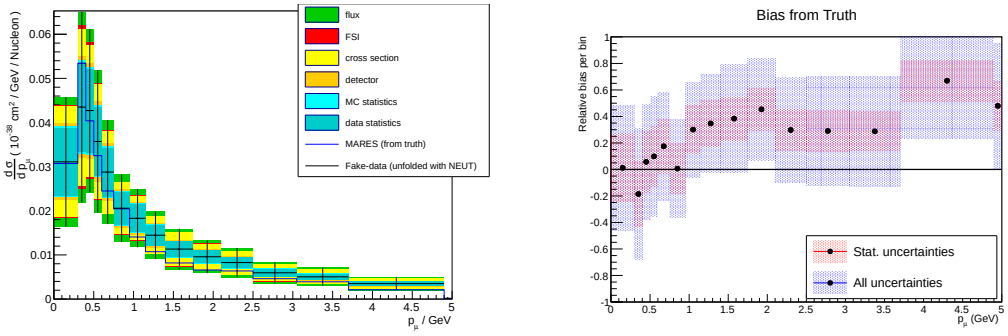

(a) Single differential cross-section in p_μ. **(b)** Relative bias per bin.

Figure 8.7: Differential cross-section results using the NEUT MC for training and the NEUT MC with M_A^{RES} increased by $5\,\sigma$ as a fake data-set.

8.2.3 Control sample normalisation constant

Before performing the background subtraction a coefficient α_β is evaluated from the control regions to re-normalise the background (as explained in Section 8.1, Equation 8.10). Table 8.4 shows the value of this coefficient for each sideband and how that changes the predicted background.

The second column of the Table shows the value of α, the third column shows the number of background events in the signal sample multiplied by α, the fourth column shows the number of background events in the fake data-set considered, and the last column shows the χ^2/NDF for the predicted and true background in the p_μ

distribution.

In general, the CCnon1π water-enhanced sideband describes the non CC1π^+ background well: the difference between the re-normalised MC background and the fake data background is below 5% in all cases except when considering GENIE as fake data-set, when the difference in the total number of events becomes almost 16%. This behaviour is also reflected in the χ^2/NDF (given here only for the p_μ distribution) that is always below 1, except when considering the GENIE fake data-set.

The CC1π^+ scintillator sideband performs slightly worse, mainly because of the CC Other contamination in the sample. The largest difference is seen when using the CC Other increased fake data-set. In reality the contamination of CC Other events in this sideband causes α to be 1.19, hence the scintillator background is overestimated by almost 19%. Important to note here is that even using the CC1π^+ sample in FGD1 as sideband would work not better, since the CC Other contamination in the sample would be as high.

8.2.4 Signal contamination in control samples

The signal contamination in both the control samples used is around 6%. A high signal contamination in the control regions could bias the results. A simple check to verify when a high signal contamination could produce a biased cross-section result is performed.

The procedure is to assign a weight w to the signal contamination in the control regions and evaluate the bias in each bin as function of this weight, with $w = 0$ corresponding to no signal contamination in both control regions, $w = 1$ corresponding to the signal contamination present in the control regions of the analysis (i.e. $\approx 6\%$ in each control region), and $w = 2$ corresponding to double the signal contamination present in the control regions of the analysis. (i.e. $\approx 12\%$ in each control region).

The bias is evaluated when unfolding the reconstructed muon momentum variable using the nominal NEUT MC for training and unfolding. Since it is expected that the bias should stay within the statistical uncertainties, only statistical errors are shown in the plots.

Figures 8.8 and 8.9 show the unfolded spectra and the bias from truth in each bin for different weights applied to the signal contamination in the control regions.

Table 8.4: Summary of α coefficient for both sidebands and all the fake data-sets considered. The second column shows the value of α, the third column shows the number of background events in the signal sample multiplied by α ($Signal^{MC}_{BKG}*\alpha$), the fourth column shows the number of background events in the fake data-set considered ($Sideband^{FakeData}_{BKG}$), and the last column shows the χ^2/NDF for the predicted and true background in the p_μ distribution.

CCnon1π water-enhanced sideband

Sample	α	$Signal^{MC}_{BKG} * \alpha$	$Sideband^{FakeData}_{BKG}$	χ^2/NDF
NEUT	1.00	704.1	704.1	0/10
GENIE	1.17	823.4	710.2	68/10
Scintillator increased	1.17	826.5	824.8	0.2/10
CC Other increased	1.40	984.0	955.8	3.5/10
"Crazy" signal	0.99	699.3	704.1	0.0001/10
Altered M_A^{RES}	1.04	732.1	710.8	2.2/10

CC1π^+ scintillator sideband

Sample	α	$Signal^{MC}_{BKG} * \alpha$	$Sideband^{FakeData}_{BKG}$	χ^2/NDF
NEUT	1.00	278.2	278.2	0/10
GENIE	1.13	314.1	377.0	44/10
Scintillator increased	1.37	382.0	384.3	0.06/10
CC Other increased	1.19	330.1	278.2	0.0001/10
"Crazy" signal	0.93	258.1	231.9	11/10
Altered M_A^{RES}	1.18	328.5	379.0	14/10

The NEUT truth value for the total cross-section in the restricted phase-space considered is $4.71{\cdot}10^{-40}$ cm^2/ Nucleon. Table 8.5 shows a summary of the total cross-section and statistical uncertainty for different weights applied to the signal contamination in the control regions.

The plots of the bias and the table with the summary of the cross-section results suggest that the bias starts getting larger when the weight applied is 1.5 (i.e the signal

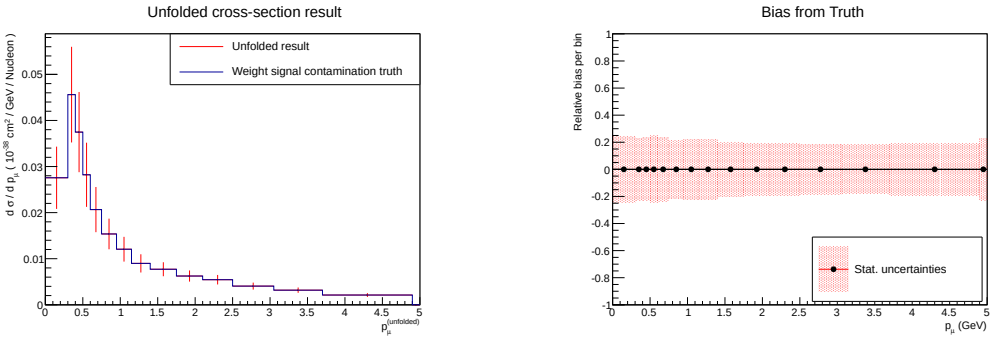

(a) Signal contamination weight = 0.

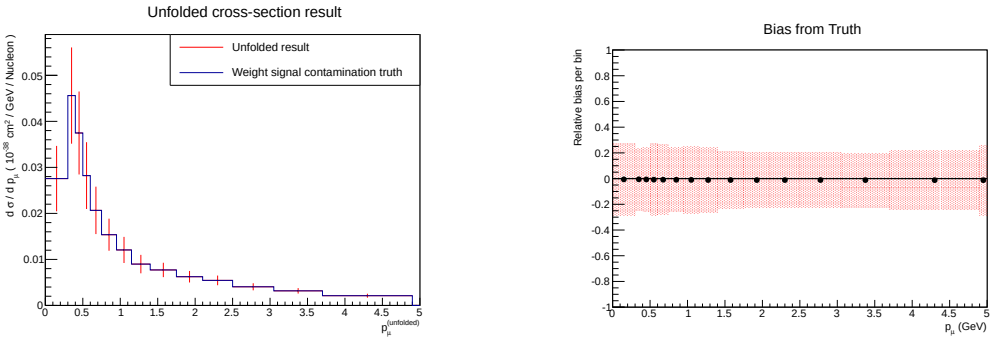

(b) Signal contamination weight = 0.5.

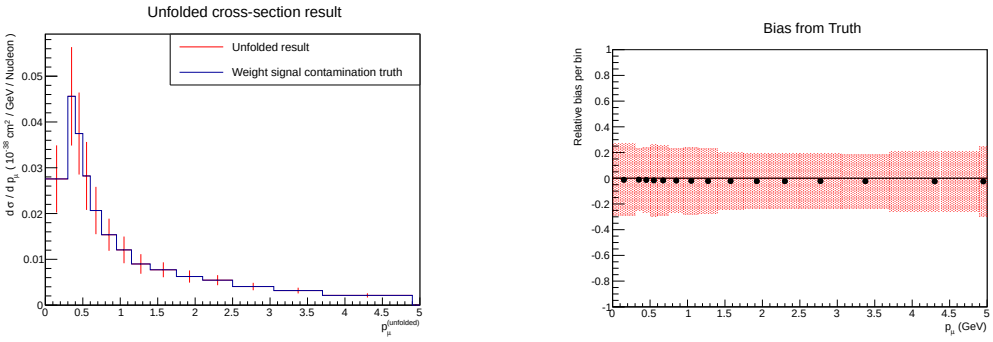

(c) Signal contamination weight = 1.

Figure 8.8: Signal contamination in control samples: each row shows the unfolded spectrum (left) and the bias from truth in each bin (right) for different weights applied to the signal contamination in the control regions.

contamination in the control region is 9%). Nonetheless, even when the signal contamination is as large as 15% the bias from truth in the single bins of the cross-section is still within the statistical uncertainties.

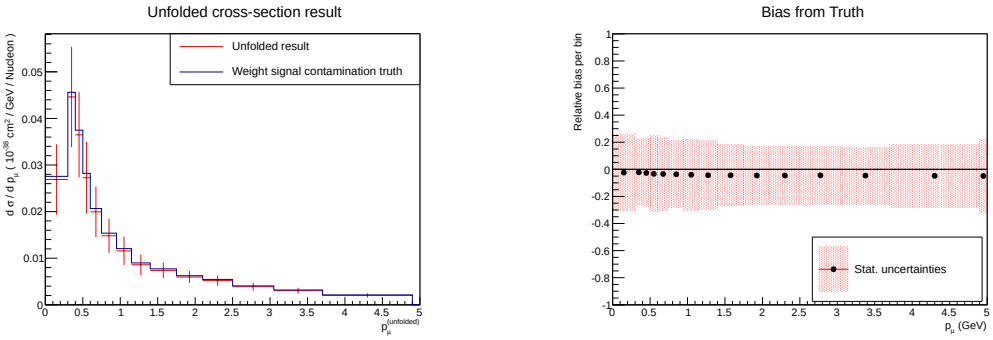

(a) Signal contamination weight = 1.5

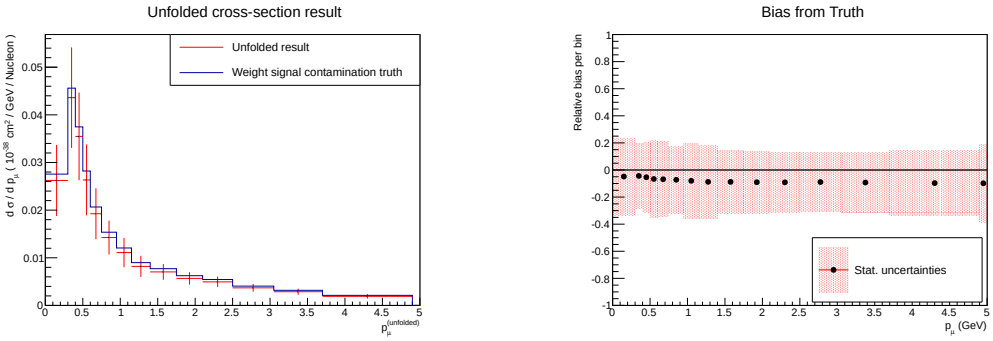

(b) Signal contamination weight = 2.

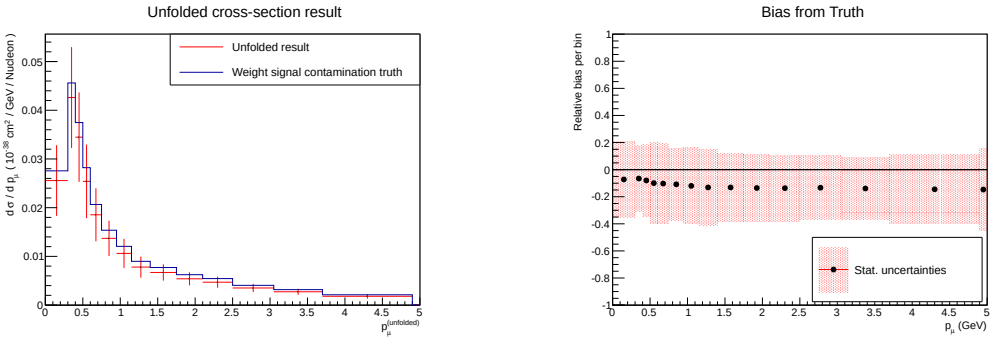

(c) Signal contamination weight = 2.5.

Figure 8.9: Signal contamination in control samples: each row shows the unfolded spectrum (left) and the bias from truth in each bin (right) for different weights applied to the signal contamination in the control regions.

Table 8.5: Total cross-section results as a function of the different weights applied to the signal contamination in the control region. The total cross-section and statistical uncertainty are expressed in units of 10^{-40} cm^2/ Nucleon.

Weight	Cross-section	Total statistical uncertainty
0	4.71	0.41
0.5	4.71	0.44
1	4.71	0.46
1.5	4.54	0.47
2	4.37	0.49
2.5	4.20	0.49

8.2.5 Shape and normalisation uncertainties with/without sidebands

This Subsection shows an analysis on the change in the shape and normalisation uncertainties when using (or not using) the sideband samples to control the background.

This study has been developed using the NEUT MC fake data-set and unfolding the p_μ distribution.

To evaluate the shape-only covariance matrix, the cross-section distribution for each pseudo-experiment is scaled to have the same integral as the nominal distribution:

$$V_{ij}^{shape} = \frac{1}{N}\sum_{s_n=1}^{N}\left(\frac{\sigma_{total}^{(nom)}}{\sigma_{total}^{(s_n)}}\sigma_i^{(s_n)} - \sigma_i^{(nom)}\right)\left(\frac{\sigma_{total}^{(nom)}}{\sigma_{total}^{(s_n)}}\sigma_j^{(s_n)} - \sigma_j^{(nom)}\right) . \tag{8.18}$$

The normalisation error is then inferred from the total error, simply subtracting the shape-only part.

Table 8.6 shows the shape-only uncertainties evaluated when unfolding with and without sidebands. Table 8.7 shows the normalisation-only uncertainties evaluated when unfolding with and without sidebands.

The background normalisation as applied in the analysis can constrain the $\sigma_{BKG}\cdot\Phi$, where σ_{BKG} is the background cross-section and Φ is the neutrino flux. Disentagling the two contributions is impossible using this method, and that is reason why both

the flux and cross-section uncertainties are constrained when using sidebands to control the background. A future improvement of the analysis will unfold the signal and background region simultaneously providing a better constraint on the flux and cross-section uncertainties.

The method used to constrain the background only re-scales the background predicted by NEUT, without affecting the shape: this is reflected in the reduction of the shape uncertainties which is much smaller than the reduction seen in the normalisation uncertainties.

The ECal reconstruction systematic uncertainty is seems to be increasing from without sidebands to with sidebands, but this increase is not significant compared to statistical error on these numbers.

Table 8.6: Shape uncertainties. Fractional error (in %) on the total cross-section when unfolding p_μ using the NEUT MC.

	without sidebands	with sidebands
Cross-section	13.6 %	9.4 %
FSI	2.5 %	2.2 %
Flux	6.7 %	4.4 %

Detector	without sidebands	with sidebands
B field distortion	0.2 %	0.2 %
TPC charge confusion	0.2 %	0.2 %
FGD2 backward migrations	0.3 %	0.2 %
FGD2 forward migrations	0.8 %	0.9 %
FGD mass scintillator	0.02 %	0.006 %
FGD mass water	0.02 %	0.01 %
TPC momentum resolution	0.2 %	0.1 %
TPC momentum scale	0.5 %	0.5 %
Out of FV	0.2 %	0.2 %
ECal PID	0.1 %	0.03 %
Pile up	0.02 %	0.002 %
ECal reconstruction	0.1 %	0.1 %
Pion secondary interactions	2.3 %	2.2 %
TPC quality cut	0.0002 %	0.0002 %
TPC-FGD matching efficiency	0.01 %	0.01 %
TPC PID	0.3 %	0.3 %
TPC track efficiency	0.1 %	0.1 %

Table 8.7: Normalisation uncertainties. Fractional error (in %) on the total cross-section when unfolding p_μ using the NEUT MC.

	without sidebands	with sidebands
Cross-section	49.5 %	27.9 %
FSI	10.5 %	6.5 %
Flux	47.3 %	30.1 %

Detector	without sidebands	with sidebands
B field distortion	0.1 %	0.1 %
TPC charge confusion	0.1 %	0.1 %
FGD2 backward migrations	3.3 %	2.3 %
FGD2 forward migrations	7.1 %	4.7 %
FGD mass scintillator	0.9 %	0.4 %
FGD mass water	1.1 %	0.8 %
TPC momentum resolution	0.8 %	0.64 %
TPC momentum scale	0.5 %	0.5 %
Out of FV	1.5 %	1.0 %
ECal PID	0.2 %	0.03 %
Pile up	0.6 %	0.3 %
ECal Reconstruction	0.7 %	0.4 %
Pion secondary interactions	9.7 %	7.5 %
TPC quality cut	0.001 %	0.0001 %
TPC-FGD matching efficiency	0.1 %	0.02 %
TPC PID	1.3 %	0.9 %
TPC track efficiency	0.2 %	0.2 %

8.3 Results with GENIE fake data-sets

In this section the complete results using GENIE as fake data-sets are shown for each variable together with the size of all the systematic uncertainties considered.

Table 8.8 shows the results from the total flux averaged cross-section, evaluated when unfolding different variables. The GENIE prediction is $\sigma_{\mathrm{t,GENIE}} = 6.471 \times 10^{-40}\mathrm{cm}^2/\mathrm{Nucleon}$, and in all cases the extracted total cross-section is compatible with the GENIE prediction within the statistical uncertainties.

Figures 8.10-8.14 show the single differential results when unfolding the pion/muon kinematics using the GENIE fake data-set. In all cases the unfolded single differential cross-section is compatible with the prediction from the GENIE truth. The relative size of each uncertainty (both statistical and systematic) is given for every bin, although the breakdown of all the detector uncertainties is not shown here for brevity.

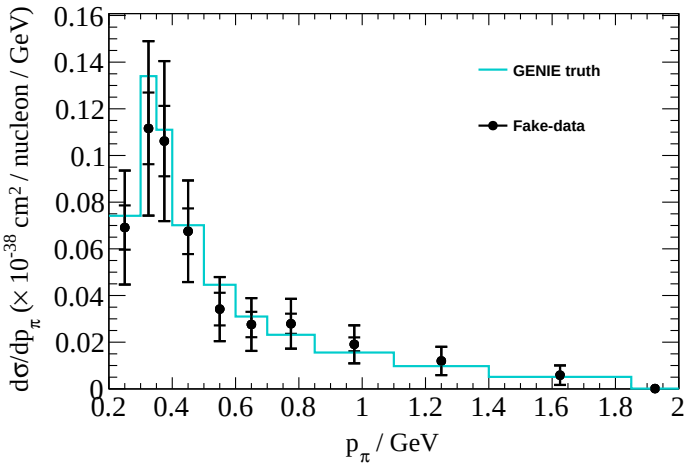

(a) Differential cross-section obtained by unfolding the p_{π^+} distribution.

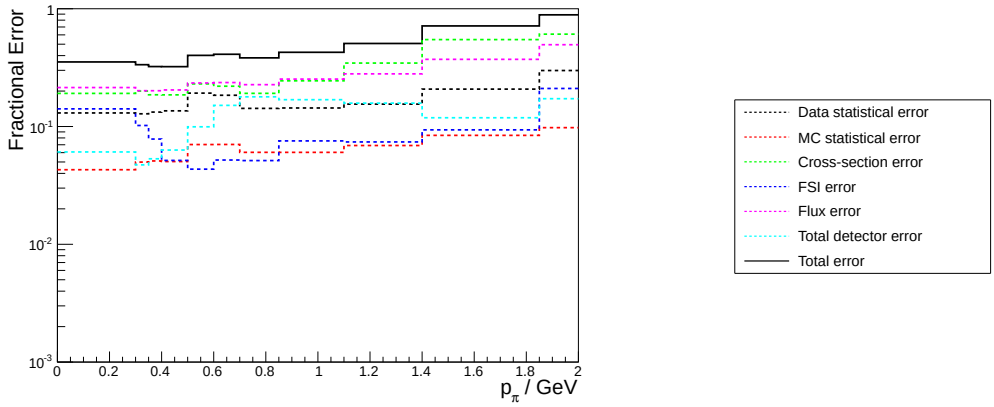

(b) Total and fractional error components as a function of the p_{π^+} binned distribution.

Figure 8.10: Single differential cross-section in p_{π^+} obtained when using the GENIE fake data-set.

Table 8.8: Total flux-averaged cross-section evaluated when unfolding the GENIE distributions. Cross-sections and total errors are given in units of 10^{-40}cm^2 / Nucleon. The GENIE prediction is $\sigma_{\mathrm{t,GENIE}} = 6.471 \times 10^{-40}$cm^2/Nucleon. "negl" stands for negligible and indicates that the uncertainty is below 0.001%.

	p_{π^+}	$\cos\theta_{\pi^+}$	p_{μ^-}	$\cos\theta_{\mu^-}$	$\cos\theta_{\mu^+,\pi^+}$
Flux-averaged σ	6.289	6.807	6.497	6.451	6.686
Total stat. error	0.496	0.549	0.513	0.537	0.535
Total syst. error	2.089	2.273	2.145	2.235	2.286
Fractional uncertainties in %					
Data statistics	7.46	7.62	7.48	7.89	7.60
MC statistics	2.58	2.61	2.55	2.65	2.49
Theory cross-section	21.92	22.50	21.17	23.05	23.31
FSI	6.63	5.94	5.73	6.22	5.54
Flux	23.51	23.02	23.79	24.28	23.42
B field distortion	0.12	0.07	0.14	0.07	0.08
TPC charge confusion	0.12	0.07	0.14	0.07	0.08
FGD2 backward migrations	0.46	0.19	0.12	0.30	0.15
FGD2 forward migrations	0.72	0.96	1.00	0.57	0.50
FGD mass scintillator	0.17	0.23	0.19	0.26	0.24
FGD mass water	0.67	0.69	0.69	0.71	0.67
TPC momentum resolution	0.38	0.17	0.58	0.19	0.17
TPC momentum scale	0.52	negl	0.40	negl	negl
Out of FV	0.40	0.26	0.54	0.67	0.24
ECal PID	0.06	0.06	0.07	0.05	0.05
Pile up	0.27	0.27	0.28	0.28	0.27
ECal reconstruction	0.36	0.39	0.38	0.44	0.43
Pion secondary interactions	4.78	6.47	6.32	6.19	6.66
TPC quality cut	negl	negl	negl	negl	negl
TPC-FGD matching efficiency	0.03	0.01	0.02	0.01	0.02
TPC PID	0.82	0.49	0.48	0.74	0.85
TPC track efficiency	0.18	0.12	0.22	0.24	0.16

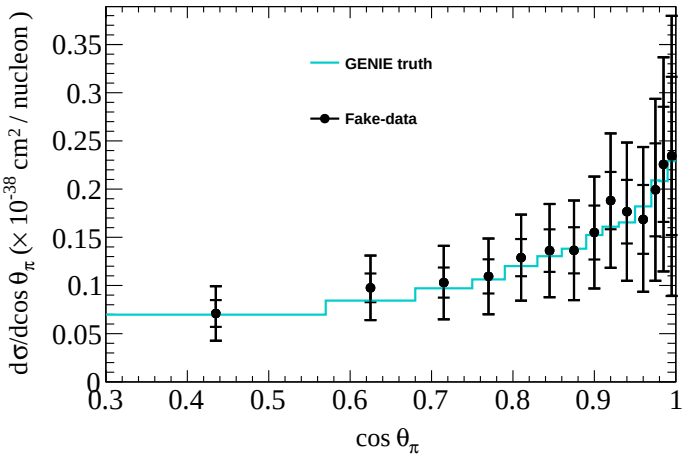

(a) Differential cross-section obtained by unfolding the $\cos\theta_{\pi^+}$ distribution.

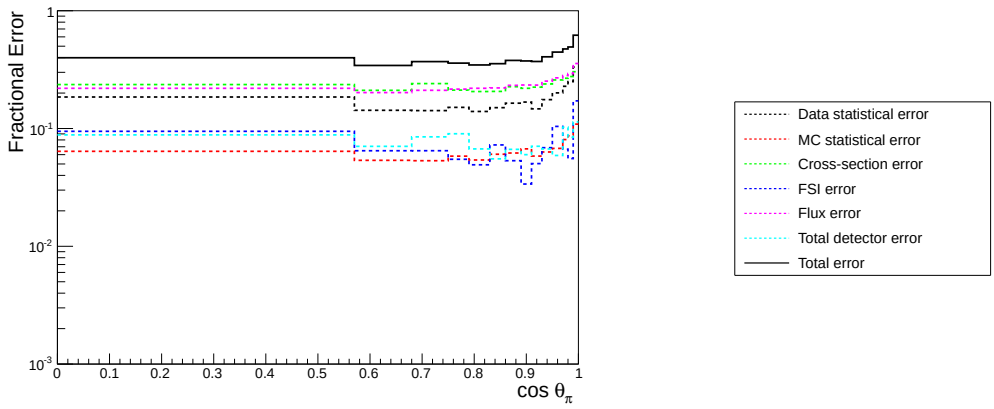

(b) Total and fractional error components as a function of the $\cos\theta_{\pi^+}$ binned distribution.

Figure 8.11: Single differential cross-section in $\cos\theta_{\pi^+}$ obtained when using the GENIE fake data-set.

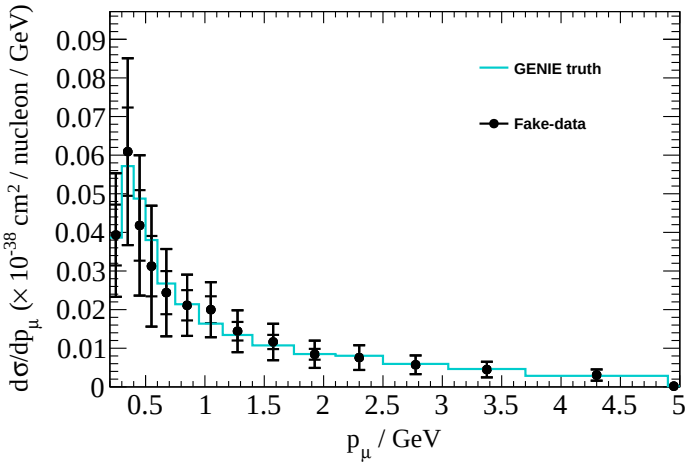

(a) Differential cross-section obtained by unfolding the p_{μ^-} distribution.

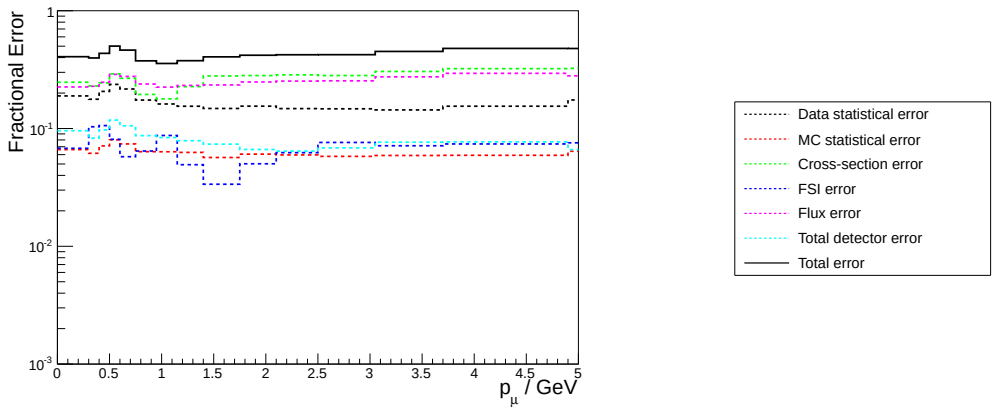

(b) Total and fractional error components as a function of the p_{μ^-} binned distribution.

Figure 8.12: Single differential cross-section in p_{μ^-} obtained when using the GENIE fake data-set.

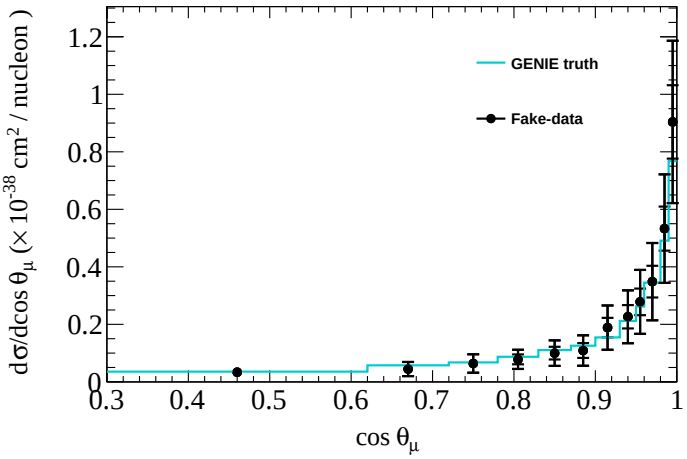

(a) Differential cross-section obtained by unfolding the $\cos\theta_{\mu^-}$ distribution.

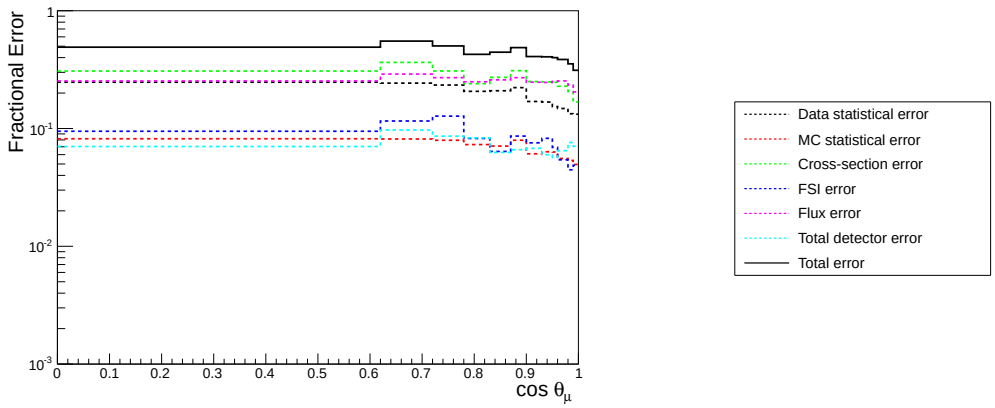

(b) Total and fractional error components as a function of the $\cos\theta_{\mu^-}$ binned distribution.

Figure 8.13: Single differential cross-section in $\cos\theta_{\mu^-}$ obtained when using the GENIE fake data-set.

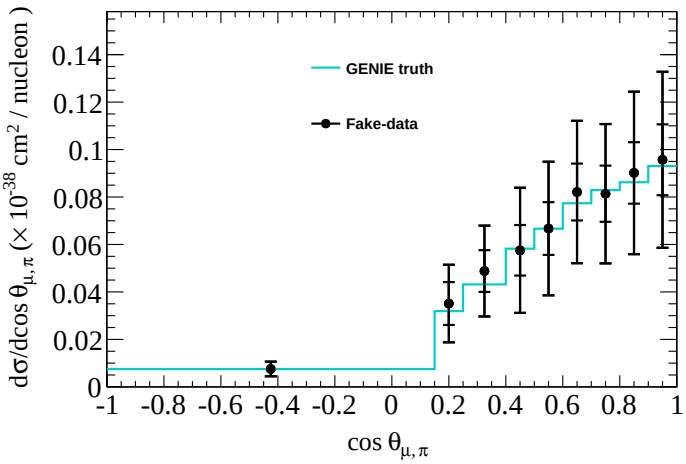

(a) Differential cross-section obtained by unfolding the $\cos\theta_{\mu^-,\pi^+}$ distribution.

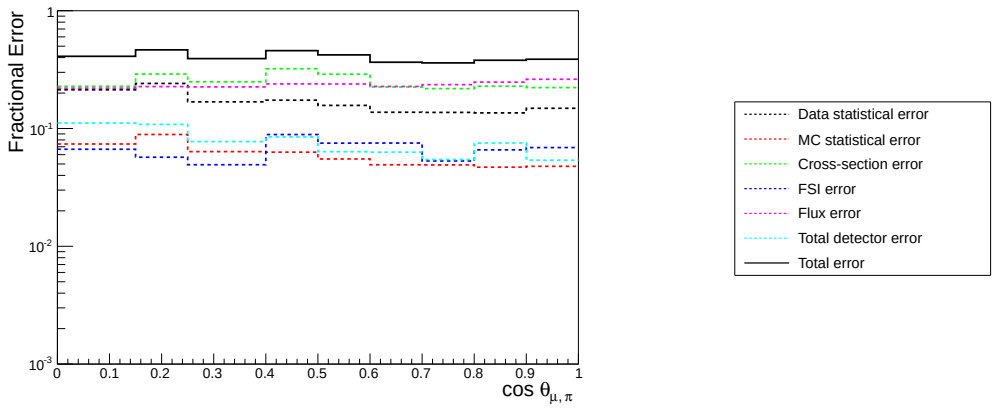

(b) Total and fractional error components as a function of the $\cos\theta_{\mu^-,\pi^+}$ binned distribution.

Figure 8.14: Single differential cross-section in $\cos\theta_{\mu^-,\pi^+}$ obtained when using the GENIE fake data-set.

The flux averaged cross-sections $\sigma(E)$ are evaluated from the reconstructed neutrino energy with Δ resonance or with the MiniBooNE formula and unfolded to the neutrino energy simulated by NEUT. Figures 8.15 and 8.16 show the $\sigma(E)$ results when using the Δ resonance formula and the MiniBooNE formula, respectively. In both cases the unfolded cross-section result is completely consistent with the GENIE prediction.

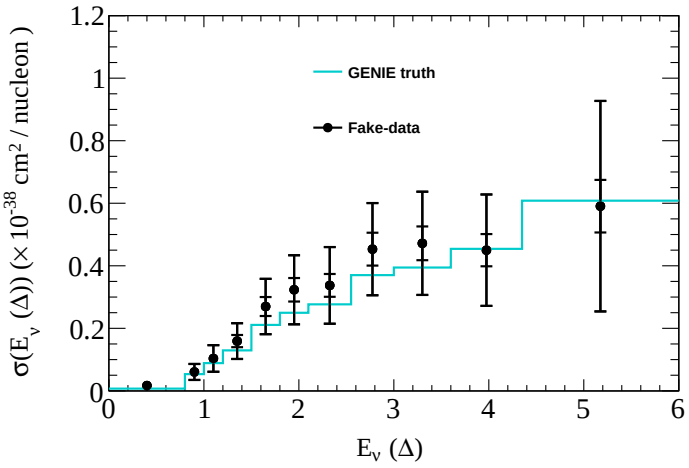

(a) Differential cross-section obtained by unfolding the $E_{\nu\ \mathrm{REC}\ \Delta}$ distribution.

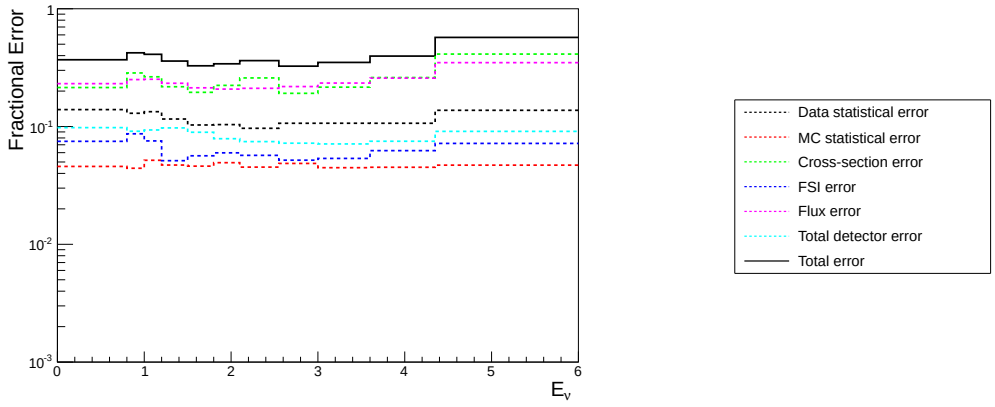

(b) Total and fractional error components as a function of the $E_{\nu\ \mathrm{REC}\ \Delta}$ binned distribution.

Figure 8.15: Single differential cross-section in $E_{\nu\ \mathrm{REC}\ \Delta}$ obtained when using the GENIE fake data-set.

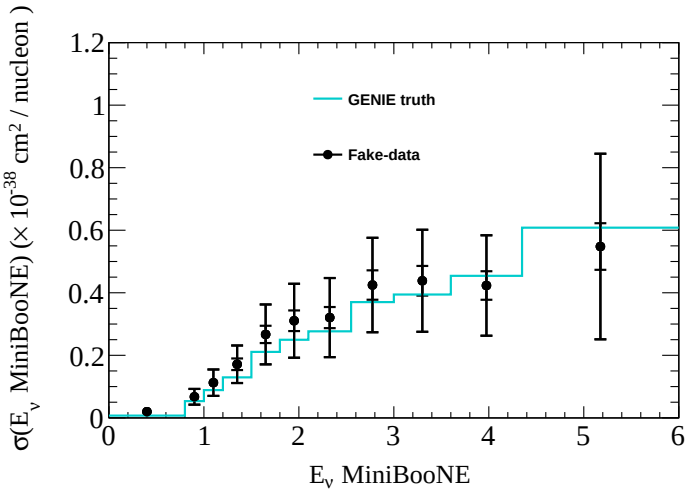

(a) Differential cross-section obtained by unfolding the $E_{\nu\ \mathrm{REC,\ MB}}$ distribution.

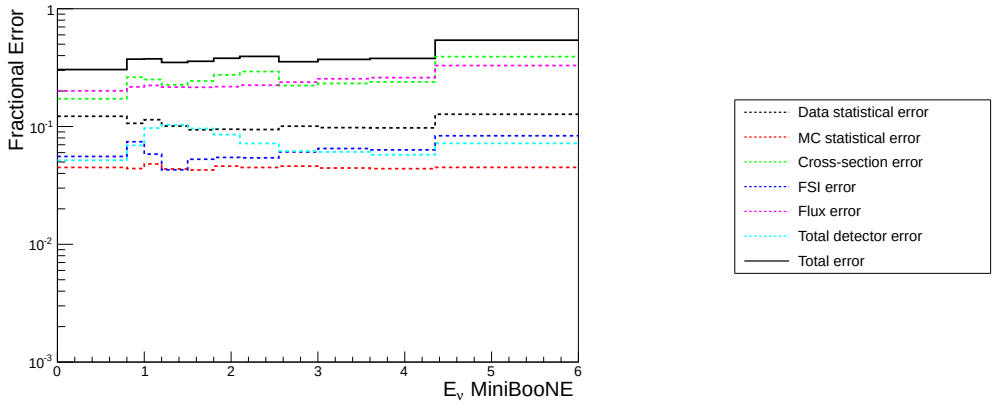

(b) Total and fractional error components as a function of the $E_{\nu\ \mathrm{REC,\ MB}}$ binned distribution.

Figure 8.16: Single differential cross-section in $E_{\nu\ \mathrm{REC,\ MB}}$ obtained when using the GENIE fake data-set.

8.4 Results

This Section presents the results obtained when unfolding the data sample from Run II to Run IV to obtain the single pion production cross-section on water.

For each variable the distributions of the signal and two sideband samples (before the MC has been scaled with the sideband normalisation constant α)) are also presented, to better compare the unfolded results with the distributions pre-unfolding. The total and differential cross-section, and the size of the uncertainties after unfolding are presented.

In all cases, the largest systematic uncertainties are those coming from the flux and cross-section. The main detector systematic uncertainties are those coming from pion secondary interactions (that has large uncertainties in all the phase space), and the TPC PID.

The sideband normalisation constants are found to be $\alpha_{CCOTHER} = 1.10457$ and $\alpha_{SCINT} = 0.9866$.

All the distributions are slightly lower than the NEUT prediction (but still compatible with it), and in general $1.5\,\sigma$ lower than the GENIE prection. A small suppression is seen at low pion momentum that might be linked to the model for CC coherent interactions used in NEUT: NEUT highly over-estimates the amount of coherent interactions especially at low E_π, as seen by the latest results of the MINERνA experiment (see Subsection 2.5.4 and Reference [50]).

Table 8.9 summarises the total cross-sections obtained when unfolding different variables. The fractional systematic uncertainties are also presented. Because of the different efficiency of each variable, the total cross-sections evaluated differ slightly between each other, but they are still compatible with each other (within statistical uncertainties) and with the NEUT prediction ($\sigma_{\mathrm{t,NEUT}} = 3.795 \times 10^{-40}\mathrm{cm}^2/\mathrm{Nucleon}$). The GENIE prediction is $\sigma_{\mathrm{t,GENIE}} = 5.493 \times 10^{-40}\mathrm{cm}^2/\mathrm{Nucleon}$, and when unfolding the muon kinematics the results are more than $1\,\sigma$ away from it.

Table 8.9: Total flux-averaged cross-section evaluated when unfolding the T2K data Run II-IV. "negl" stands for negligible and indicates that the uncertainty is below 0.001%.

Cross-section results (10^{-40}cm^2 / Nucleon)					
	p_{π^+}	$\cos\theta_{\pi^+}$	p_{μ^-}	$\cos\theta_{\mu^-}$	$\cos\theta_{\mu^+,\pi^+}$
Flux-averaged σ	3.22	3.13	2.98	2.77	3.12
Total stat. error	0.42	0.44	0.43	0.44	0.44
Total syst. error	1.44	1.70	1.47	1.25	1.67
Fractional uncertainties in %					
Data statistics	12.4	13.3	13.9	15.2	13.5
MC statistics	3.9	4.1	4.0	4.5	4.1
Theory cross-section	32.0	40.6	34.8	35.3	41.0
FSI	6.9	7.9	7.4	16.1	7.1
Flux	29.5	33.8	32.9	21.5	32.2
B field distortion	0.1	0.1	0.2	0.1	0.1
TPC charge confusion	0.1	0.1	0.2	0.1	0.1
FGD2 backward migrations	0.5	0.3	0.4	0.8	0.3
FGD2 forward migrations	1.1	0.7	0.8	0.8	0.7
FGD mass scintillator	0.2	0.4	0.3	0.5	0.4
FGD mass water	0.7	0.7	0.8	0.8	0.8
TPC momentum resolution	1.3	0.7	1.5	1.0	0.7
TPC momentum scale	0.4	0.4	0.4	0.6	0.3
Out of FV	0.4	0.3	0.8	1.0	0.3
ECal PID	0.1	0.1	0.1	0.1	0.1
Pile up	0.3	0.3	0.3	0.4	0.3
ECal reconstruction	0.4	0.4	0.3	0.5	0.5
Pion secondary interactions	6.8	8.9	8.6	7.7	9.1
TPC quality cut	negl	negl	negl	negl	negl
TPC-FGD matching efficiency	0.03	0.03	0.03	0.03	0.03
TPC PID	1.0	1.3	0.8	1.9	2.2
TPC track efficiency	0.3	0.2	0.2	0.4	0.2

8.4.1 Positive pion momentum

The distributions pre-unfolding of the positive pion momentum for the NEUT MC and Data Run II-IV are shown in Figure 8.17.

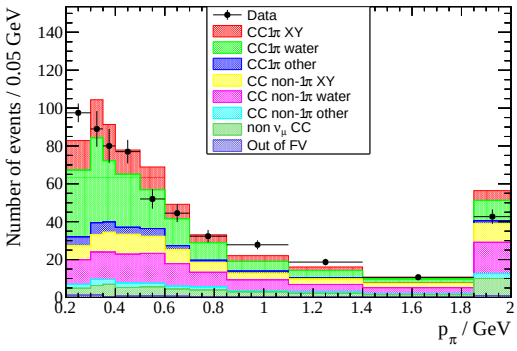

(a) CC1π^+ water-enhanced sample.

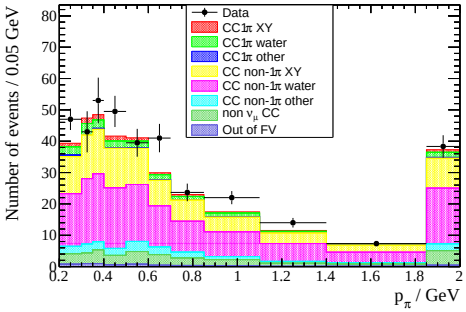

(b) CC Other sideband sample.

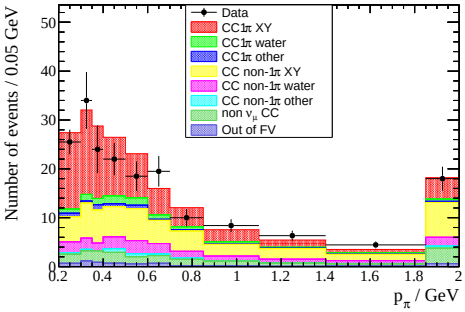

(c) Scintillator sideband sample.

Figure 8.17: p_{π^+} distributions: Data/MC comparison.

The differential results are shown in Figure 8.18, where the unfolding results are compatible with the NEUT prediction and at $p_\pi < 0.9\,\text{GeV/c}$ more than 1σ lower than the GENIE prediction.

Using GENIE as means to compare these results to the MiniBooNE and MINERνa ones in Figure 2.7, we find that the T2K data are more similar to the MINERνa data than to the MiniBooNE one (we both see a suppression compared to the GENIE prediction). Nonetheless, MiniBooNE and MINERνa have access to lower momentum pions and a direct comparison cannot be easily done.

Table 8.10 and Figure 8.19 show the fractional error in % per each error source.

Only the total detector error is presented in the table, but the components can be seen in the bottom plot in Figure 8.19.

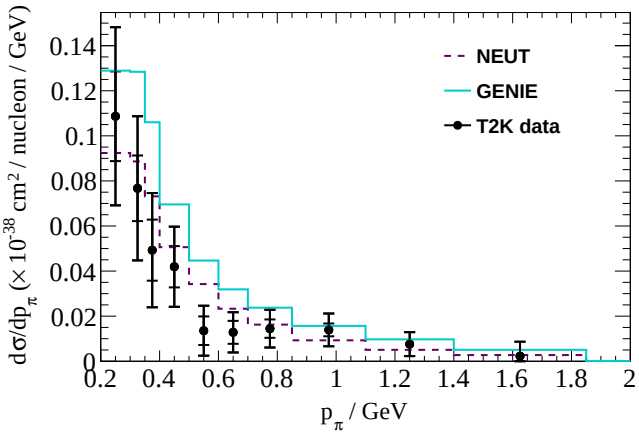

Figure 8.18: Differential cross-section obtained by unfolding the p_{π^+} distribution. Data from Run II to Run IV is used for the unfolding.

Table 8.10: Fractional error (in %) when unfolding p_{π^+} using the Data Run II-IV sample.

	Fractional error in %					
p_{π^+} binning (GeV)	Data stat.	MC stat.	Cross-section uncertainty	Final state interactions	Flux uncertainty	Detector uncertainty
0-0.3	17.47	5.48	17.19	13.72	21.76	5.47
0.3-0.35	17.99	6.00	24.04	15.49	22.80	6.30
0.35-0.4	26.25	8.15	27.90	19.18	25.36	10.01
0.4-0.5	20.82	6.65	24.23	8.28	24.07	9.21
0.5-0.6	44.54	14.23	48.30	20.10	36.41	20.99
0.6-0.7	37.84	11.81	39.00	16.87	33.26	18.90
0.7-0.85	26.68	9.03	32.39	11.78	30.02	21.65
0.85-1.1	19.19	7.06	31.80	9.88	29.80	17.78
1.1-1.4	22.37	8.11	50.38	10.59	36.32	18.77
1.4-1.85	46.92	15.51	242.7	51.65	120.3	27.61
>1.85	89.46	31.03	66.00	34.64	42.19	75.09

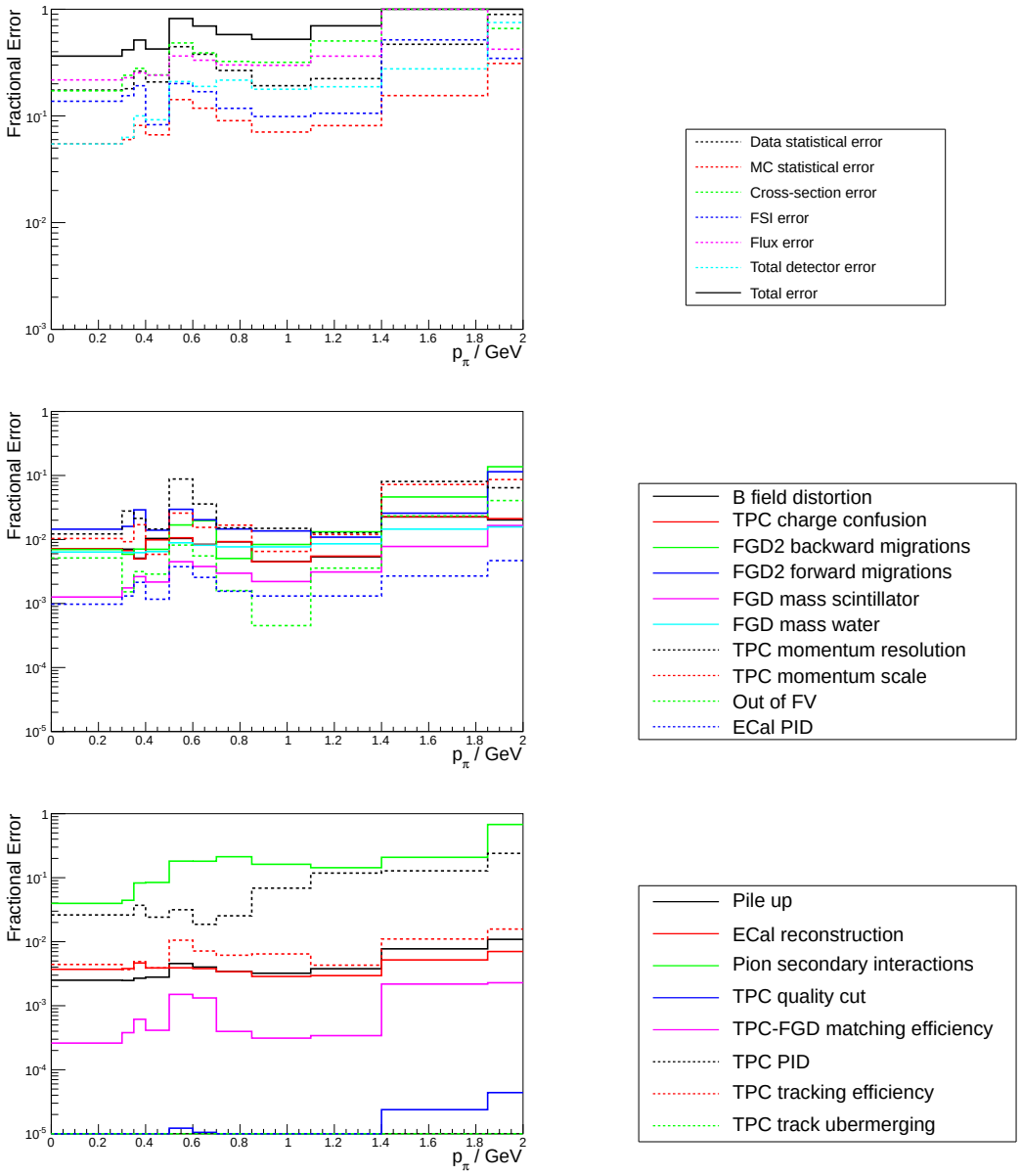

Figure 8.19: Total and fractional error components as a function of the p_{π^+} binned distribution are shown in the upper plots. The lower plot shows the contributions of the different detector errors.

8.4.2 Positive pion $\cos\theta$

The pre-unfolding distributions of the positive pion angle for the NEUT MC and Data Run II-IV are shown in Figure 8.20.

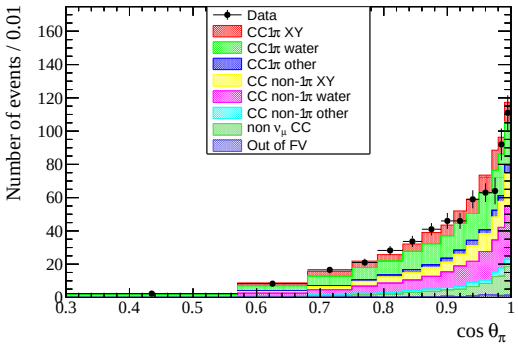

(a) CC1π^+ water-enhanced sample.

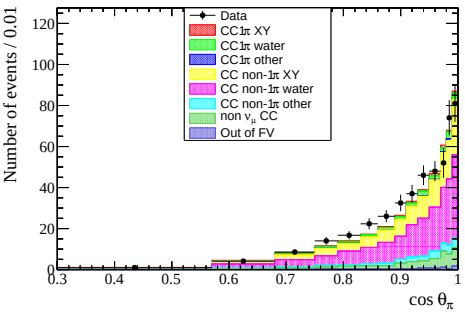

(b) CC Other sideband sample.

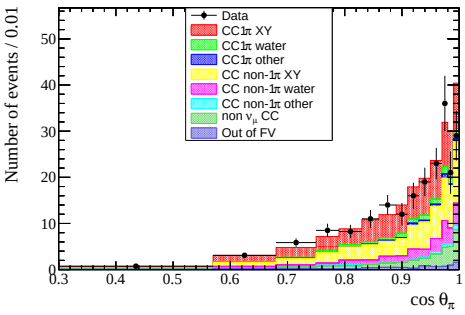

(c) Scintillator sideband sample.

Figure 8.20: $\cos\theta_{\pi^+}$ distributions: Data/MC comparison.

The differential results are shown in Figure 8.21. At $\cos\theta_\pi > 0.9$ the measured cross-section is much lower than the NEUT and GENIE prediction, but this suppression is not significant given the size of the statistical and systematic uncertainties. Overall the unfolded data are compatible with the NEUT prediction and a bit more than 1σ lower than the GENIE prediction.

Table 8.11 and Figure 8.22 show the fractional error in % per each error source. Only the total detector error is presented in the table, but the components can be seen in the bottom plot in Figure 8.22.

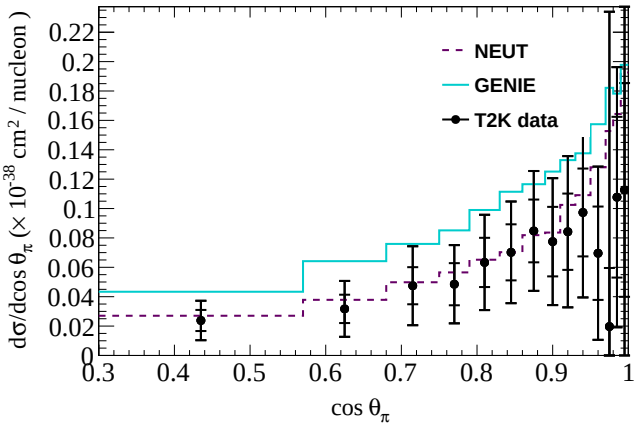

Figure 8.21: Differential cross-section obtained unfolding the $\cos\theta_{\pi^+}$.

Table 8.11: Fractional error (in %) when unfolding $\cos\theta_{\pi^+}$ using the Data Run II-IV sample.

	Fractional error in %					
$\cos\theta_{\pi^+}$ binning	Data stat.	MC stat.	Cross-section uncertainty	Final state interactions	Flux uncertainty	Detector uncertainty
0.30-0.57	28.89	8.62	36.48	9.78	27.03	10.61
0.57-0.68	29.07	8.96	42.01	6.66	27.28	10.96
0.68-0.75	25.42	7.83	39.82	7.73	27.04	11.05
0.75-0.79	28.23	8.78	33.85	8.56	27.88	12.01
0.79-0.83	25.19	8.10	32.20	7.11	27.53	8.84
0.83-0.86	25.91	8.22	29.46	6.75	27.04	6.91
0.86-0.89	23.94	7.87	29.13	3.89	27.52	7.75
0.89-0.91	29.08	9.31	34.11	5.05	30.21	8.62
0.91-0.93	29.37	9.39	38.40	10.76	32.64	11.36
0.93-0.95	29.18	9.62	35.38	9.65	33.58	10.68
0.95-0.97	43.71	13.18	49.73	22.77	44.45	11.21
0.97-0.98	192.2	63.82	812.7	316.8	614.3	79.87
0.98-0.99	48.62	14.68	42.84	8.88	43.53	19.14
0.99-1	61.94	18.22	54.56	34.79	60.02	26.50

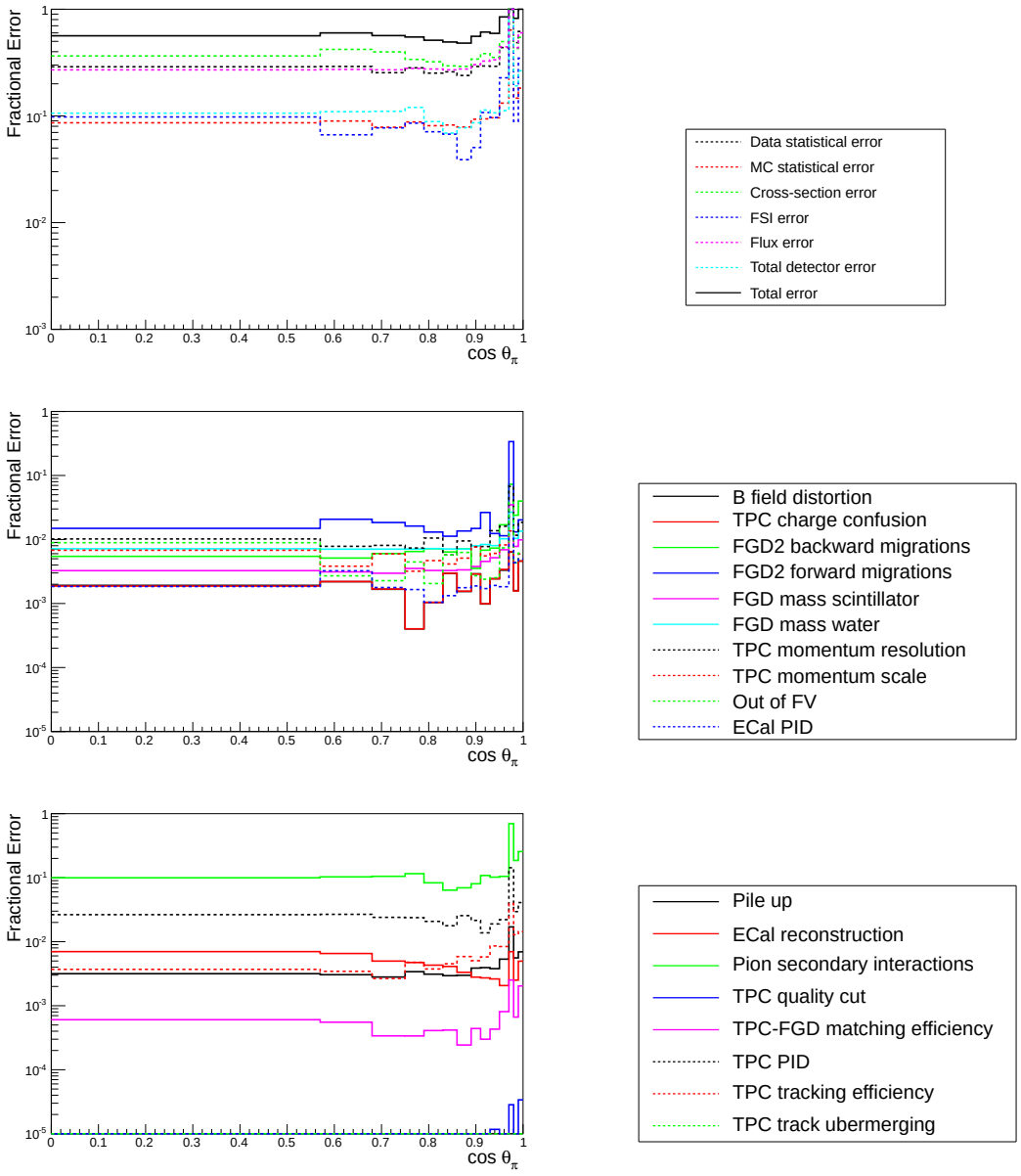

Figure 8.22: Total and fractional error components as a function of the $\cos\theta_{\pi^+}$ binned distribution are shown in the upper plots. The lower plot shows the contributions of the different detector errors.

8.4.3 Muon momentum

The pre-unfolding distributions of the muon momentum for the NEUT MC and Data Run II-IV are shown in Figure 8.23.

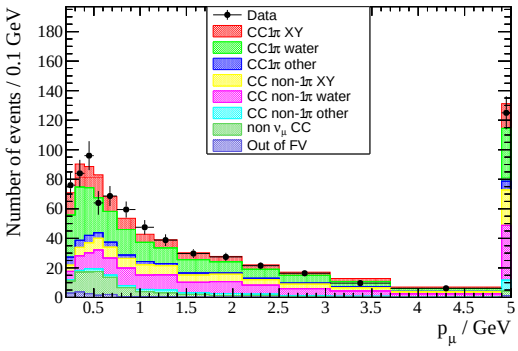

(a) CC1π^+ water-enhanced sample.

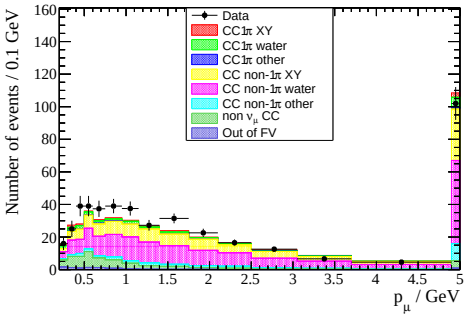

(b) CC Other sideband sample.

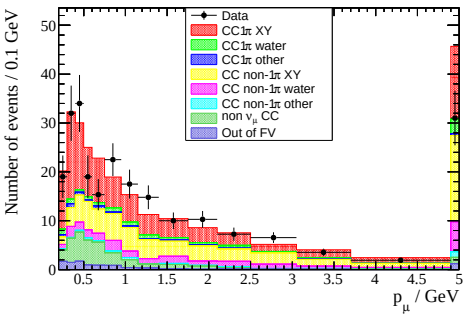

(c) Scintillator sideband sample.

Figure 8.23: p_μ distributions: Data/MC comparison.

The differential results are shown in Figure 8.24. Apart from a fluctuation seen at $0.5 < p_\mu < 0.6\,\text{GeV}$, the unfolded data are compatible with the NEUT prediction and mostly lower than the GENIE prediction.

Table 8.12 and Figure 8.25 show the fractional error in % per each error source. Only the total detector error is presented in the table, but the components can be seen in the bottom plot in Figure 8.25.

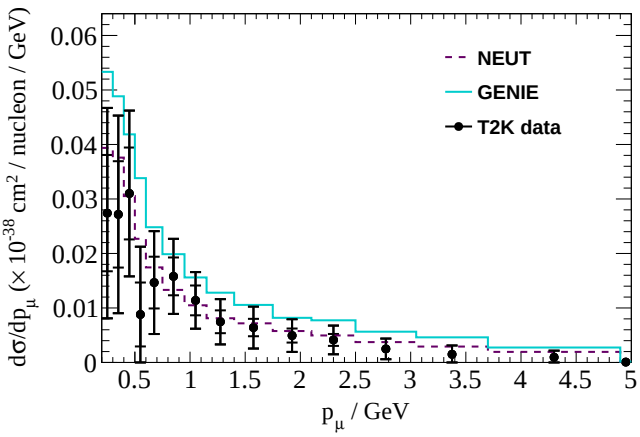

Figure 8.24: Differential cross-section obtained unfolding p_{μ^-}.

Table 8.12: Fractional error (in %) when unfolding p_{μ^-} using the Data Run II-IV sample.

	Fractional error in %					
p_{μ^-} binning (GeV)	Data stat.	MC stat.	Cross-section uncertainty	Final state interactions	Flux uncertainty	Detector uncertainty
0-0.3	37.38	10.91	43.92	15.88	33.14	12.88
0.3-0.4	34.41	10.28	41.19	15.85	32.47	12.71
0.4-0.5	25.87	8.36	26.18	10.16	27.48	11.12
0.5-0.6	63.25	20.96	98.01	17.86	68.75	29.45
0.6-0.75	30.83	9.93	39.66	4.49	35.87	14.72
0.75-0.95	20.82	7.01	23.08	6.53	27.31	9.91
0.95-1.15	22.75	7.70	23.02	11.18	27.04	10.92
1.15-1.4	26.74	8.46	34.31	8.17	29.98	12.80
1.4-1.75	23.71	7.70	43.74	7.65	30.24	10.24
1.75-2.1	24.73	8.34	43.23	8.01	31.73	8.66
2.1-2.5	25.06	8.43	45.89	8.65	32.86	9.83
2.5-3.05	30.03	9.76	54.39	13.74	37.76	14.87
3.05-3.7	35.22	11.85	79.95	20.33	54.20	24.36
3.7-4.9	40.88	12.44	91.05	24.47	68.36	25.57
>4.9	39.19	11.85	75.64	17.90	58.15	17.78

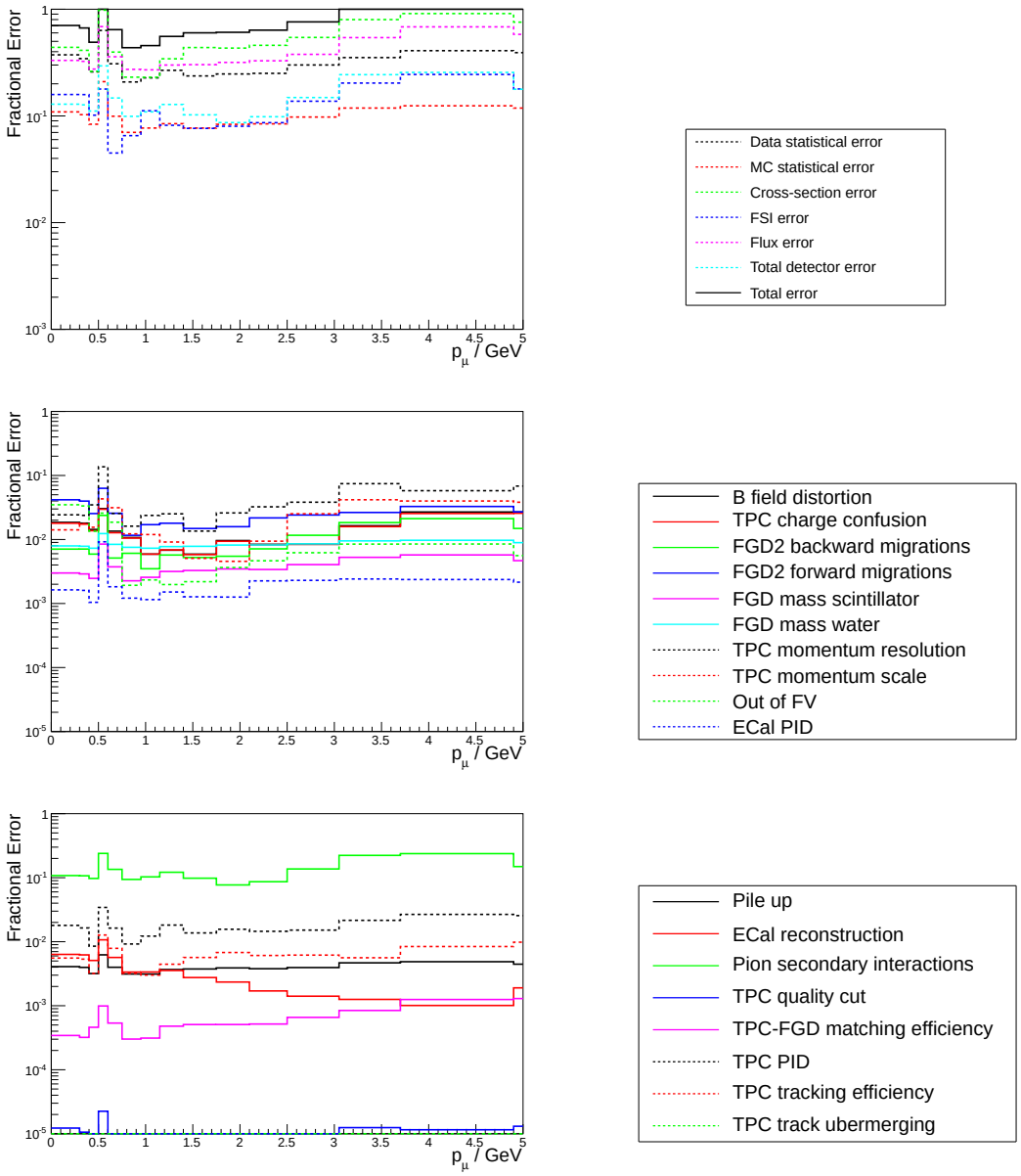

Figure 8.25: Total and fractional error components as a function of the p_μ binned distribution are shown in the upper plots. The lower plot shows the contributions of the different detector errors.

8.4.4 Muon $\cos\theta$

The pre-unfolding distributions of the muon angle for the NEUT MC and Data Run II-IV are shown in Figure 8.26.

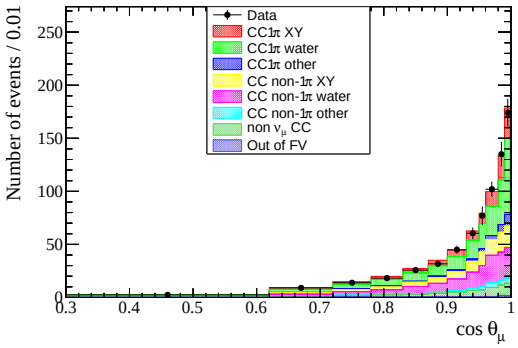

(a) CC1π^+ water-enhanced sample.

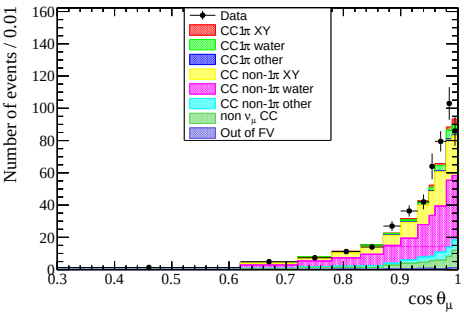

(b) CC Other sideband sample.

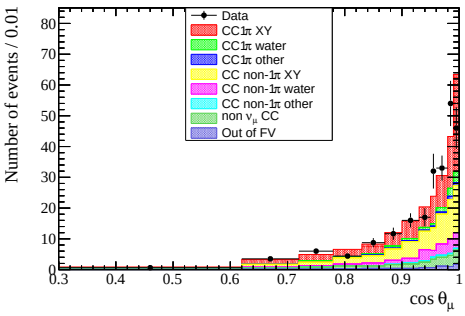

(c) Scintillator sideband sample.

Figure 8.26: $\cos\theta_\mu$ distributions: Data/MC comparison.

The differential results are shown in Figure 8.27. NEUT and GENIE both reproduce well the unfolded data shape. The results are compatible with the NEUT prediction in all bins and are $\approx 1.5\sigma$ lower than the GENIE prediction in most bins.

Table 8.13 and Figure 8.28 show the fractional error in % per each error source. Only the total detector error is presented in the table, but the components can be seen in the bottom plot in Figure 8.28.

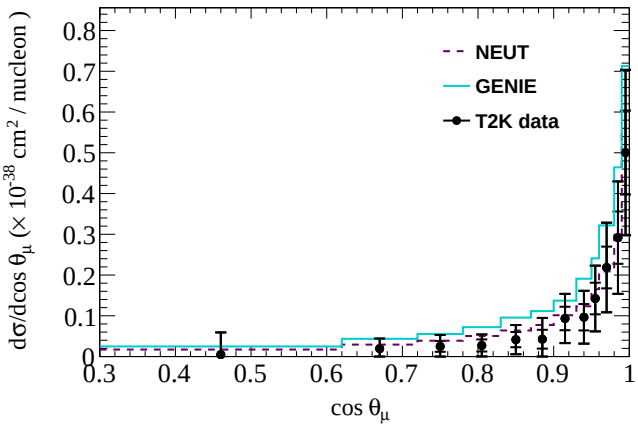

Figure 8.27: Differential cross-section obtained unfolding the $\cos\theta_{\mu^-}$. Data from Run II to Run IV is used for the unfolding.

Table 8.13: Fractional error (in %) when unfolding $\cos\theta_{\mu^-}$ using the Data Run II-IV sample.

	Fractional error in %					
$\cos\theta_{\mu^-}$ binning	Data stat.	MC stat.	Cross-section uncertainty	Final state interactions	Flux uncertainty	Detector uncertainty
0.30-0.62	130.1	37.55	979.9	350.1	424.3	42.17
0.62-0.72	51.49	15.49	97.40	16.99	54.70	17.44
0.72-0.78	50.87	15.66	80.81	22.48	50.38	14.59
0.78-0.83	52.13	15.65	63.72	18.85	47.03	14.60
0.83-0.87	43.07	12.80	58.13	17.78	40.66	9.84
0.87-0.90	51.97	15.70	87.45	38.97	52.94	12.36
0.90-0.93	29.46	9.17	42.25	15.02	33.91	8.27
0.93-0.95	31.99	10.07	43.92	12.66	34.95	8.82
0.95-0.96	25.81	8.68	35.55	8.63	32.70	7.55
0.96-0.98	22.36	7.04	30.34	5.92	31.21	7.14
0.98-0.99	20.92	6.81	28.20	4.44	29.56	7.94
0.99-1	19.59	6.31	22.44	5.75	24.85	8.11

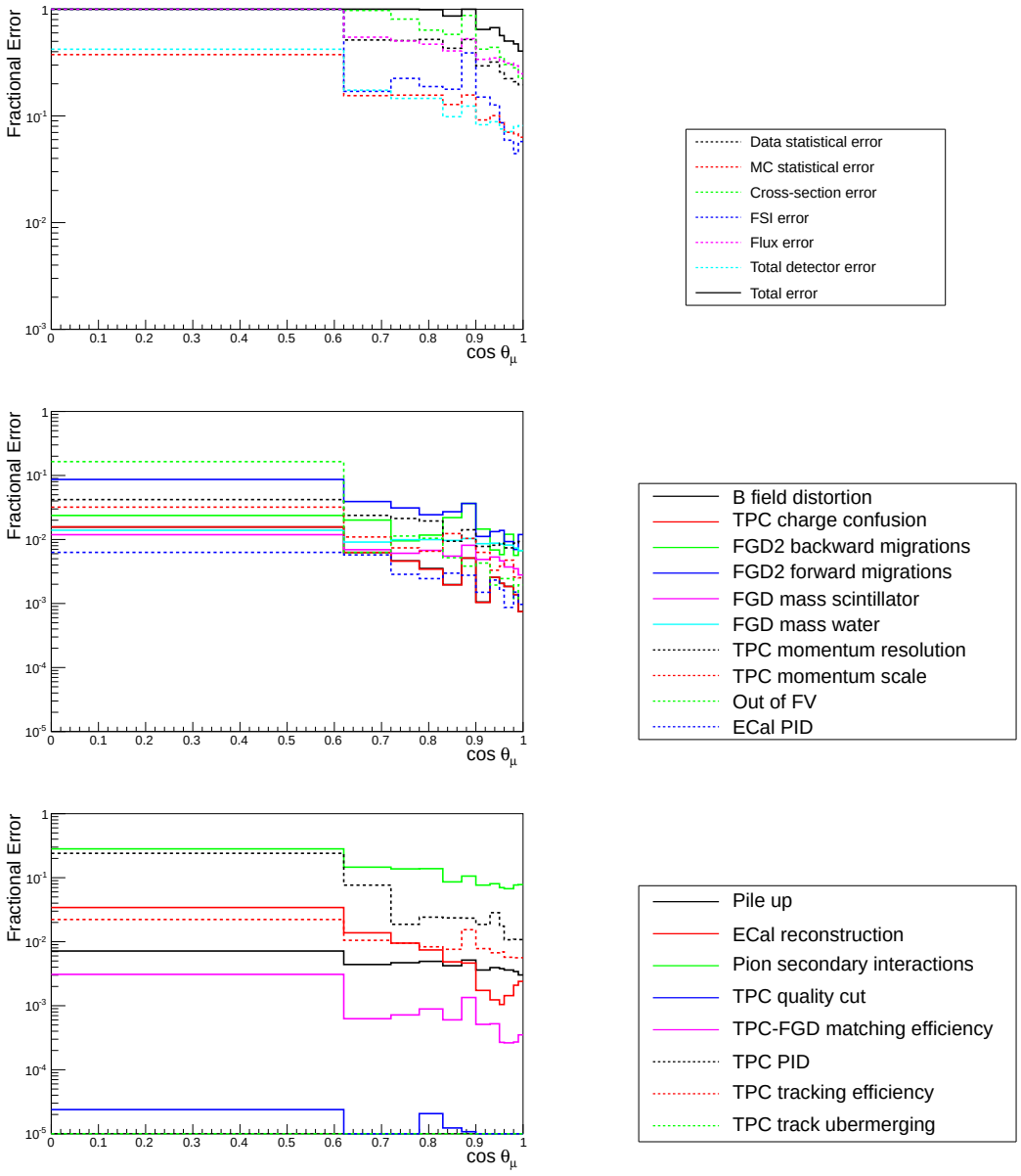

Figure 8.28: Total and fractional error components as a function of the $\cos\theta_\mu$ binned distribution are shown in the upper plots. The lower plot shows the contributions of the different detector errors.

8.4.5 Muon-Pion $\cos\theta$

The pre-unfolding distributions of the muon-pion angle for the NEUT MC and Data Run II-IV are shown in Figure 8.29.

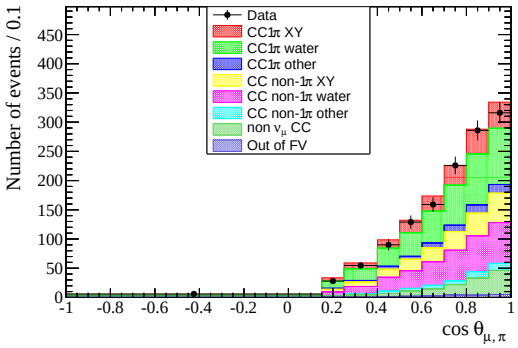

(a) CC1π^+ water-enhanced sample.

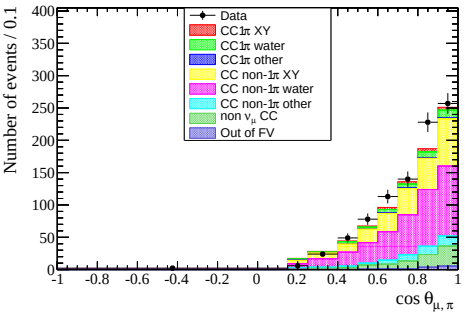

(b) CC Other sideband sample.

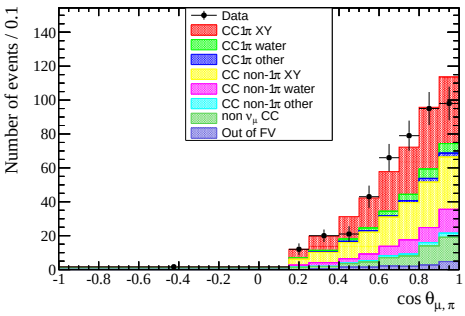

(c) Scintillator sideband sample.

Figure 8.29: $\cos\theta_{\mu,\pi}$ distributions: Data/MC comparison.

The differential results are shown in Figure 8.30. Even in this case, the results are compatible with the NEUT prediction and 1-1.5σ lower than the GENIE prediction. Table 8.14 and Figure 8.31 show the fractional error in % per each error source. Only the total detector error is presented in the table, but the components can be seen in the bottom plot in Figure 8.31.

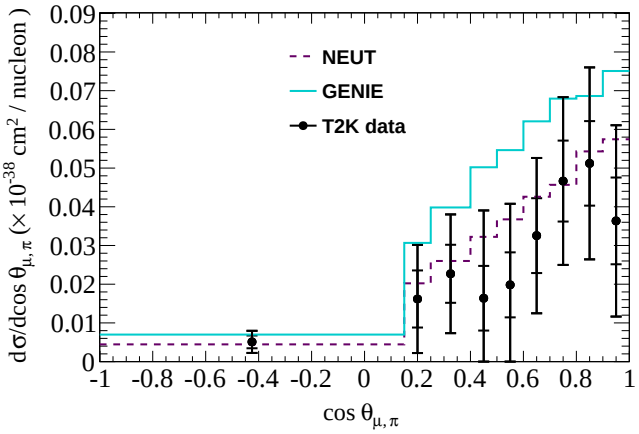

Figure 8.30: Differential cross-section obtained unfolding $\cos\theta_{\mu,\pi^+}$. Data from Run II to Run IV is used for the unfolding.

Table 8.14: Fractional error (in %) when unfolding $\cos\theta_{\mu,\pi^+}$ using the Data Run II-IV sample.

	Fractional error in %					
$\cos\theta_{\mu^-,\pi^+}$ binning	Data stat.	MC stat.	Cross-section uncertainty	Final state interactions	Flux uncertainty	Detector uncertainty
-1-0.15	30.88	9.54	34.33	5.29	26.39	14.22
0.15-0.25	43.68	13.05	63.35	8.44	32.96	14.03
0.25-0.4	31.56	9.78	48.30	8.08	31.34	9.95
0.4-0.5	48.83	14.72	114.7	23.13	51.13	16.58
0.5-0.6	40.41	12.68	80.35	25.70	44.92	14.95
0.6-0.7	28.40	8.69	40.90	8.99	32.17	11.30
0.7-0.8	21.38	6.73	27.67	5.80	28.31	7.34
0.8-0.9	20.27	6.61	28.50	7.81	30.47	9.36
0.9-1	29.43	9.17	39.51	13.93	41.69	13.38

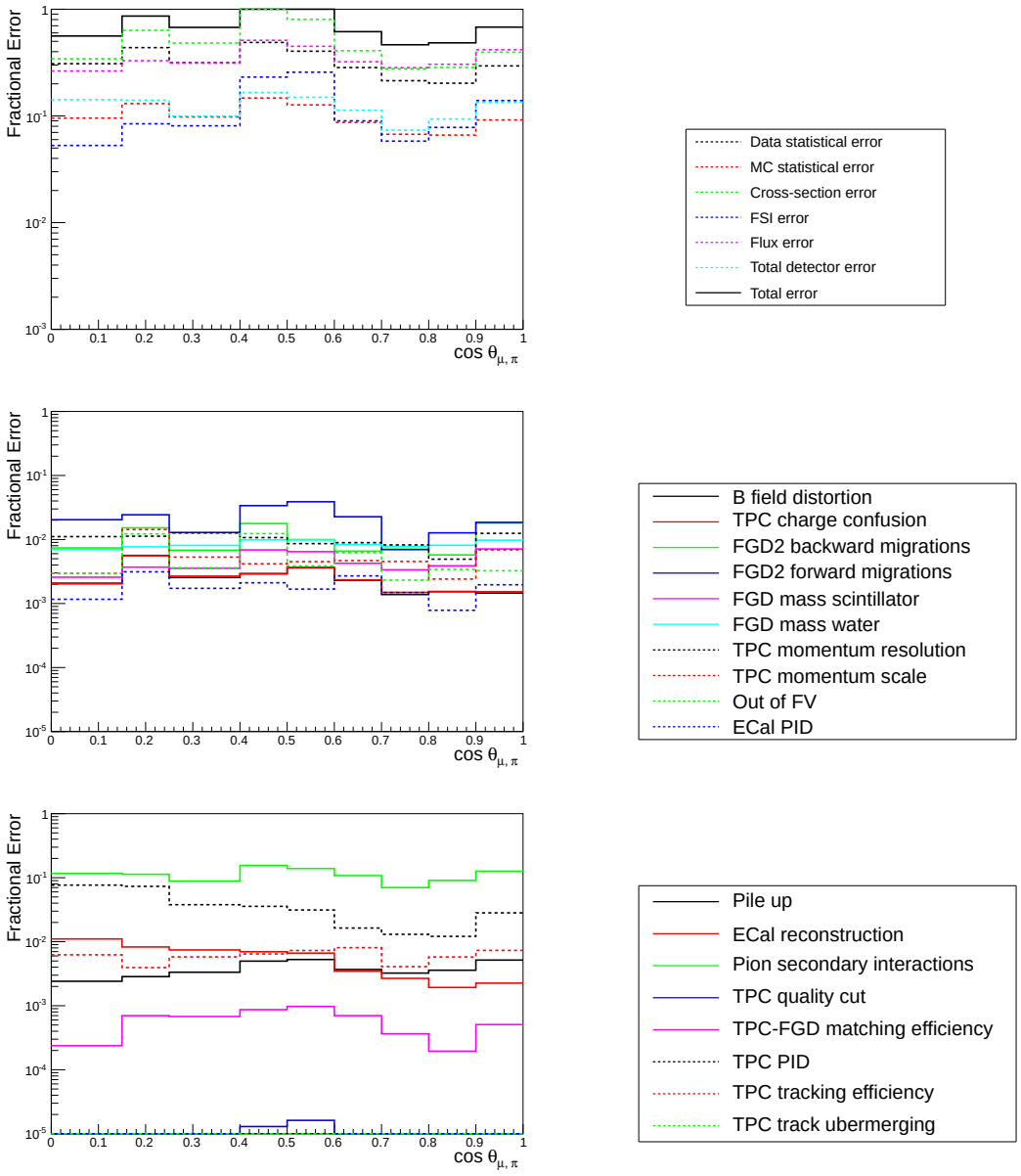

Figure 8.31: Total and fractional error components as a function of the $\cos\theta_{\mu,\pi^+}$ binned distribution are shown in the upper plots. The lower plot shows the contributions of the different detector errors.

8.4.6 Neutrino energy reconstructed with Δ resonance

For the neutrino energy variables the flux averaged cross-section $\sigma(E)$, is presented, with the neutrino energy reconstructed according to the two formulae presented in Equations 6.8 and 6.9, unfolded to the true NEUT prediction.

The pre-unfolding distributions of the reconstructed neutrino energy using the Δ resonance formula for the NEUT MC and Data Run II-IV are shown in Figure 8.32.

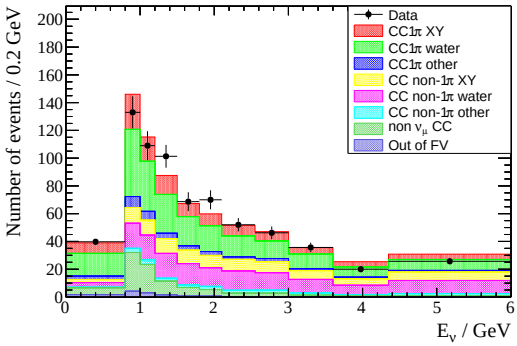

(a) CC1π^+ water-enhanced sample.

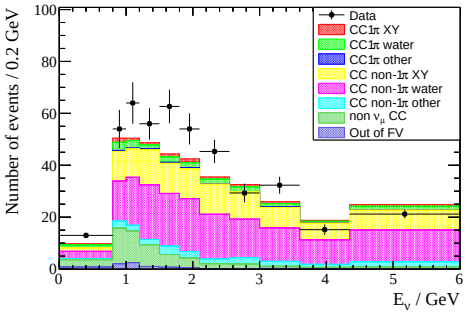

(b) CC Other sideband sample.

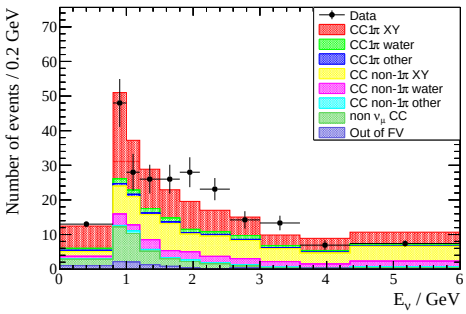

(c) Scintillator sideband sample.

Figure 8.32: $E_{\nu,\Delta}$ distributions: Data/MC comparison.

The $\sigma(E)$ results are shown in Figure 8.33, with the results being compatible with NEUT in all bins and lower than the GENIE prediction at $E_\nu > 3\,\text{GeV}$.

Table 8.15 and Figure 8.34 show the fractional error in % per each error source. Only the total detector error is presented in the table, but the components can be seen in the bottom plot in Figure 8.34.

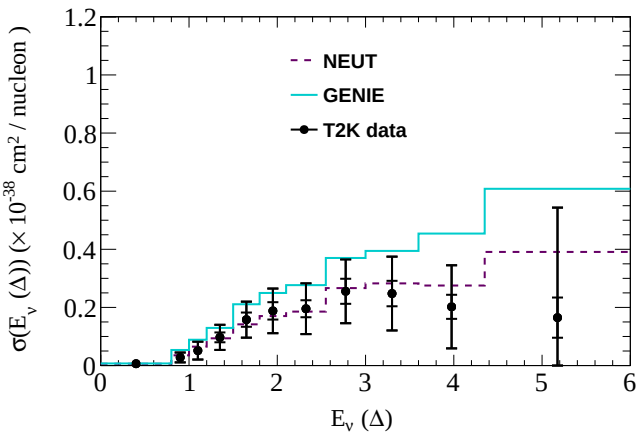

Figure 8.33: Cross-section as a function of the reconstructed neutrino energy $E_{\nu\ \mathrm{REC}\ \Delta}$. Data from Run II to Run IV is used for the unfolding.

Table 8.15: Fractional error (in %) when unfolding $E_{\nu\ \mathrm{REC}\ \Delta}$ using the Data Run II-IV sample.

	Fractional error in %					
E_ν binning (GeV)	Data stat.	MC stat.	Cross-section uncertainty	Final state interactions	Flux uncertainty	Detector uncertainty
0-0.8	19.55	6.29	27.51	8.41	27.49	11.20
0.8-1	21.34	6.90	42.48	11.58	33.85	11.32
1-1.2	22.66	7.55	40.02	7.72	34.78	11.65
1.2-1.5	16.40	5.94	26.64	5.39	28.52	11.52
1.5-1.8	14.41	5.76	22.59	5.28	25.80	9.77
1.8-2.1	14.71	5.99	26.18	5.58	25.22	7.91
2.1-2.55	13.83	5.67	31.74	5.69	25.89	7.72
2.55-3	15.80	5.92	26.38	6.07	27.60	8.35
3-3.6	16.59	6.06	35.30	6.05	30.86	9.05
3.6-4.35	19.23	7.10	53.40	11.28	38.46	11.35
> 4.35	40.09	12.39	190.1	33.94	113.3	29.16

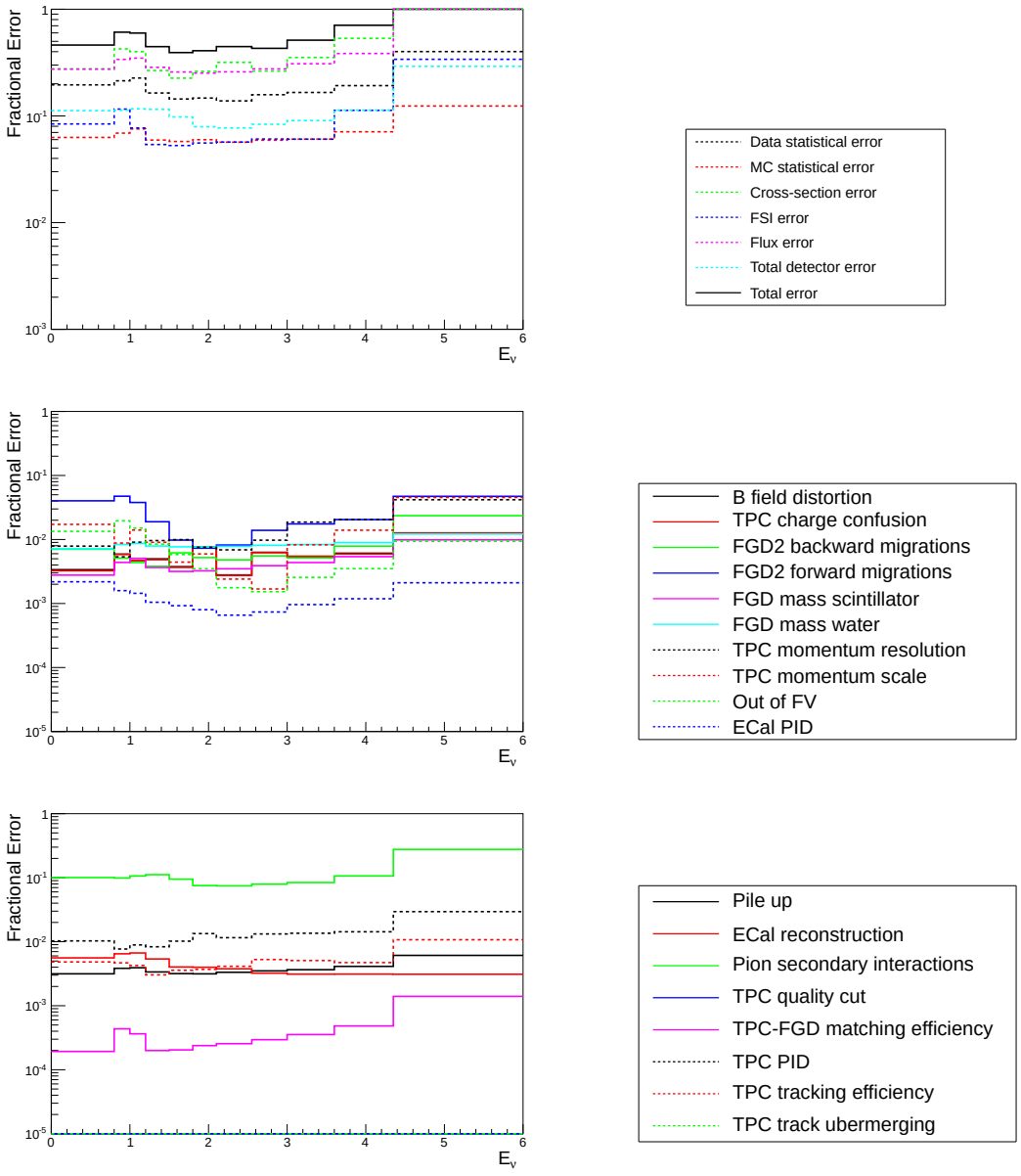

Figure 8.34: Total and fractional error components as a function of the $E_{\nu\ \mathrm{REC}\ \Delta}$ binned distribution are shown in the upper plots. The lower plot shows the contributions of the different detector errors.

8.4.7 Neutrino energy reconstructed with MiniBooNE formula

The pre-unfolding distributions of the reconstructed neutrino energy using the MiniBooNE formula for the NEUT MC and Data Run II-IV are shown in Figure 8.35.

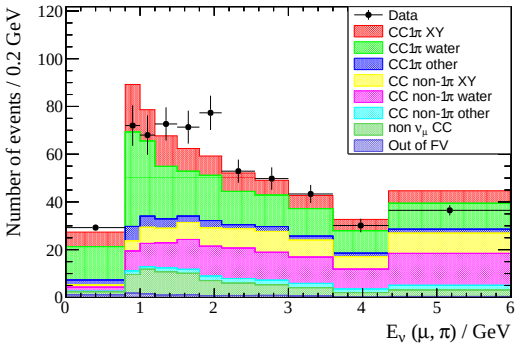

(a) CC1π^+ water-enhanced sample.

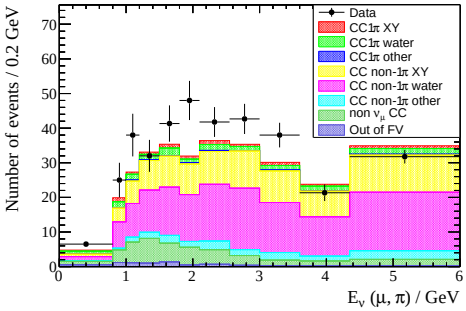

(b) CC Other sideband sample.

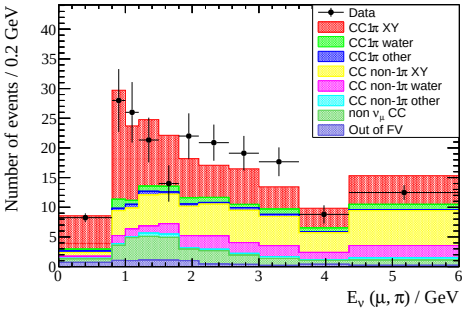

(c) Scintillator sideband sample.

Figure 8.35: $E_{\nu,\text{MiniBooNE}}$ distributions: Data/MC comparison.

The $\sigma(E)$ cross-section results are shown in Figure 8.36. The cross-section results are compatible with both the NEUT and GENIE prediction (only one bin shows a cross-section value 1.5σ lower than the GENIE prediction). Table 8.16 and Figure 8.37 show the fractional error in % per each error source. Only the total detector error is presented in the table, but the components can be seen in the bottom plot in Figure 8.37.

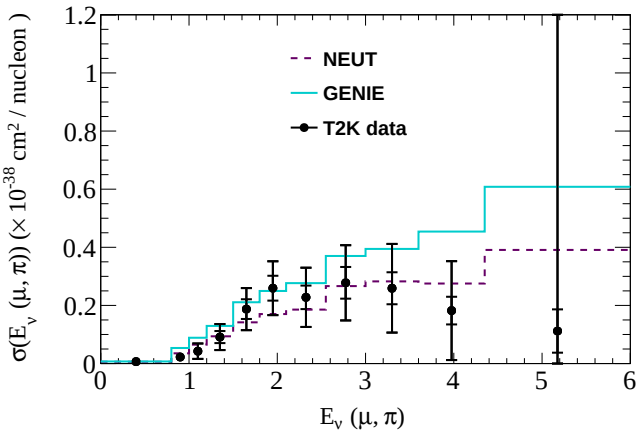

Figure 8.36: Cross-section as a function of the reconstructed neutrino energy $E_{\nu\ \mathrm{REC,\ MB}}$. Data from Run II to Run IV is used for the unfolding.

Table 8.16: Fractional error (in %) when unfolding $E_{\nu\ \mathrm{REC,\ MB}}$ using the Data Run II-IV sample.

	Fractional error in %					
E_ν binning (GeV)	Data stat.	MC stat.	Cross-section uncertainty	Final state interactions	Flux uncertainty	Detector uncertainty
0-0.8	20.20	6.63	20.85	6.05	22.80	6.62
0.8-1	26.70	8.09	42.84	13.75	29.97	7.87
1-1.2	28.38	8.99	40.67	11.43	32.78	12.35
1.2-1.5	21.61	7.21	30.12	8.00	28.28	10.94
1.5-1.8	16.93	6.44	21.94	4.15	23.84	10.02
1.8-2.1	15.25	6.29	19.26	5.08	22.47	10.16
2.1-2.55	16.54	6.48	30.35	5.87	25.13	9.96
2.55-3	18.42	6.77	28.56	6.36	29.01	9.38
3-3.6	20.10	6.86	41.45	9.08	33.64	9.17
3.6-4.35	24.77	8.27	70.84	19.71	49.49	13.40
> 4.35	63.92	18.70	832.2	206.3	500.5	45.53

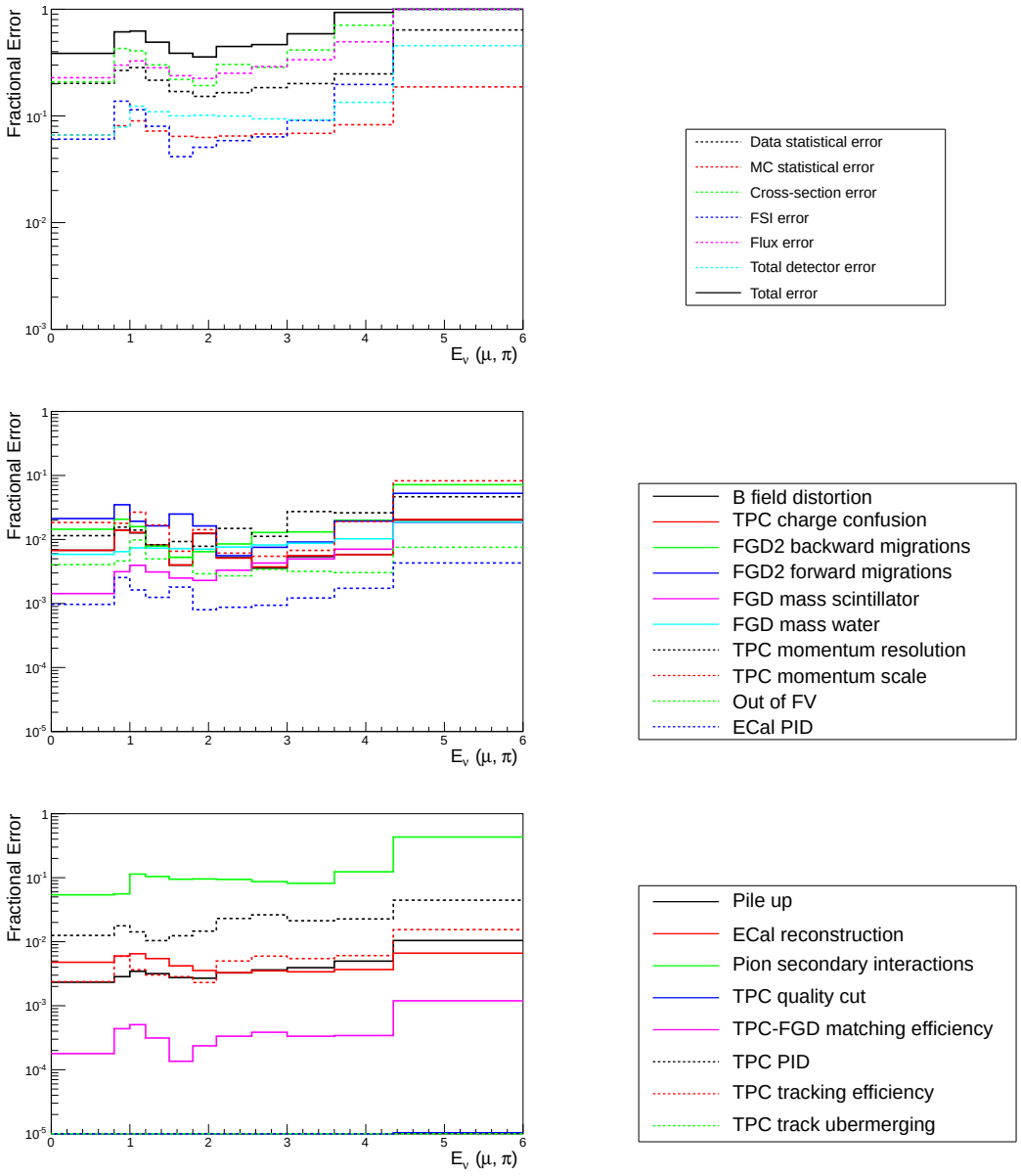

Figure 8.37: Total and fractional error components as a function of the $E_{\nu\ \mathrm{REC,\ MB}}$ binned distribution are shown in the upper plots. The lower plot shows the contributions of the different detector errors.

8.5 Discussion

The CC single pion production cross-section on water is evaluated with a Bayesian unfolding method using 1 iteration. Section 8.4 highlights the cross-sections unfolded using the T2K data from Run II-IV and starting from the nominal NEUT distribution.

The background is constrained by using two control regions. The normalisation constant found from the CC1π^+ control region is $\alpha_{SCINT} = 0.9831$, indicating that the scintillator background is slightly less than the amount predicted by NEUT. The normalisation constant related to the CC Other background is $\alpha_{CCOTHER} = 1.0836$, meaning that the CC Other interactions are slightly more in data than in the MC. These two constants are used to re-normalise the background, and hence constrain the systematic uncertainties.

Table 8.9 shows the total averaged cross-sections, which differ slightly depending on which variable is used for the unfolding. This is expected because of the different efficiency of the various variables. Nonetheless all the results are compatible with each other (within statistical uncertainties), and with the NEUT prediction ($\sigma_{\mathrm{t,NEUT}} = 3.795 \times 10^{-40}\mathrm{cm}^2/\mathrm{Nucleon}$). The GENIE prediction is slightly higher ($\sigma_{\mathrm{t,GENIE}} = 5.493 \times 10^{-40}\mathrm{cm}^2/\mathrm{Nucleon}$) and the total cross-sections extracted from the muon kinematics are more than $1\,\sigma$ away from it.

The main uncertainties related to CC1π^+ cross-section measurement are the flux and theory cross-section uncertainties, which are both around 30% for all the variables used in the unfolding. In the future the flux uncertainties should be reduced by using more data from the NA61 experiment in the flux prediction. The theory cross-section systematic uncertainties could be reduced by unfolding the signal and control regions simultaneously. This technique will allow to control the signal and other backgrounds leaking in the control regions. As more data will be available, the data statistical uncertainties will also be reduced in the future. The detector systematic uncertainties are dominated by the pion secondary interactions, TPC PID and FGD forward migration systematics. Future analysis might consider the use of the FGD2 and FGD1 samples simultaneously, and hence eliminating the necessity to divide the FGD2 sample in the x and y layers.

The single differential cross-section results are, in general, compatible with the NEUT prediction and 1.5σ lower than the GENIE prediction. At low pion momen-

tum and high pion scattering angle, the results show a small suppression compared to the NEUT prediction. The CC coherent interactions represent the 14.1% of the true CC1π^+ sample, and they are expected to produce forward-going pions. The MINERνA experiment reported a large suppression of CC coherent interactions at low E_π compared to the NEUT prediction, which could explain the suppression seen in the data. Appendix B shows the results from unfolding the Run II-IV data when starting from MC NEUT distributions with reweighted CC interactions according to the MINERνA experiment results. The results with this method differ very slightly from the ones presented in this Chapter and still show the suppression at high $\cos\theta_\pi$.

The GENIE prediction can also be used to compare these these results to the MiniBooNE and MINERνa ones in Figure 2.7, even though MiniBooNE and MINERνa have access to lower momentum pions ($p_\pi = 0.3\,\text{GeV}$ implies $T_\pi = 0.32\text{GeV}$). The T2K data are 1.5σ lower than the GENIE prediction, which is compatible with MINERνa sees, whereas the MiniBooNE data points sit higher than the GENIE prediction.

The muon kinematics results are compatible with the NEUT prediction. The GENIE prediction reproduces well the shape of the unfolded data but the normalisation is about 1.5σ higher.

The flux averaged single differential cross-sections as a function of the neutrino energy, with both the formulae used, are compatible with both the NEUT and GENIE prediction.

9

Looking at the future: Hyper-Kamiokande

As introduced in Chapter 2, future long baseline experiments will have the sensitivity to discover CP violation in the lepton sector and resolve the octant ambiguity in the measurement of θ_{23}. Hyper-Kamiokande (Hyper-K) is a proposed water Cherenkov detector, the natural successor of SK. Hyper-K will serve a wide spectrum of physics topics, from the detection of supernova neutrinos, to the study of solar and atmospheric neutrinos, and the search for proton decay. Similarly to T2K, Hyper-K can act as far detector of a long baseline neutrino experiment using a neutrino beam from J-PARC [12, 98].

Hyper-K is scheduled to start construction in 2019 and data-taking in 2025.

Section 9.1 describes the Hyper-Kamiokande experiment, including upgrades from the current T2K setup. Section 9.2 presents the expected observables at Hyper-K. The analysis tools used for the physics potential studies are described in Section 9.3.

9.1 Experimental setup

The experimental setup will be similar to that of the T2K experiment. A highly pure beam of muon (anti-)neutrinos will be produced at the J-PARC accelerator. A set of near detectors at 280 m and possibly also at 1-2 km distance from the beam target will measure the flux and cross-section of the neutrinos produced. The intermediate detector

at 1-2 km will see a neutrino flux more similar to the one at the far detector. Finally Hyper-Kamiokande, 295 km away from the production, will detect the disappearance of muon (anti-)neutrinos and the appearance of electron (anti-)neutrinos with the aim of setting more stringent limits on the oscillation parameters and discovering CP violation.

9.1.1 Upgraded neutrino beamline

Section 3.1 presented the current features of the beamline used by the T2K experiment. Upgraded facilities at J-PARC will deliver a higher beam power (anti)neutrino beam to Hyper-K.

A first phase of upgrade is scheduled for the next few years [99], consisting in replacing the magnet power supplies, replacing the radio frequency system, and upgrading the injection/extraction devices. This will allow the J-PARC accelerator to reach the design power 750 kW.

Raising the top energy of the rapid-cycling synchrotron, and enlarging the main ring aperture are some of the features under study to reach 1$\sim$2 MW beam power.

9.1.2 Near and intermediate detectors

The near detectors at 280 m, INGRID (see Section 3.2) and ND280 (see Section 3.3) will be refurbished and possibly upgraded.

The proposed upgrades include:

- the substitution of the water targets in FGD2 with heavy water (D_2O). A subtraction analysis of heavy water data with the water data will allow the extraction of the neutrino cross-section on the "quasi" free neutron of deuterium.

- the use of water-based liquid scintillator (WbLS) developed at BNL [100]. A WbLS will allow to study neutrino interactions on water with the precise reconstruction capabilities of a scintillator.

- the use of a high pressure TPC [101], containing various noble gases (He, Ne, Ar). Serving both as target and tracking medium, a high-pressure TPC will allow studies on the cross-sections of different materials as well as test our model of final state interactions.

The largest uncertainty on the neutrino cross-section models come from nuclear effects, that could be better understood with an additional intermediate water Cherenkov detector. A water Cherenkov detector at 280 m would be too close to the neutrino production causing pile-up between interactions in the same bunch. Hence the preferred location would be at 1–2 km from the the neutrino production.

Distinguishing neutrino and antineutrino interactions in a water Cherenkov detector is not easy, because it cannot resolve the charge of leptons (i.e. distinguish μ^+ from μ^-). Adding Gadolinium to the water would make it possible to detect neutrons and make the separations possible. Other strategies involve the use of WbLS compounds to detect protons, or the construction of a magnetised tracking detector in conjunction with the water Cherenkov detector.

There are two conceptual designs for the intermediate detector:

- The Tokai Intermediate Tank for the Unoscillated Spectrum (TITUS) is a 2 kton off-axis water Cherenkov detector at 2 km from the target. The baseline is optimised to see the same fluxes of NC and ν_e backgrounds as Hyper-K. A muon range detector could help detecting the high momentum tail of the muon spectrum and Gadolinium would be used to separate ν and $\bar{\nu}$ interactions.

- The νPRISM [102] detector is a 50 m tall water Cherenkov detector located at 1 km from the target. Spanning an off-axis angle of 1–4°, it can see different neutrino energy spectra peaking between 0.4 and 1 GeV. These spectra can be used to link the incoming neutrino energy and the outgoing lepton kinematics, consequently reducing the uncertainties on the interaction cross-section models.

9.1.3 Hyper-Kamiokande

Hyper-Kamiokande will be the third generation water Cherenkov detector in Kamioka, with a total (fiducial) mass of 1 (0.56) million tons, equivalent to 20 (25) times that of Super-Kamiokande.

The candidate site will be at the Tochibora mine in Kamioka town (Gifu, Japan), keeping the same distance (295 km) from the production target and off-axis angle (2.5°) as those of the T2K experiment.

The Hyper-K detector is composed of two separated caverns, as shown in Figure 9.1, each having an egg-shape cross-section 48 meters wide, 54 meters tall, and 250 meters

long. Segmentation walls located every 49.5 m form 5 separate compartments for each tank. Each compartment is optically separated and can run event triggering and reconstruction independently from the others.

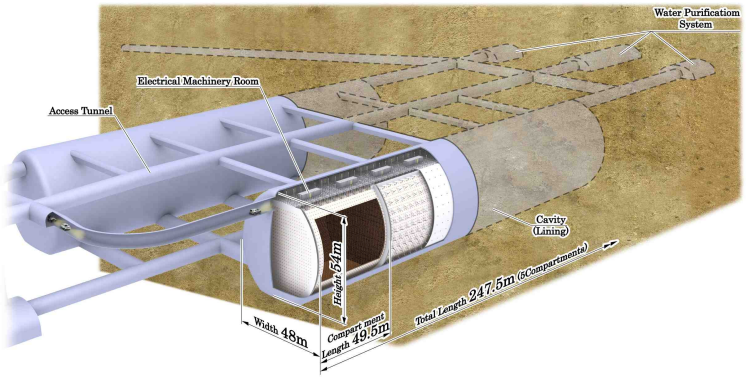

Figure 9.1: Schematic view of the Hyper-Kamiokande detector [98].

The inner region is viewed by 99,000 20-inch PMTs, giving a 20% photocatode coverage. The outer region is equipped with 25,000 8-inch PMTs. Similarly to Super-K (as seen in Subsection 3.4), the outer region provides a veto to reject the cosmic ray muon background.

The total water mass of the inner region is 0.74 million tons and the total fiducial mass is 10 times 0.056 = 0.56 million tons, where the fiducial volume is defined by a virtual boundary located 2 m away from the inner PMT plane.

The Tochibora site has 648 m rock overburden, meaning that the cosmic-ray muon rate is $\sim 8 \times 10^{-7}$ sec^{-1}cm^{-2} which is roughly 5 times larger than the flux at the Super-K location ($\sim 1.5 \times 10^{-7}$ sec^{-1}cm^{-2}), due to the shallower location. Nonetheless, the expected pile-up is less than 1% and it is negligible for long baseline experiments, as well as nucleon decay searches and atmospheric neutrino studies.

The EGADS (Evaluating Gadolinium's Action on Detector Systems) project [103] in Kamioka is performing a feasibility study on adding Gadolinium to Super-K (and thus it could be useful also for Hyper-K), that will allow to tag neutrons and consequently enhance the physics capability of the experiment.

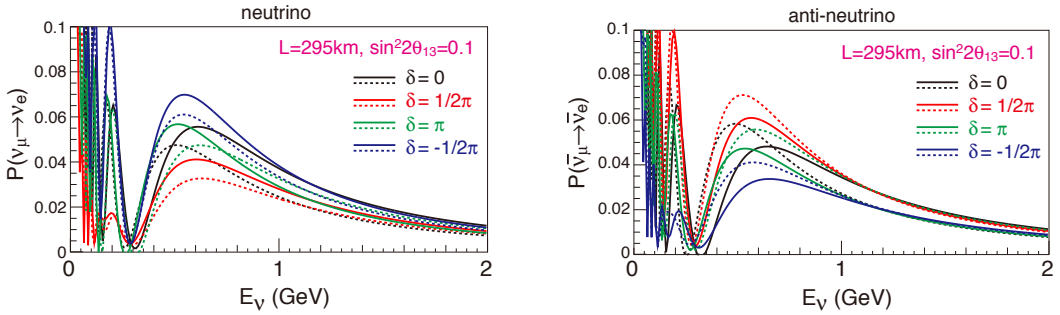

(a) $\nu_\mu \to \nu_\mathrm{e}$ transitions.

(b) $\overline{\nu}_\mu \to \overline{\nu}_\mathrm{e}$ transitions.

Figure 9.2: Oscillation probabilities as a function of the neutrino energy, considering a baseline of 295 km and $\sin^2 2\theta_{13} = 0.1$. Black, red, green, and blue lines correspond to $\delta_{CP} = 0, 90°, 180°$, and $-90°$, respectively [12].

A new reconstruction algorithm developed for Super-K/T2K, ("fiTQun") is used for the Hyper-K studies. *fiTQun* is a maximum likelihood fit that evaluates charge and time probability density functions for each PMT hit assuming several sets of physics variables (such as vertex, direction, momentum, and particle type) [53].

Reference [12] compares the performance of Hyper-K with that of SK-II (20% photocatode coverage) and SK-IV (40% photocatode coverage), concluding that the new reconstruction algorithm gives to Hyper-K a reconstruction performance similar or possibly better than both SK-II and SK-IV.

9.2 Analysis framework

As seen in Chapter 2, the observation of electron neutrino appearance in a muon neutrino beam could lead to the discovery of CP violation in the lepton sector.

Figure 9.2 shows the electron (anti-)neutrino appearance probabilities ($\nu_\mu \to \nu_\mathrm{e}$ in Figure 9.2a and $\overline{\nu}_\mu \to \overline{\nu}_\mathrm{e}$ in Figure 9.2b as a function of the true neutrino energy for a baseline of 295 km, where the solid line indicates normal mass ordering ($\Delta m^2_{32} > 0$) and the dashed line indicates inverted mass ordering ($\Delta m^2_{32} < 0$). By comparing neutrinos and antineutrinos results, one can see the effect of δ_{CP}.

For the sensitivity studies presented in this Thesis, the mass ordering is assumed to be known. A number of experiments plan to determine the mass ordering before

Table 9.1: Oscillation parameters used for the sensitivity analysis and treatment in the fit. The *nominal* values are used for figures and numbers in this section, unless otherwise stated.

Parameter	Nominal value	Treatment
$\sin^2 2\theta_{13}$	0.10	Fitted
δ_{CP}	0	Fitted
$\sin^2 \theta_{23}$	0.50	Fitted
Δm^2_{32}	2.4×10^{-3} eV^2	Fitted
Mass ordering	Normal or Inverted	Fixed
$\sin^2 2\theta_{12}$	0.8704	Fixed
Δm^2_{21}	7.6×10^{-5} eV^2	Fixed

Hyper-K will start data-taking in 2025. If that is not the case, the strategy of Hyper-K is to combine the atmospheric and the accelerator neutrino measurements to resolve this ambiguity (see Subsection 9.3.3).

These studies assume an integrated beam power of 7.5 MW$\times 10^7$ sec[1] (corresponding to 1.56×10^{22} protons on target with a 30 GeV J-PARC beam), which could be reach in 10 years with a 0.75 kW beam, or less with higher beam power. It was found that the sensitivity to δ_{CP} is independent of the ν:$\bar{\nu}$ running mode ratio, if ν:$\bar{\nu}$ is between 1:1 and 1:5 (this is because the Hyper-K sensitivity is limited by systematic uncertainties but not by statistical uncertainties). A 1:3 ratio is chosen to have a similar number of expected ν_e ($\overline{\nu}_e$) appearance events in neutrino and antineutrino running modes.

Table 9.1 shows the nominal oscillation parameters used and their treatment in the fit (see Section 9.2.2 for a description of the fitting method).

9.2.1 Expected observables at Hyper-K

The performance of Hyper-K in detecting neutrinos from the J-PARC beam is expected to be similar to that of Super-K. Therefore, the same tools for the neutrino simulation (NEUT [73]), detector response (GEANT3 [70]) and reconstruction are used. The upgrade in electronics and DAQ system is also taken into account.

[1] 1 year of J-PARC beam is considered 10^7 seconds.

The selection criteria for the ν_e appearance and ν_μ disappearance analyses are those developed for the Super-K and T2K experiments. Both selections require the events to be fully contained (FC) with a reconstructed vertex inside the fiducial volume (FV) and visible energy (E_{vis}) greater then 30 MeV. In addition, events with a single Cherenkov ring are required in order to select CCQE interactions.

The incoming neutrino energy can be reconstructed from the lepton kinematics assuming a CCQE interaction and considering the 4-momentum consertation:

$$E_\nu^{rec} = \frac{2(m_n - V)E_l + m_p^2 - (m_n - V)^2 - m_l^2}{2(m_n - V - E_l + p_l \cos\theta_l)}, \tag{9.1}$$

where m_n, m_p, m_l are the mass of neutron, proton, and charged lepton, respectively; p_l is the charged lepton momentum; V is the nuclear potential energy (27 MeV); and θ_l is the angle between the charged lepton and the neutrino direction.

The ν_e and $\bar{\nu_e}$ appearance analyses also apply these criteria:

- the ring likelihood is reconstructed as electron-like (e-like);
- $E_{\rm vis} > 100\,{\rm MeV}$;
- there is no decay electron associated to the event;
- $E_\nu^{rec} < 1.25\,{\rm GeV}$;
- the *fiTQun* algorithm is used to further eliminate π^0 background, as described in Reference [54].

Figure 9.3 shows the reconstructed neutrino energy distributions of ν_e and $\overline{\nu}_e$ candidate events. The expected number of events, divided into the different neutrino and antineutrino components, is shown in Table 9.2. In the neutrino mode, the dominant background component is intrinsic ν_e contamination in the beam. The improved *fiTQun* algorithm manages to suppress the NCπ^0 events to 30% with respect to previous analyses. In the antineutrino mode, the wrong sign background (i.e. ν_e and ν_μ) have significant contributions due to larger fluxes and cross-sections compared to the $\overline{\nu}_e$ and $\overline{\nu}_\mu$ background in the neutrino mode.

The ν_μ and $\overline{\nu}_\mu$ disappearance analyses also apply these criteria:

- the ring likelihood is reconstructed as as muon-like (μ-like);

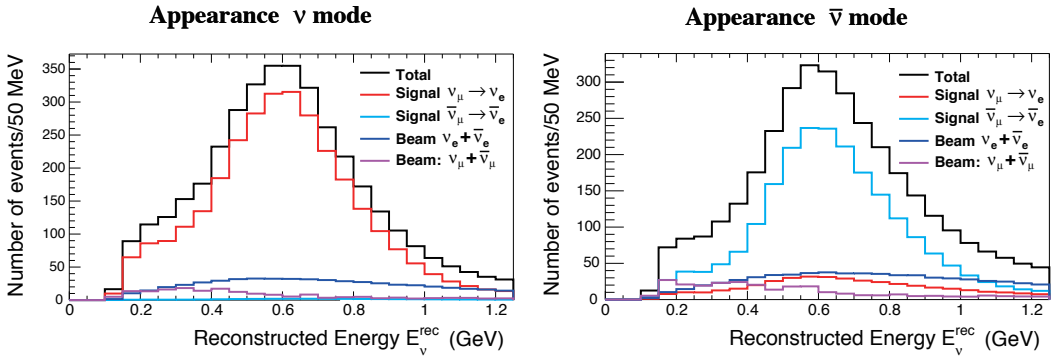

Figure 9.3: Appearance analysis: reconstructed neutrino energy distribution for ν (left plot) and $\overline{\nu}$ (right plot) running modes.

Table 9.2: The expected number of ν_e and $\overline{\nu}_e$ candidate events. Background is categorised by the flavour before oscillation.

	signal		Background						Total
	$\nu_\mu \to \nu_e$	$\overline{\nu}_\mu \to \overline{\nu}_e$	ν_μ CC	$\overline{\nu}_\mu$ CC	ν_e CC	$\overline{\nu}_e$ CC	NC	BG Total	
ν mode	3016	28	11	0	503	20	172	706	3750
$\bar{\nu}$ mode	396	2110	4	5	222	396	265	891	3397

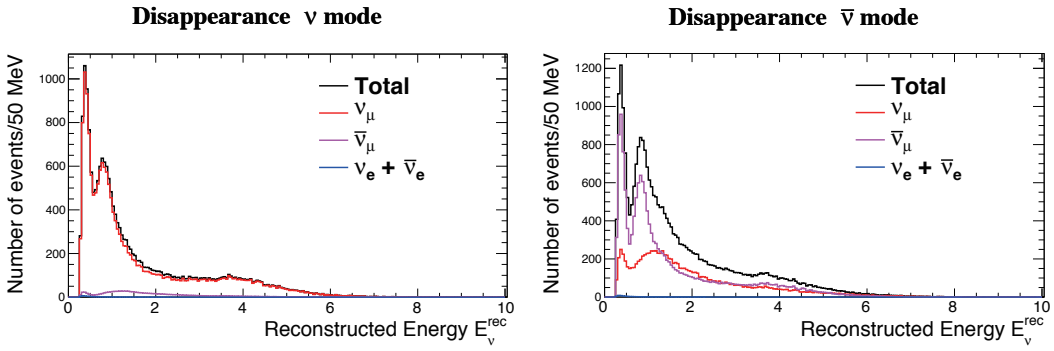

Figure 9.4: Disappearance analysis: reconstructed neutrino energy distribution for ν (left plot) and $\overline{\nu}$ (right plot) running modes.

Table 9.3: The expected number of ν_μ and $\overline{\nu}_\mu$ candidate events.

	ν_μ CC	$\overline{\nu}_\mu$ CC	ν_e CC	$\overline{\nu}_e$ CC	NC	$\nu_\mu \to \nu_e$	Total
ν mode	17225	1088	11	1	999	49	19372
$\bar{\nu}$ mode	10066	15597	7	7	1281	6	26964

- $p_\mu > 200\,\mathrm{MeV/c}$;
- there is at most one decay electron associated to the event;

Figure 9.4 shows the reconstructed neutrino energy distributions of the ν_μ and $\overline{\nu}_\mu$ candidate events. The expected number of events, divided into the different neutrino and antineutrino components is shown in Table 9.3. For the neutrino mode, the sample is dominated by ν_μ events, while in the antineutrino mode the wrong sign background (i.e. ν_μ) is non non-negligible.

The value of δ_{CP} affects the shape of the reconstructed neutrino energy distribution, so that the cases of $\delta_{CP} = 0°$ and $\delta_{CP} = 180°$ could be distinguished. Figure 9.5 shows the reconstructed neutrino energy distribution for the ν_e apperance analysis for different values of δ_{CP}. The bottom plots show the difference between the reconstructed energy spectrum for $\delta_{CP} = 0$ and for $\delta_{CP} = 90°, 180°, -90°$. The error bars only show the statistical uncertainties.

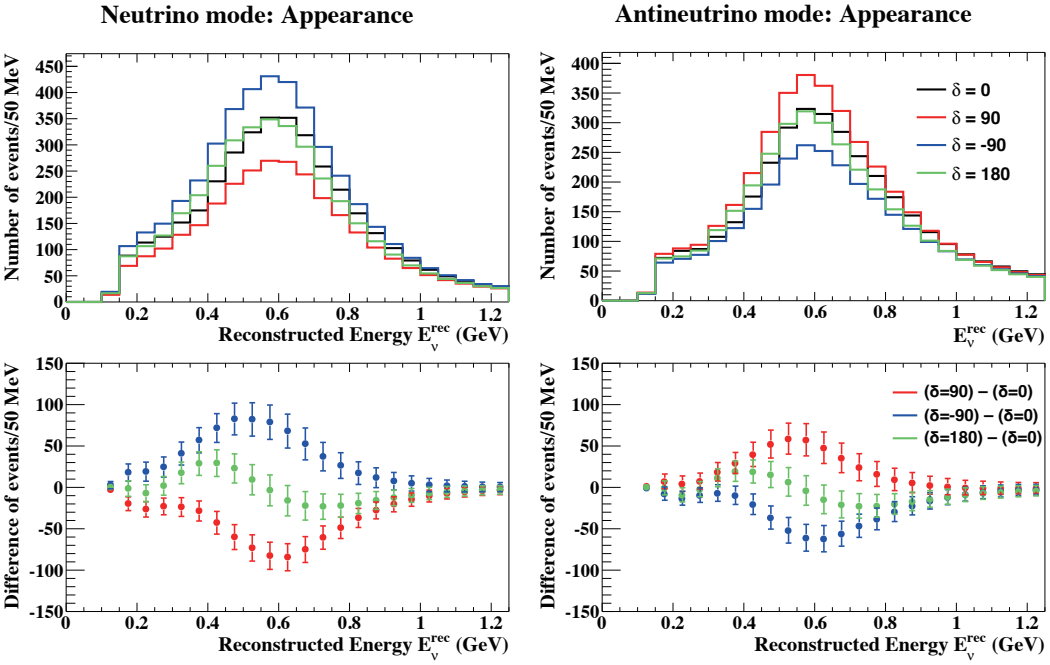

Figure 9.5: Top: reconstructed neutrino energy distribution for several values of δ_{CP}. Bottom: difference of the reconstructed neutrino energy distribution from the case with $\delta_{CP} = 0°$.

9.2.2 Analysis method

The framework used for these studies was developed for the sensitivity studies by T2K [104] and then adapted to the Hyper-K experiment. Both the ν_{e} ($\overline{\nu}_{\mathrm{e}}$) appearance and ν_μ ($\overline{\nu}_\mu$) disappearance spectra are used simultaneously in a binned likelihood fit based on the reconstructed neutrino energy distribution. The values of $\sin^2 2\theta_{13}$, δ_{CP}, $\sin^2\theta_{23}$, and Δm^2_{32} are left as free parameters. Table 9.1 shows the nominal oscillation parameters used and their treatment in the fit. A covariance matrix in reconstructed neutrino energy bins takes into account of the systematic uncertainties which will be explained in Subsection 9.2.3.

The χ^2 used in this study is defined as:

$$\chi^2 = -2\ln\mathcal{L} + P\ , \tag{9.2}$$

where $\ln\mathcal{L}$ is the log likelihood for a Poisson distribution:

$$-2\ln\mathcal{L} = \sum_k \left\{-N_k^{\mathrm{test}}(1+f_i) + N_k^{\mathrm{true}}\ln\left[N_k^{\mathrm{test}}(1+f_i)\right]\right\}\ . \tag{9.3}$$

Here, the index k indicates the reconstructed energy bins from the ν_{e} and ν_μ analyses in ν and $\bar{\nu}$ running mode; N_k^{true} (N_k^{test}) is the number of events in k-th bin for the true (test) oscillation parameters; the parameters f_i represent the systematic uncertainties. In the antineutrino mode running, an additional overall normalisation parameter with 6% prior uncertainty is used to account for differences in the neutrino and antineutrino interaction cross-sections.

The penalty term P in Equation 9.2 accounts for the systematic parameters f_i with the normalised covariance matrix C:

$$P = \sum_{i,j} f_i (C^{-1})_{i,j} f_j\ . \tag{9.4}$$

9.2.3 Systematic uncertainties

Systematic uncertainties are implemented as a covariance matrix in reconstructed neutrino energy bins. The size of the systematic uncertainties is evaluated assuming the T2K neutrino beamline, the already existing near detectors, the possible contribution of an additional intermediate detector (as described in Subsection 9.1.2), the upgrades

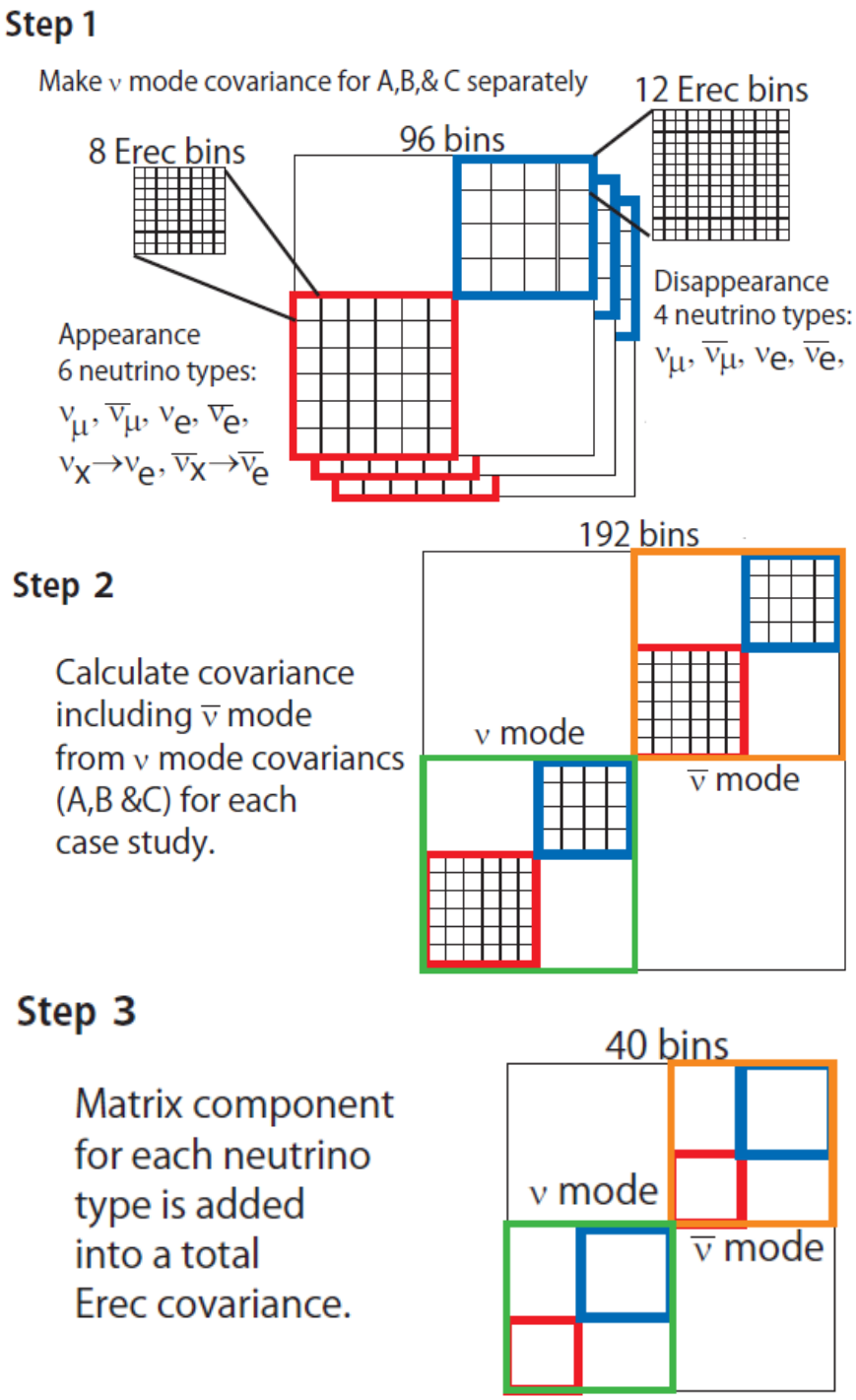

Figure 9.6: Schematics of the 3 steps used to calculate the covariance matrix. Diagrams were drawn by Motoyasu Ikeda.

to the beamline (as described in Subsection 9.1.1), and improvements in detector calibration, analysis techniques, and the future understanding of neutrino interaction.

The systematic uncertainties are divided into three categories as follows:

A) Flux and cross section uncertainties constrained by the ND fit: these uncertainties arise from the near detector samples. Even though the understanding of the detector will improve in the future, these uncertainties are conservatively assumed to stay at the same level as T2K.

B) Cross section uncertainties that are not constrained by the ND fit: these errors are assumed to get reduced by more measurements available in the near detector samples. Moreover, the presence of intermediate water Cherenkov detector will neglect the uncertainties arising from different target nucleus between the near and the far detectors. Table 9.4 shows a list of the parameters considered and their uncertainty in the T2K and HyperK analyses.

C) Uncertainties on the far detector efficiency and reconstruction modelling: most of these uncertainties are estimated by using atmospheric neutrinos as a control sample, hence these errors are expected to decrease with more than an order of magnitude due to the larger statistics available with Hyper-K. All the other uncertainties are kept the same.

Figure 9.6 shows the procedure used to produce the covariance matrix. In step 1, 10,000 toy MC are used to generate reconstructed energy covariance matrices separately for each error source A, B and C. Each of these matrices has 6 flavours $\times$ 8 reconstructed energy bins for appearance + 4 flavours $\times$ 12 reconstructed energy bins for disappearance (96 bins in total). In step 2, covariances for ν and $\bar{\nu}$ mode are calculated based on different correlation assumptions for each error source A, B, and C. Thus, the number of bins in this single covariance matrix is increased to (96 for ν mode and 96 for $\bar{\nu}$ mode). The first two categories of uncertainties (A, B) are assumed to be uncorrelated in ν and $\bar{\nu}$ mode running, except for the uncertainty on the ν_e/ν_μ cross section ratio which is treated to be anti-correlated. The far detector uncertainty (C) is treated to be fully correlated in ν and $\bar{\nu}$ mode running. The three matrices generated for each error source are then summed bin-by-bin into a single matrix. In step 3, the

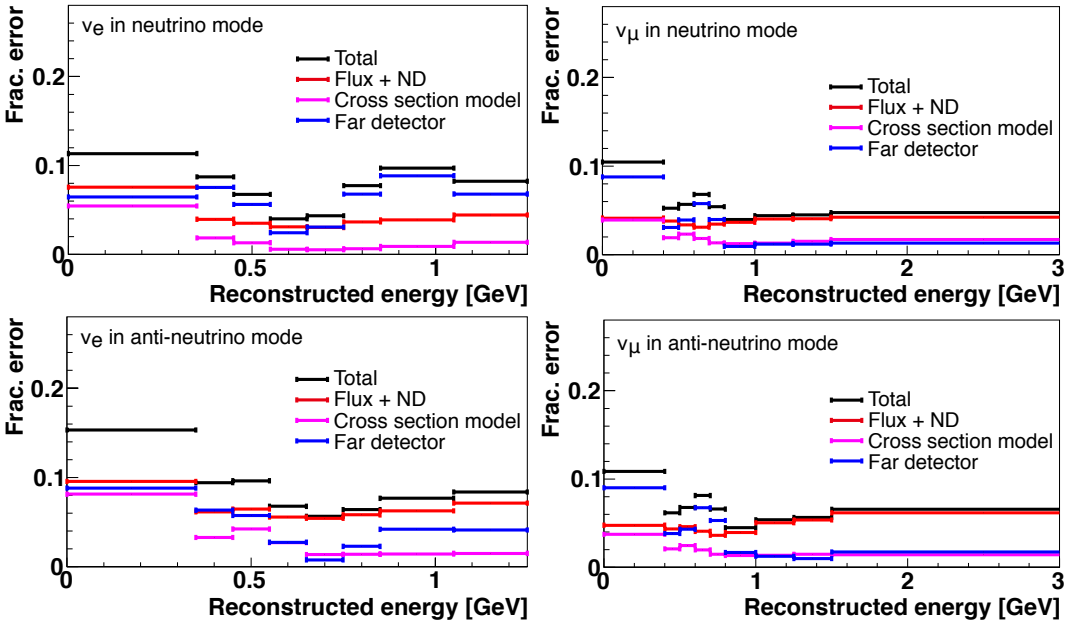

Figure 9.7: Fractional error size for the appearance (left) and the disappearance (right) samples in the ν (top row) and $\bar{\nu}$ (bottom row) running modes. Black: total uncertainty, red: the flux and cross-section constrained by the near detector, magenta: the near detector non-constrained cross section, blue: the far detector error [12].

Table 9.4: List of cross-section uncertainties that are not constrained by the ND fit and their value considered in the T2K and HyperK analyses.

Parameter	T2K	HyperK
CC Other shape	0.4	0
Spectral Function	1	0
Fermi Momentum	0.14	0
Binding Energy	0.36	0
CC Coherent	1	0.5
NC Other	0.3	0.3
NC Coherent	0.3	0.3
π-less Δ decay	0.2	0.05
CC ν_e/ν_μ	N/A	0.03
CC $\bar{\nu}/\nu$	N/A	0.06

fractional covariance for each neutrino flavour is summed bin-by-bin (resulting in 40 bins total) using the expected number of events in each bin for each flavour.

The fractional systematic uncertainties for the appearance and disappearance reconstructed energy spectra in ν and $\bar{\nu}$ mode are shown in Figure 9.7 and then summarised in Table 9.5. Black lines represent the total uncertainties (i.e. the systematic parameters f_i), while coloured lines show the contribution from each uncertainty source.

Table 9.5: Uncertainties (in %) for the expected number of events at Hyper-K from the systematic uncertainties assumed in this study [12].

	Flux & ND-constrained cross section	ND-independent cross section	Far detector	Total
ν_e appearance	3.0	1.2	0.7	3.3
ν_μ disappearance	2.8	1.5	1.0	3.3
$\overline{\nu}_e$ appearance	5.6	2.0	1.7	6.2
$\overline{\nu}_\mu$ disappearance	4.2	1.4	1.1	4.5

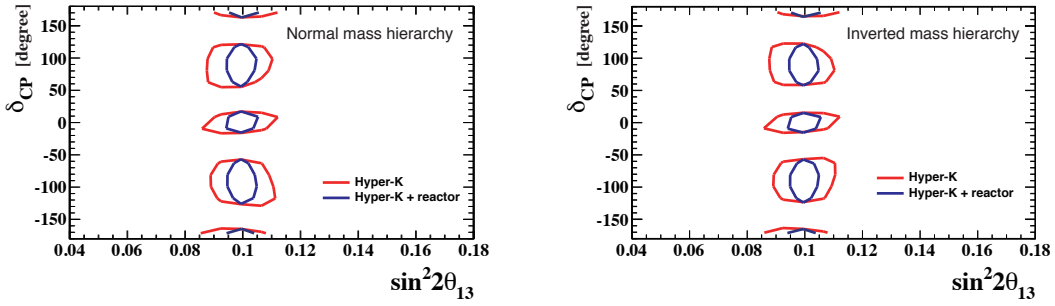

(a) Normal mass ordering **(b)** Inverted mass ordering

Figure 9.8: The 90% CL allowed regions in the $\sin^2 2\theta_{13}$-δ_{CP} plane. The results for the true values of $\delta_{CP} = (-90°, 0, 90°, 180°)$ are overlaid. Red (blue) lines show the result with Hyper-K only (with $\sin^2 2\theta_{13}$ constraint from reactor experiments).

9.3 Sensitivity of a long baseline experiment between J-PARC and Hyper-K

In this Section the result of the sensitivity studies on the CP violation phase δ_{CP} (Subsection 9.3.1), the Δm^2_{32} and θ_{32} oscillation parameters (Subsection 9.3.2), and the mass ordering (Subsection 9.3.3) are presented.

9.3.1 Sensitivity to CP violation

Figure 9.8 shows the 90% confidence level (CL) allowed regions on the $\sin^2 2\theta_{13}$-δ_{CP} plane. The results for the true values of $\delta_{CP} = (-90°, 0, 90°, 180°)$ are overlaid. When including constraints on θ_{13} coming from the reactor experiments ($\sin^2 2\theta_{13} = 0.100 \pm 0.005$), the contours get narrower in the direction of $\sin^2 2\theta_{13}$, but the sensitivity to δ_{CP} does not significantly change.

Figure 9.9 shows the expected significance to exclude $\sin\delta_{CP} = 0$ (i.e. the case where CP is not violated). Here, the significance is calculated as $\sqrt{\Delta\chi^2}$, where $\Delta\chi^2$ is the difference of χ^2 for the *trial* value of δ_{CP} and for $\delta_{CP} = 0°$ or $180°$ (the smaller value of difference is taken). Adding the reactor constraints does not improve the sensitivity to δ_{CP} significantly.

As explained in Section 9.1, for this study $7.5\,\mathrm{MW} \times 10^7\,\mathrm{sec}$ of exposure is assumed. Keeping the ratio of neutrino and antineutrino running mode fixed to 1:3, the fraction

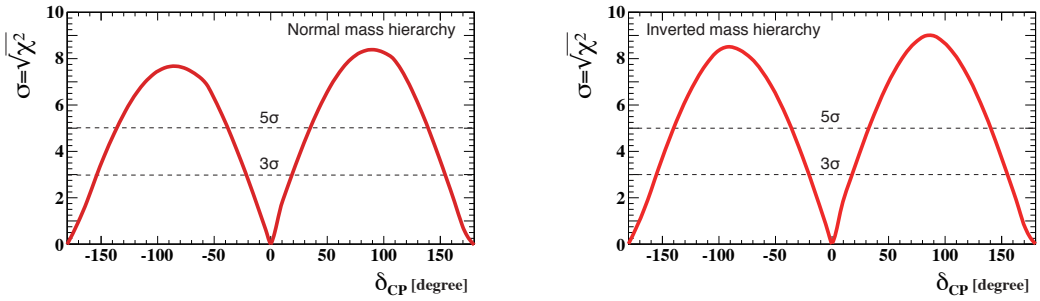

(a) Normal mass ordering **(b)** Inverted mass ordering

Figure 9.9: Expected significance to exclude $\sin\delta_{CP} = 0$.

of δ_{CP} for which $\sin\delta_{CP} = 0$ is excluded with more than $3\,\sigma$ and $5\,\sigma$ of significance can be studied as a function of the integrated beam power. The results are shown in Figure 9.10a. At $7.5\,\text{MW} \times 10^7$ sec of exposure δ_{CP} can be measured with more than $3(5)\,\sigma$ significance for 76(58)% of the possible values of δ_{CP}.

Figure 9.10b shows the $1\,\sigma$ uncertainty of δ_{CP} as a function of the integrated beam power. With nominal exposure, CP violation in the lepton sector can be determined to better than 19° for all values of δ_{CP}.

The sensitivity to CP violation depends on the value of θ_{23}: Figure 9.10c shows the fraction of δ_{CP} for which $\sin\delta_{CP} = 0$ is excluded with more than $3\,\sigma$ and $5\,\sigma$ of significance as a function of the true value of $\sin^2\theta_{23}$. Vertical dashed lines indicate 90% confidence intervals of $\sin^2\theta_{23}$ from the recent T2K measurement [54].

9.3.2 Sensitivity to Δm^2_{32} and $\sin^2\theta_{23}$

As explained in Section 9.2, the appearance and disappearance spectra are fitter simultaneously to get the values of δ_{CP}, $\sin^2 2\theta_{13}$, $\sin^2\theta_{23}$ and Δm^2_{32}. The 90% CL allowed regions for the true value of $\sin^2\theta_{23} = 0.5$ and $\sin^2\theta_{23} = 0.45$ are shown in Figures 9.11 and 9.12 respectively. The 90% CL contour by the T2K ν_μ disappearance measurement is also shown [54]. Hyper-K will be able to provide a precise measurement of $\sin^2\theta_{23}$ and Δm^2_{32}, and with a constraint on $\sin^2 2\theta_{13}$ from the reactor experiments, the octant degeneracy can also be resolved.

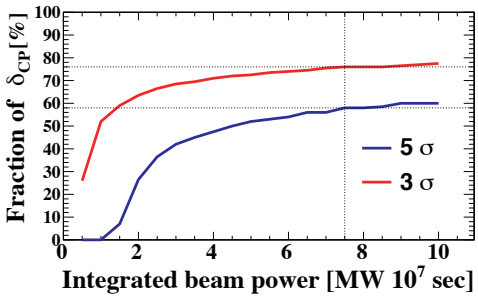

(a) Fraction of δ_{CP} for which $\sin\delta_{CP} = 0$ can be excluded with more than $3\,\sigma$ (red) and $5\,\sigma$ (blue) significance as a function of the integrated beam power.

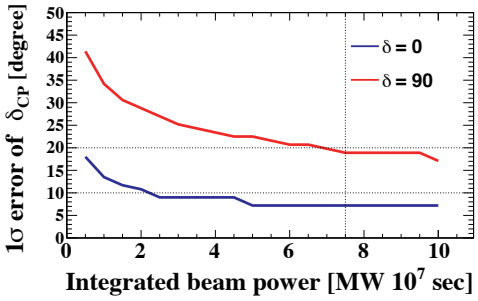

(b) Expected 1σ uncertainty of δ_{CP} as a function of integrated beam power.

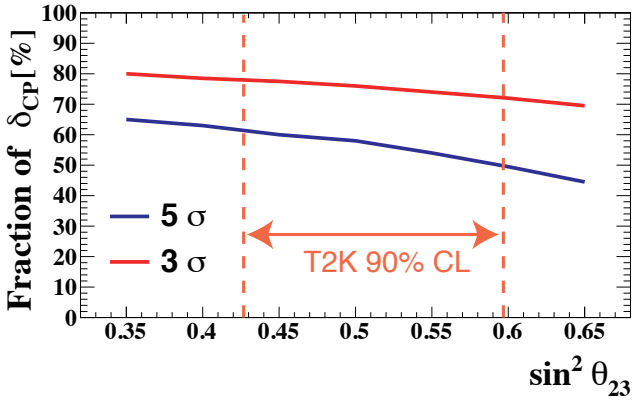

(c) Fraction of δ_{CP} for which $\sin\delta_{CP} = 0$ can be excluded with more than $3\,\sigma$ (red) and $5\,\sigma$ (blue) significance as a function of the true value of $\sin^2\theta_{23}$, for the normal mass ordering case.

Figure 9.10: Sensitivity to $\sin\delta_{CP}$.

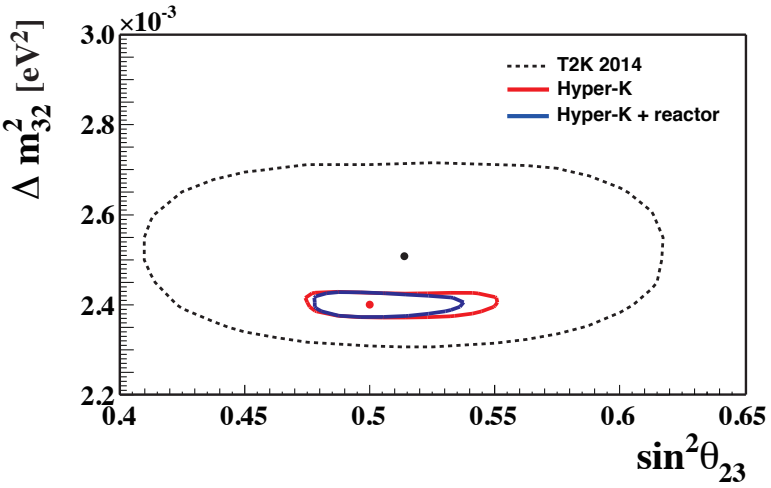

Figure 9.11: The 90% CL allowed regions in the $\sin^2\theta_{23}$–Δm^2_{32} plane. The true values are $\sin^2\theta_{23} = 0.5$ and $\Delta m^2_{32} = 2.4 \times 10^{-3}$ eV^2 (red point). Effect of systematic uncertainties is included. The red (blue) line corresponds to the result with Hyper-K alone (with a reactor constraint on $\sin^2 2\theta_{13}$). The dotted line is the 90% CL contour from T2K experiment [54] with the best fit values indicated by a black point.

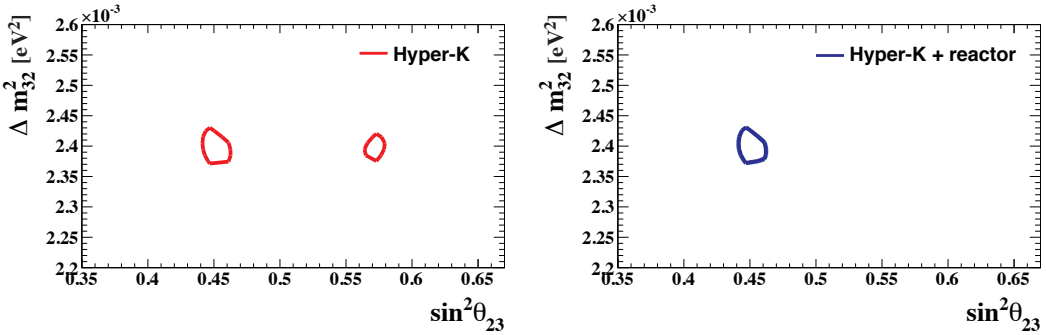

Figure 9.12: 90% CL allowed regions in the $\sin^2\theta_{23}$–Δm^2_{32} plane. The true values are $\sin^2\theta_{23} = 0.45$ and $\Delta m^2_{32} = 2.4 \times 10^{-3}$ eV^2. Effect of systematic uncertainties is included. Left: Hyper-K only. Right: with a reactor constraint.

9.3.3 Sensitivity to mass ordering

So far the known mass ordering scenario is assumed. If the mass ordering in not known before the start of the experiment, Hyper-K will proceed to measure δ_{CP} by combining the atmospheric and accelerator data.

To have a rough idea of the sensitivity to the mass ordering, a simple study of summing the $\Delta\chi^2$ from the two measurements has been performed. In a real experiment a more sophisticated analysis is expected. Assuming the true normal ordering and no CP violation ($\delta_{CP} = 0$), the values of expected $\Delta\chi^2$ as a function of δ_{CP} for each of the accelerator and atmospheric neutrino measurements, *without* assumption of the prior mass ordering knowledge, are shown in the left plot of Figure 9.13. The second minimum near $\delta_{CP} = 150^{\circ}$ in the accelerator neutrino measurement, is generated by a degeneracy with the mass ordering assumption. The atmospheric neutrino measurement does not show any second minimum (i.e. it can discriminate the mass ordering), but the sensitivity to δ_{CP} is worse than that of the accelerator measurement. The right plot of Figure 9.13 shows the results of adding the two measurements; the fake solution can be eliminated and a precise measurement of δ_{CP} will be possible.

After 10 years of data-taking, the wrong mass hierarchy can be rejected with better than 3σ for all values of θ_{23} currently allowed (Figure 9.14).

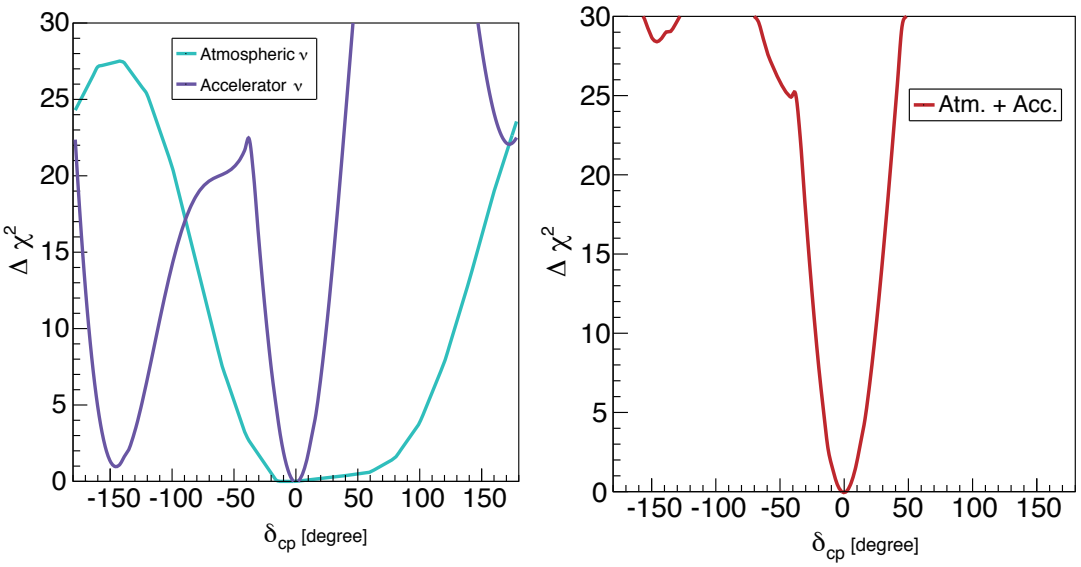

Figure 9.13: Combination of the accelerator and atmospheric data. Left: expected $\Delta\chi^2$ values for accelerator and atmospheric neutrino measurements assuming that the mass hierarchy is unknown. The true mass hierarchy is normal hierarchy and the true value of $\delta_{CP} = 0$. Right: by combining the two measurements, the sensitivity can be enhanced. In this example study, the $\Delta\chi^2$ is simply added. Plots are curtesy of Roger Wendell.

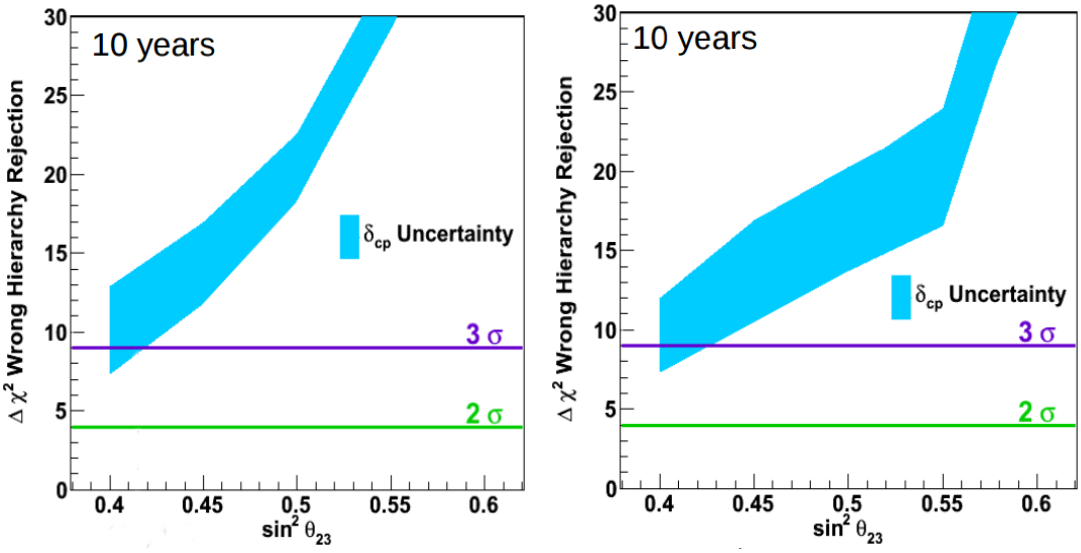

Figure 9.14: Wrong hierarchy rejection sensitivity when true normal hierarchy (left) or true inverted hierarchy (right) is assumed. Plots assume 10 years of data taking. Plots are curtesy of Roger Wendell.

10

Conclusion

To reach precise measurements of the neutrino oscillation parameters, and consequently hints of CP violation in the lepton sector, oscillation experiments need to have a good understanding of the neutrino interaction model. Chapter 2 summarises the history, current status and open questions in neutrino physics.

The T2K experiment is outlined in Chapter 3. The main goal of the T2K experiment is the precise measurement of neutrino oscillation parameters. At the same time, the near detector ND280 can be used to provide cross-section measurements that will help understanding the neutrino interaction model. The ND280 simulation software is presented in Chapter 4.

The quality of data-taking is essential for any analysis, and the methods used to asses the data quality of the ECals are explained in Chapter 5. A good data quality for the whole ND280 is the first requirement for the events selected in this analysis.

ν_μ CC interactions producing a single positive pion in the water layers of the FGD2 are selected as explained in Chapter 6. Detector and theory systematic uncertainties associated with the event selection are summarised in Chapter 7.

The Bayesian unfolding method has been used to extract the ν_μ CC single pion production cross-section in water at the ND280 detector. Single differential cross-sections in the pion kinematics, muon kinematics, muon-pion angle, and neutrino energy are also produced. The cross-section results are expressed in the reduced phase-space defined by $p_{\mu^-} > 0.2\,\text{GeV}$, $p_{\pi^+} > 0.2\,\text{GeV}$, $\cos\theta_{\mu^-} > 0.3$ and $\cos\theta_{\pi^+} > 0.3$, to avoid relying on the simulation to unfold in regions where the efficiency is very low.

The total cross-sections differ slightly when unfolding different variables, but they are all compatible with each other. The cross-sections extracted are all consistent with the NEUT prediction, $\sigma_{\mathrm{t,NEUT}} = 3.795 \times 10^{-40}\mathrm{cm}^2/\mathrm{Nucleon}$, and in most cases also with the GENIE prediction, $\sigma_{\mathrm{t,GENIE}} = 5.493 \times 10^{-40}\mathrm{cm}^2/\mathrm{Nucleon}$), except for the muon kinematics.

The single diffential cross-sections are, in general, compatible with the NEUT prediction and 1-1.5σ lower than the GENIE prediction. When looking at the p_{π^+} results the T2K data are more similar to the MINERνA results which also showed a suppression compared to the GENIE prediction, whereas the MiniBooNE results sit higher than GENIE.

Measuring the ν_μ single pion production cross-section in water is extremely important for both the T2K experiment and the neutrino community. The T2K experiment currently uses a fit to the near detector data (on carbon) to constrain the flux and theory cross-section parameters at the far detector. The sample selected with this analysis will be used as an input to the near detector fit and will enable the T2K experiment to eliminate the uncertainties arising from the carbon/oxygen differences.

This work also provides additional data to the CC single pion production puzzle, which sees the MiniBooNE and MINERνA experiment in disagreement. Additional data might also help understanding the role played by the correlations between nucleons inside the nucleus, or by the final state interactions.

Future experiments will also find the new cross-section data available beneficial. Better constrained cross-section models will result in smaller uncertainties for the oscillation measurements, hence a better chance to measure CP violation in the lepton sector. The future long baseline experiment between J-PARC and Hyper-Kamiokande is presented as a natural continuation to the T2K experiment. With a total (fiducial) mass of 0.99 (0.56) million metric tons and a total exposure of $7.5\,\mathrm{MW} \times 10^7\,\mathrm{sec}$ integrated beam power from J-PARC, Hyper-Kamiokande will lead to the measurement of δ_{CP} to better than 19 degrees for all possible values of δ_{CP}. CP violation in the lepton sector could be established at better than $3\,\sigma$ ($5\,\sigma$) for 76% (58%) of the δ_{CP} parameter space.

Appendix A

Distributions

For all the variables used in the unfolding, these features are studied:

- the correlation between the true and the reconstructed variable (in the plots shown the sum of the reconstructed bins in each true bin is normalised to 1);
- the resolution of the CC1π^+ water-enhanced sample, evaluated as $\frac{(true-reconstructed)}{true}$;
- the CC1π^+ background in the CC1π^+ water-enhanced sample;
- the CC1π^+scintillator sample (used as a sideband for the CC1π^+ background);
- the non-CC1π^+ background in the CC1π^+ water-enhanced sample;
- the CC Other (with maximum 4 tracks) water-enhanced sample (used as a sideband for the non-CC1π^+ background);

The distributions are presented **before** a phase-space cut is applied to them.

Figure A.1 show these distributions for the reconstructed positive pion momentum (p_{π^+}).

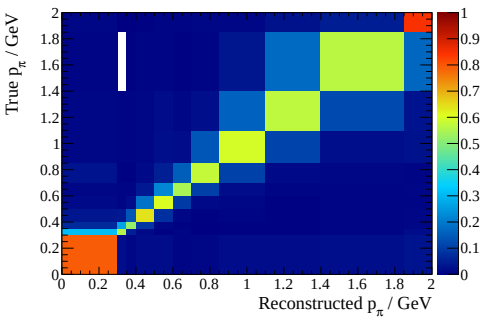

(a) True versus reconstructed variable for the whole CC1π^+ water-enhanced sample.

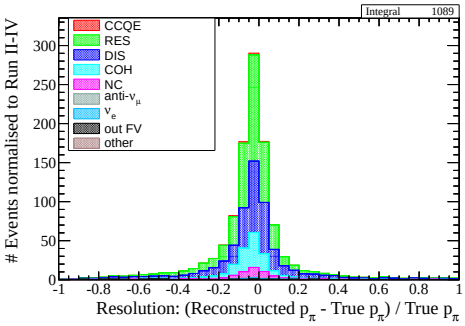

(b) Resolution of the whole CC1π^+ water-enhanced sample.

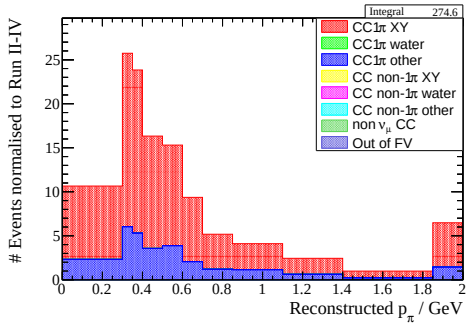

(c) CC1π^+ background in CC1π^+ water-enhanced sample.

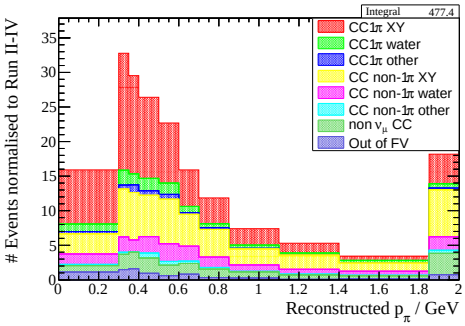

(d) CC1π^+ scintillator sample.

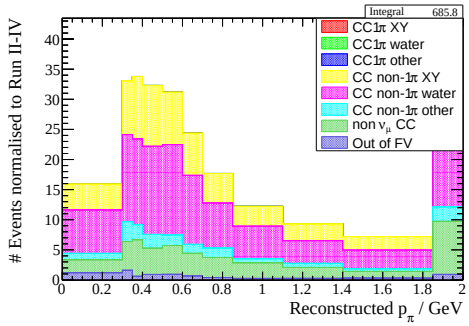

(e) non-CC1π^+ background in CC1π^+ water-enhanced sample.

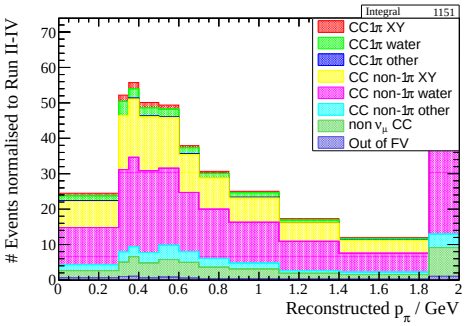

(f) CC Other (max 4 tracks) water-enhanced sample.

Figure A.1: p_{π^+} distributions: CC1π^+ water-enhanced sample.

Figure A.2 shows these distributions for the cosine of the angle between the beam direction and the π^+ direction ($\cos\theta_{\pi^+}$).

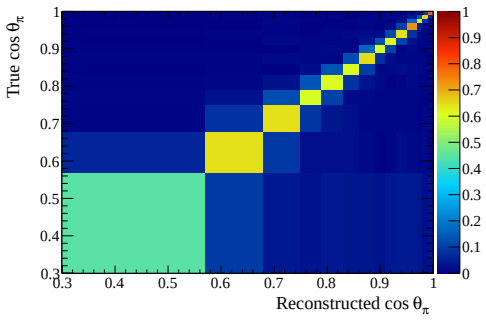

(a) True versus reconstructed variable for the whole CC1π^+ water-enhanced sample.

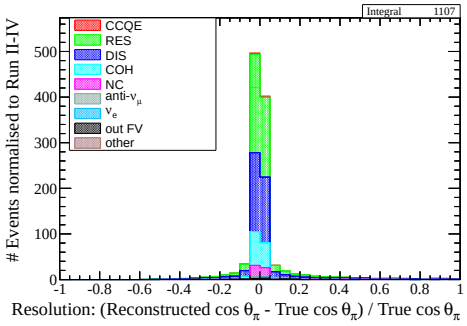

(b) Resolution of the whole CC1π^+ water-enhanced sample.

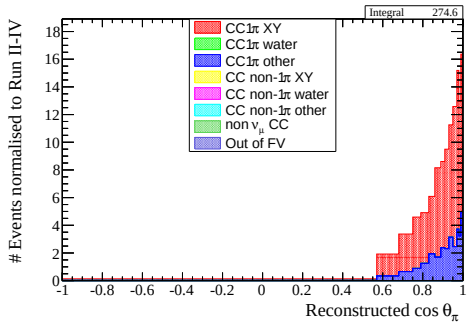

(c) CC1π^+ background in CC1π^+ water-enhanced sample.

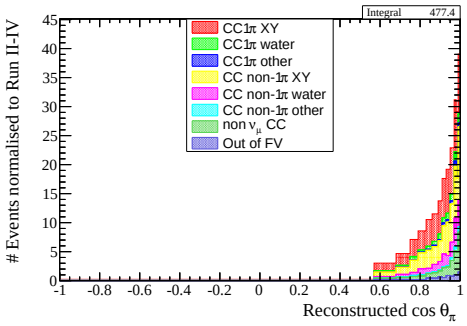

(d) CC1π^+ scintillator sample.

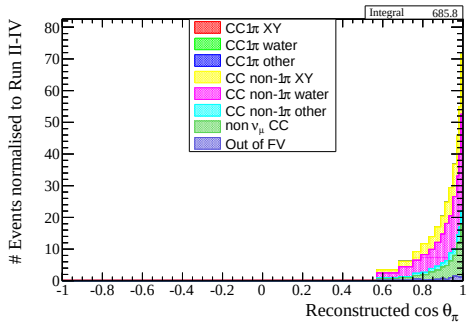

(e) non-CC1π^+ background in CC1π^+ water-enhanced sample.

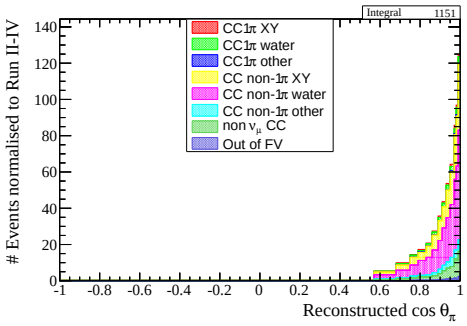

(f) CC Other (max 4 tracks) water-enhanced sample.

Figure A.2: $\cos\theta_{\pi^+}$ distributions: CC1π^+ water-enhanced sample.

Figure A.3 shows these distributions for the reconstructed muon momentum (p_{μ^-}).

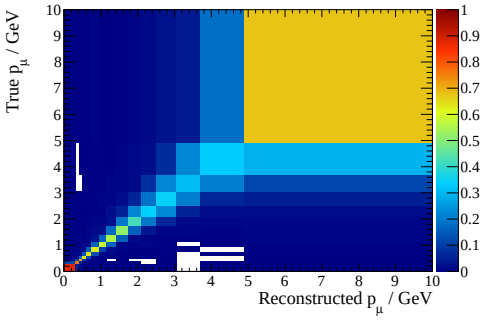

(a) True versus reconstructed variable for the whole CC1π^+ water-enhanced sample.

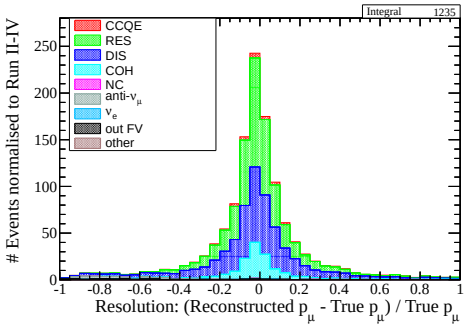

(b) Resolution of the whole CC1π^+ water-enhanced sample.

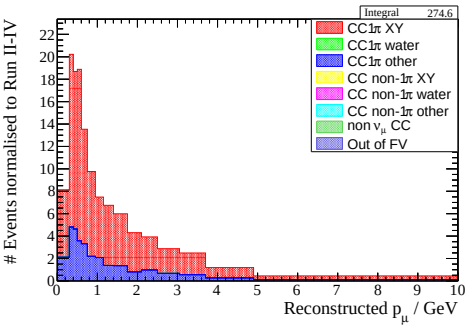

(c) CC1π^+ background in CC1π^+ water-enhanced sample.

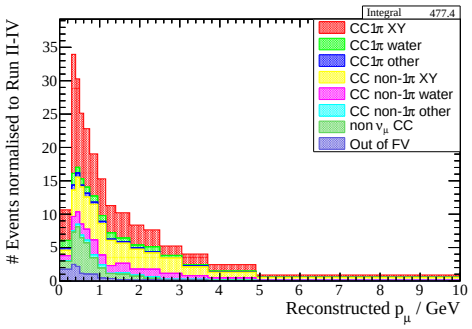

(d) CC1π^+ scintillator sample.

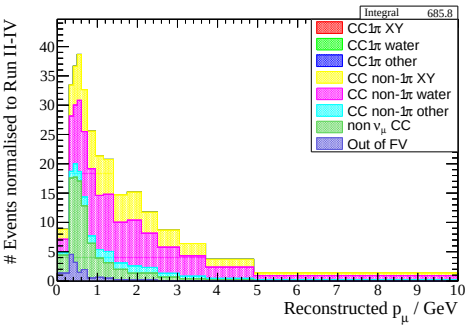

(e) non-CC1π^+ background in CC1π^+ water-enhanced sample.

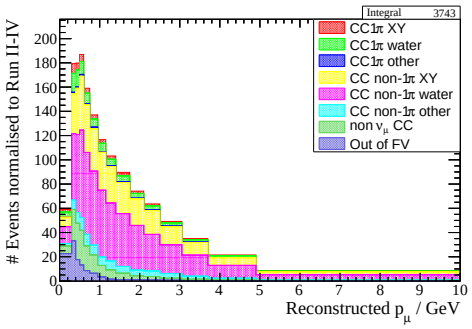

(f) CC Other (max 4 tracks) water-enhanced sample.

Figure A.3: p_{μ^-} distributions: CC1π^+ water-enhanced sample.

Figure A.4 shows these distributions for the cosine of the between the beam direction and the μ^- direction ($\cos\theta_{\mu^-}$).

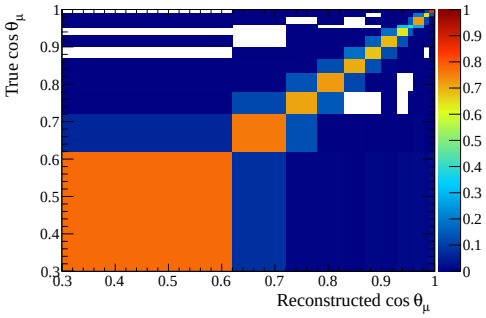

(a) True versus reconstructed variable for the whole CC1π^+ water-enhanced sample.

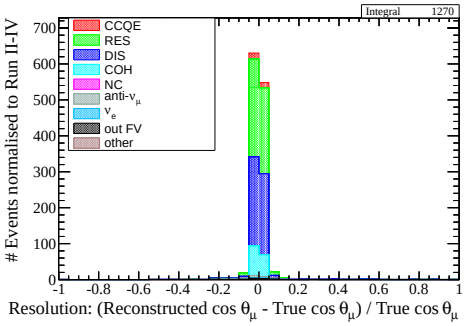

(b) Resolution of the whole CC1π^+ water-enhanced sample.

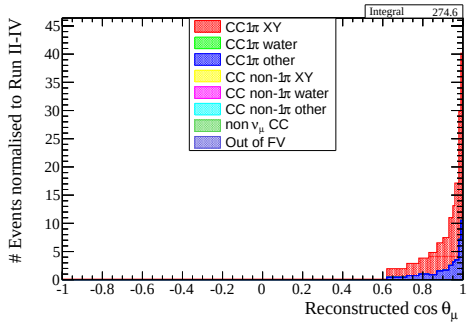

(c) CC1π^+ background in CC1π^+ water-enhanced sample.

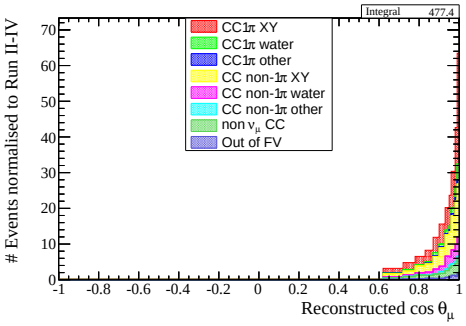

(d) CC1π^+ scintillator sample.

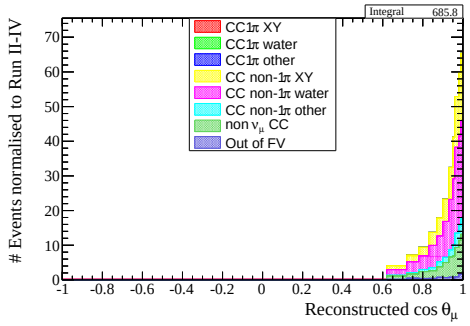

(e) non-CC1π^+ background in CC1π^+ water-enhanced sample.

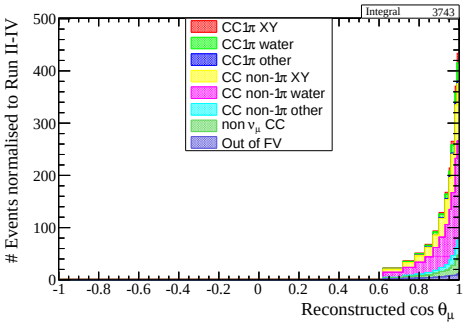

(f) CC Other (max 4 tracks) water-enhanced sample.

Figure A.4: $\cos\theta_{\mu^-}$ distributions: CC1π^+ water-enhanced sample.

Figure A.5 shows the $\cos\theta_{\mu^-,\pi^+}$ (where θ_{μ^-,π^+} is the angle between μ^- and the π^+ direction) distributions input to this analysis.

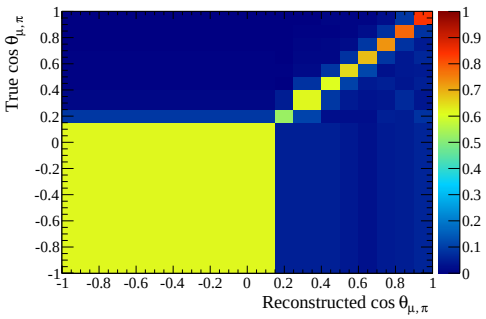

(a) True versus reconstructed variable for the whole CC1π^+ water-enhanced sample.

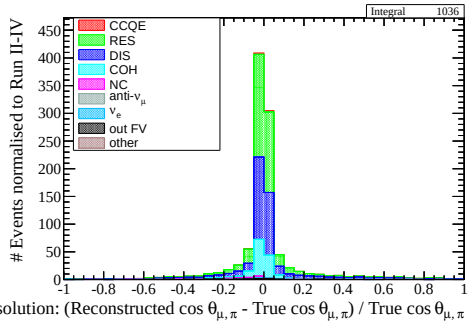

(b) Resolution of the whole CC1π^+ water-enhanced sample.

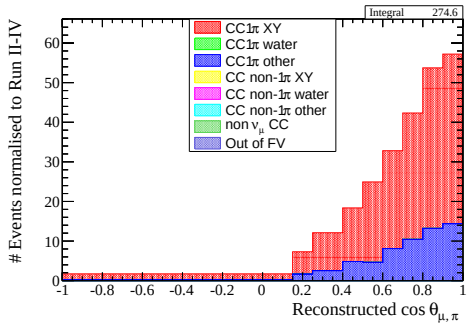

(c) CC1π^+ background in CC1π^+ water-enhanced sample.

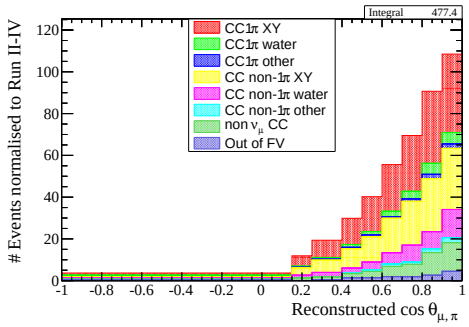

(d) CC1π^+ scintillator sample.

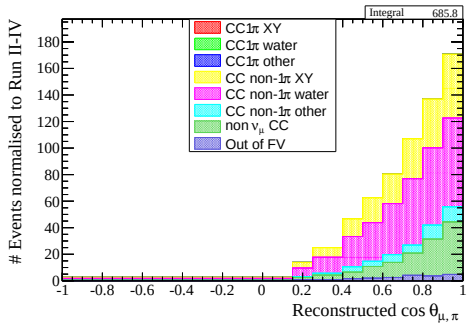

(e) non-CC1π^+ background in CC1π^+ water-enhanced sample.

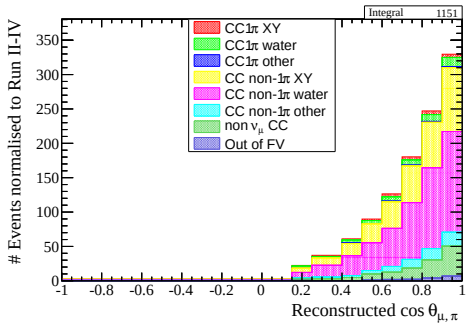

(f) CC Other (max 4 tracks) water-enhanced sample.

Figure A.5: $\cos\theta_{\mu^-,\pi^+}$ distributions: CC1π^+ water-enhanced sample.

Following the formulae of the reconstructed neutrino energy introduced in Section 6.1.8, Figure A.6 shows the distributions of the E_ν as defined by the Δ resonance formula (Equation 6.8).

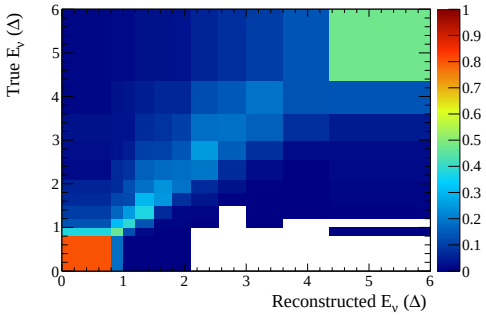

(a) True versus reconstructed variable for the whole CC1π^+ water-enhanced sample.

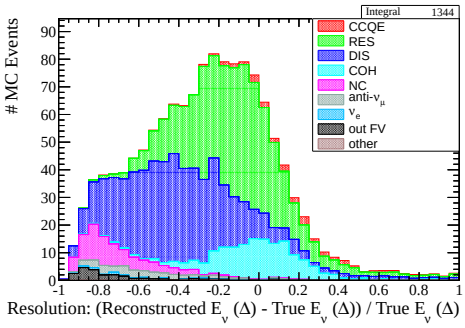

(b) Resolution of the whole CC1π^+ water-enhanced sample.

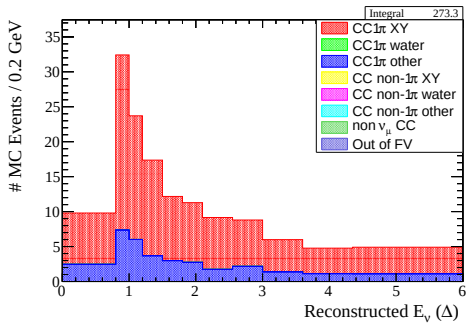

(c) CC1π^+ background in CC1π^+ water-enhanced sample.

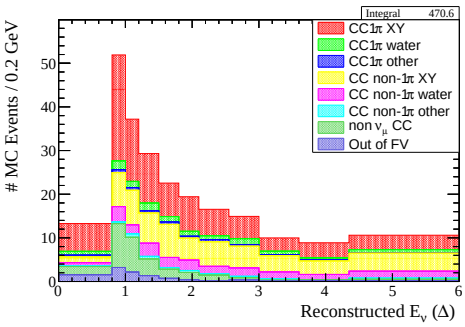

(d) CC1π^+ scintillator sample.

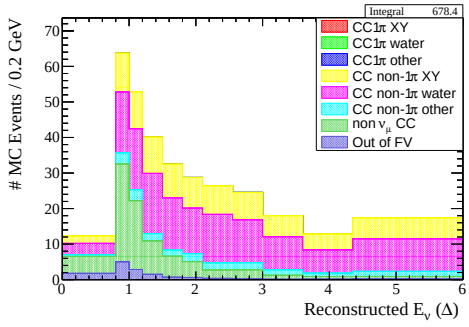

(e) non-CC1π^+ background in CC1π^+ water-enhanced sample.

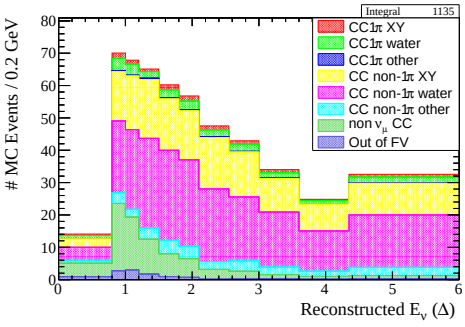

(f) CC Other (max 4 tracks) water-enhanced sample.

Figure A.6: $E_{\nu,\Delta}$ (Δ resonance formula) distributions: CC1π^+ water-enhanced sample.

Figure A.7 shows the distributions of the E_ν as defined by the MiniBooNE formula (Equation 6.9).

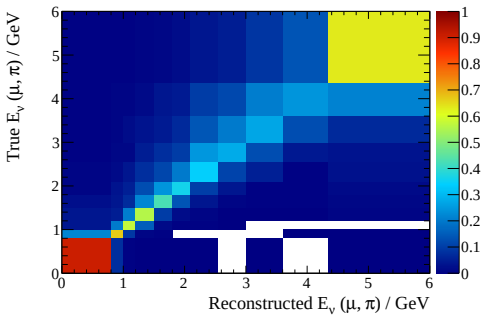

(a) True versus reconstructed variable for the whole CC1π^+ water-enhanced sample.

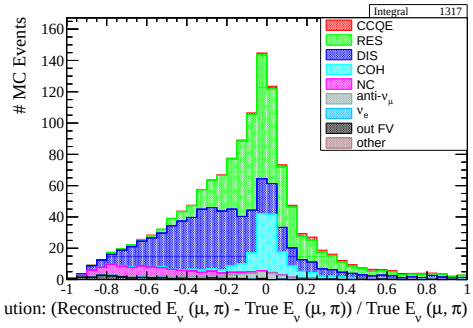

(b) Resolution of the whole CC1π^+ water-enhanced sample.

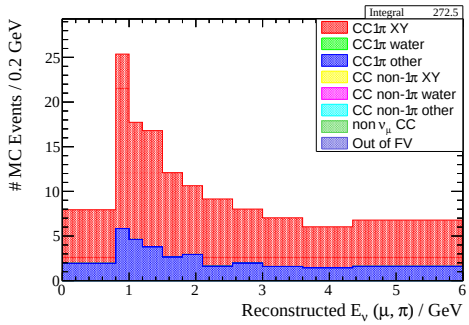

(c) CC1π^+ background in CC1π^+ water-enhanced sample.

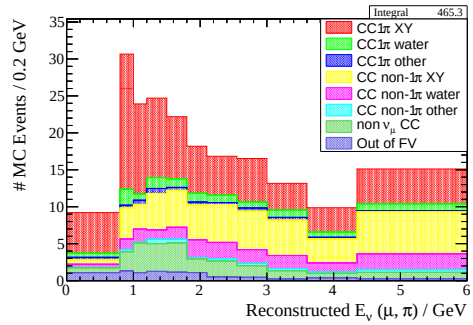

(d) CC1π^+ scintillator sample.

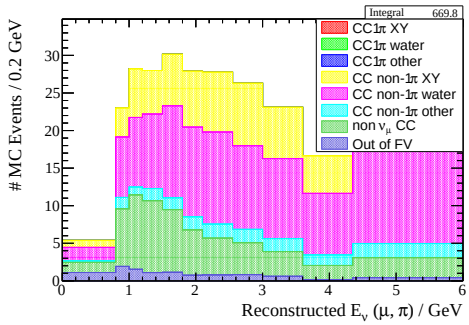

(e) non-CC1π^+ background in CC1π^+ water-enhanced sample.

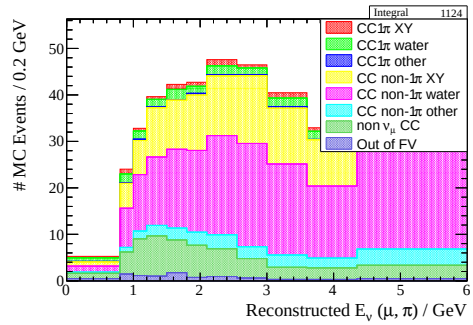

(f) CC Other (max 4 tracks) water-enhanced sample.

Figure A.7: $E_{\nu,MB}$ (MiniBooNE formula) distributions: CC1π^+ water-enhanced sample.

Appendix B

Results using Data Run II-IV and improved CC coherent model in NEUT

As seen in Subsection 2.5.4, recent results published by the MINERνA experiment confirm that the NEUT simulation over-estimates the amount of CC coherent interactions at low pion energy and high scattering angle (see Figure 2.9).

The results from the MINERνA experiment are used to re-weight the NEUT MC prediction in the region where they disagree the most. Table B.1 shows the NEUT prediction and MINERνA cross-section results for $d\sigma/dE_\pi$ when $E_\pi < 0.75\,\text{GeV}$. The third column of the table gives the ratio between the cross-section results and the NEUT prediction. At $E_\pi > 0.75\,\text{GeV}$ the cross-section results obtained by MINERνA are in in good agreement with the NEUT prediction.

The numbers in the third column of Table B.1 are used to re-weighted the CC coherent interactions in the NEUT MC sample **before** unfolding, since CC coherent interactions are both part of the signal and of the background of this analysis. An uncertainty of 100 % is already assigned to the CC coherent normalisation parameter (see Table 7.13), thus no other error is added to take into account of this re-weighting.

Table B.2 shows the total cross-sections obtained when unfolding the data Run II-IV sample starting from the NEUT MC sample with CC coherent interactions reweighted

Table B.1: NEUT prediction and MINERνA measurement of $d\sigma/dE_\pi$ when $E_\pi < 0.75\,\text{GeV}$. The single differential cross-section is expressed in units of $10^{-39}\text{cm}^2/\text{GeV}/\text{C}^{12}$. The third column is the ratio between the cross-section found by MINERνA and the NEUT prediction.

Bins	$d\sigma_{NEUT}$	$d\sigma_{MINERvA}$	Ratio
0.00-0.25 GeV	4.2	0.567	0.135
0.25-0.50 GeV	8.7	3.473	0.4
0.50-0.75 GeV	4.85	1.426	0.294

according to the MINERνA experiment result. These results are slightly higher than the ones presented in Table 8.9, but still compatible with them and with the NEUT prediction with reweighted CC coherent, $\sigma_{\text{t,NEUT}} = 4.158 \times 10^{-38}\text{cm}^2/\text{Nucleon}$.

Figures B.1-B.5 show the single differential results when unfolding the pion/muon kinematics using this method. In all cases the unfolded single differential cross-section is slightly higher than the one shown in Figures 8.18-8.30, but still compatible with them. The unfolded cross-section sits between the NEUT and GENIE prediction in most cases. The exceptions are at $0.5 < p_{\pi^+} < 0.7\,\text{GeV/c}$ and $\cos\theta_{\pi^+} > 0.95$ where the unfolded cross-section is lower than both the NEUT (with reweighted CC coherent interactions) and GENIE predictions.

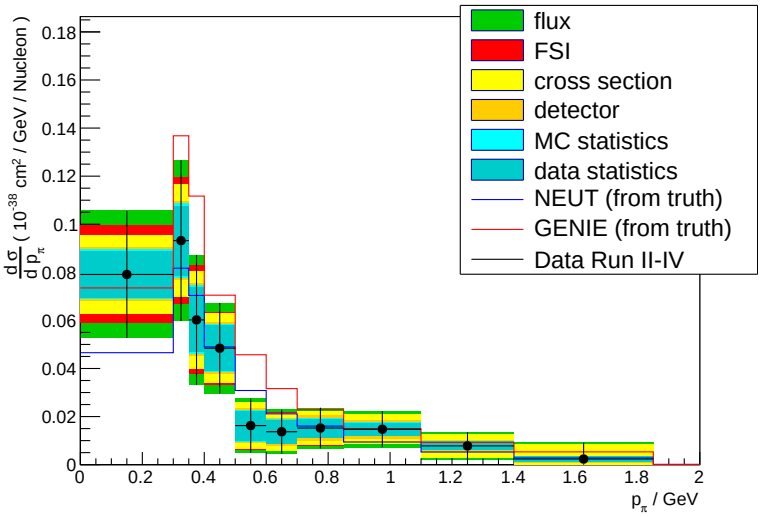

(a) Differential cross-section obtained by unfolding the p_{π^+} distribution.

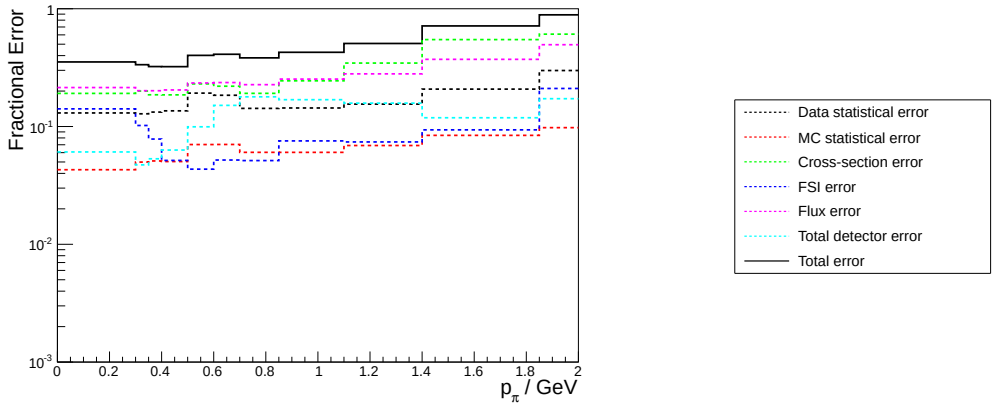

(b) Total and fractional error components as a function of the p_{π^+} binned distribution.

Figure B.1: Single differential cross-section in p_{π^+} obtained when unfolding the Run II-IV T2K data starting from the NEUT MC with reweighted CC coherent interactions.

Table B.2: Total flux-averaged cross-section evaluated when unfolding the T2K data Run II-IV starting from the NEUT MC with reweighted CC coherent interactions. "negl" stands for negligible and indicates that the uncertainty is below 0.001%.

Cross-section results (10^{-40}cm^2 / Nucleon)					
	$p_{\pi+}$	$\cos\theta_{\pi+}$	$p_{\mu-}$	$\cos\theta_{\mu-}$	$\cos\theta_{\mu+,\pi+}$
Flux-averaged σ	4.780	4.352	4.446	4.022	4.382
Total stat. error	0.507	0.500	0.506	0.496	0.506
Total syst. error	1.849	1.928	1.828	1.939	1.970
Fractional uncertainties in %					
Data statistics	10.05	10.93	10.86	11.78	11.00
MC statistics	3.41	3.52	3.41	3.66	3.52
Theory cross-section	26.15	32.22	27.47	35.02	33.06
FSI	8.80	7.66	7.76	8.85	7.50
Flux	26.52	28.60	28.77	31.02	28.67
B field distortion	0.17	0.11	0.15	0.12	0.12
TPC charge confusion	0.17	0.11	0.15	0.11	0.12
FGD2 backward migrations	0.90	0.35	0.21	0.55	0.30
FGD2 forward migrations	0.94	0.89	1.25	0.75	0.56
FGD mass scintillator	0.22	0.36	0.28	0.39	0.36
FGD mass water	0.73	0.75	0.74	0.78	0.77
TPC momentum resolution	0.44	0.28	0.57	0.33	0.28
TPC momentum scale	0.75	negl	0.57	negl	negl
Out of FV	0.60	0.41	0.92	1.09	0.37
ECal PID	0.08	0.08	0.10	0.06	0.06
Pile up	0.31	0.34	0.35	0.35	0.33
ECal reconstruction	0.43	0.48	0.49	0.53	0.51
Pion secondary interactions	5.20	6.74	6.53	7.22	6.82
TPC quality cut	negl	negl	negl	negl	negl
TPC-FGD matching efficiency	0.04	0.01	0.03	0.02	0.02
TPC PID	1.14	0.72	0.64	1.26	1.21
TPC track efficiency	0.26	0.17	0.28	0.36	0.24

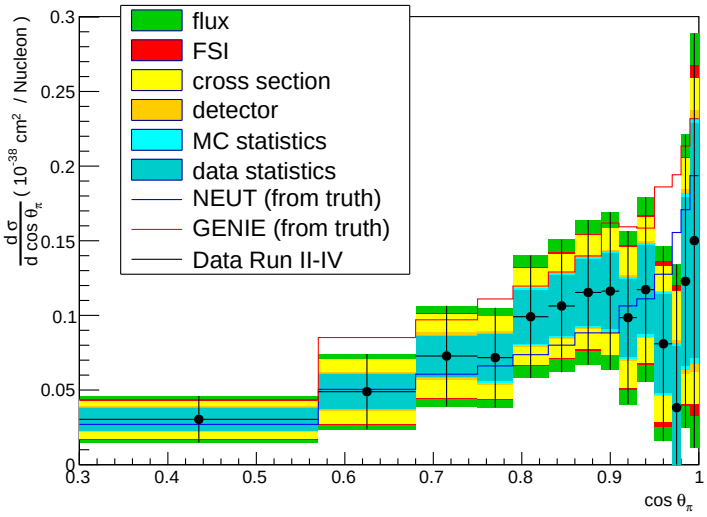

(a) Differential cross-section obtained by unfolding the $\cos\theta_{\pi^+}$ distribution.

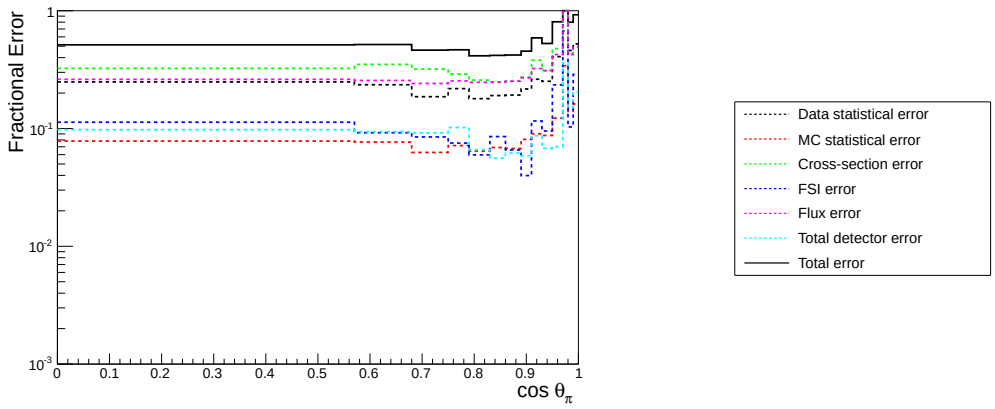

(b) Total and fractional error components as a function of the $\cos\theta_{\pi^+}$ binned distribution.

Figure B.2: Single differential cross-section in $\cos\theta_{\pi^+}$ obtained when unfolding the Run II-IV T2K data starting from the NEUT MC with reweighted CC coherent interactions.

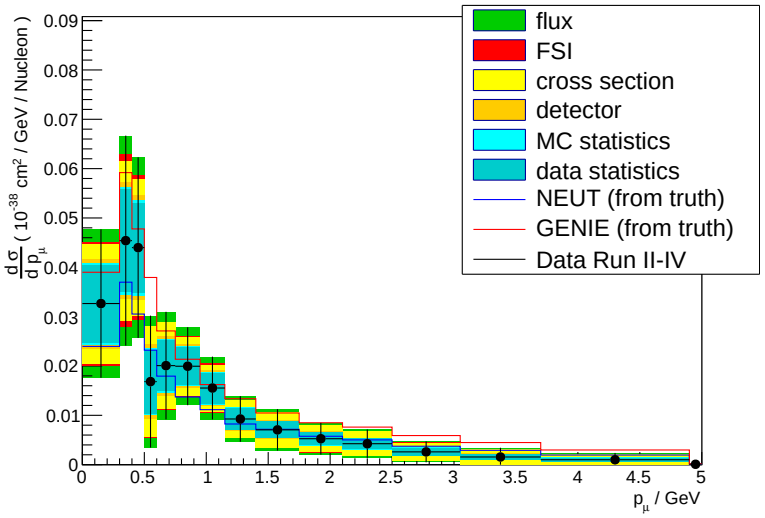

(a) Differential cross-section obtained by unfolding the p_{μ^-} distribution.

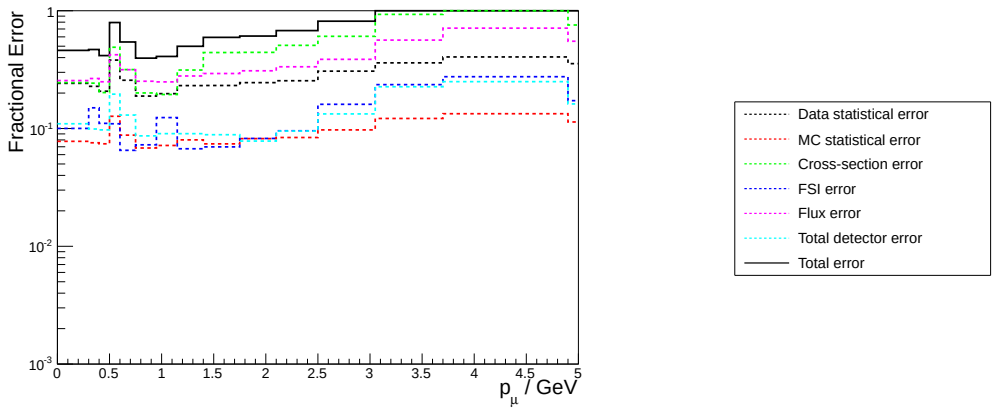

(b) Total and fractional error components as a function of the p_{μ^-} binned distribution.

Figure B.3: Single differential cross-section in p_{μ^-} obtained when unfolding the Run II-IV T2K data starting from the NEUT MC with reweighted CC coherent interactions.

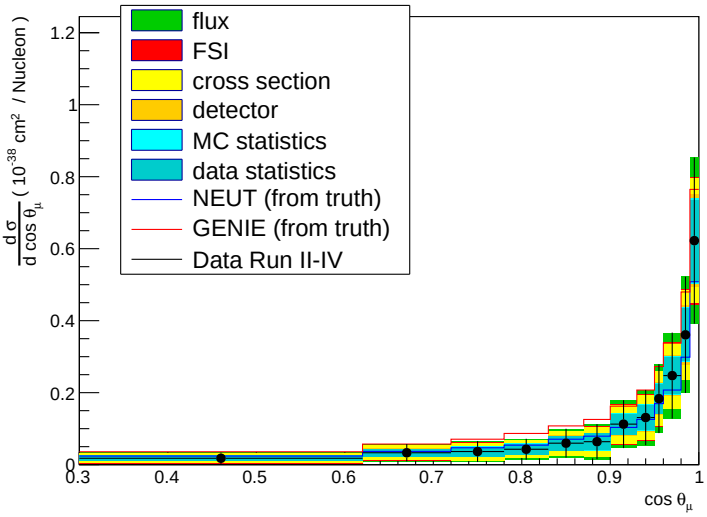

(a) Differential cross-section obtained by unfolding the $\cos\theta_{\mu^-}$ distribution.

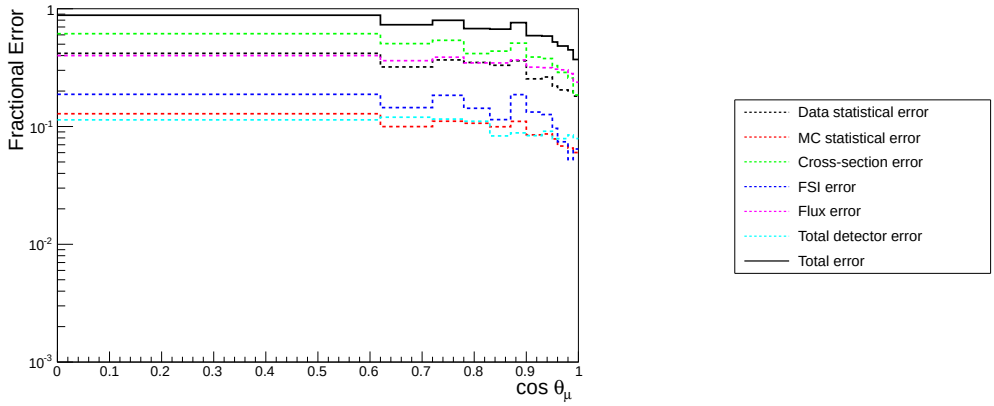

(b) Total and fractional error components as a function of the $\cos\theta_{\mu^-}$ binned distribution.

Figure B.4: Single differential cross-section in $\cos\theta_{\mu^-}$ obtained when unfolding the Run II-IV T2K data starting from the NEUT MC with reweighted CC coherent interactions.

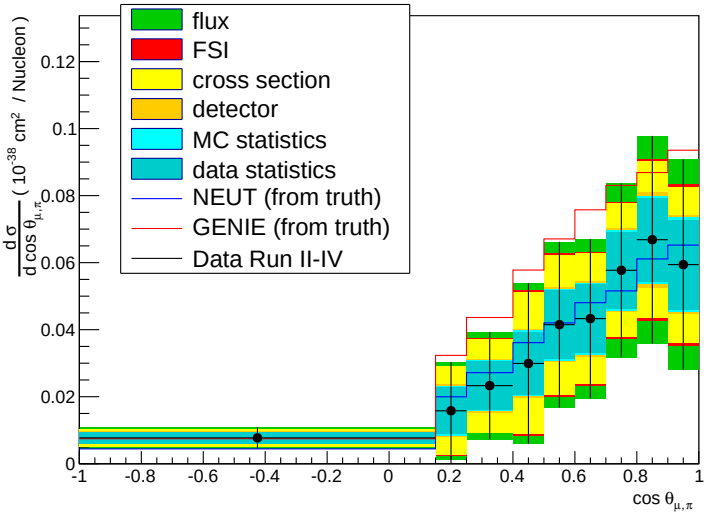

(a) Differential cross-section obtained by unfolding the $\cos\theta_{\mu^-,\pi^+}$ distribution.

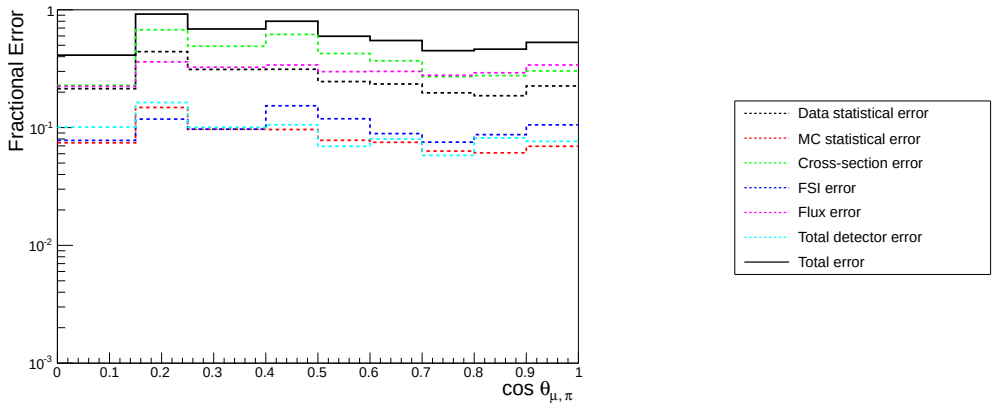

(b) Total and fractional error components as a function of the $\cos\theta_{\mu^-,\pi^+}$ binned distribution.

Figure B.5: Single differential cross-section in $\cos\theta_{\mu^-,\pi^+}$ obtained when unfolding the Run II-IV T2K data starting from the NEUT MC with reweighted CC coherent interactions.

Figures B.6 and B.7 show the $\sigma(E)$ results when using the Δ resonance formula and the MiniBooNE formula, respectively. In both cases the unfolded cross-section result is completely consistent with the NEUT (with reweighted CC coherent interactions) prediction.

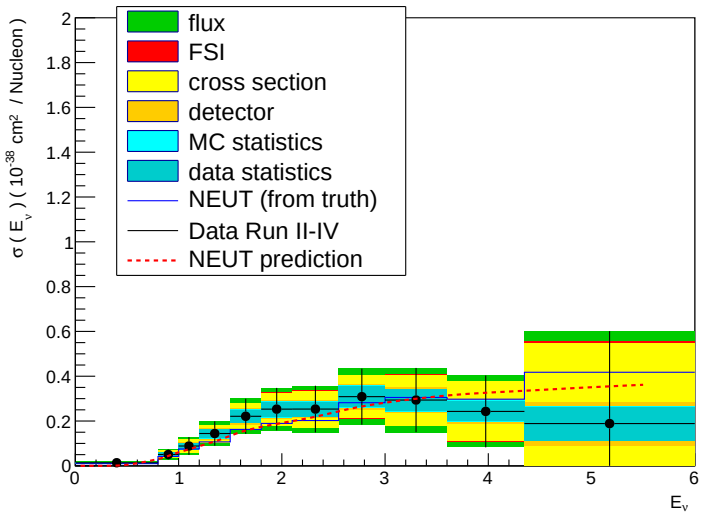

(a) Differential cross-section obtained by unfolding the $E_{\nu\ \mathrm{REC}\ \Delta}$ distribution.

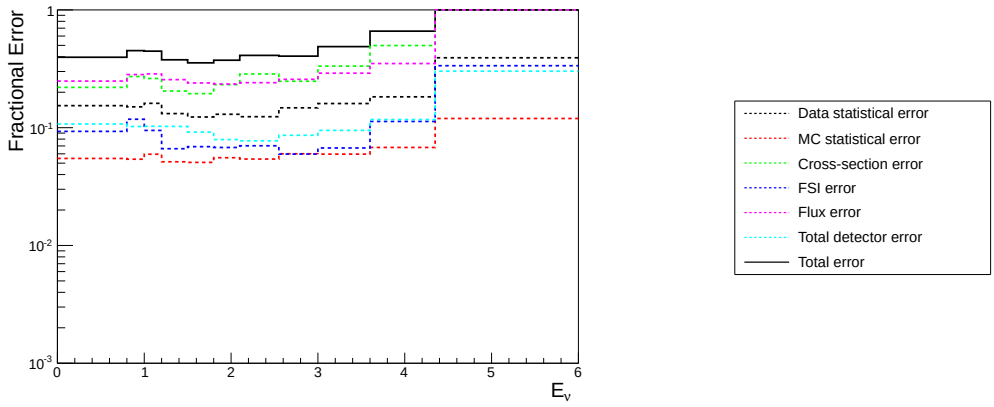

(b) Total and fractional error components as a function of the $E_{\nu\ \mathrm{REC}\ \Delta}$ binned distribution.

Figure B.6: Single differential cross-section in $E_{\nu\ \mathrm{REC}\ \Delta}$ obtained when unfolding the Run II-IV T2K data starting from the NEUT MC with reweighted CC coherent interactions.

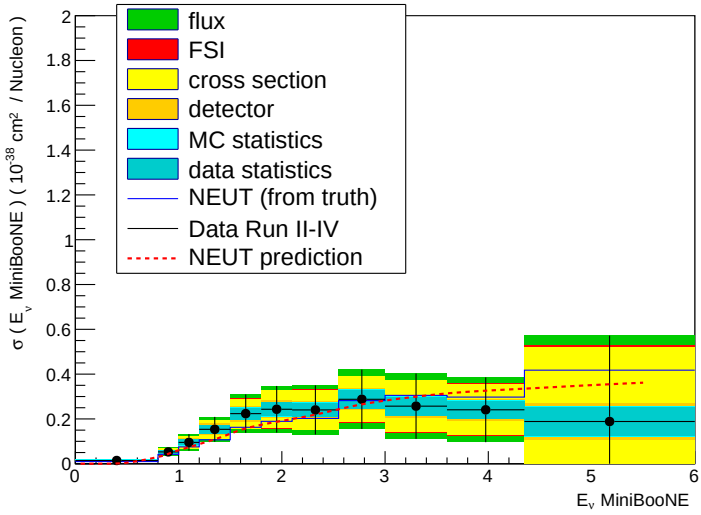

(a) Differential cross-section obtained by unfolding the $E_{\nu\ \mathrm{REC,\ MB}}$ distribution.

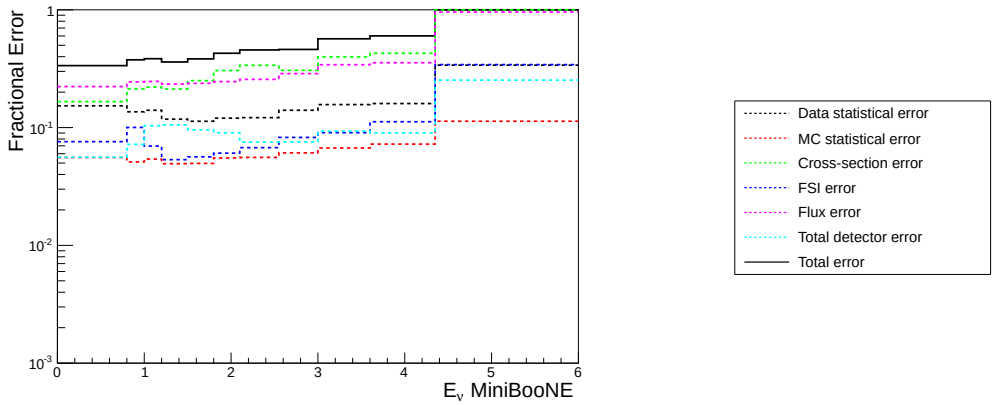

(b) Total and fractional error components as a function of the $E_{\nu\ \mathrm{REC,\ MB}}$ binned distribution.

Figure B.7: Single differential cross-section in $E_{\nu\ \mathrm{REC,\ MB}}$ obtained when unfolding the Run II-IV T2K data starting from the NEUT MC with reweighted CC coherent interactions.

References

[1] Wolfgang Pauli. **Dear radioactive ladies and gentlemen**. *Phys. Today, 31N9*, **27**, 1978.

[2] Frederick Reines and CL Cowan. **Detection of the free neutrino**. *Physical Review*, **92**(3):830–831, 1953.

[3] S Schael, R Barate, R Bruneliere, D Buskulic, I De Bonis, D Décamp, P Ghez, C Goy, S Jézéquel, JP Lees, et al. **Precision electroweak measurements on the Z resonance**. *Physics Reports A Review Section of Physics Letters*, **427**(5-6):257–454, 2006.

[4] Raymond Davis Jr, Don S Harmer, and Kenneth C Hoffman. **Search for neutrinos from the sun**. *Physical Review Letters*, **20**(21):1205, 1968.

[5] SAGE Collaboration. **Measurement of the solar neutrino capture rate with gallium metal**. *Physical Review C*, **60**(5):055801, 1999.

[6] GALLEX Collaboration. **GALLEX solar neutrino observations: Complete results for GALLEX II**. *Physics Letters B*, **357**(1):237–247, 1995.

[7] Bruno Pontecorvo. **Mesonium and antimesonium**. *Zhur. Eksptl'. i Teoret. Fiz.*, **33**, 1957.

[8] Ziro Maki, Masami Nakagawa, and Shoichi Sakata. **Remarks on the unified model of elementary particles**. *Progress of Theoretical Physics*, **28**(5):870–880, 1962.

[9] Y Fukuda, T Hayakawa, E Ichihara, K Inoue, K Ishihara, H Ishino, Y Itow, T Kajita, J Kameda, S Kasuga, et al. **Evidence for oscillation of atmospheric neutrinos**. *Physical Review Letters*, **81**(8):1562, 1998.

[10] SNO Collaboration. **Measurement of the Rate of ν e+ d p+ p+ e- Interactions Produced by B 8 Solar Neutrinos at the Sudbury Neutrino Observatory**. *Physical Review Letters*, **87**(7):071301, 2001.

[11] Carlo Giunti and Chung W Kim. *Fundamentals of neutrino physics and astrophysics*. Oxford university press, 2007.

[12] Hyper-Kamiokande Proto-Collaboration. **Physics Potential of a Long Baseline Neutrino Oscillation Experiment Using J-PARC Neutrino Beam and Hyper-Kamiokande**. *arXiv preprint arXiv:1502.05199*, 2015.

[13] Matthew Bass, Daniel Cherdack, and Robert J Wilson. **Future Neutrino Oscillation Sensitivities for LBNE**. *arXiv preprint arXiv:1310.6812*, 2013. LBNE is the predecessor of DUNE.

[14] Lincoln Wolfenstein. **Neutrino oscillations in matter**. *Physical Review D*, **17**(9):2369, 1978.

[15] Jiro Arafune, Masafumi Koike, and Joe Sato. **CP violation and matter effect in long baseline neutrino oscillation experiments**. *Physical Review D*, **56**(5):3093, 1997.

[16] MINOS Collaboration. **Measurements of atmospheric neutrinos and antineutrinos in the MINOS far detector**. *Physical Review D*, **86**(5):052007, 2012.

[17] KamLAND Collaboration. **Precision measurement of neutrino oscillation parameters with KamLAND**. *Physical Review Letters*, **100**(22):221803, 2008.

[18] Daya Bay Collaboration. **Observation of electron-antineutrino disappearance at Daya Bay**. *Physical Review Letters*, **108**(17):171803, 2012.

[19] RENO Collaboration. **Observation of reactor electron antineutrinos disappearance in the RENO experiment**. *Physical Review Letters*, **108**(19):191802, 2012.

[20] Double CHOOZ Collaboration. **Indication of reactor ν e disappearance in the Double Chooz experiment**. *Physical Review Letters*, **108**(13):131801, 2012.

[21] NOvA Collaboration. **NOvA proposal to build a 30 kiloton off-axis detector to study neutrino oscillations in the fermilab NuMI beamline**. *arXiv preprint hep-ex/0503053*, 2005.

[22] K.A. Olive et al. **Review of Particle Physics**. *Chinese Physics C*, **38**(9):090001, 2014.

[23] KN Abazajian, E Calabrese, A Cooray, F De Bernardis, S Dodelson, A Friedland, GM Fuller, Steen Hannestad, BG Keating, EV Linder, et al. **Cosmological and astrophysical neutrino mass measurements**. *Astroparticle Physics*, **35**(4):177–184, 2011.

[24] KATRIN Collaboration and others. **KATRIN: A next generation tritium beta decay experiment with sub-eV sensitivity for the electron neutrino mass**. *arXiv preprint hep-ex/0109033*, 2001.

[25] SuperNEMO Collaboration. **Probing new physics models of neutrinoless double beta decay with SuperNEMO**. *The European Physical Journal C-Particles and Fields*, **70**(4):927–943, 2010.

[26] Christine Kraus and Simon JM Peeters. **The rich neutrino programme of the SNO+ experiment**. *Progress in Particle and Nuclear Physics*, **64**(2):273–277, 2010.

[27] A Aguilar et al. **Evidence for neutrino oscillations from the observation of ν^- e appearance in a ν^- μ beam**. *Physical Review D*, **64**(11):112007, 2001.

[28] MiniBooNE Collaboration. **Improved Search for ν^- μ ν^- e Oscillations in the MiniBooNE Experiment**. *Physical review letters*, **110**(16):161801, 2013.

[29] Samoil M Bilenky, C Giunti, Walter Grimus, and T Schwetz. **Four-neutrino mass spectra and the Super-Kamiokande atmospheric up-down asymmetry**. *Physical Review D*, **60**(7):073007, 1999.

[30] Maria Archidiacono, Nicolao Fornengo, Carlo Giunti, and Alessandro Melchiorri. **Testing 3+ 1 and 3+ 2 neutrino mass models with cosmology and short baseline experiments**. *Physical Review D*, **86**(6):065028, 2012.

[31] Joseph A Formaggio and GP Zeller. **From eV to EeV: Neutrino cross sections across energy scales**. *Reviews of Modern Physics*, **84**(3):1307, 2012.

[32] J Nieves, I Ruiz Simo, and MJ Vicente Vacas. **The nucleon axial mass and the MiniBooNE quasielastic neutrino–nucleus scattering problem**. *Physics Letters B*, **707**(1):72–75, 2012.

[33] Marco Martini, Magda Ericson, Guy Chanfray, and Jacques Marteau. **Unified approach for nucleon knock-out and coherent and incoherent pion production in neutrino interactions with nuclei**. *Physical Review C*, **80**(6):065501, 2009.

[34] Callum Wilkinson. **NEUT development for T2K and relevance of updated 2p2h models**, 2014. NuFact 2014.

[35] NOMAD Collaboration. **A study of quasi-elastic muon neutrino and antineutrino scattering in the NOMAD experiment**.

[36] MiniBooNE Collaboration. **First measurement of the muon neutrino charged current quasielastic double differential cross section**. *Physical Review D*, **81**(9):092005, 2010.

[37] MINERνA Collaboration. **Measurement of Muon Neutrino Quasielastic Scattering on a Hydrocarbon Target at E ν 3.5 GeV**. *Physical review letters*, **111**(2):022502, 2013.

[38] Dieter Rein and Lalit M Sehgal. **Neutrino-excitation of baryon resonances and single pion production**. *Annals of Physics*, **133**(1):79–153, 1981.

[39] GM Radecky et al. **Study of single-pion production by weak charged currents in low-energy ν d interactions**. *Physical Review D*, **25**(5):1161, 1982.

[40] T Kitagaki, H Yuta, S Tanaka, A Yamaguchi, K Abe, K Hasegawa, K Tamai, S Kunori, Y Otani, H Hayano, et al. **Charged-current exclusive pion production in neutrino-deuterium interactions**. *Physical Review D*, **34**(9):2554, 1986.

[41] Callum Wilkinson, Philip Rodrigues, Susan Cartwright, Lee Thompson, and Kevin McFarland. **Reanalysis of bubble chamber measurements of muon-neutrino induced single pion production**. *Physical Review D*, **90**(11):112017, 2014.

[42] KM Graczyk, D Kiełczewska, P Przewłocki, and JT Sobczyk. **C_5^A axial form factor from bubble chamber experiments**. *Physical Review D*, **80**(9):093001, 2009.

[43] MiniBooNE Collaboration. **Measurement of neutrino-induced charged-current charged pion production cross sections on mineral oil at E ν 1 GeV**. *Physical Review D*, **83**(5):052007, 2011.

[44] MINERνA Collaboration. **Charged Pion Production in ν_μ Interactions on Hydrocarbon at E = 4.0 GeV**. *arXiv preprint arXiv:1406.6415*, 2014.

[45] PA Rodrigues. **Comparing pion production models to MiniBooNE data**. *arXiv preprint arXiv:1402.4709*, 2014.

[46] CHARM-II collaboration. **Coherent single charged pion production by neutrinos**. *Physics Letters B*, **313**(1):267–275, 1993.

[47] K2K collaboration. **Search for coherent charged pion production in neutrino-carbon interactions**. *Physical review letters*, **95**(25):252301, 2005.

[48] SciBooNE collaboration. **Search for charged current coherent pion production on carbon in a few-GeV neutrino beam**. *Physical Review D*, **78**(11):112004, 2008.

[49] SciBooNE collaboration. **Improved measurement of neutral current coherent π 0 production on carbon in a few-GeV neutrino beam**. *Physical Review D*, **81**(11):111102, 2010.

[50] MINERνA Collaboration. **Measurement of Coherent Production of $\pi\pm$in Neutrino and Antineutrino Beams on Carbon from E ν of 1.5 to 20 GeV**. *Physical Review Letters*, **113**(26):261802, 2014.

[51] Y. Ajima et al. **Tokai-to-Kamioka (T2K) Long Baseline Neutrino Oscillation Experiment Proposal**, 2006.

[52] T2K Collaboration. **Indication of electron neutrino appearance from an accelerator-produced off-axis muon neutrino beam**. *Physical Review Letters*, **107**(4):041801, 2011.

[53] T2K Collaboration. **Observation of electron neutrino appearance in a muon neutrino beam**. *Physical review letters*, **112**(6):061802, 2014.

[54] T2K Collaboration. **Measurement of neutrino oscillation parameters from muon neutrino disappearance with an off-axis beam**. *Physical review letters*, **111**(21):211803, 2013.

[55] T2K Collaboration. **Measurements of neutrino oscillation in appearance and disappearance channels by the T2K experiment with 6.6 E20 protons on target**. *arXiv preprint arXiv:1502.01550*, 2015.

[56] T2K Collaboration. **Measurement of the inclusive ν μ charged current cross section on carbon in the near detector of the T2K experiment**. *Physical Review D*, **87**(9):092003, 2013.

[57] T2K Collaboration. **Measurement of the Inclusive Electron Neutrino Charged Current Cross Section on Carbon with the T2K Near Detector**. *Physical review letters*, **113**(24):241803, 2014.

[58] T2K Collaboration. **Measurement of the ν_μ CCQE cross section on carbon with the ND280 detector at T2K**. *arXiv preprint arXiv:1411.6264*, 2014.

[59] T2K Collaboration. **Measurement of the inclusive ν_μ charged current cross section on iron and hydrocarbon in the T2K on-axis neutrino beam**. *Phys. Rev. D*, **90**:052010, Sep 2014.

[60] D Beavis, A Carroll, and I Chiang. **Long baseline neutrino oscillation experiment at the AGS**. *Physics Design Report Brookhaven National Lab., Upton, NY.*, **1**, 1995.

[61] T2K Collaboration. **T2K neutrino flux prediction**. *Physical Review D*, **87**(1):012001, 2013.

[62] K Matsuoka, AK Ichikawa, H Kubo, K Maeda, T Maruyama, C Matsumura, A Murakami, T Nakaya, K Nishikawa, T Ozaki, et al. **Design and performance of the muon monitor for the T2K neutrino oscillation experiment**. *Nuclear Instruments and Methods in Physics Research Section A: Accelerators, Spectrometers, Detectors and Associated Equipment*, **624**(3):591–600, 2010.

[63] P-A Amaudruz, M Barbi, D Bishop, N Braam, DG Brook-Roberge, S Giffin, S Gomi, P Gumplinger, K Hamano, NC Hastings, et al. **The T2K fine-grained detectors**. *Nuclear Instruments and Methods in Physics Research Section A: Accelerators, Spectrometers, Detectors and Associated Equipment*, **696**:1–31, 2012.

[64] Nicolas Abgrall, B Andrieu, P Baron, P Bene, V Berardi, J Beucher, P Birney, F Blaszczyk, Alain Blondel, C Bojechko, et al. **Time projection chambers for the T2K near detectors**. *Nuclear Instruments and Methods in Physics Research Section A: Accelerators, Spectrometers, Detectors and Associated Equipment*, **637**(1):25–46, 2011.

[65] S Assylbekov, G Barr, BE Berger, H Berns, D Beznosko, A Bodek, R Bradford, N Buchanan, H Budd, Y Caffari, et al. **The T2K ND280**

off-axis pi–zero detector. *Nuclear Instruments and Methods in Physics Research Section A: Accelerators, Spectrometers, Detectors and Associated Equipment*, **686**:48–63, 2012.

[66] D Allan, C Andreopoulos, C Angelsen, GJ Barker, G Barr, S Bentham, I Bertram, S Boyd, K Briggs, RG Calland, et al. **The electromagnetic calorimeter for the T2K near detector ND280**. *Journal of Instrumentation*, **8**(10):P10019, 2013.

[67] S Aoki, G Barr, M Batkiewicz, J Błocki, JD Brinson, W Coleman, A Dabrowska, I Danko, M Dziewiecki, B Ellison, et al. **The T2K side muon range detector (SMRD)**. *Nuclear Instruments and Methods in Physics Research Section A: Accelerators, Spectrometers, Detectors and Associated Equipment*, **698**:135–146, 2013.

[68] Pavel A Cherenkov. **Visible emission of clean liquids by action of γ radiation**. *Doklady Akademii Nauk SSSR*, **2**:451, 1934.

[69] Rene Brun and Fons Rademakers. **ROOTan object oriented data analysis framework**. *Nuclear Instruments and Methods in Physics Research Section A: Accelerators, Spectrometers, Detectors and Associated Equipment*, **389**(1):81–86, 1997.

[70] Rene Brun, Federico Carminati, Simone Giani, et al. **GEANT detector description and simulation tool**. *CERN program library long writeup W*, **5013**:1993, 1993.

[71] Giuseppe Battistoni, F Cerutti, A Fasso, A Ferrari, S Muraro, J Ranft, S Roesler, and PR Sala. **The FLUKA code: Description and benchmarking**. In *Hadronic Shower Simulation Workshop(AIP Conference Proceedings Volume 896)*, **896**, pages 31–49, 2007.

[72] Marek Gazdzicki, NA61/SHINE Collaboration, et al. **Ion program of NA61/SHINE at the CERN SPS**. *Journal of Physics G: Nuclear and Particle Physics*, **36**(6):064039, 2009.

[73] Yoshinari Hayato. **A neutrino interaction simulation program library NEUT**. *Acta Physica Polonica B*, **40**(9):2477, 2009.

[74] CH Llewellyn Smith. **Neutrino reactions at accelerator energies**. *Physics Reports*, **3**(5):261–379, 1972.

[75] RA Smith and EJ Moniz. **Neutrino reactions on nuclear targets**. *Nuclear Physics B*, **43**:605–622, 1972.

[76] Dieter Rein and Lalit M Sehgal. **Coherent π^0 production in neutrino reactions**. *Nuclear Physics B*, **223**(1):29–44, 1983.

[77] D Rein and LM Sehgal. **PCAC and the Deficit of Forward Muons in $\pi+$ Production by Neutrinos**. *Physics Letters B*, **657**(4):207–209, 2007.

[78] M Glück, E Reya, and A Vogt. **Dynamical parton distributions revisited**. *The European Physical Journal C-Particles and Fields*, **5**(3):461–470, 1998.

[79] A Bodek and UK Yang. **Modeling neutrino and electron scattering inelastic cross sections**. *arXiv preprint hep-ex/0308007*, 2003.

[80] Torbjörn Sjöstrand. **High-energy-physics event generation with PYTHIA 5.7 and JETSET 7.4**. *Computer Physics Communications*, **82**(1):74–89, 1994.

[81] Costas Andreopoulos, A Bell, D Bhattacharya, F Cavanna, J Dobson, S Dytman, H Gallagher, P Guzowski, R Hatcher, P Kehayias, et al. **The GENIE neutrino monte carlo generator**. *Nuclear Instruments and Methods in Physics Research Section A: Accelerators, Spectrometers, Detectors and Associated Equipment*, **614**(1):87–104, 2010.

[82] Arie Bodek and JL Ritchie. **Fermi-motion effects in deep-inelastic lepton scattering from nuclear targets**. *Physical Review D*, **23**(5):1070, 1981.

[83] Arie Bodek and UK Yang. **Higher twist, ξw scaling, and effective LO PDFs for lepton scattering in the few GeV region**. *Journal of Physics G: Nuclear and Particle Physics*, **29**(8):1899, 2003.

[84] T Yang, C Andreopoulos, H Gallagher, K Hofmann, and P Kehayias. **A hadronization model for few-GeV neutrino interactions**. *The European Physical Journal C-Particles and Fields*, **63**(1):1–10, 2009.

[85] The ND280 NuMu Group. **CC multiple pion nu-mu event selections in the ND280 tracker using Run 1+2+3+4 data**. T2K Technical note TN-152, available upon request.

[86] Antonin Vacheret, Sarah Greenwood, Matt Noy, Mark Raymond, and Alfons Weber. **The front end readout system for the T2K-ND280 detectors**. In *Nuclear Science Symposium Conference Record, 2007. NSS'07. IEEE*, **3**, pages 1984–1991. IEEE, 2007.

[87] The ND280 NuMu Group. **ν_μ CC event selections in the ND280 tracker using Run 2+3+4**. T2K Technical note TN-212, available upon request.

[88] The ND280 NuMu Group. **CCQE-like and CC-non-QE-like NuMu event selections in the ND280 tracker using Run 1+2 data**. T2K Technical note TN-093, available upon request.

[89] C Giganti and M Zito. **Particle Identification with the T2K TPC**. T2K Technical note TN-001, available upon request.

[90] J Mysilik. **Determination of pion secondary interaction systematics for the ND280 tracker ν_μ analysis**. T2K Technical note TN-125, available upon request.

[91] F Dufour, L Haegel, T Lindner, and S Oser. **Systematics on Out-of-Fiducial-Volume Backgrounds in the ND280 Tracker**. T2K Technical note TN-098, available upon request.

[92] MiniBooNE collaboration. **Measurement of ν μ-induced charged-current neutral pion production cross sections on mineral oil at E ν 0.5–2.0 GeV**. *Physical Review D*, **83**(5):052009, 2011.

[93] MiniBooNE collaboration. **Measurement of ν μ and ν^- μ induced neutral current single π 0 production cross sections on mineral oil at E ν O (1 GeV)**. *Physical Review D*, **81**(1):013005, 2010.

[94] C Ciofi Degli Atti and S Simula. **Realistic model of the nucleon spectral function in few-and many-nucleon systems**. *Physical Review C*, **53**(4):1689, 1996.

[95] Giulio D'Agostini. **A multidimensional unfolding method based on Bayes' theorem**. *Nuclear Instruments and Methods in Physics Research Section A: Accelerators, Spectrometers, Detectors and Associated Equipment*, **362**(2):487–498, 1995.

[96] Tim Adye. **Unfolding algorithms and tests using RooUnfold**. *arXiv preprint arXiv:1105.1160*, 2011.

[97] A Furmanski et al. **Model-independent CC0π cross section measurement on carbon using unfolding**. T2K Technical note TN-215, available upon request.

[98] K Abe, T Abe, H Aihara, Y Fukuda, Y Hayato, K Huang, AK Ichikawa, M Ikeda, K Inoue, H Ishino, et al. **Letter of Intent: The Hyper-Kamiokande Experiment—Detector Design and Physics Potential—**. *arXiv preprint arXiv:1109.3262*, 2011.

[99] T Koseki. **J-PARC Accelerator status, capacity and future pla**, 2014. 2nd international symposium on science at J-PARC.

[100] M Yeh, S Hans, W Beriguete, R Rosero, L Hu, RL Hahn, MV Diwan, DE Jaffe, SH Kettell, and L Littenberg. **A new water-based liquid scintillator and potential applications**. *Nuclear Instruments and Methods in Physics Research Section A: Accelerators, Spectrometers, Detectors and Associated Equipment*, **660**(1):51–56, 2011.

[101] F Sanchez and M Ravonel. **High pressure TPC**, 2014. Near detector workshop at J-PARC.

[102] S Bhadra, A Blondel, S Bordoni, A Bravar, C Bronner, J Caravaca-Rodriguez, M Dziewiecki, T Feusels, GA Fiorentini-Aguirre, M Friend, et al. **Letter of Intent to Construct a nuPRISM Detector in the J-PARC Neutrino Beamline**. *arXiv preprint arXiv:1412.3086*, 2014.

[103] M Vagins. **Gadolinium studies in Mozumi**, 2015. 6th Hyper-K Collaboration Meeting.

[104] K Abe, J Adam, H Aihara, T Akiri, C Andreopoulos, S Aoki, A Ariga, S Assylbekov, D Autiero, M Barbi, et al. **Neutrino Oscillation Physics Potential of the T2K Experiment**. *arXiv preprint arXiv:1409.7469*, 2014.